UNIVERSITÉ DE GRENOBLE

THÈSE

Pour obtenir le grade de

DOCTEUR DE L'UNIVERSITÉ DE GRENOBLE

Spécialité : **Physique de la matière condensée et du rayonnement**

Arrêté ministériel : 7 août 2006

Présentée par

Alexandra PALACIO MORALES

Thèse dirigée par **Daniel BRAITHWAITE**
et codirigée par **Alexandre POURRET**

préparée au sein **du Service de Physique Statistique, Magnétisme et Supraconductivité (SPSMS) au CEA Grenoble**
et de **l'École Doctorale de Physique, Grenoble**

Thermoélectricité des composés fortement corrélés sous conditions extrêmes

Thèse soutenue publiquement le **07 novembre 2014**,
devant le jury composé de :

Dr. Marc-Henri JULIEN
CNRS, LNCMI Grenoble, Examinateur, Président
Prof. Hermann SUDEROW
Universidad Autónoma de Madrid, LBT , Rapporteur
Dr. Sylvie HEBERT
CNRS, CRISMAT, Rapporteur
Prof. Didier JACCARD
Université de Genève, Examinateur
Dr. Daniel BRAITHWAITE
CEA Grenoble, Directeur de thèse
Mcf. Alexandre POURRET
UJF Grenoble, Co-Directeur de thèse

Thermopower under Extreme Conditions in Strongly Correlated Electron Systems

Alexandra PALACIO MORALES

Abstract

Thermopower is a technique whose importance is related to the possibility of directly measuring electronic properties of the systems, as it is sensitive to the derivative of the density of states. In this work, the low temperature regime of strongly correlated electron systems has been studied using this technique. For that, a new pressure-field thermopower device was developed, and used, to determine (T, P, H) phase diagrams of the itinerant ferromagnets UCoAl and UGe_2, and of the weak antiferromagnet $CeRh_2Si_2$.

For example, in the case of UCoAl, this same technique was used to analyze the metamagnetic transition from paramagnetic (PM) to ferromagnetic (FM) phases and to study its evolution towards the quantum critical end point. The existence of exotic magnetic excitations in the ground state and around the critical end point were also evidenced.

On the compound $CeRh_2Si_2$, the suppression of the antiferromagnetic (AF) order by magnetic field and pressure was explored. A strong change of the Fermi surface at H_c, the field at which the suppression of the AF into the paramagnetic polarized (PPM) phase, was observed. We also show that under pressure, the magnetic fluctuations around the critical pressure P_c masked the Fermi surface reconstruction of the AF phase into the PM phase. The analysis of the (T, P, H) phase diagram revealed that the non-ordered phases of this compound (PM and PPM) are different, therefore pressure and field behave as different suppressor mechanisms.

In the UGe_2 compound, the analysis of its Fermi surface by thermopower quantum oscillations was performed as a last example of the utility and of the importance of this technique. To the best of the author knowledge, this is the first time that this technique was used in heavy fermion systems. A comparison to traditional probes such as de Haas-van Alphen and Shubnikov–de Haas effects was done. We observed a good agreement between them and we explain the advantages and the disadvantages of thermopower quantum oscillations technique over the traditional probes.

Keywords
Strongly Correlated Electron Systems - Heavy Fermions
Quantum Criticality
Thermoelectric Coefficients
Fermi Surface Mapping
Extreme Conditions: Low Temperatures, High Magnetic Fields and High Pressures

Acknowledgements
Remerciements

La première chose qui me vient à la tête après avoir fini la thèse, c'est la grande chance que j'ai eu d'avoir pu faire partie d'un si bon laboratoire, le SPSMS.

Je voudrais remercier, en premier lieu, les membres du jury Sylvie Hebert, Hermann Suderow, Didier Jaccard et Marc-Henri Julien pour avoir accepté de faire partie d'un jour si important pour moi. Un grand merci à tous pour avoir lu soigneusement mon manuscrit de thèse; j'ai beaucoup apprécié tous vos commentaires et remarques.

Daniel et Alexandre, merci beaucoup pour m'avoir accepté comme thésarde et aussi d'avoir partagé avec moi les techniques dans lesquelles vous êtes des spécialistes reconnus. Georg sans tes mesures de SdH et tes connaissances des oscillations quantiques, je n'aurais jamais pu finir sans ça; merci beaucoup. An important aspect of my work was the extremely good quality samples I used, Dai and Tristan, thank you very much for giving me so good crystals. Pas de technique ni d'échantillon dans votre cas, Jean-Pascal et Jacques, mais des tonnes de connaissances qui ont su donner de la cohérence à mon projet de thèse. Vôtres investissements dans ma thèse m'ont fait énormément plaisir.

D'un point de vue technique, ma thèse n'aurait pas pu être possible sans l'aide de Jean Michel et Iulian. Merci beaucoup pour avoir été toujours disponible à m'aider et à résoudre les problèmes avec les dilutions. Travailler avec vous a été un plaisir. Merci Marie-Jo, Michel, Pierre, Poletti et Marielle pour le support technique et/ou fournissement de matériel. A toute l'équipe du D5, merci beaucoup pour bien veiller à notre sécurité anti-Uranium et rayons-X et pour la sécurité cryogénie un grand merci à Jean-Luc.

Scheilla y Eduardo, muchísimas gracias de todo corazón. Sin vosotros estos dos últimos años de tesis no hubieran sido los mismos. Scheilla te estoy muy agradecida por todo el esfuerzo y empeño que has puesto en nuestra celda Bridgman, así como, por todo el tiempo que me has dedicado cada vez que te realizaba alguna pregunta. Gracias también por la rigurosidad que te caracteriza, no la pierdas nunca. Eduardo thank you very much for everything; I spent a very good time with you in the office and I learned a lot of your experience. I wish you all the best and lots of luck.

I will also like to acknowledge Yusei, thank you for bringing the japanese culture to the lab; Mathieu et Amalia, pour m'avoir reçue avec les bras ouvertes et me faire sentir comme chez moi en votre compagnie dans le laboratoire, Mounir, sans toi ces trois années auraient été insupportables, Beilun et Gaël je vous souhaite à tous les deux une très bonne continuation et une très bonne chance pour la suite.

Hopefully, I had the opportunity to work at the LNCMI de Grenoble with Gabriel and

Steffen and at the ESRF with Andrei and Fabrice. I learned a lot of new things during these experiments, thank you very much for giving me these opportunities. I will also thank Profs. Onuki, Araki and Mike for your useful advices related to $CeRh_2Si_2$.

Claude, Xavier, François, Max, Marc, Bernard, Louis, Silvano, Christophe, Vladimir, Andrea, Salha, Paul, Anaïs, Andreas, Alexander, Dibyendu, Alexandre A., Alexandre B., Toai, Charlène, Benoit V., Benoit R., Audrei, Eduard, Patrick, Juan Carlos... I am sorry if I forgot someone in this long list of names. All of you have been involved for different reasons in my thesis, thank you very much for your help.

My last words are dedicated to my family and Jean-Eudes. A vosotros os dedico mi tesis; gracias por estar constantemente a mi lado, al frente de cada nuevo día. Os quiero muchísimo.

Contents

Introduction

Contex and Motivations

Heavy fermions are a family of strongly correlated electron systems behaving like Fermi liquids with renormalized parameters, notably the electronic effective mass. This renormalization is due to the presence of magnetic moments coming from the partially filled f orbitals, close to the Fermi energy, of lanthanide or actinide atoms. Indeed, the f shells can hybridize with broader bands such as s, p and d bands leading to competing magnetic orders on the system. This competing order can be explained, in general, through the Doniach phase diagram and a special interest is focused on the study of quantum critical points. In addition, heavy fermion compounds have a Fermi energy that is quite small, contrary to other strongly correlated electron systems such as High-Temperature superconductors (like cuprates or pnictides systems) that also present competing orders. The low Fermi energy of heavy fermion systems gives the opportunity to explore this competition quite easily by applying pressure, doping and magnetic field as external parameters. This easy access made that these systems became so popular.

From an experimental point of view, heavy fermions are very challenging as extreme conditions, i.e, low temperatures, high pressures/doping and/or high magnetic fields are required to study their physical properties. To carry out that study, we choose pressure rather than chemical doping as control parameter as pressure is a clean one to tune the system; it does not introduce disorder. In addition, pressure can be applied in a controlled and almost reversible way.

During the last years, thermopower get a renewed interest to study strongly correlated electron systems. It has been demonstrated that this probe gives significant information about phase transitions and electronic properties at low temperatures. The aim of this thesis is to study the family of heavy fermion compounds by thermopower measurements. One of the strong aspects of this thesis was to develop an adequate pressure-thermopower setup in the low temperature and high magnetic field conditions to study the competing orders induced by pressure in those systems. Indeed, the different physical phenomena that arise near a quantum critical point like suppression/appearance of magnetic order, non Fermi liquid behavior and/or superconductivity, generally exhibit a strong pressure dependence. Moreover, this thesis was also focused on the understanding of magnetic phase transitions induced by magnetic fields using thermopower as mainly probe. Finally, the low noise thermopower measurements and the temperature and field extreme conditions of the experiments carried out during this thesis yielded to the determination of the parameters of the Fermi surface *via* thermopower quantum oscillations.

The thermopower studies presented in this thesis are focused on the heavy fermion compounds UGe_2, UCoAl and $CeRh_2Si_2$. These studies concern the analysis, from the thermopower point of view, of the topology of the Fermi surface of the ferromagnetic phase of UGe_2, the analysis of the magnetic structure called "wing structure" in UCoAl and the comparison of the suppression of the antiferromagnetic ground state of $CeRh_2Si_2$ by magnetic field and pressure.

Plan of the thesis

This thesis is divided in five chapters. The first chapter gives an overview of the theoretical background for understanding the physics of the heavy fermion systems. It also describes the thermopower models and the information obtained from the thermoelectric coefficients. The second chapter explains the different probes and extreme conditions of pressure, magnetic field and temperature under which the measurements were carried on. Each of the following chapters are focused on the study of one compound. Chapter 3 shows the measurements of UCoAl. The study of the metamagnetic transition induced by magnetic field and of the wings under pressure are shown in the first and second parts of this chapter, respectively. Chapter 4 is dedicated to the FM2 phase of UGe_2 determined by thermopower quantum oscillations technique. The last chapter presents the results of $CeRh_2Si_2$. This chapter is also divided into two sub-chapters; the first focuses on the suppression of the antiferromagnetic order of this compound by magnetic field and the second one on the suppression of the antiferromagnetic order by pressure. We finish with the general conclusion of the thesis.

Chapter 1

Physical Background

In this chapter, I expose briefly the physical concepts that will be useful for the understanding of this thesis. First, I introduce heavy fermion systems and the Fermi liquid theory. Second, I discuss the different competing ground states and the complex phase diagrams that occur at low temperature in these systems. A brief description of the breakdown of the Fermi liquid theory is exposed in the third part. In the last one, I show the Seebeck and Nernst coefficients used as a probe to study the properties of heavy fermion systems.

1.1 Heavy Fermions

[1] Heavy fermion systems were discovered in the 70's with the appearance of inter-metallic compounds such as $CeAl_3$ characterized by electronic excitations with an effective mass as much as 1000 times larger than normal metals. These materials have become the focus of intense research as they can be easily tuned to quantum phase transitions by external

[1] This introduction is inspired from [Coleman, 2007, Stewart, 1984, Flouquet, 2005] in which more details can be found.

parameters such as pressure, magnetic field or chemical doping. Actually, this is due the high Grüneisen[2] exponent, which in turn is due to a small Fermi energy.

Heavy fermion compounds are itinerant intermetallic compounds characterized by including rare earth or actinide atoms in their chemical composition. Their ground state can be non-ordered such as $CeAl_3$ or ordered such as $CeIn_5$. In the case of an ordered ground state, the magnetic moment is due to the incomplete f shell of the previous atoms. The magnetic moment may be considered as localized in these systems as the radial probability of the f electrons appears close to the nucleus. Sometimes, heavy fermions present itinerant magnetism due to the coupling between the magnetic f shells and the electronic properties given by the incomplete and large volume s, p or d orbitals. This coupling is produced when the energy of the f band is close to the Fermi energy and it is analyzed by the hybridization mechanism called "Kondo effect". It occurs at temperatures lower than a characteristic temperature, the Kondo temperature T_K. The Kondo effect describes the process by which a free magnetic ion becomes screened by the spins of the conduction electrons to form a spinless scattering center at low temperatures and low magnetic fields. This screening process is continuous. Above T_K, the no direct overlap of the f shells indicates that the f electrons can be treated as completely localized impurities in the lattice with a Fermi sea given by the electrons of the s, p, d bands.

In addition, this overlapping induces an increase of the electronic effective mass increases due to interactions; i.e., the delocalization of the f electrons induces strong correlations in the conduction electrons and then the formation of itinerant quasi-particles which present a large effective mass. This was observed in the electronic specific heat measurements that achieve values of the order of hundreds of $mJmol^{-1}K^{-1}$. The existence of these high effective masses was also verified by the de Hass-van Alphen effect (dHvA) that shows the formation of heavy quasi-particles. Heavy fermion systems can have effective masses of the order of $m^* \sim 10 - 1000m_0$ with m_0 the electron mass. In fact, the f electrons are responsible for the rich variety of electronic phases of heavy fermion systems. For example, heavy fermion compounds display an interplay between magnetism and superconductivity.

Heavy fermion systems can be described by the Fermi liquid theory below a coherence temperature appearing in the low temperature regime $T_{coh} \sim 10K$. As a result of the strong correlations, this theory renormalizes the parameters of the Fermi gas theory into quasi-particles with high effective mass. The strong renormalization of the mass induces a reduction of the Fermi temperature down to $T_F \sim 10K$ which is quite small compared to the Fermi temperature of normal metals $T_F \sim 1000K$. This leads to a greater sensitivity of the ground state to low excitations induced by external parameters (pressure, magnetic field...).

Fermi Liquid Theory

[3] The Fermi liquid theory is a many-body theory that treats the metals as condensed Fermi gases; e.g., a Fermi gas (non-interacting system) with short-range interactions. The ground state of the interacting Fermi liquid is obtained by forming quasi-particles adiabatically with a distinct mass. Fermi liquid theory is valid at low temperature, much lower than the Fermi

[2] Grüneisen exponent is defined as the ratio of the volume thermal expansion to the specific heat, $\Gamma = \beta/C_p$.

[3] The Fermi liquid theory explanation is inspired from refs. [Abrikosov and Khalatnikov, 1959] and [Schulz, 1995] in which more details can be found.

energy, $T_F/10$, in the normal state. In addition, there is no phase transition or broken symmetry reaching this regime.

Landau theory considers the conduction electrons and their interactions as quasi-particles. These quasi-particles conserve the spin, the charge and the momentum of the Fermi gas while a renormalization of the mass of the quasi-particles is produced as a result of the tiny interactions between the almost free electrons. The condensation of these quasi-particles moves the system from a Fermi gas to a Fermi liquid because it entails non free movements of the quasi-particles unlike in Fermi gases. This occurs when the interactions (magnetic moments, Coulomb repulsion, Pauli principle...) start to be significantly large due to the short distance and the static positions.

As a consequence, the thermodynamic quantities of the Fermi gas will be renormalized for the Fermi liquid regime. Here, we focus on the specific heat γ:

$$\gamma_0 = \frac{2\pi^2}{3} g(E_F) k_B^2 T = \frac{m_0 k_F}{3} k_B^2 T \tag{1.1}$$

with $g(E_F) = k_F m^*/2\pi^2$. In the Fermi liquid regime, it can be re-written as:

$$\gamma = \frac{m^* k_F}{3} k_B^2 T = \gamma_0 \frac{m^*}{m_0} = \gamma_0 (1 + \frac{F_1^s}{3}) \tag{1.2}$$

with m_0 the mass of the free electron, m^* the effective mass and F_1^s the Landau parameter of first order interactions.

The signature of Fermi liquid in heavy fermion systems is related to the approximate validity of the scaling relations:

$$\frac{\chi}{\gamma} \approx cts \qquad \frac{A}{\gamma^2} \approx cts \tag{1.3}$$

with χ the Pauli susceptibility, γ the electronic specific heat and A the coefficient of the T^2 resistivity-law ($\rho = \rho_0 + AT^2$). The first ratio is called Wilson ratio (R_W) and the second one Kadowaki and Woods (KW) ratio.

1.2 Competing Orders

The origin of the competition between different ordered ground states is based on the hybridization of the partially filled f orbitals with the conduction electrons which is a main characteristic of heavy fermion systems. The hybridization of the f electrons can be dominated by Ruderman-Kittel-Kasuya-Yosida (RKKY) interaction or dominated by Kondo interaction. The result is that these f states, which in principle present a localized behaviour, can become itinerant. Thus, the hybridization governs the itinerant/localized character of the magnetization of the compound which can be explained by the Doniach Phase diagram through the J^W coupling constant as both interactions, RKKY and Kondo, depend on this parameter. The J^W coupling constant, magnetic exchange parameter, can be modified by external parameters such as pressure, doping or magnetic field. Moreover, special attention will be put into quantum phase transitions and quantum criticality.

1.2.1 Doniach Phase Diagram: RKKY vs Kondo

The RKKY interaction is a long range interaction between the localized magnetic moments of a lattice mediated by the conduction electrons. The interaction is extended over a long range and it is damped with a sinusoidal oscillation of wave vector k_F as shown the model of the RKKY interaction represented in Fig.1.1 -left. Here, the localized atoms are represented in grey and the conduction electrons in yellow. Depending on the distance between the magnetic moments, the interaction can be antiferromagnetic or ferromagnetic [Ruderman and Kittel, 1954]. This interaction appears for temperatures below:

$$T_{RKKY} = J^2 g(E_F) \frac{cos(k_F r)}{(k_F r)^3} \tag{1.4}$$

with $g(E_F)$ the density of states, J^W the coupling constant between the spin wave functions and k_F the Fermi wave vector of the conduction electrons.

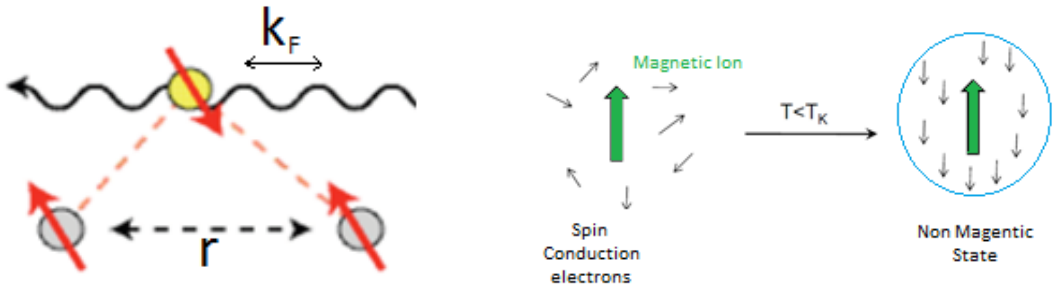

Figure 1.1: *Simple pictures of the RRKY (left) and Kondo (right) interactions.*

The Kondo effect describes the process by which the localized magnetic ions of a lattice becomes screened by the spins of the conduction electrons to ultimately form a spinless scattering center at low temperature and low magnetic field (Kondo singlet) [Kondo, 1964]. This interaction can be expressed by the Hamiltonian:

$$H_K = -2J\overrightarrow{S} \cdot \overrightarrow{s} \tag{1.5}$$

which describes the scattering of conduction electrons, with spin $\overrightarrow{s}$, to the local magnetic moment of the impurity, $\overrightarrow{S}$. J^W represents the strength of the interaction between $\overrightarrow{s}$ and $\overrightarrow{S}$. In the Kondo effect, the screening process, which entails antiferromagnetic coupling, is continuous. It takes place once the temperature drops below a characteristic energy scale, the Kondo temperature T_K. T_K is given by:

$$T_K \propto Dexp\left(-\frac{1}{J^2 g(E_F)}\right) \tag{1.6}$$

The "quench" of the magnetic moments acts as strong elastic scattering potentials for conduction electrons, which gives rise to an increase of the resistivity produced by isolated magnetic ions (single Kondo impurity). When the same process takes place inside a heavy electron material, it leads to a spin quenching at every site in the lattice, but now, the strong coherence scattering leads to a sudden drop in the resistivity at low temperatures (Kondo lattice). As

shown in [Sumiyama et al., 1986], these single Kondo impurity and Kondo lattice behaviours depend on the magnetic doping concentration in the system. In Fig.1.2, resistivity measurements for different concentrations of Ce (magnetic atom) in $Ce_xLa_{1-x}Cu_6$ are shown. At low doping concentration, dopants behave as isolated impurities and the resistivity behaviour is the one shown in red color (single Kondo impurity). If the concentration increases high enough, the dopants show a lattice organization, then the system is considered as a Kondo lattice and the resistivity behaviour is the one shown by the blue curve.

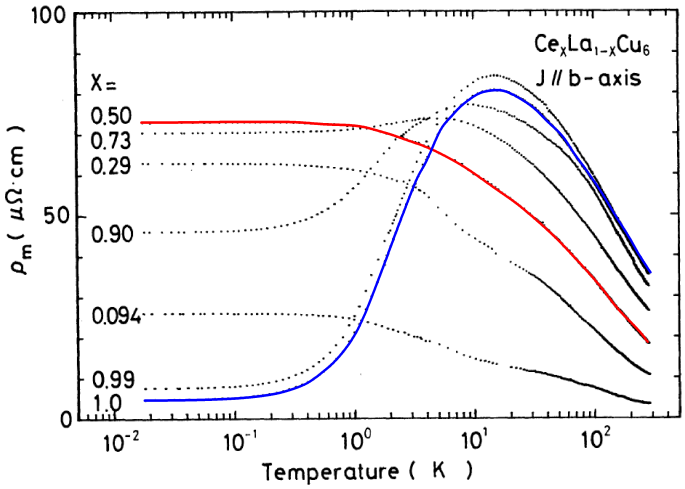

Figure 1.2: *Resistivity measurements for $Ce_xLa_{1-x}Cu_6$. Increasing the Ce concentration the system moves from single Kondo impurity (red curve) to Kondo lattice (blue curve) [Sumiyama et al., 1986].*

The Doniach phase diagram shows the competition between RKKY and Kondo interactions as a function of the J^W coupling constant. The interactions from which both competing orders depend on can be represented by pressure, doping or magnetic field as these external

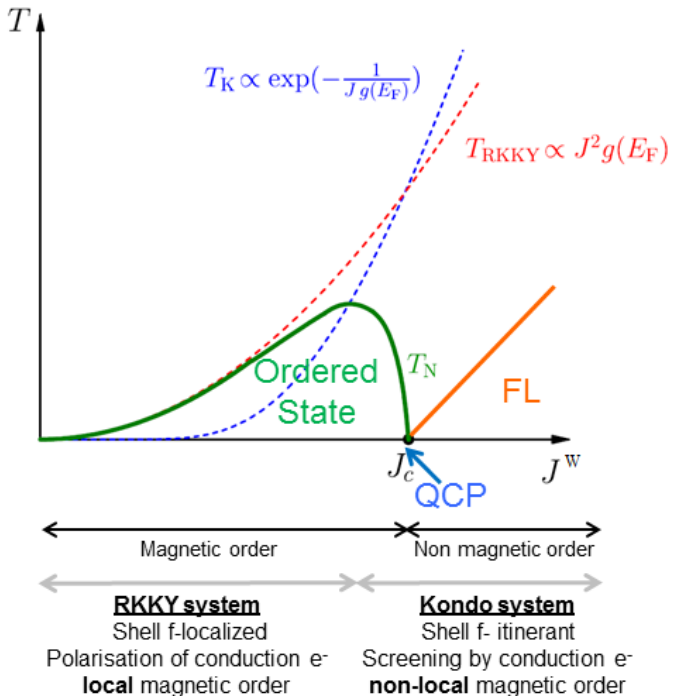

Figure 1.3: *The Doniach phase diagram illustrates the competition between RKKY and Kondo interactions as a function of the J^W coupling contant. The image was taken from [Doniach, 1977].*

parameters modify the value of J^W [Doniach, 1977]. Their temperature scales T_{RKKY} and T_K are shown in red and blue lines, respectively, in Fig.1.3. At low values of J^W, the RKKY interaction dominates and then the ground state of the system will be magnetic whereas when the Kondo interaction dominates (high values of J^W), the ground state will be a non-magnetic one. Heavy fermion systems are characterized by having a value of J^W for which the T_{RKKY} and the T_K are quite similar. Consequently, in heavy fermion systems small changes in the J^W coupling constant can tune the system from magnetic to non magnetic orders crossing a QCP. In the frontier region, quantum critical fluctuations lead to exotic behaviours such as non-Fermi liquid behaviour or unconventional superconductivity.

1.2.2 Quantum Criticality in Heavy Fermions

[4] Many classical phase transitions are obtained by increasing temperature. They are driven by thermal fluctuations and occur at finite critical temperature. When the critical temperature is brought to the limit $T \to 0$, we find what we call quantum phase transitions. In this limit, the ground state undergoes a continuous transition from one phase to another driven by a non-thermal mechanism. Often we speak about the enhanced role of quantum fluctuations in the experimental phenomena observed close to a quantum critical point. For example, when a magnetic phase transition is brought down to zero temperature by some means (pressure, doping or magnetic field), the quantum fluctuations related to the transition, identified as low energy excitations, present an infinite correlation length, ξ, and an infinite correlation time, τ_0, that cover the entire material. ξ and τ_0 scale as $\tau_0 \propto \xi^z$ with z the dynamic exponent.

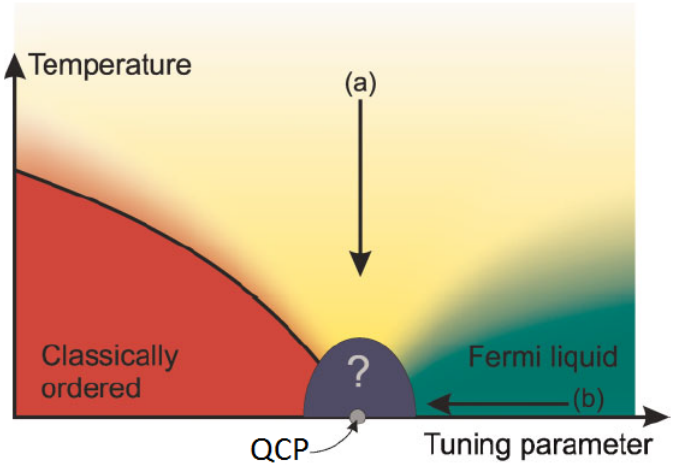

Figure 1.4: *Schematic phase diagram of a quantum critical metal. The phase labeled "?" represents a novel phase centered over the quantum critical point. (a) and (b) arrows indicate temperature and non-thermal tunning parameter approaches to the QCP. The image was taken from [Schofield, 2010].*

In Fig.1.4, temperature-tuning parameter phase diagram (T, δ) is shown. We observe that as δ increases, the system moves from an ordered to a non-ordered state crossing the QCP. Approaching the QCP by varying δ will lead to a divergence of the spatial correlation length.

[4] This subsection is inspired from [Gegenwart and Steglich, 2008, Si and Steglich, 2010] in which more details can be found.

If the approach to the QCP is done by the reduction of the temperature, then an increase of the size of the temporal dimension β with $\beta = 1/k_B T$ towards infinity, due to $T \to 0$, is produced.

Around the QCP the standard theory of metals can break down. The fluctuations related to the quantum criticality serve as a mechanism for novel condensed matter behaviours such as non-Fermi liquid or phases such as unconventional superconductivity. The signature of the QCPs has been deeply studied; the violation of the standard theory of metals has been observed in the divergence of the specific heat and the Grüneisen exponent and in a sudden reconstruction of the Fermi surface and/or in the vanishing of multiple energy scales. The strong accumulation of entropy in the vicinity of the QCP is supposed to be responsible for the appearance of new electronic phases.

There are two classes of quantum criticality for heavy fermion systems; the first one which consists in the extension of the standard theory of second order transitions to the quantum case and the second one that involves new critical quantum mechanical excitations. They are called spin-density-wave type and critical Kondo breakdown, respectively. The critical Kondo breakdown is characterized by the destruction of the Kondo effect entering in the AF phase from the PM phase. As a consequence, the slow fluctuations of the AF order parameter and the degrees of freedom associated with the breakup of the Kondo singlet will be incorporated at the QCP. The spin-density-wave QCP type presents only fluctuations related to the magnetic order. These two scenarii of quantum criticality can be also differentiated as a function of the energy scale E^*_{loc}. This E^*_{loc} generates the breakup of the entangled Kondo single states as the system moves from the heavy-Fermi liquid side toward the quantum critical regime. In the case E^*_{loc} ends up the QCP (δ_c), we have the critical Kondo destruction case and when the ordered line intersects with the E^*_{loc} the magnetic QCP falls in the category of the spin-density-wave theory. Experiments are still ongoing to test these theories.

1.3 Non-Fermi Liquid Theory

[5]The term non-Fermi liquid is used to describe a system which displays breakdown of Fermi-liquid behaviour instead of the expected Fermi-liquid behaviour. In heavy fermion systems, this behaviour appears close to the QCPs or under exotic magnetic ground states in which there are strong spin or valence fluctuations which, in turn, induce strong deviations from the Fermi liquid behaviour.

Concerning the analysis around the QCP, the renormalization group theory is a very powerful technique for studying strongly interacting systems. It emerged from the renormalization of the quantum field variables. It is a mathematics apparatus that allows investigation of the changes of the physical system by the re-scale of the energy while it maintains invariant the symmetries of the system. For that, the renormalization group theory maps an action, characterized by a certain set of coupling constants, to a new action where the values of the coupling constants have changed in two steps. First, an integration over the high-momentum degrees of freedom is carried out, where the effect of this integration is absorbed in the coupling constants of the action. Second, a rescaling of all momenta and fields is performed to bring

[5]This section is inspired from [Moriya and Kawabata, 1973, Millis, 1993] in which more details can be found.

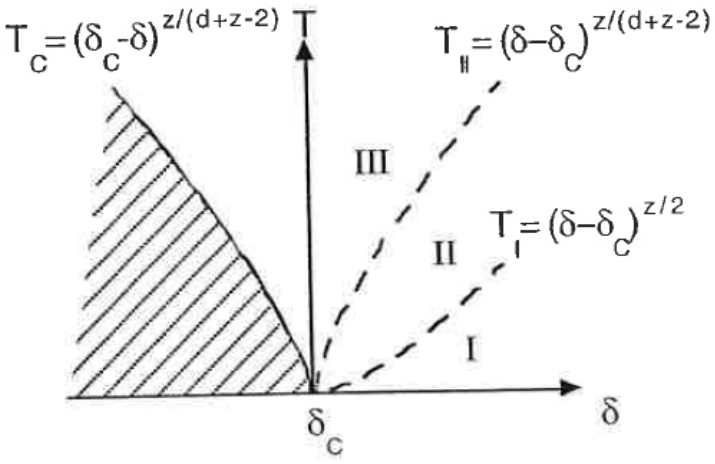

Figure 1.5: (T, δ) *phase diagram obtained by renormalization group theory [Millis, 1993].*

the relevant momenta of the action back to their original domain. To apply this mathematics into real systems, the systems are studies from a macroscopic point of view with microscopic degrees of freedom eliminated or integrated in a quantum effective field theory. This technique analyses the properties involving long wavelengths or small fluctuations energies. In strongly correlated systems, the invariant symmetry can be the QCP. The re-scaling energy allow to observe different scale of critical fluctuations approaching the QCP. In Fig.1.5, we show the (T, δ) phase diagram close to a QCP obtained by the renormalization group theory. The dashed area corresponds to the magnetic ordered state that appears below T_C. The region III is the classical Gaussian regime in which the thermal fluctuations govern; the region II is the perturbative classical regime and the region I corresponds to the quantum regime in which a Fermi liquid regime is expected. The temperature laws as a function of the control parameter depend on the difference between the control parameter and its value at the QCP $(\delta - \delta_C)$, the dynamic exponent z (with $z = 2$ for AF state and $z = 3$ for FM state) and the spatial dimension of the system.

		C/T	$\rho \sim T^n$
FM	3d	$-ln(T)$	$T^{5/3}$
	2d	$T^{-1/3}$	$T^{4/3}$
AF	3d	$T^{1/2}$	$T^{3/2}$
	2d	$-ln(T)$	T

Table 1.1: *Temperature variations of specific heat C/T and resistivity ρ in the non-Fermi liquid regime for a ferromagnetic (FM) and paramagnetic (AF) systems. The d parameter corresponds to the number of geometric dimensions of the fluctuations.*

Experimentally, the non-Fermi liquid behaviour was identified with a logarithmic divergence of the γ value at low temperatures, the non saturation of the susceptibility χ or with an evolution of the resistivity with temperature as $\rho = \rho_0 + AT^n$ with $n < 2$. A mathematical approach to the non-Fermi liquid behaviour was performed by the renormalization group theory. This theory calculated the temperature evolution of the specific heat C/T and

resistivity ρ for two and three dimensional spin fluctuations in ferro- (FM) or antiferromagnet (AF) systems. These temperature dependence laws are given in Table 1.1.

1.4 Thermoelectric Coefficients

1.4.1 Seebeck Coefficient

[6] The Seebeck effect is the longitudinal electrical response to a longitudinal thermal gradient. The magnitude of the Seebeck coefficient is directly dependent on the transport properties of the system. It measures the entropy of the system, then it should be equal to 0 at $T = 0$. It can be expressed from the linear response of the electrical j^e and thermal j^q currents when the electrical current in the system is $j^e = 0$. We know that the thermal current density, j^q, is just the product of the temperature with the entropy current density, j^s:

$$j^q = Tj^s. \tag{1.7}$$

Since the volume is fixed, the changes in the entropy are related to changes in the internal energy and in the number of electrons by the thermodynamic identity:

$$TdS = dU - \mu dN \equiv Tj^s = j^\varepsilon - \mu j^n \tag{1.8}$$

thus, the electrical and thermal current densities in the linear response can be written as:

$$j^e = L^{11}\varepsilon + L^{12}(-\nabla T) \tag{1.9a}$$
$$j^q = TL^{21}\varepsilon + TL^{22}(-\nabla T) \tag{1.9b}$$

with L^{ij} defined in terms of $\xi^\alpha = e^2 \int \frac{dk}{4\pi^3}\left(\frac{\partial f}{\partial \varepsilon}\right)\tau(\varepsilon(k))$. ξ^α can be expressed, at the same time, in terms of electrical conductivity $\sigma(\varepsilon)$. As a result, the L^{ij} in terms of $\sigma(\varepsilon)$ are:

$$L^{11} = \xi^0 = \sigma(\varepsilon_F) = \sigma \tag{1.10a}$$
$$L^{21} = -\frac{1}{e}\xi^1 = TL^{12} = -\frac{\pi^2}{3e}(k_B T)^2\sigma' \tag{1.10b}$$
$$L^{22} = \frac{1}{e^2 T}\xi^2 = \frac{\pi^2}{3}\frac{(k_B^2 T)}{e^2}\sigma \tag{1.10c}$$

where $\sigma' = \frac{\partial}{\partial \varepsilon}\sigma(\varepsilon)|_{\varepsilon_F}$. We notice that these equations are valid for multiband compounds because $\sigma(\varepsilon) = \sum_{ij}\sigma_{ij}(\varepsilon)$. We note that eqs. 1.10a and 1.10c correspond to the Ohm's law ($\mathrm{j}^e = \sigma\varepsilon$) and the Wiedemann-Franz law ($L = \frac{\kappa}{\sigma T} = \frac{L^{22}}{\sigma T} = 2.44 \cdot 10^{-8} W\Omega K^{-2}$), respectively.

In terms of the conductivity tensors σ (electrical conductivity), α (Peltier coefficient) and κ(thermal conductivity) the equations become:

$$j^e = \sigma\varepsilon + \alpha(-\nabla T) \tag{1.11a}$$
$$j^q = T\sigma\varepsilon + \kappa(-\nabla T) \tag{1.11b}$$

[6] This subsection is inspired from the books (i) Thermoelectricity: An introduction to the Principles [MacDonald, 2006] and (ii) Solid State Physics [N.W. Ashcroft, 1976] in which more details can be found.

then, thermopower can be expressed as:

$$S = \frac{\nabla_x \varepsilon}{\nabla_x T} = -\frac{\Delta V_x}{\Delta T_x} \tag{1.12}$$

in agreement with the configuration shown in Fig.1.6. In this figure, the thermal gradient ∇T and its longitudinal E_x and transverse E_y electrical responses are represented. We consider that the x-axis is placed along the length of the sample, the y-axis along the width and the magnetic field is applied along the z-axis.

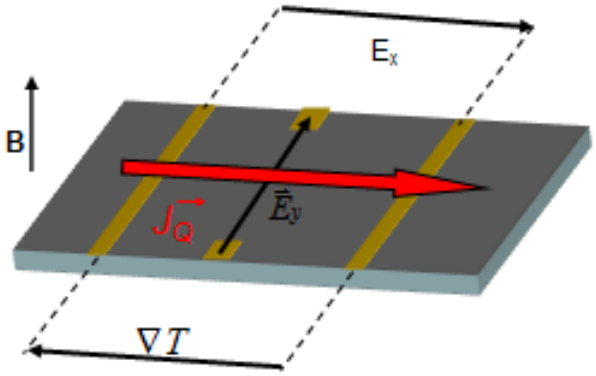

Figure 1.6: *Simple model of the applied thermal gradient ∇T and magnetic field B to the sample and its electrical responses E_x, E_y.*

The Seebeck coefficient depends on the temperature, on the concentration of impurities and on the crystal structure. The contributions to the Seebeck coefficient are the charge-carrier diffusion and the phonon-drag terms. The diffusive thermopower contribution is generated by the diffusive movement of electrons in the absence of the phononic current. The phonon-drag contribution arises when it is no longer possible to ignore the transport of energy through the lattice in comparison to the transport through conduction electrons. Hence, the phonon-drag appears when there is a large electron-phonon coupling. This term dominates the temperature dependence of many metals in a wide temperature range because it is proportional to the lattice specific heat. It varies as T^3; therefore, in the zero temperature limit, the phonon-drag contribution can be neglected. Recently, a new contribution to the Seebeck effect carried by the spin magnetization waves has been observed. It is called spin Seebeck contribution. These spin currents are generated by modifications in the magnetization of the system induced by the thermal gradient [Uchida et al., 2008].

In multiband systems, the total thermopower is expected to be the weighted sum of the contributions of the different bands. First, we considered the case in which one band metal presents several types of scattering. In this case, thermopower will be weighted by the different resistivity contributions ρ_i following:

$$S = \frac{\Sigma \rho_i S_i}{\Sigma \rho_i} \tag{1.13}$$

In the case of several types of carriers, each contribution will be weighted by their respective electrical conductivity σ_i, which is directly proportional to the density of states, following:

$$S = \frac{\Sigma \sigma_i S_i}{\Sigma \sigma_i} \tag{1.14}$$

In real multiband systems, a combination of these two phenomena should describe thermopower. Moreover, we indicate that the sign of thermopower will depend exclusively on S_i because σ_i is always positive. In addition, in a multiband compound the contribution of hole-like and electron-like carriers would cancel out diminishing the total absolute value of thermopower. Nevertheless, S is $\neq 0$ in compensated metals because hole and electron like bands have each their own ρ and σ values.

To finish, I briefly talk about the figure of merit ZT which relates the Seebeck coefficient S with the electrical conductivity σ, the thermal conductivity κ and the temperature T as $ZT = \frac{S^2 T\sigma}{\kappa}$. This factor is related to the performance of energy conversion. Nowadays, research to obtain compounds with high figure of merit ZT is strongly motivated. The purpose is to develop new and more productive sources of electric power or cooling systems. For example, in the case of the sources of power, we know that a high value of ZT implies that for the same thermal gradient, higher voltages will be generated, thus higher performances.

1.4.2 Nernst Coefficient

[7] If the system is submitted to a perpendicular magnetic field to the thermal gradient, a transverse electrical response to this thermal gradient appears. This transverse electrical response is called Nernst effect which can be expressed as:

$$N = S_{xy} = \frac{\nabla_y \varepsilon}{\nabla_x T} = K \frac{\Delta V_y}{\Delta T_x} \tag{1.15}$$

with K the geometric factor ($K = l/w$ where l is the length of the sample and w corresponds the width of the sample). At low temperatures, $N(T)$ is linear. This linear behaviour is also observe in $N(H)$ in the paramagnetic state.

The Nernst effect measures the ratio of the electron mobility to the Fermi energy and it is enhanced when there is a large electronic mobility and a small Fermi energy. The distinct sources in the Nernst signal are: (i) the normal quasi-particles in metals, (ii) the short-lived Cooper pairs (amplitude fluctuations) and the short-lived vortices (phase fluctuations) in superconductors and (iii) the magnetic impurities source, which generates an anomalous Nernst effect, in ferromagnetic compounds.

There are two conventions to define the sign in the Nernst effect. The first one identifies a positive value of the Nernst coefficient with the Nernst signal expected by the vortices moving from the hot to the cold side of the sample. The second convention identifies the positive Nernst value when the following configuration was respected: the positive electric field along the y axis appears when the thermal gradient is along the x-axis and the magnetic field along the z-axis. The second convention is the one I use in the thesis.

1.4.3 Mott Formula

[8] For the free electron gas obeying Fermi statistics, e.g., in the temperature regime $T < T_F$ with T_F the Fermi temperature, the Seebeck coefficient of a metallic system is expected to be

[7] This subsection is inspired from [Behnia, 2009] in which more details can be found.

[8] This subsection is inspired from the book Thermoelectricity: An introduction to the Principles [MacDonald, 2006] and the article [Behnia et al., 2004] in which more details can be found.

linear with temperature:

$$S = \frac{\pi^2}{3}\frac{k_B}{e}\frac{T}{T_F} \tag{1.16}$$

In these conditions, S becomes scattering-independent, if the mean free path is independent of energy.

In a normal metal, only the states close to the Fermi energy contribute to the Seebeck coefficient through the diffusion term of the Seebeck effect which is dominated by the existence of a non-independent scattering. That yields the Seebeck coefficient to be written as:

$$S = \frac{\pi^2}{3}\frac{k_B^2}{e}T\frac{\partial\sigma}{\partial\varepsilon}|_{\varepsilon=E_F} \tag{1.17}$$

This equation is known as the Mott formula. In the Mott formula, we consider the existence of two different contributions to the Seebeck coefficient that are weakly coupling. One comes from the light carriers and the other corresponds to the heavy charges. The motion of each contribution can be described independently from the others and it is independent to other dynamics as phonon-drag. The dominant mechanism is the scattering of the light charges from the wider bands to the narrower bands. Consequently, an additional scattering rate, which is proportional to the density of states of the narrower bands following $1/\tau \propto g_{narrow-bands}(E_F)$, will be summed to the thermopower contribution. This term dominates the free-electron contribution.

In this approach, the Nernst coefficient can be expressed as:

$$N = \frac{\pi^2}{3}\frac{k_B^2 T}{e}\frac{\partial\Theta_H}{\partial\varepsilon}|_{E_F} \tag{1.18}$$

where $\Theta_H = \sigma_{xy}/\sigma_{xx}$ is the Hall angle.

The Mott formula provides a qualitative explanation for the enhanced diffusion thermopower in multiband compounds with heavy (localized band) and light (delocalized bands) heat carriers. Mott still provides a natural explanation of the sign of thermopower. In addition, Mott indicates that thermopower is dominated by many factors which do not correlated with their specific heat. However, we will see in the next subsection that they are strongly linked in spite of the physical origin of the Seebeck coefficient does not correlate with the one of the specific heat.

1.4.4 Thermopower in the Zero-Temperature Limit

[9] In this subsection, we introduce the third discovered ratio connecting two distinct signatures of strong correlations among electrons, the q-factor. The other two ratios are the Kadowaki and Woods ratio (KW) and the Wilson ratio (R_W). KW ratio relates the electronic specific heat γ to the A term of the T^2 fit of the resistivity following $A \propto \gamma^2$. This ratio reflects the large energy dependence of the conduction electron's self-energy and the enhancement has been attributed to the unusual large electron-electron scattering. The R_W ratio links γ to the Pauli spin susceptibility χ_0 as $R_W = \frac{\pi^2 k_B^2 \chi_0}{3\mu_B^2 \gamma}$ with k_B the Boltzmann constant and μ_B

[9] The analysis of thermopower in the zero-temperature limit is inspired from [Behnia et al., 2004, Miyake and Kohno, 2005, Zlatić et al., 2007] in which more details can be found.

the Bohr magneton. This ratio reflects the effect of spin-orbit coupling, that slightly modifies the value of R_W, and the incompressible and local character of heavy Fermi liquids because R_W remains ~ 1 even thought the density of states varies in a factor 100 in heavy fermion systems. In Fig.1.7, the R_W (on the left) and KW (on the right) ratio plots are shown to demonstrate the approximate constancy of these ratios in heavy fermion compounds.

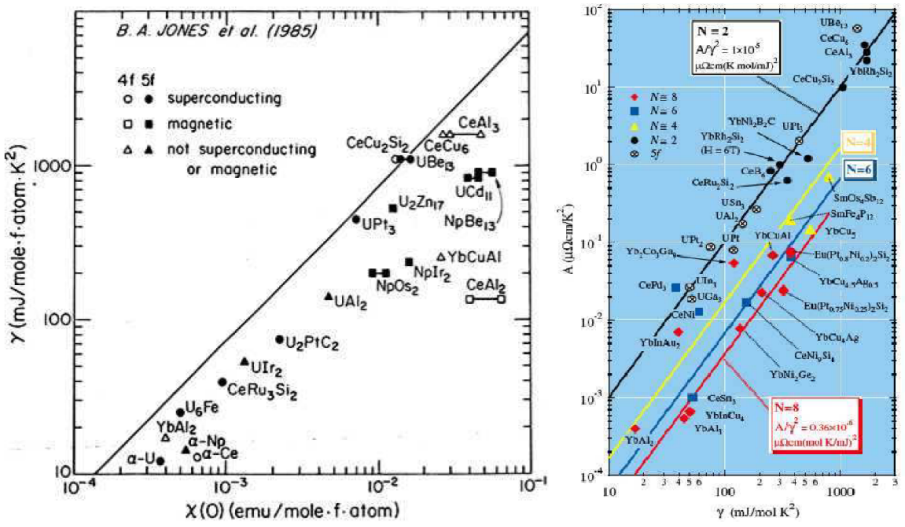

Figure 1.7: *R_W ratio plot (γ vs χ) on the left and KW ratio plot (A vs γ) on the right. The figures are taken from ref. [Coleman, 2007].*

The q-factor ratio links the Seebeck coefficient over temperature at zero temperature in the limit of free electron gas S/T (entropy per charge carrier) with the electronic specific heat γ (entropy per mole); i.e., two zero-energy properties of the system. In this limit, the Seebeck coefficient S is directly proportional to the density of states at the Fermi energy and the high temperature contributions to the thermopower like the phonon contribution are negligible. In these conditions, the S can be written in the Boltzmann picture as (Mott formula):

$$S = -\frac{\pi^2}{3}\frac{k_B^2 T}{e}\left(\frac{\partial ln\sigma(\varepsilon)}{\partial \varepsilon}\right)_{E_F} \tag{1.19}$$

with $\sigma(\varepsilon)$ the dc electric conductivity of the system:

$$\sigma(\varepsilon) = e^2\tau(\varepsilon)\int \frac{d\overrightarrow{k}}{4\pi^3}\delta(\varepsilon - \varepsilon(\overrightarrow{k}))v(\overrightarrow{k})v(\overrightarrow{k}) \tag{1.20}$$

The substitution of $\sigma(\varepsilon)$ in the S coefficient yields to:

$$S = -\frac{\pi^2}{3}\frac{k_B^2 T}{e}\left[e^2\left(\frac{\partial ln\tau(\varepsilon)}{\partial \varepsilon}\right)_{E_F} + \frac{\int d\overrightarrow{k}\,\delta(E_F - \varepsilon(\overrightarrow{k}))M^{-1}(\overrightarrow{k}))}{\int d\overrightarrow{k}\,\delta(E_F - \varepsilon(\overrightarrow{k}))v(\overrightarrow{k})v(\overrightarrow{k}))}\right] \tag{1.21}$$

where $M_{ij}^{-1} = \pm\frac{1}{\partial^2}\frac{\partial^2\varepsilon(\overrightarrow{k})}{\partial k_i \partial k_j}$ is the inverse of the effective mass tensor. The first term of eq.1.21 corresponds to the energy dependence of the Seebeck coefficient through the transport properties and the second term contains information about the thermodynamic properties of the system.

In the free electron limit and zero temperature we can write $\tau(\varepsilon) = \tau_0 \varepsilon^{\zeta}$, and consequently, $\left(\frac{\partial ln\tau(\varepsilon)}{\partial \varepsilon}\right)_{E_F} = \zeta/E_F$ and the second thermodynamic term can be replace by $\frac{3}{2E_F}$. Transforming the E_F following the equation $g(E_F) = \frac{3n}{eE_F}$ for the free electron gas, we can re-write the Seebeck coefficient as:

$$S = -\frac{\pi^2}{3}\frac{k_B^2 T}{e}\frac{g(E_F)}{n}\left(1 + \frac{2\zeta}{3}\right) \tag{1.22}$$

This equation is quite similar to γ equation:

$$\gamma = C_{el}/T = \frac{\pi^2}{3}k_K^2 g(E_F) \tag{1.23}$$

Both quantities are directly proportional to the $g(E_F)$, and the ratio between S/T and γ gives a dimensionless parameter which is inversely proportional to the number of heat carriers per formula unit, n. In addition, this ration presents an almost constant value ± 1 in most heavy fermion systems (with $\zeta = 0$). The reason is that strong renormalization effects in S/T and γ cancel out each other in spite of the different physical origin of these thermodynamic quantities. Then, this ratio characterizes thermoelectric materials in terms of an effective charge carrier concentration per formula unit. The $+1$ corresponds to 1 hole heat carrier per forumla unit (f.u.) and the -1 to 1 electron heat carrier per f.u.. This ratio is the q-factor:

$$q = \frac{S}{T}\frac{N_{av}e}{\gamma} \tag{1.24}$$

with $N_{av}e = 9.6 \cdot 10^5 \mathrm{Cmol}^{-1}$ called Faraday number.

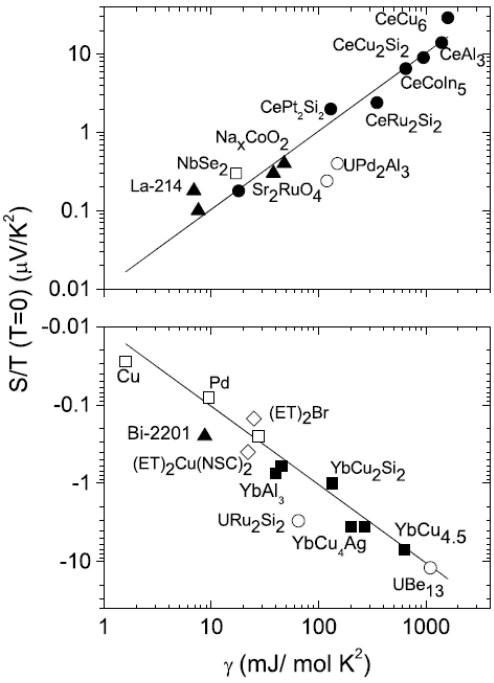

Figure 1.8: *S/T vs γ plot for heavy fermions systems (solid symbols) and other types of families such as oxides, metals or organic conductors (open symbols).*

In Fig.1.8, we show the S/T vs γ ratio plot of Ce-based heavy fermion systems in solid circles, the Yb-based heavy fermion compounds in solid squares and the U-based heavy fermion systems in open circles. We also observe that this tendency is also preserved in metallic oxides (triangles), organic conductors (diamonds) and common metals (open squares). We notice that all the systems constitute a cloud around the straight line $q/N_{av}e$ with $q = \pm 1$. We remark the high correlations between the enhancement of the specific heat and the thermopower. We note that $q = \pm 1$ corresponds to a metallic behaviour with ± 1 carrier per f.u.. Deviations from this line are observed for low carrier compounds which are in agreement with the high values obtained for the q-factor; an example is URh_2Si_2.

1.4.5 Information from Thermoelectric Coefficients

The thermoelectric coefficients are very sensitive to the electronic density of states. Thus, we can study modifications of the density of states, follow phase transitions, even close to quantum critical points, and crossovers and study the topology of the of the Fermi surface using quantum oscillations.

For example, the FL regime corresponds to a constant value of S/T in the low temperature regime and in the case of heavy fermion systems, the $S/T = cts$ behaviour is achieved in the very low temperature regime. We expect to have a divergence of the Seebeck coefficient approaching the QCP at $T = 0$ due to the accumulation of entropy. The phase transitions are characterized by a modification in the values of the S which can be smooth (2^{nd} order or crossover transitions) or sharp (1^{st} order transition). The topology of the Fermi surface is measured through the analysis of quantum oscillations.

Moreover, the Seebeck coefficient measures the entropy per charge flow and the sign of carriers, giving the + sign for holes and the − sign for electrons. However, to talk about holes or electrons in a multiband system is a rather difficult task as the sign of the thermopower effect depends not only in the type of carriers, but also in the derivative of the density of states. In addition, the Seebeck effect measures spin currents. The Nernst coefficient also measures anomalous currents related to magnetic scattering.

Some examples of our practical heavy fermion studies are the detection of quantum phase transitions between an ordered state to an non-ordered phase such as the metamagnetic transition between the FM and the PM phases in UCoAl, the detection of the characteristics of the Fermi surface *via* thermopower quantum oscillations as the analysis of the topology of the Fermi surface of UGe_2. We also studied the physics related to quantum critical points like the competing orders between the AF and the PM in $CeRh_2Si_2$ compound. In this case, the pressure was used to modify the J^W coupling constant of the system. The physical background explained in this section will be a valuable asset to deal with the understanding of the competing orders in heavy fermion systems and its analysis by thermopower.

Chapter 2

Experimental Techniques

In this chapter, I show the experimental techniques used during my PhD. First, I present vacuum and pressure thermopower setups developed during my thesis to study heavy fermion systems under extreme conditions of temperature, magnetic field and pressure. Second, I show the different techniques used to determine these thermoelectric coefficients. In the third part, resistivity measurements are shown and finally, the extreme conditions of temperature and magnetic field in which the measurements were performed are presented.

2.1 Introduction to Thermoelectric Measurements

To determine the thermoelectric coefficients, first, we apply heat power to generate the thermal gradient along the sample. When the system is in stable conditions, we measure this thermal gradient and its electrical response. For the Seebeck coefficient, the thermal gradient and the electrical response, $V_{Seebeck}$, are measured at the same contacts. The Nernst coefficient corresponds to the transverse electrical response, V_{Nernst}, thus a magnetic field perpendicular to the sample must be applied. For measuring V_{Nernst}, two new contacts at middle-length and at the edge of the width of the sample are needed (see Fig.1.6).

The interest on thermopower measurements was renewed recently. Consequently, modifications in this probe were put into practice to expand this technique to other kind of studies. In the context of this thesis, the study of heavy fermion systems, the improvements of thermoelectric setups are: the sensitivity and the conception of novel thermopower setups under pressure.

Our upgrades concern the effort to increase the signal/noise ratio and to increase the thermal coupling between heater, sample and heat sink elements as they are the main problems of thermoelectric measurements. To increase this first ratio, we use copper wires without soldering from 300K to the lowest temperature stage of the fridge. We put special attention to avoid the ground loops of current and parasite currents through the measuring setup system. We also add low pass filters between the output of the analogical Nanovoltmeter and the input of the multimeter K2000 that converts the analogical signal into digital one. These aspects allow to decrease the noise measurement level, which is lower than 1nV in the low temperature regime and $1-10$nV in the $[4-50]$K temperature regime. Finally, to improve the second ratio, a strong effort to increase the thermal coupling between the heater and the sample and between the sample and the sample holder was done. We reduce the thermal resistances by good thermal contacts (spot-welding and silver paste) with the objective to improve the generation of the thermal gradient along the sample.

The conception of novel thermopower devices under pressure is the most relevant development for this thesis. In the last 10 years, thermopower under pressure technique started to be developed. Nowadays, only few groups around the world take advantage of this probe due to the difficulty to perform thermopower measurements in these conditions. The idea is to be able to analyze the (T, P, H) phase diagram of these compounds with this high sensitive probe. In the following sections, I will show our novel and reliable pressure thermopower setup adaptable at different kind of transmitting mediums and/or pressure cells.

In general, the error sources on thermopower measurements are the sensitivity of Nanovoltmeters (1nV of noise), the stabilization time that could be longer than expected and the temperature stabilization of the bath. For the vacuum setup, an extra error usually come from the sensitivity of individual thermometers. Under pressure, the usual error is related to the thermocouples and it appears if the two wires forming the thermocouples are not connected in one point; then the thermal gradient and the thermoelectric coefficient are not measuring from the same point and introduce an error in the ratio between the Seebeck voltage and the thermal gradient.

2.2 Thermopower Setups

In this section, we explain the thermoelectric setups: the vacuum setup conditions and the under pressure setups. The design of the pressure devices has been one on the main objectives of my PhD.

2.2.1 Vacuum Setup

The vacuum setup is also called "One heater - Two thermometers" setup due to the configuration. A schematic representation is shown in Fig.2.1. This setup is based on a heater that

generates a thermal gradient along the sample by Joule heating and two independent thermometers that measure the absolute temperature values of the cold and the hot sides of the thermal gradient. The heater is attached to one side of the sample and the sample is in turn attached to the copper block (the heat sink) in the opposite side. These series of connections allow to establish the thermal gradient on the sample. The thermometers are thermalized independently, from the heat coming from the hot and the cold sides of the thermal gradient of the sample, through the thermoelectric wires. This thermoelectric wires are contacted to the sample by the spot welding technique and they are made of gold or silver.

The thermal decoupling of the heater and the thermometer to the heat sink is a key point of this setup to get a precise value of the thermal conductivity and thermopower. For that reason, the leakage of power from the heater to the bath must be negligible as absolute values of the applied power are required and the leakage of power from the thermometers to the heat sink must be small because stable temperatures are needed to measure precisely the absolute thermal gradient on the sample. To avoid these leakage of power to the cold finger, we decoupled them thermally to the copper block by manganin wires. This kind of wire presents two higher magnitude order resistance than copper wire causing a reduce of heat transport along it.

All the electrical connections are done by silver paste because its contribution at low temperature can be neglected even if the silver paste contacts are submitted to a thermal gradient. In addition, the contacts done on silver paste present a low thermal resistance.

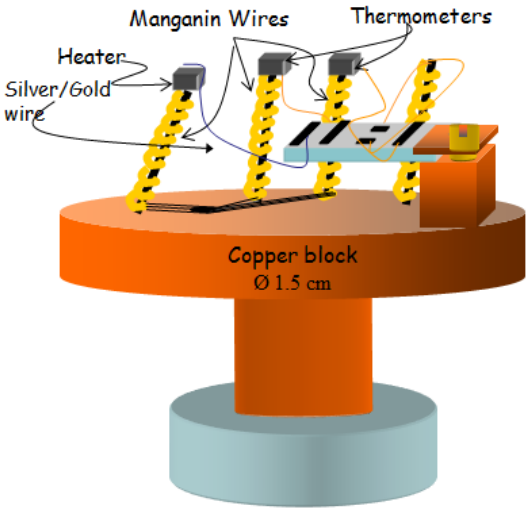

Figure 2.1: *"One heater - Two thermometers" vacuum setup.*

The type of thermometers we use to measure the thermoelectric coefficients depends on the temperature range of the measurements. Cernox thermometers are used for $[4-50]$K temperature range and RuOx for the low temperature regime, $T < 4$K. Under high magnetic fields, we use preferably RuOx thermometers because they present a strong magnetoresistance at low magnetic fields, $[0-2]T$, and a weak magnetoresistance at high fields. We note that our RuOx thermometers at 360mK present $\Delta R << \Delta T/T = 0.01\%$ in the field range of $[0-34]$T. This error is much smaller than the usual relative thermal gradient ($\Delta T/T = 3\%$).

One of the key point of this setup is it can measure simultaneously thermal conductivity

and thermoelectric coefficients. Thermopower can be measured in transverse ($J \perp H$) and longitudinal ($J \parallel H$) configurations, with J, the heat current and H, the magnetic field. In addition, if we apply an electrical current instead of a thermal current, we can use this setup to measure resistivity and Hall resistance. All these measurements use the same wire connections.

2.2.2 Pressure Setups

A major aim of this PhD was to set up thermopower under pressure. As a consequence of the existence of the pressure transmitting medium and the small size of the pressure chamber, it was not possible to use under pressure the same kind of setup as the vacuum one to measure the thermoelectric coefficients. In the beginning, thermopower setups were designed to fit in large pressure chamber volumes; e.g., for piston cylinder pressure cells. Nevertheless, due to the necessity of exploring higher pressure ranges, a second setup was built for the Bridgman pressure cell. The two main aspects to conceive these thermopower pressure setups were the small size of the setup, due to the small volume of the pressure chamber, and the thermal coupling between the sample and the heater and between the sample and the heat sink, due to a good thermal contact among them is essential to create a thermal gradient on the sample. A schematic picture of the new thermopower setup under pressure is presented in Fig.2.2.

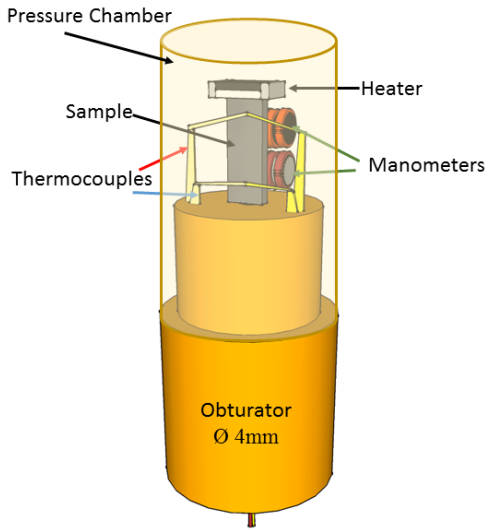

Figure 2.2: *Schematic thermopower setup under pressure.*

The presence of the pressure transmitting medium blocks the possibility of the thermalization of the independent thermometers as a result of the existence of the power-leaks from the "sample-thermometers-setup" to the medium. We replace the two independent thermometers of the vacuum setup for two thermocouples. The thermocouples are AuFe(0.08% Fe)-Au wires. The AuFe(0.08% Fe) wire is a $50\mu m$ diameter wire flatted up to $15\mu m$ thick and cut in $50-70\mu m$ width and the Au wire is $15\mu m$ diameter wire. The length of the wires depends on the distance from the hot/cold side of the sample to the cold finger. The thermocouples are thermalized between the hot/cold side of the sample and the bath. For the hot and cold thermocouples, the bath temperature is the same and both thermocouples have a similar

power decay path inside the pressure cell. Moreover, the coupling between the heater and the sample was optimized. The purpose was to enable that the major part of the total Joule heating of the heater-resistance pass through the sample instead of being widespread in the pressure transmitting medium. Depending on the configuration setup, we can use mechanical contact, silver paste or GE-varnish to improve the heater-sample contact.

As a consequence of the small volume of the pressure chamber, the sample-heater-thermocouples setup must be minimized. In addition, manometers to follow the pressure must be included inside the pressure chamber. This complicates the configuration due to the lack of space. There are usually two manometers inside the chamber: one working at room temperature and the other at low temperature. We usually use manganin wire and a piece of lead respectively. Using these two, we can follow the variations of the pressure during the loading and the final pressure at low temperature. Small modifications of the pressure are expected as a consequence of the solidification of the transmitting medium. The transmitting mediums, which are used in our pressure systems, are hydrostatic at room temperature and at low pressure and the choice depends on the type of pressure cell. For the piston Cylinder pressure cell, the transmitting medium is DAPHNE oil and for the Bridgman cell, it is Fluorinert.

Finally, it is necessary to take into account the sensitivity of thermocouples and the leakage of power to generate a substantial thermal gradient. The applied power, in the μW to mW range, depends on the characteristics of the sample, the power leakage and on the temperature at which the measurements are taken. The power applied under pressure is in the same order than in vacuum technique; however, the thermal gradient in vacuum is around 10 times bigger than the one under pressure. Thanks to the high sensitivity of thermocouples, the measurements are carried out with $\Delta T/T \simeq 0.5 - 0.8\%$ for the piston cylinder pressure cell and $\Delta T/T \simeq 0.3 - 0.6\%$ for the Bridgman one. These small ranges of $\Delta T/T$ are possible to be measured because the stabilization of the bath temperature is of the order of $\Delta T/T < 0.05\%$.

Thermocouples Sensitivity

We use AuFe(0.08% Fe)-Au thermocouples because of their high sensitivity in the temperature range $[0 - 50]$K [Chaussy et al., 1981]. Thermocouples have higher sensitivity than the independent thermometers. We demonstrate this high sensitivity for the case $T = 4$K. At this temperature, thermocouple temperature uncertainty is 1nV. This voltage is equivalent to an absolute error in temperature of $1nV/S_{AuFe|_{4K}} = 0.08$mK and a relative error of $10^{-3}\%$. This extremely high sensitivity allows to measure thermopower at 4K with thermal gradients of the order of $\Delta T/T = 0.02\%$, if we consider that the signal must be at least 10 times higher than the uncertainty. Consequently, this $\Delta T/T$ for thermocouples can be reduced up to 100 times compared to the $\Delta T/T$ of the value of the "One heater- Two thermometers" setup. Hence, we can significantly reduce the relative thermal gradient to determine the Seebeck coefficient under pressure.

Power Leak

We analyze the needed power to create the thermal gradient. For the piston cylinder pressure cell, it is observed that when we apply the same quantity of power as in the vacuum setup, the thermal gradient under pressure is reduced by a factor $5 - 10$. Then, the corresponding thermal gradient is $\Delta T/T = 0.3 - 0.8\%$ which is higher than the sensitive limit for a thermal gradient ($\Delta T/T = 0.02\%$). In the case of a Bridgman pressure cell, the gradient is reduced by a factor $20 - 30$ and the $\Delta T/T$ is still over the sensitive limit. The higher decrease of the

relative thermal gradient in the Bridgman than in the piston cylinder pressure cell is related to the different type of thermal connections between the heater and the sample. In the case of the Bridgman cell, the heater and the sample are connected by mechanical contact whereas for the piston cell, an electrical contact connects the heater to the sample. Despite of the leakage of power from the heater to the transmitting medium, the propagation of this leakage through the transmitting medium is really small. For the Bridgman pressure cell, the propagation was quantified. For that, the thermal gradient between two thermocouples (one connected to the hot side of the sample and the other placed in the cold side of the pressure chamber without touching the sample) was measured obtaining a $\Delta T/T \gg (\Delta T/T|_{sample} \sim 1\%)$. This high value of $\Delta T/T$ means that the transmitting medium is a bad thermal conductor and the Joule heating is located in the vicinity of the heater. The cooling of the sample is done by the thermocouples.

Piston-Cylinder Pressure Cell

In Fig.2.3, a schematic picture of a piston cylinder pressure cell is shown. A piston cylinder pressure cell consists of an external cell body made of CuBe, enforced with an inner cylinder of non-magnetic nickel-chromel-aluminum alloy (Ni-Cr-Al). The setup for the measurements is placed in the pressure chamber (Teflon cap) and the wires for the measurements go outside the chamber trough a small hole in the obturator (plug) which is closed by black Stycast epoxy. The plug is held by a fixed locking nut (lower screw). On the top, a tungsten carbide (CW) piston and a piston backup are pressed by a second upper locking nut (upper screw) over the pressure chamber to seal it. This upper screw allows to choose the pressure inside the Teflon cap and the two rings (pressure chamber). The pressure transmitting medium is DAPHNE oil 7373 which is an hydrostatic medium at room temperature in the low pressure regime of the piston cylinder pressure cell, $P \leq 2.2$GPa [Yokogawa et al., 2007]. The piston cylinder cells used in those experiments can apply a maximum pressure of 2GPa. Above this value, the strangulation of the Teflon cap invades the pressure chamber cutting the wires of the thermopower setup. For smaller setups, such as resistivity setups, the pressure limit for these cells is almost 3GPa.

To determine the pressure inside the chamber, there are two coils; one coil made of manganin wire (Mng-coil) and a wound round piece of lead by copper wire (Pb-coil). We follow the resistance of the Mng-coil at room temperature to adjust precisely the pressure. The resistance (R) of the manganin wire increases with pressure (P) following:

$$\Delta P = 434 \frac{\Delta R}{R} \tag{2.1}$$

The precision of the measurement of pressure increases with higher resistance of the Mng-coil because the variation of the resistance, ΔR, is stronger for the same pressure modification. The pressure at low temperatures corresponds to the lead superconducting transition of the Pb-coil. For measuring it, we analyze the inductance of the lead transition of the Pb-coil instead of the usual measure, susceptibility measurements. This is due to susceptibility measurements need two overlapping coils; then, we will need a rather large space and double number of wires passing through the hole of the plug. We note that we imposed the large Mng-coil as heater and the measurement of the inductance of the Pb-coil to reduce the number of wires and the setup volume inside the pressure chamber.

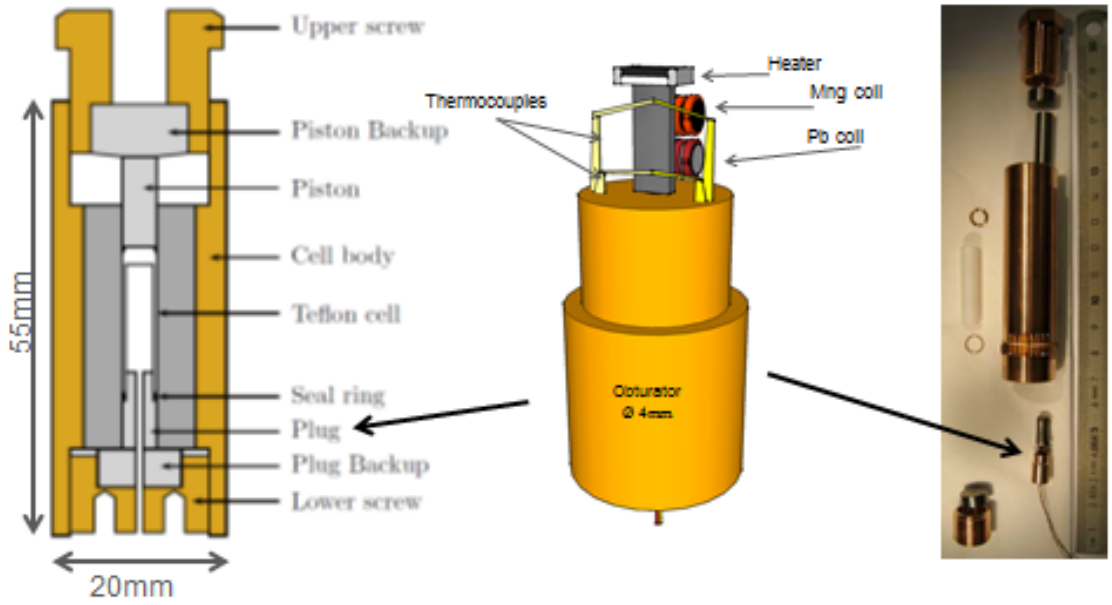

Figure 2.3: *Piston Cylinder Pressure Cell. The left picture is a schematic model of the different parts of the pressure cell; in the middle, we have the thermopower pressure setup inside the pressure chamber and in the right part, a photo of the piston cylinder pressure cells I used to perform the measurements.*

The thermocouples are soldered to the sample by spot welding technique; the heater and the sample are connected by a silver wire going from the core of the Mng-coil to the top of the sample at which it is glued by silver paste. The silver paste has also been used in the pressure chamber for thermocouples and copper wires connections to avoid any thermopower contribution from the contacts. The rest of the contacts are done by normal soldering because they are at stable temperature conditions; thus, no extra contribution from them to the themopower signal is expected.

Bridgman Pressure Cell

The transmitting medium of the Bridgman pressure cells is usually a solid medium. Nevertheless, an adaptation to use a liquid transmitting medium in this type of pressure cell was developed [Colombier and Braithwaite, 2007, Jaccard and Sengupta, 2010]. The advantage of pressurizing the system with a liquid medium is the higher hydrostaticity. Based on the latter liquid technique, we have designed a novel thermopower setup for the Bridgman pressure cells.

In Fig.2.4, we show the schematic picture of the Bridgman pressure cell. It consist in an external cylindrical body of CuBe and two CW anvils with flat and co-planar surfaces. The bottom anvil is held by a fixed locking nut (lower screw); the upper anvil is fixed to the piston. The pressure inside the pressure chamber is chosen by the upper locking nut (upper screw). The pressure chamber is located inside the two flat rings of pyrophylite with external diameter of 3.2mm and internal diameter of 1.5mm. Inside the pressure chamber, we place the sample setup and pressure manometers submerged by the transmitting medium, Fluorinert FC70/FC77. To seal the pressure chamber, we apply rapidly pressures higher than 0.8GPa during the first loading of the pressure cell as pyrophylite is a porous material that becomes

hermetic when a P higher than 0.8GPa is applied to it. The Fluorinert transmitting medium has an hydrostatic limit higher than 2.5GPa at 300K [Sidorov and Sadykov, 2005] and the pressure range for this cell is $[1-8]$GPa.

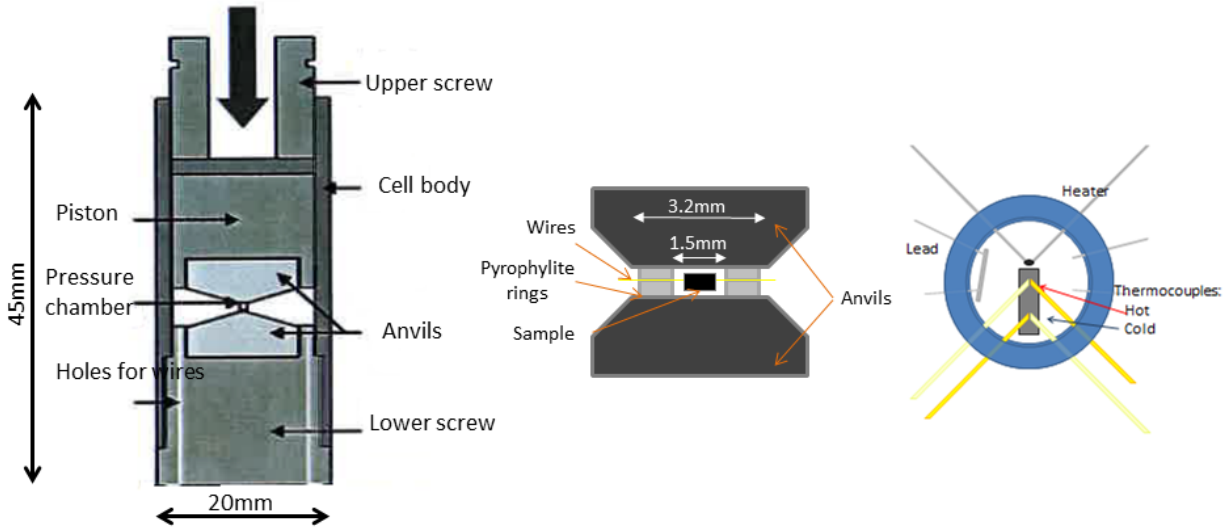

Figure 2.4: *Bridgman Pressure Cell. On the left side, a schematic picture of the anvils and pressure system, on the middle, a zoom of the anvils and pressure chamber and in the right side, a schematic picture of the setup inside the pressure chamber of the Bridgman Pressure Cell.*

The dimensions of the cylindrical pressure chamber of the Bridgman cell are 1.5mm diameter and less than 200μm height. For that reason, it is not possible to put Mng-coil as a heater inside the pressure chamber. Therefore, we modify the heater and the manometers for this cell. In the Bridgman pressure cell, the heater consists of two platinum wires connected by a carbon epoxy. This epoxy is used to join electrically the two wires obtaining contacts with resistance around $50-100\Omega$. This resistance is high enough to heat the sample. As a manometer, we measure, in a four-contact configuration, the evolution of the resistance of a bar shape piece of lead that decreases with pressure. Nevertheless, the four-contact connection was done just outside the rings (see the two small red circles in Fig.2.5) as the number of slots in the rings that can be made to pass the wires from the inside of the pressure chamber to the external part are limited. At low temperatures, the superconducting transition of the lead at zero magnetic field could be followed to determine the pressure in the chamber.

We observe in Fig.2.5 that thermocouples are AuFe(0.08% Fe)-Au long wires coming from the sample to the pad without interruption. The pad is an electrical support used to connect the wires coming from the pressure chamber to the external measuring wires that it is thermalized at the bath temperature. The connections of thermocouples at the pad are made by silver paste because if the pad presents small non negligible thermal gradients, the soldering can generate an important Seebeck coefficient that can mask the behaviour of the sample. Moreover, to insulate electrically the wires, inside and outside the rings, we spread a layer of white Stycast over the anvils. The white Stycast outside the ring also keeps the pressure during the first loading of the pressure cell until the porosity of the pyrophylite is reduced to avoid any loss of the transmitting medium (by evaporation). We indicate that it is very important to keep the symmetry of the slots in the rings to have an homogeneous stress on

them when the pressure is applied.

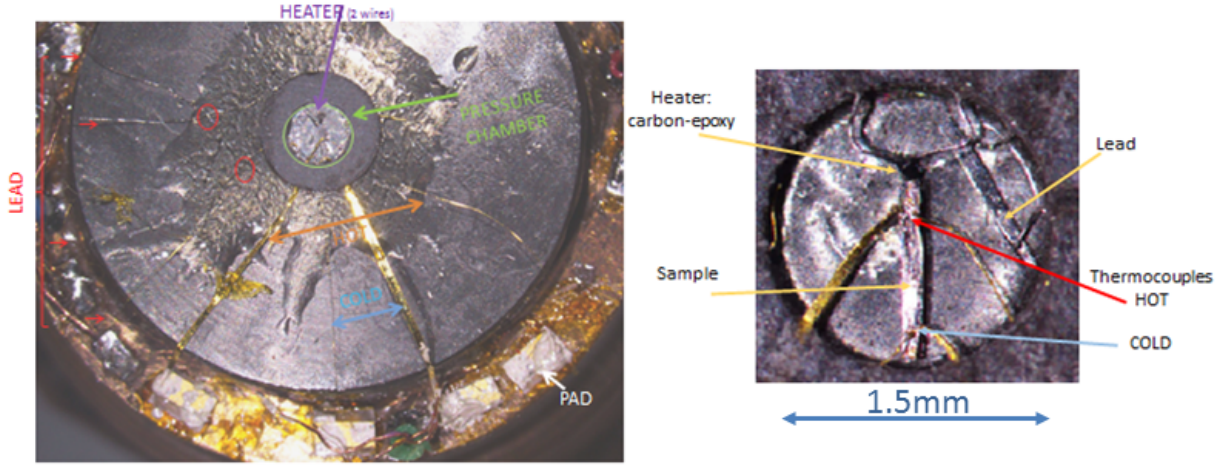

Figure 2.5: *Photo of a real setup in a Bridgman Pressure Cell. Thermocouples, heater, manometer, pressure chamber and pad are indicated by legends and colored arrows. A zoom of the pressure chamber and its different components are shown on the right figure.*

2.3 Thermoelectric Measurement Techniques

As it was introduced in section 2.1, to determine the thermoelectric coefficients, we measure the thermal gradient and the electrical response generated by this temperature difference. Depending on the kind of experiments we want to perform, there are two different ways of measuring the thermoelectric coefficients. The first one consists in averaging the data; called "Thermopower in Stable Conditions", and the second one in acquiring continuously the data; called "Thermopower Quantum Oscillations".

2.3.1 Thermopower in Stable Conditions

This technique is the most usual and consists in measuring the thermal gradient and its electrical response for each temperature or magnetic field point in stable conditions. At each point, the measurement is performed with and without thermal gradient. As we observe in Fig.2.6, the acquisition data, with and without applied power, is preceded by a stabilization time. This stabilization time could be from 3 to 10 minutes depending on the characteristic of the sample (cross section and length size, quality sample and thermal resistance to the cold finger). The acquisition starts when all the temperatures verify $\Delta T/T < 0.05\%$ or in the case of the stabilization time runs out to avoid being blocked in one point of the sequence of measurements. Each temperature point corresponds to the average of temperatures, electrical response and applied power parameters during 30s. The temperatures are measured with a locking or MMR3 instrument (AC current mode) and the electrical response with a Nanovoltmeter instrument (DC current).

In stable thermal conditions, sometimes the thermal gradient is not exactly 0 when no gradient is applied to the sample. We suggest two possibilities: this thermal gradient can

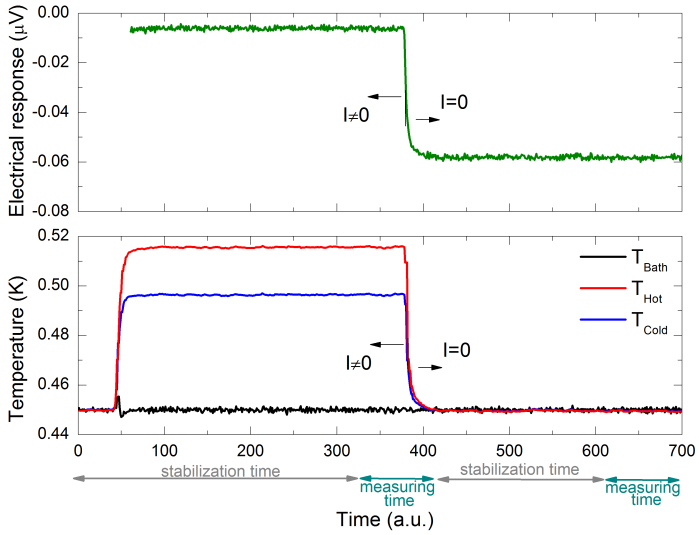

Figure 2.6: *Temperatures and Seebeck voltage as a function of time for the vacuum stable conditions acquisition.*

be due to a calibration error of the thermometers (apparent thermal gradient) or it can be real. In the latest case, we indicate that it may be related to parasite currents. To avoid the problems coming from these situations, thermal gradient and electrical response are measured with and without applied Joule heating for each temperature point.

From the point of view of the electrical responses, analogous to the thermal gradient situation, it could occur that there is an no zero electrical response although no power is applied to the sample (see Fig.2.6 - green curve). This offset in the electrical response can be due to the contribution of the copper wires going from 300K to the sample holder and in this case, the thermal gradient is 0 or due to the existence of parasite currents when this behaviour goes with a non 0 thermal gradient.

Considering this, we show the data treatment to determine the thermoelectric coefficients in vacuum and under pressure conditions.

Vacuum Technique

The non-zero thermal gradient in the absence of power can be treated: (i) renormalizing one thermometer in relation to the other or (ii) considering that the real thermal gradient corresponds to the difference between the thermal gradient with and without power. The renormalization method is applied when the thermal gradient can be considered apparent and the subtraction method when the thermal difference is real or non negligible.

- Re-calibration method. We re-calibrate the thermometer(2) in relation to the thermometer(1). For that, we use the calibration of the thermometer(1) and the resistances, with and without power, of the thermometer(2). First, we fit the resistance(2) at $I = 0$ regarding the resistance(1) at $I = 0$ by a polynomial fit. Then, this polynomial fit is used to recalculate the resistances of the thermometer(2) and finally, the temperatures are obtained, for all the resistances, from the calibration of the thermometer(1). The

equation used to determine the absolute value of the thermopower coefficients (TEP) is:

$$TEP = \frac{Volt_{I\neq 0} - Volt_{I=0}}{(T_{HOT} - T_{COLD})_{I\neq 0}} \tag{2.2}$$

- The subtraction method. The equation to determine the real value of the thermopower coefficients (TEP) is:

$$TEP = \frac{Volt_{I\neq 0} - Volt_{I=0}}{(T_{HOT} - T_{COLD})_{I\neq 0} - (T_{HOT} - T_{COLD})_{I=0}} \tag{2.3}$$

We note that the treatment of the non zero thermal gradient coincides by both approximations at $I = 0$ and at $H = 0$T. Under field, the re-calibration method cannot be used in the low temperature regime because of the magnetoresistance of the thermometers (each thermometer has a different magnetoresistance behaviour). However, if the magnetoresistance is negligible, both methods can be used.

Pressure Technique

The pressure technique uses the same assumptions about the stabilization time that the vacuum technique. The main difference between them is the temperature acquisition. In vacuum, individuals thermometers are used while under pressure, the temperature is determine by thermocouples. The AuFe(0.08% Fe)-Au thermocouples are placed from the hot/cold side of the sample to the cold finger or bath (T_{Bath}) which is used as the reference for determining the temperatures of the sample.

The thermocouples are calibrated as a function of temperature and as a function of magnetic field. We note that the AuFe(0.08% Fe) wire is really sensitive to the field conditions. One of the advantage of thermocouples is they have the same magnetoresistance behavior. In addition, the thermocouples technique can measure the thermal gradient and the electrical response simultaneously in a continuous way. This is possible if T_{Bath} is swept slowly enough that the transmitting medium follows this temperature change and the applied power is modified accordingly with the bath temperature variation. This is not possible in the case of the vacuum setup because the thermalization of thermometers is longer than the thermalization of the sample. In all the cases, the measure of the real absolute value in this continuous way is true only if the background remains constant.

In relation with the stabilization time, once T_{Bath} is stable, the stabilization time of hot and cold temperatures of the sample under pressure are in the same order of magnitude than in the vacuum setup. However, the time to thermalize the setup is longer as the thermal relaxation time of the transmitting medium is longer than the metal one.

To determine the thermopower of a compound under pressure, we measure the electrical response of thermocouples (AuFe(0.08% Fe)-Au) and the electrical response of the sample by Nanovoltmeter instruments (DC voltage). The possibilities to determine the absolute value of the thermopower signal for this setup are:

- Cold and Hot Absolute Temperature (CHAT) Technique. In this technique, three Nanovoltmeters are needed to follow the voltage of the hot and the cold thermocouples and

the voltage of the Seebeck coefficient simultaneously. The hot and cold thermocouple voltages are transformed into temperature following the equations:

$$\Delta T_{Hot/Cold} = \frac{\Delta Voltage_{Hot/Cold}(\mu V)}{TEP_{AuFe}|_{Tbath}(\mu V K^{-1})} \tag{2.4}$$

$$T_{Hot/Cold} = T_{bath} + \Delta T_{Hot/Cold} \tag{2.5}$$

with $\Delta Voltage = V_{I\neq 0} - V_{I=0}$. It is important to highlight that in the conversion of the voltage into temperature, we only consider the absolute value of the thermopower of the AuFe(0.08% Fe) as the thermopower of Au wire is negligible. Once the temperatures are determined, the value of the Seebeck coefficient is obtained by:

$$\Delta T = \Delta T_{Hot} - \Delta T_{Cold} \tag{2.6}$$

and then,

$$TEP = \frac{V_{Seebeck}|_I - V_{Seebeck}|_0}{\Delta T} \tag{2.7}$$

- Relative Thermal Gradient (RTG) Technique. In RTG technique, we use 2 Nanovoltmeters to follow the difference of voltage of hot and cold sides through the sample $V_{AuFe_{Hot}-Seebeck-AuFe_{Cold}}$ and the voltage of the Seebeck coefficient $V_{Seebeck}$ at the same time. This technique is only valid when $T_{Cold} \backsimeq T_{bath}$ and the $\Delta T_{Cold} << \Delta T_{Hot}$. Then, the thermal gradient is determined by:

$$\Delta T|_{I,0} = \frac{[V_{AuFe_{Hot}-Seebeck-AuFe_{Cold}} - V_{Seebeck}](\mu V)}{TEP_{AuFe}|_{Tbath}(\mu V K^{-1})}|_{I,0} \tag{2.8}$$

and the thermopower following the equation (2.7) with:

$$\Delta T = \Delta T_{I\neq 0} - \Delta T_{I=0} = \Delta T_I - \Delta T_0 \tag{2.9}$$

.

In Fig.2.7, a schematic representation of the measuring configuration of the previous techniques are shown. On the left, the CHAT technique is shown and on the right side of the figure, we show the RTG technique. We note the position of the Nanovoltmeters for CHAT and RTG techniques. CHAT technique has three Nanovoltmeters; two of them are connected to hot and cold thermocouples voltages (orange and blue Nanovoltmeters, respectively) and the third one to the $V_{Seebeck}$ through the Au wires (green Nanovoltmeter). RTG technique use only two Nanovoltmeters. One corresponds to the measure of the $V_{Seebeck}$ through the Au wires (green Nanovoltmeter) and the other one to the differential hot-cold thermopocouples gradient through the sample (red to blue Nanovoltmeter).

The CHAT technique is useful when a high thermal resistance exits between the cold edge side of the sample and the cold finger that causes the high thermal gradient between the cold side of the sample and the cold finger. However, if we can consider that the cold side of the sample has the same temperature as the cold finger, the RTG technique is more powerful. The CHAT technique presents some inconveniences related to the RTG technique: the number of copper wires on the chamber of the fridge increases from 4 wires to 6 (higher amount of heat reach the chamber increasing the lowest based-temperature of the fridge) and a third Nanovoltmeter is needed.

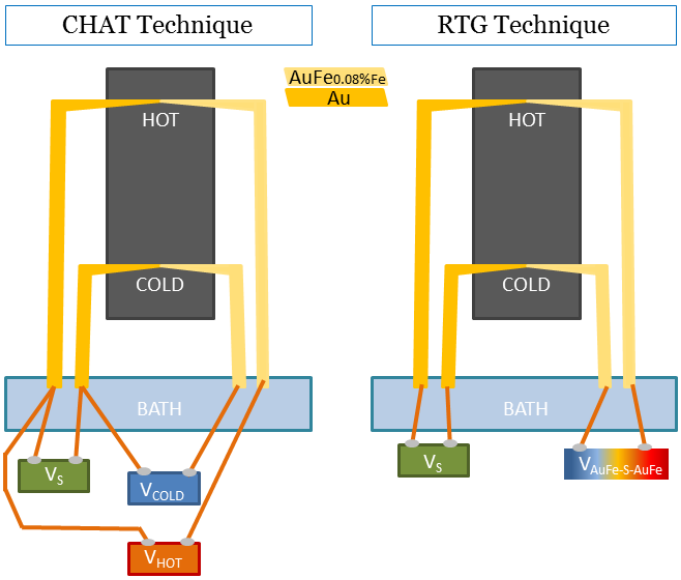

Figure 2.7: *Schematic picture of the thermopower techniques to determine the Seebeck coefficient under pressure. On the left, we show the picture of CHAT technique and on the right, we represent the one of RTG technique.*

2.3.2 Thermopower Quantum Oscillations

This technique is used to measure the Fermi surface of a compound. The electronic motion around the orbits is measured only if low temperature, high magnetic field and high quality sample conditions are fulfilled. The orbits are observed as a result of the modification of the Fermi energy by magnetic field. From this data, the information about the Fermi surface such as the frequencies, the effective mass and mean free path for each orbit is extracted. Here, we focus only on the experimental technique that allows the reconstruction of the Fermi surface: "Thermopower Quantum Oscillations" technique.

Contrary to thermopower stable conditions analysis, these measurements are done in a non-equilibrium system. The Fig.2.8 shows the three steps to follow in this kind of measurements to determine absolute values. First of all, the background for the Seebeck voltage and the Hot/Cold/Bath temperatures at $I = 0$ (without power) are measured. Second, we fix the thermal gradient and when it is stable, then the magnetic field is set off. The sweep of the magnetic field induces an extra magnetic response on the thermopower wires, the magnetic field induction.

To determine the absolute value of the thermoelectric coefficients, we remove from the measured thermoelectric signal: the induced voltage due to the sweep of the magnetic field ΔV_{Field} and the background $V_{background}$. Then thermopower (TEP) is determined following the equation:

$$TEP(H) = \frac{V_{measured}(H) - \Delta V_{Field} - V_{background}}{[T_{Hot} - T_{Cold}](H)} \tag{2.10}$$

In Eq.2.10, the thermal gradient is evaluated at each magnetic field value. The $1k\Omega$- RuOx thermometers of the setup are calibrated for magnetic fields from 0 to 16T. We verified that we can neglect the magnetoresistance to recalculate the temperature under magnetic field.

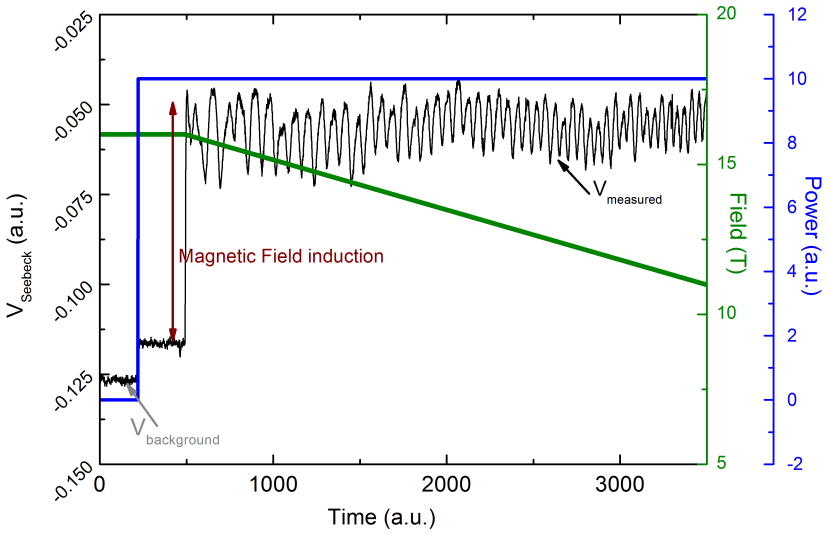

Figure 2.8: *Analysis of the Seebeck signal (black curve), applied power (blue curve) and magnetic field sweep (green curve) in "Thermopower Quantum Oscillations" technique.*

The temperature modification was estimated lower than 0.10% of the absolute temperature in the lowest temperature regime. Besides, as temperature increases, the magnetoresistance decreases and the temperature modification becomes smaller than 0.10%. For example, at 4K, the upper limit variation of the temperature in the completed field range, $[0-34]$T, due to magnetoresistance is smaller than 4mK. The change in the resistance value transformed into temperature is significantly smaller than the applied thermal gradient at this temperature, $\Delta T = 120$mK for a $\Delta T/T = 3\%$. Consequently, at high magnetic fields, we can neglect the magnetoresistance of the $1k\Omega$- RuOx thermometers of our setup.

2.4 Electrical Resistivity

The electrical resistivity is an intrinsic property of a given material while its resistance R depends on its dimension. For certain geometries, such as the bar-shape, there is a simple relation between resistivity and resistance:

$$R = \frac{V}{I} = \frac{l}{S}\rho \tag{2.11}$$

with l/S the so-called geometrical factor. Resistivity measurements were used to determine the quality of the sample through the residual-resistance-ratio (RRR) and to perform magnetoresistance measurements ($\rho(H)$) of the compounds at ambient pressure. For measuring those intrinsic characteristics of the compound, AC four-contact probe was used.

The RRR is defined as the ratio of the resistivity of a compound at room temperature and the extrapolation of the resistivity at 0K:

$$RRR = \frac{\rho_{300K}}{\rho_{0K}} \tag{2.12}$$

It depends on the amount of impurities and other crystallographic defects; for that reason, it is considered as a parameter of the quality of the sample.

2.5 Extreme Conditions

In order to fully explore the (T,P,H) phase diagram of heavy fermion compounds, the measurements have been performed in extreme conditions of temperature (down to the mK range), high fields (up to 34T) and high pressure ranges. In this section, temperature and magnetic fields regimes in which the measurements were performed are shown.

2.5.1 Low Temperatures

To achieve the quantum phase transitions and the reorganization of the magnetic structures in heavy fermion systems, low temperature regimes are needed. To reach these temperatures, dilution cryostats, ^{3}He refrigerators and ^{4}He fridges were used.

To perform thermopower measurements in the low temperature regime a dilution fridge with based temperature 100mK and fields up to 16T was used. For the high temperature regime $[1.8 - 300]$K, we used a PPMS cryostat with home-made-inserts for vacuum and for pressure setups. Finally, for the high magnetic field measurements performed at LNCMI, we employed an ^{3}He refrigerator with lowest temperature 360mK.

To measure the magnetoresistance of heavy fermion compounds, a 50mK dilution fridge with magnetic fields up to 13.4T and the PPMS cryostat, with standard inserts, for the high temperature regime were utilized.

The principles of dilution cryostats, ^{3}He refrigerators and ^{4}He fridges, as they are exhaustively described in the literature [Lounasmaa, 1979, Enss and Hunklinger, 2005], will not be mentioned here.

2.5.2 High Magnetic Fields

Magnetic fields are used to induce magnetic transitions and then to analyze the band structure modifications. For these studies performed following the "Thermopower in Stable Conditions" technique, the fields were produced by a superconducting magnet of 9T in the temperature regime of $[1.8 - 50]$K and one of 16T in the dilution refrigerator. The magnetic field mode for the stable conditions technique consisted in modifying the magnetic field by steps.

For mapping the Fermi surface of these compounds through the quantum oscillations, superconducting magnets up to 16T and resistive magnet with highest field of 34T were used. In these cases, the magnetic field was swept at the constant rate of $0.05 - 0.1$T/min for the superconductor magnet and with a rate of $200 - 300$Oe for the resistive one. We note that this swept in field increased T_{Bath} in a negligible value and as a consequence, no perturbation on the sample-temperatures was observed.

Chapter 3

Thermopower Study of UCoAl

This chapter is focused on the thermoelectric study of UCoAl system. First, we show thermopower behaviour at ambient pressure conditions and then, we present the results under pressure. At ambient pressure, the evolution of the metamagnetic transition with temperature and the changes on the heat carriers through the metamagnetic transition were studied in the longitudinal and transverse configurations. A simple analysis of the Fermi surface change at the metamagnetic transition was obtained as a result of the comparison between thermopower and Hall effect measurements. Exotic magnetic excitations were observed around the Critical End Point and in the ground state of UCoAl. Under pressure, the evolution of the magnetic structure, called wing structure, towards the Quantum Critical End Point was analyzed. Finally, a comparison of the evolution of the wing structure to other probes such as magnetization or Hall resistance was performed.

3.1 Context and Motivation

The study of the quantum phase transitions in intermetallic strongly correlated electron systems such as the transition from an antiferromagnetic (AF) ordered state to a paramagnetic (PM) state, or from a ferromagnetic (FM) to PM ground state has recently motivated a large variety of experimental and theoretical studies [Flouquet, 2005, Löhneysen et al., 2007, Si and Steglich, 2010]. In the case of an AF instability, the restoration of a PM ground state at the quantum phase transition is often induced by the application of pressure or magnetic field [Stewart, 2006]. In weak itinerant ferromagnets, the Curie temperature T_C, indicating the PM-FM second order transition, changes from second order to first order metamagnetic character at the finite temperature of the Tricritical Point (TCP) before collapsing at the critical pressure p_c [Belitz et al., 1999]. To suppress the magnetic order, pressure and magnetic field must be applied simultaneously as the FM domain is extended above p_c following the FM wing structure. The wings start at the TCP and ends at the Quantum Critical End Point (QCEP) [Belitz et al., 2005, Taufour et al., 2010, Kotegawa et al., 2011]. A recent example is the FM superconducting compound UGe_2 which at zero magnetic field has a tricritical point at $p_c \backsim 1.46$GPa [Pfleiderer and Huxley, 2002]. Under magnetic field, the FM wings were observed and they collapse at the QCEP located at $p_{QCEP} \backsim 3.5$ GPa and $H \backsim 17$ T (see Fig.3.1).

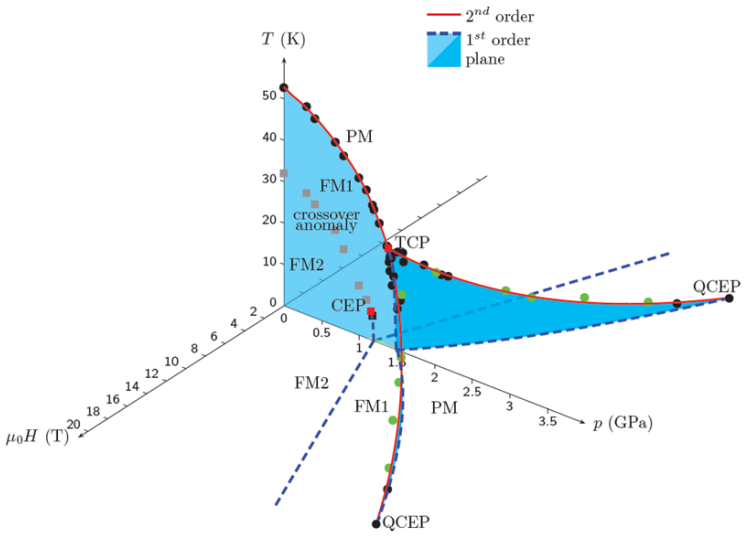

Figure 3.1: *(T, P, H) phase diagram of UGe_2 [Taufour et al., 2010].*

The interest to study UCoAl comes from its relation to the weak ferromagnet compound UGe_2. Both present a similar (T, P, H) phase diagram with comparable magnetic behaviours. For UCoAl, at $P = 0$, the compound presents a PM ground state instead of a FM state as occurs in UGe_2, the wing structure already exits at ambient pressure. Nevertheless, UCoAl is close to a FM state. Pressure studies in UCoAl estimated that for this compound the PM-FM plane at $H = 0$T, equivalent to the one of UGe_2, ends up at $p_c = -0.2$GPa [Mushnikov et al., 1999] and that the intersection of this plane and the wings at the TCP occurs at $p_c \lesssim -0.2$GPa. These pressure conditions allow to perform thermoelectric measurements inside the wings at ambient pressure. The temperature evolution of the wings is

characterized by the evolution of the critical field of the metamagnetic transition from a first order H_M, below the Critical End Point (CEP), to a crossover regime H_m for temperatures above the CEP(T_0, H_M^*) with $T_0 \sim 11$K (see Fig.3.2a). Under pressure, the wings show an increase of the critical field, H_M (see Fig.3.2b) and a continuous decrease of T_0 ending at the QCEP ($T_{\text{QCEP}} = 0$K, $p_{\text{QCEP}} = 1.5$GPa and $H_{\text{QCEP}} = 7$T) [Aoki et al., 2011]. A schematic (T, P, H) phase diagram of UCoAl is shown in Fig.3.3. The extreme conditions of pressure, temperature and magnetic field of the (T, P, H) phase diagram are easily reachable in UCoAl compare to UGe_2. For this reason, UCoAl is a good candidate to study the weak ferromagnetism of the wings, the induced metamagnetic transition and the behaviour around the QCEP.

(a) (T, H) *phase diagram of UCoAl at* $P = 0$. *The* 1^{st} *order line ends at CEP(*$11K$,$\sim 1T$*).*

(b) (H, P) *phase diagram of UCoAl. The CEP line ends at the QCEP (*$1.5GPa$, $7T$*).*

Figure 3.2: *Evolution of the metamagnetic transition of UCoAl (a) as a function of temperature and (b) as a function pressure [Aoki et al., 2011].*

3.2 Introduction to UCoAl

UCoAl belongs to the class of uranium ternary intermetallic compound (UTX series). Its crystal lattice presents an hexagonal ZrNiAl-type structure with basal plane layers of U-Co(2) and Al-Co(1) intercalated among them. The inter-uranium distance is 0.349nm placing this compound in the range of the Hill limit[1]. The structure of the basal plane of UCoAl represented in Fig.3.4 shows that the U-atoms form on a quasi-kagome lattice structure with two well defined Co-atoms positions (Co(1) which is surrounded by 6 U-atoms and Co(2) surrounded by 3 U-atoms). These structural characteristics are going to play a major role in the magnetism of this compound.

The magnetization of UCoAl presents a strong anisotropy. When the magnetic field is applied along the c-axis, a strong change in the magnetization of the systems occurs at $H_M \sim$ 1T that marks the metamagnetic transition whereas when the magnetic field is applied on the basal plane, UCoAl shows a Pauli paramagnetism behaviour (see Fig.3.5). Just above the

[1]Hill realized a systematic study of uranium compounds as a function of the interatomic distance between two uranium atoms, d_{U-U}. He found that for $d_{U-U} < 3.4$Å, the ground state is PM which is interpreted by the overlap of the $5f$ orbitals. For $d_{U-U} > 3.6$Å, the ground state is magnetic, which is interpreted by the result of local magnetic moments. The region $3.4 < d_{U-U} < 3.6$ Å is the critical region which is called Hill limit [Hill, 1970].

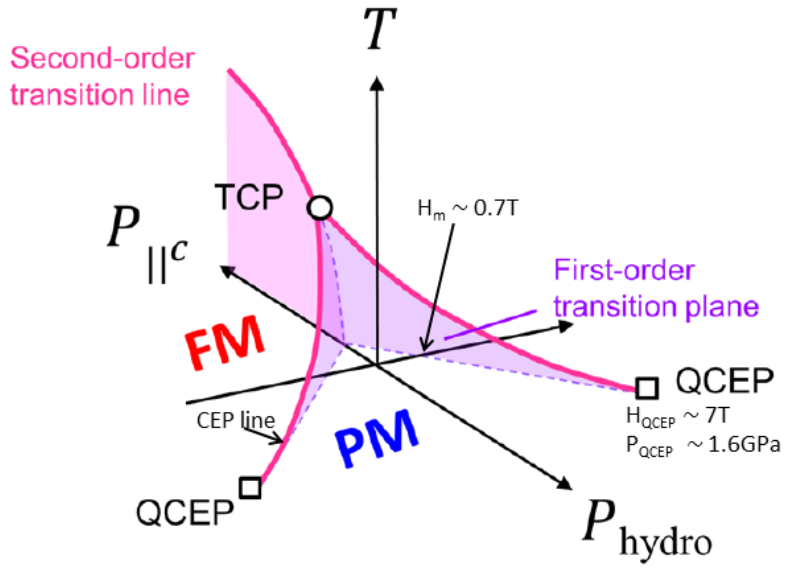

Figure 3.3: *(T, P, H) phase diagram of UCoAl [Karube et al., 2014]. The pink area shows the FM-PM second-order transition that becomes first order for $P > P_{TCP}$. Above P_{TCP}, this FM-PM first-order transition defines the wings structure (purple planes). The evolution under uniaxial pressure along the c-axis and under hydrostatic pressure (which are opposite behaviours) are indicated by arrows.*

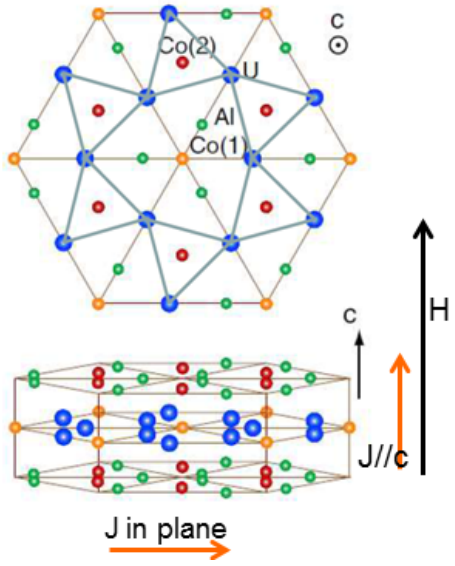

Figure 3.4: *Lattice of UCoAl. In blue, U atoms forming a quasi-kagome lattice structure, in red and yellow Co(2) and Co(1) atoms, respectively and in green Al atoms [Nohara et al., 2011]. The arrows indicate the thermal currents and magnetic field orientations of the thermopower measurements of our studies.*

metamagnetic transition, the magnetic moment of UCoAl is $0.3\mu_B$ per unit formula with μ_B the Bohr magneton. Magnetization measurements show that the total magnetic moment of UCoAl increases with field and no saturation is observed even for fields up to 35T. This small

value of the local magnetic moment of U-atoms in UCoAl compared to the magnetic moment of the U free ion, $1.8\mu_B$, is the consequence of the strong coupling of $5f$ bands of U-atoms with the Fermi sea (s, p and d valence states of Co-atoms). Therefore, this hybridization causes the delocalization of the $5f$ local magnetic moments [Sechovsky et al., 1986]. In addition, the magnetization carried by these itinerant electrons point along the c-axis as a result of the strong exchange interaction at the interatomic scale. The strong spin-orbit coupling causes that the orbital component of the itinerant quasi-particles is the main contribution to magnetism in UCoAl. The orbital moment is twice as large as and antiparallel to the spin moment of the itinerant electrons and the magnetic contribution of these itinerant charges is higher than the local magnetic moment of the core of the U atoms. These characteristics correspond to the description of the itinerant ferromagnetism behaviour [Eriksson et al., 1989, Kucera et al., 2002].

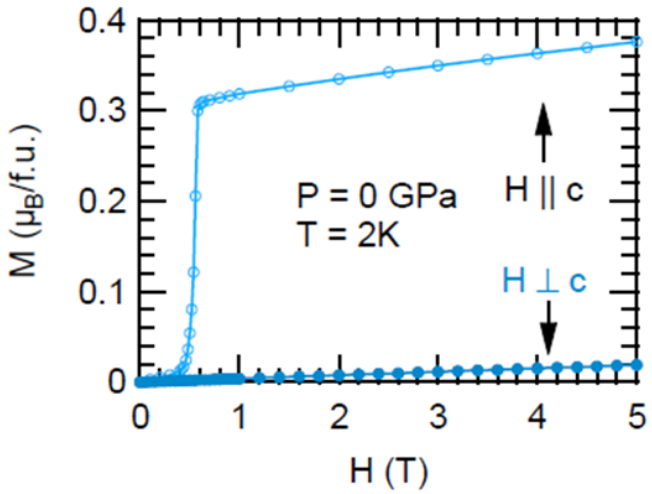

Figure 3.5: *UCoAl magnetization measurements as a function a magnetic field applied along the c-axis (open circles) and on the basal plane (filled circles) at $T = 2K$.*

In relation to the density of state (DOS), band structure calculations determine that the 70% of the total DOS at the Fermi level is carried by the $5f$ electrons due to the hybridization of the U-atoms with the bands close to the Fermi energy. The $3d$ bands of Co have a small contribution because they are almost filled as a result of the strong hybridization with the $5f$ U-states. From NMR measurements and simulations, it has been demonstrated that the position of the U-atoms in the lattice has an important role in the distribution of the DOS. For example, the interatomic distance between U-Co(1) and U-Co(2) are similar; nevertheless, their contribution to the DOS is quite different as a consequence of the correlations with first neighborhoods. Co(1) takes a major role in the DOS as Co(1) has twice as main neighbors U-atoms than Co(2) [Betsuyaku and Harima, 2000, Javorský et al., 2001].

Recently, some full potential band structure calculations with local spin density approximation (FLAPW+LSDA) have been performed in the PM phase (see Fig.3.6), using 592 sampling k points in the irreducible Brillouin zone for this moderated heavy fermion compound. UCoAl is a compensated metal where the number of hole carriers, near 0.05 holes per UCoAl formula, comes from the 78 hole band and the electron carriers are distributed among the 79 and the 80 electron bands. The bands 79 and 80 are paired. The large differences

observed in the topology of the Fermi surfaces of 79 and 80 bands are induced by the strong spin splitting in the PM phase of UCoAl which is cause by the parity violation. The Fermi surface is shown in Fig.3.6. In the FM phase, we expect the shrinking of the spin up contribution and the enlargement of the spin down contribution, generating a non zero magnetic moment.

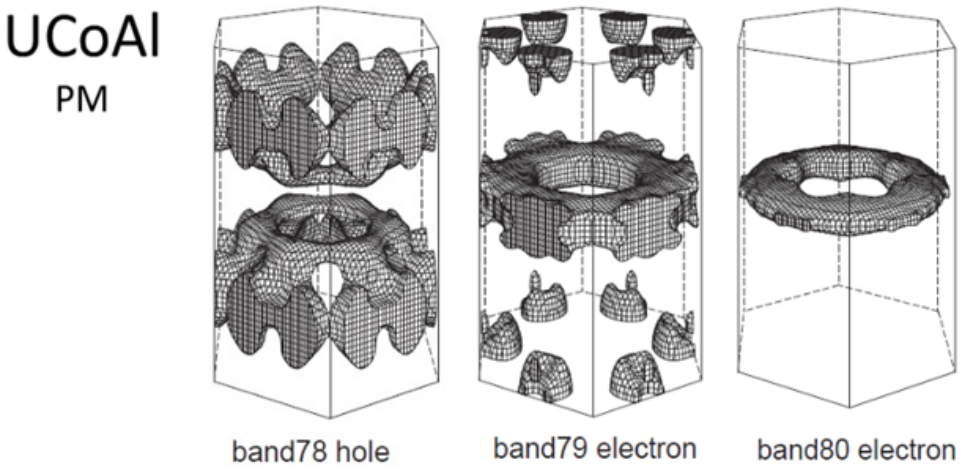

Figure 3.6: *Paramagnetic Fermi surface of UCoAl obtained by FLAPW+LSDA band structure calculations (H. Harima, unpublished). This Fermi surface has one hole and two electron bands. The non inversion symmetry causes the large differences between the two electron-like bands.*

Although the FLAPW+LSDA calculation cannot treat completely the electronic correlations, it will give a good estimation of the relative mass enhancement between hole and electron quasi-particles. The density of states of hole bands is 260 states/Ry/(primitive cell) corresponding to 15 mJ/molK^2, while the density of states of the electron bands is 121 states/Ry/(primitive cell) corresponding to 7 mJ/molK^2, showing nearly twice heavier hole band than electronic bands in the PM state. A reduction of the specific heat in the FM phase is expected related with the higher arrangement of the system. To my knowledge, the highest quality sample of UCoAl in the literature presents a RRR= 27. This quality is still not good enough to measure the FM Fermi surface of the system by quantum oscillations methods such as the de Haas–van Alphen effect or Shubnikov–de Haas effect. In any case, it is not possible to determine the ground state of UCoAl by these techniques because of the low magnetic field range of the PM phase.

UCoAl is very sensitive to pressure and to doping rate. The FM phase of UCoAl can be stabilized applying an effective negative pressure bigger than p_c by doping or applying uniaxial pressure along the c-axis. Some studies show that a tiny quantity of a dopant can favor the FM state as a ground state; e.g., 2% substitution of Fe for Co in UCoAl [Mushnikov et al., 1999, Mushnikov et al., 2002]. The uniaxial pressure induces a reduction of the critical field, H_M, of the metamagnetic transition followed by the formation of ferromagnetism at higher uniaxial pressures caused by the increase of the hybridization between the ab-planes. This increase of hybridization produces localized behaviour of the $5f$ moments and enhances the FM ordered state [Karube et al., 2014]. Against this behaviour, hydrostatic pressure induces an increase of H_M. The variations in the $5f$-$3d$ hybridization within the basal plane of the ZrNiAl-type

hexagonal structure by pressure seem to be the underlying aspect of the evolution of the magnetism in UCoAl [Ishii et al., 2003, Karube et al., 2014].

Around the QCEP, not many studies have been carried out due to the extreme conditions to achieve it. Resistivity and Hall resistance measurements were performed and they present an increase of their values which was related with an increase of the effective mass at the QCEP. Above it, the metamagnetic transition is transformed in a pseudometamagnetic transition. This transition broadens with pressure [Aoki et al., 2011, Combier et al., 2013]. The understanding of the physics related to the QCEP is one of the main ongoing research project in strongly correlated electron physics.

3.3 Quality Samples and Measuring Configurations

Single crystals of UCoAl were grown by the Czochralski method in a tetra-arc furnace. The residual resistivity ratio of the studied crystals was around 10. Two bar-shaped samples, with dimensions $3.5 \times 1.5 \times 0.5$mm, from the same batch were cut by spark cutter and oriented by X-ray Laue diffractometer displaying very sharp spots.

At ambient pressure, thermopower measurements were performed on these samples with magnetic field applied along the c-axis and thermal gradients along the a-axis (transverse configuration) and c-axis (longitudinal configuration). The Nernst coefficient was also measured for the transverse configuration. Magnetoresistance measurements were performed on these samples using the same electric contacts as thermopower and as a result, thermoelectric coefficients and magnetoresistance kept the same geometric factor.

Under pressure, we started to measure a sample with similar dimensions to the at ambient pressure samples. This sample3 was too big to reach pressures close to the QCEP. Then a sample4 with dimensions $1.8 \times 0.7 \times 0.3$mm was needed. The quality of this sample was similar to the quality of the measured samples at ambient pressure; however, the width of the metamagnetic transition for this sample4 was larger and the critical field (H_M) at little bit lower. Under pressure, only the Seebeck coefficient for the longitudinal configuration was measured. The dimensions of the Inner Vacuum Chamber of the refrigerator were smaller than the length of the pressure cell preventing that magnetic field and thermal gradient were applied in perpendicular directions.

The measurements were performed at low temperatures, cooling down the setup to 100mK, and under magnetic fields up to 16T. The thermoelectric coefficients were measured at ambient pressure conditions by "One heater-Two thermometers" setup and under pressure by the designed "Thermocouples" setup for the piston cylinder pressure cell. Magnetoresistance measurements were performed using the AC locking technique on a four-contact configuration for transverse and longitudinal configurations. All data shown are obtained by upwards magnetic field sweeps.

3.4 UCoAl at Ambient Pressure

In order to study in detail the electronic properties of UCoAl, precise thermoelectric power experiments were performed, extending previous [Matsuda et al., 2000] measurements from $T = 4$K down to 150mK. We analyzed carefully thermoelectric power in the different field

and temperature regimes of the (T, H) phase diagram in order to draw the signature of $H_M(T)$ below the CEP and of the PM-FM crossover domain above the CEP. Thermoelectric power measurements show that the ratio S/T (thermoelectric power divided by temperature) has a relative stronger drop compared to the jump of the electronic specific heat γ at H_M. Our results allow us to estimate the field variation of S/T at very low temperatures and then, to give a key comparison of the interplay between thermal transport and thermodynamic properties.

3.4.1 Metamagnetic Transition

The metamagnetic transition of UCoAl has been studied by thermopower temperature dependence, $S(T)$, isothermal thermopower measurements, $S(H)$, and magnetoresistance measurements, $\rho(H)$.

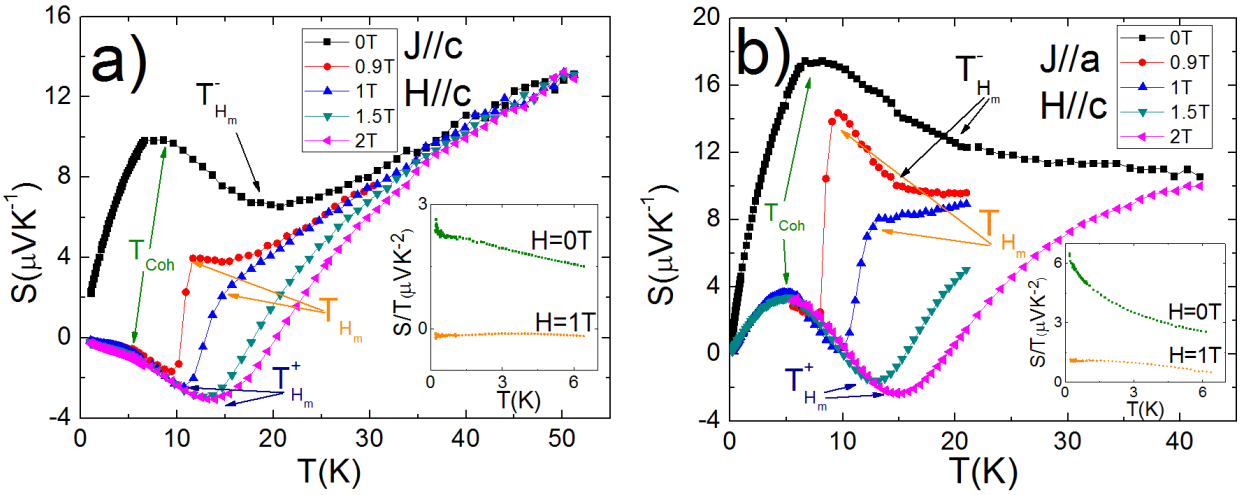

Figure 3.7: *Temperature dependence of thermopower, $S(T)$, at different magnetic fields, a) for longitudinal and b) for transverse thermal flow configurations. The insets of the figures show their corresponding $S/T(T)$ behaviour at $H = 0$ and $H = 1T$.*

Figures3.7 a) and b) show $S(T)$ at constant field for the longitudinal and the transverse configurations, respectively. The entrance in a low temperature domain, where a Fermi liquid state is expected, is achieved below the coherence temperature, T_{Coh}, defined as the maximum of $S(T)$ in the transverse and a change of slope in the longitudinal configurations. $S(T)$ drops drastically at the metamagnetic transition, therefore T_{H_m} is defined as the temperature for which the behaviour of the Seebeck coefficient drops abruptly from high values of $S(T)$, upward curvature, to low values of $S(T)$, downward curvature, in a short temperature window at fixed magnetic fields. This behaviour at T_{H_m} can also be observed from $S/T(T)$ measurements (see Fig.3.8). The width of the crossover is defined by the temperature difference between $T^-_{H_m}$, $T^+_{H_m}$, which corresponds to the minimum or inflection point of $S(T)$ for $H < H_M$ and for $H > H_M$, respectively. We note that T_{H_m} increases with magnetic field and that in the high temperature regime, $T > 40$K, all the $S(T)$ curves at different magnetic fields collapse together in one curve.

Fig.3.8 shows $S/T(T)$ for different magnetic fields. For $S/T(T)|_{H\geqslant 0.75}$, $S/T(T)$ measurements present a change of behaviour from downward curvature to upward curvature as temperature increases. This behaviour goes with a jump of $S/T(T)$ and the temperature at which this jump appears corresponds to the T_{H_m}. We observe that $S/T(T)$ diverges at low temperature for $H < 0.75$T while for $H \geq 0.75$T, the $S/T(T)$ remains constant. In the inset of Figs.3.7 a) and b), S/T is also represented in the low temperature regime for PM and FM states for transverse and longitudinal configurations. S/T is expected to be constant in a Fermi liquid, then as $S/T(T)$ diverges at low temperature for $H < 0.75$T we suggest the possible existence of an exotic PM ground state at low temperatures.

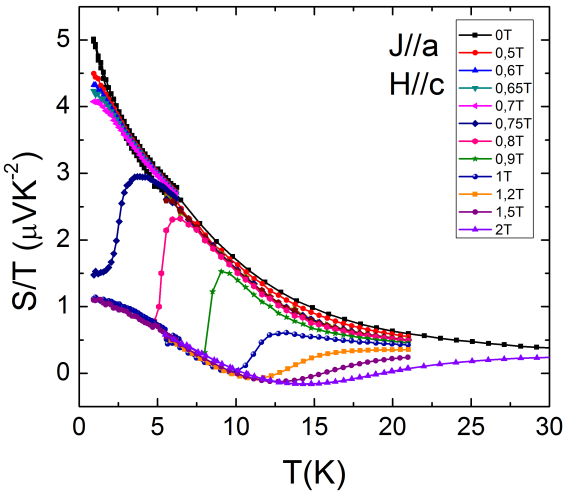

Figure 3.8: *$S/T|_{H=ctn}(H)$ at different magnetic fields for transverse thermal flow configuration.*

Fig.3.9 displays the isothermal thermopower over temperature measurements $S/T(H)$ as function of increasing field for a) transverse and b) longitudinal configurations. The critical field of the transverse configuration sample is $H_{Mtrans} = 0.75$T; being slightly higher than the one for the longitudinal configuration, $H_{Mlong} = 0.70$T. The metamagnetic transition is characterized by a sharp change on the absolute value of the Seebeck coefficient which defines the critical field H_M. For transverse configuration, the sign of thermopower remains unchanged in the PM and FM states at low temperatures and changes its sign above T_0. In the case of the longitudinal configuration, thermopower changes from hole-like to electron-like as the system crosses the metamagnetic transition from PM to FM states. In the FM phase for temperatures $T > T_0$, transverse and longitudinal configurations present the same thermopower behaviour. For $T < T_0$ regime, the heat transport is anisotropic, then it is directional dependent.

The inset of Fig.3.9 b) shows the criterion we chose to determine the first order transition and the width of the crossover from the first derivative of the $S/T(H)$ measurements. The minimum of the first derivative of the $S/T(H)$ measurements corresponds to the metamagnetic transition, H_M, for temperatures below T_0. Above $T > T_0$, the first order transition becomes a crossover defined by H_m, H_m^- and H_m^+ where H_m is the middle of the crossover and H_m^- - H_m^+ indicate the magnetic field width of the crossover. The middle of the crossover corresponds to the minimum of the first derivative of $S/T(H)$ measurements and the inflection points of the first derivative correspond to the width of the crossover.

At the metamagnetic transition, a strong hysteresis between up and down magnetic field sweeps has been observed for transverse and longitudinal configurations. This is a consequence of the first order nature of this transition. The inset of Fig.3.9 a) shows the hysteresis evolution with temperature for the transverse configuration. The width of the loop of the hysteresis increases from T_0 towards low temperatures (e.g. 40mT at 0.85K and 70mT at 0.25K for $J \parallel a$).

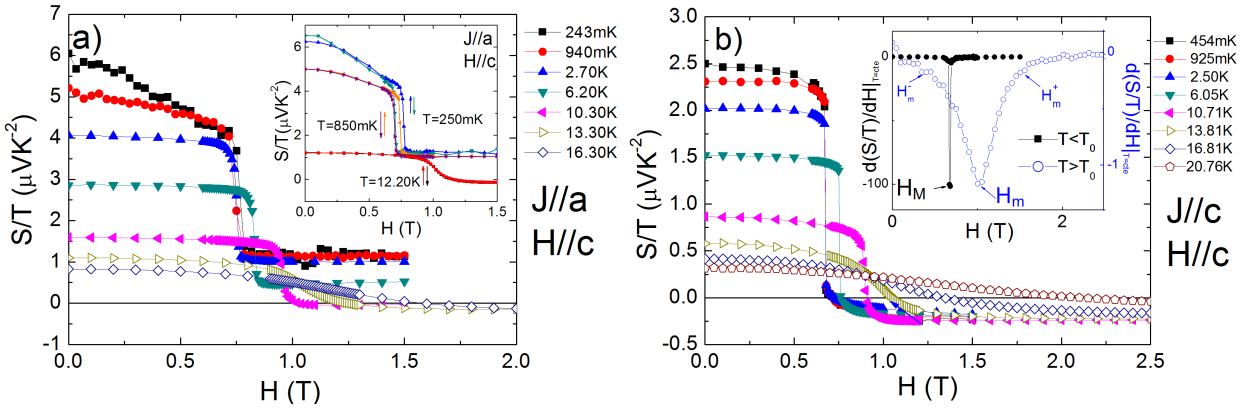

Figure 3.9: *Isothermal thermopower measurements as a function of increasing magnetic field at different temperatures in a) transverse and b) longitudinal configurations. The inset of panel 3.9 a) shows the evolution of the hysteresis loop at the metamagnetic transition from first order to crossover. The inset of panel 3.9 b) indicates the location of the metamagnetic transition lines. Open symbols correspond to the crossover regime and filled symbols to the temperature range of the first order metamagnetic transition.*

The anomalies observed in temperature and field dependencies of the thermopower are displayed in the (T, H) phase diagram shown in Fig.3.10 a) and b), respectively. Despite the complex temperature dependence of $S(T)$ at fixed field, we show that crossover lines can also be drawn from the T dependencies. This (T, H) phase diagram presents slight differences from the one determined from the field dependence of $S(H)$. In addition, the values obtained from $S(H)$ measurements present smaller relative errors in field than the values obtained from $S(T)$ measurements. This is due to the fact that H_M, H_m, $H_m^{\pm}$ are well-defined in field whereas the T_M, T_m, $T_m^{\pm}$ singularities are spread over a large temperature range; thus, a large error in temperature is entailed as a result. However, the first order line coincides perfectly for the $S(H)$ and $S(T)$ measurements. We also notice that the phase diagrams obtained for transverse and longitudinal configurations are really similar, see Figs.3.10 a) and b). The small variations in the critical field H_M are due to H_M is slightly sample dependent. The longitudinal sample has a slightly smaller H_M than the transverse one as we observed from Fig.3.10 in which the filled squares and circles correspond to the first order transition, the filled stars represent the entrance in the coherent regime where a Fermi liquid regime is expected, the open symbols correspond to the crossover (the left and right triangles delimit the width of the crossover, which is defined by H_m^- and H_m^+) and the open circles and squares indicate the middle of the crossover. The crossover regime collapses on approaching the CEP ($H_M^\star$, T_0) as represented in Fig.3.10 b). In Fig.3.10 a), we also show, in grey symbols, the phase diagram of UCoAl obtained from magnetization measurements [Matsuda et al., 2013]. The similarity

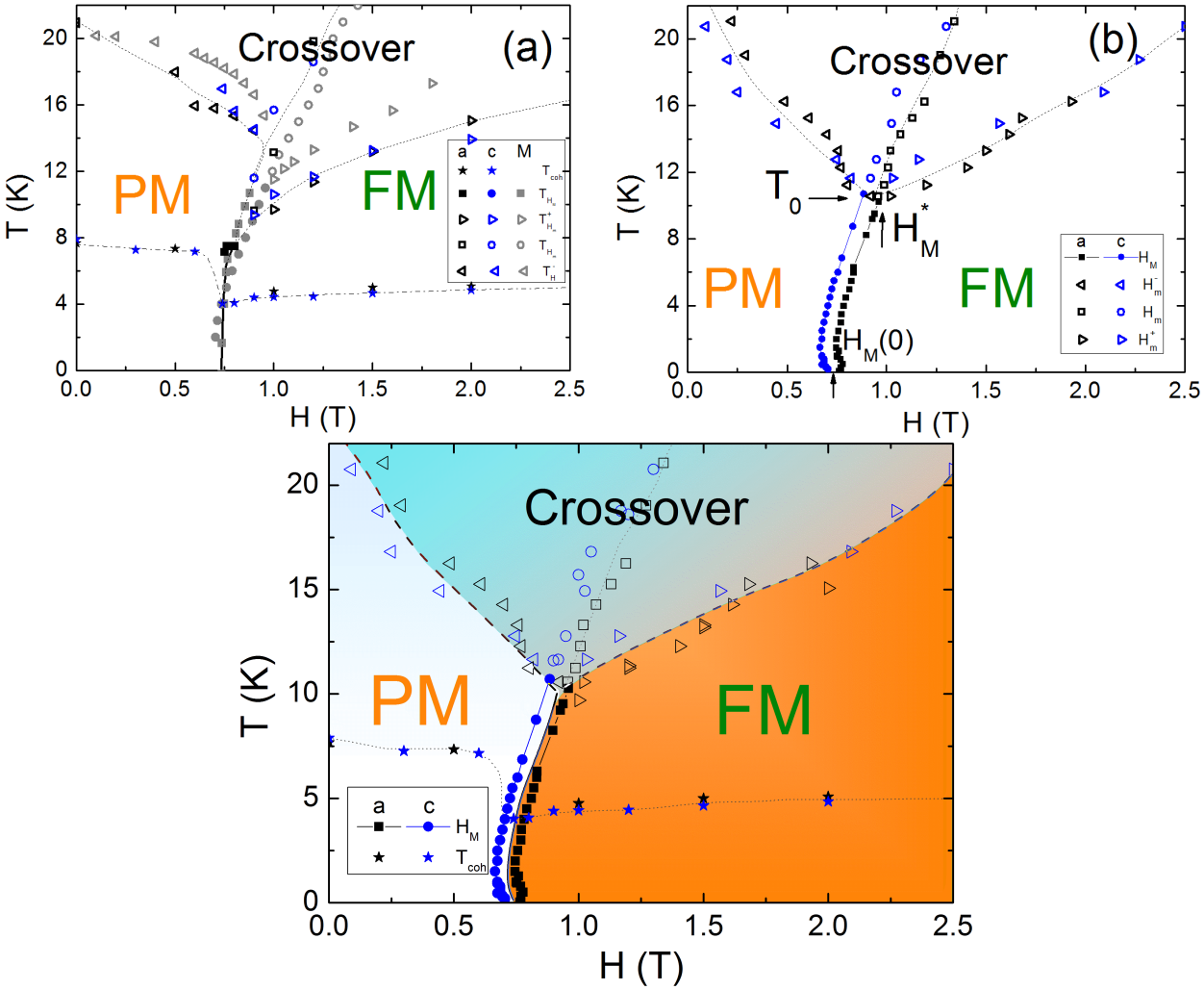

Figure 3.10: *(T, H) phase diagram drawn for $J \parallel a$ (black points) and $J \parallel c$ (blue points) configurations. The panel a) and b) show the (T, H) phase diagram from temperature and field dependence thermopower measurements, respectively. Filled symbols represent the first order transition and open symbols represent the crossover. The panel a) also shows the phase diagram determined by magnetization measurements (grey symbols) [Matsuda et al., 2013]. The down panel shows the (T, H) phase diagram resulting of the combination of temperature and magnetic field phase diagrams.*

of the phase diagrams obtained by thermopower and magnetization measurements prove the good agreement between these measurements to determine the metamagnetic transition. The only remarkable difference is the width of the crossover which is shorter in magnetization than in thermopower measurements. This difference can come from the criterion we selected to define the crossover.

In the down graph of Fig.3.10, we show the complete (T, H) phase diagram obtained from the set of temperature dependent $S(T)$ and field dependent $S(H)$ thermopower measurements. All the data are combined in order to obtain the complete (T, H) phase diagram for both configurations. From temperature dependent measurements at fixed field (see Fig.3.7), we extract the coherence temperature regime. From field dependence measurements

(Fig.3.9), the lines H_M corresponding to the first order metamagnetic transition and H_m to the middle of the crossover. In addition, from $S(H)$ measurements, we determine the lines delimiting the width of the crossover, $H_m^- - H_m^+$. The entrance in the coherent regime appears at low temperatures and a simple Fermi-liquid state, which signature is a constant value of $S/T(T)$ [Zlatić et al., 2007], occurs only for $H > H_M$ as it will be shown in subsec. 3.4.3. Above 1 K, the phase diagram is in good agreement with those previously drawn from magnetization, NMR, and Hall effect measurements [Nohara et al., 2011, Karube et al., 2012, Combier et al., 2013]. Below $T \sim 1$ K, the change of the sign in $\partial(T_M)/\partial H$ is due to the increase of the hysteresis of the first order transition.

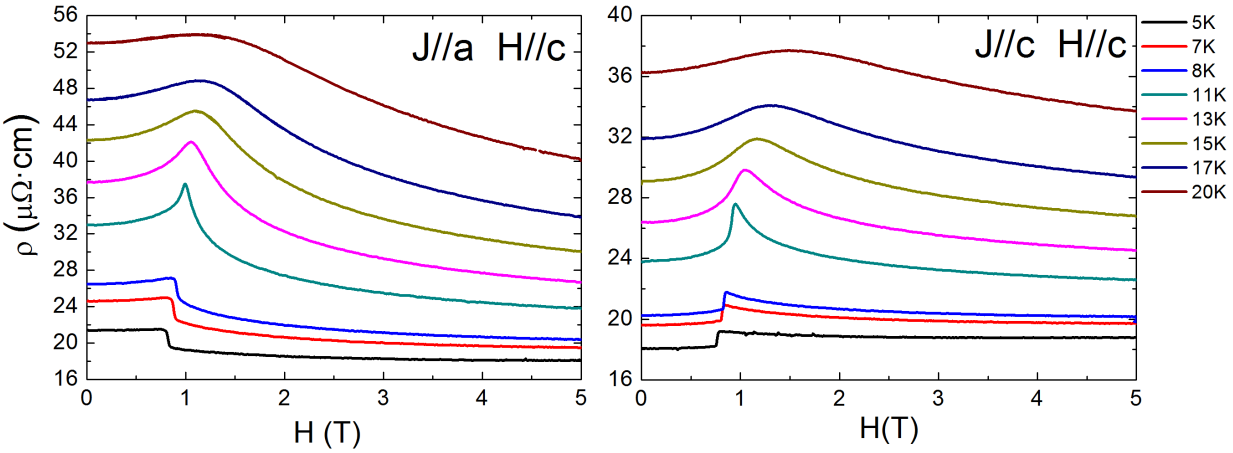

Figure 3.11: *Magnetoresistance measurements of UCoAl for transverse (left) and longitudinal (right) configurations in the high temperature regime* $[5 - 20]K$.

Magnetoresistance measurements were also performed in the transverse and in the longitudinal configurations using the same electrical contact as those used for determining the thermoelectric coefficients (see Fig.3.11). For $T < T_0$, the first order metamagnetic transition corresponds to a sharp jump in the resistivity of the compound. As temperature approaches the temperature of the CEP, a local increase of the resistivity around H_M is observed. Above T_0, as temperature increases, the maximum becomes broader and broader until it is not possible to see any inflection point on the curve. These inflection points in magnetoresistance curves match with the width of the crossover of the phase diagram of UCoAl. In Fig.3.12, the (T, H) phase diagram obtained from magnetoresistance measurements is represented. The transverse configuration is represented by black symbols and the longitudinal configuration by blue symbols. For both configurations, the filled symbols correspond to the first order transition whereas the open symbols represent the crossover regime. We conclude that magnetoresistance (T, H) phase diagram is comparable to the phase diagram determined by isothermal thermopower measurements.

In the low temperature regime, magnetoresistance measurements performed in the longitudinal configuration show a step-like increase at the metamagnetic transition. This increase in magnetoresistance has been attributed to the reduction of the number of carriers resulting from the $5f$ band splitting. However, magnetoresistance measurements of the transverse configuration show a step-like decrease at the metamagnetic transition. This anisotropy in magnetoresistance can come from the anisotropy of the spin-orbit coupling that matches with

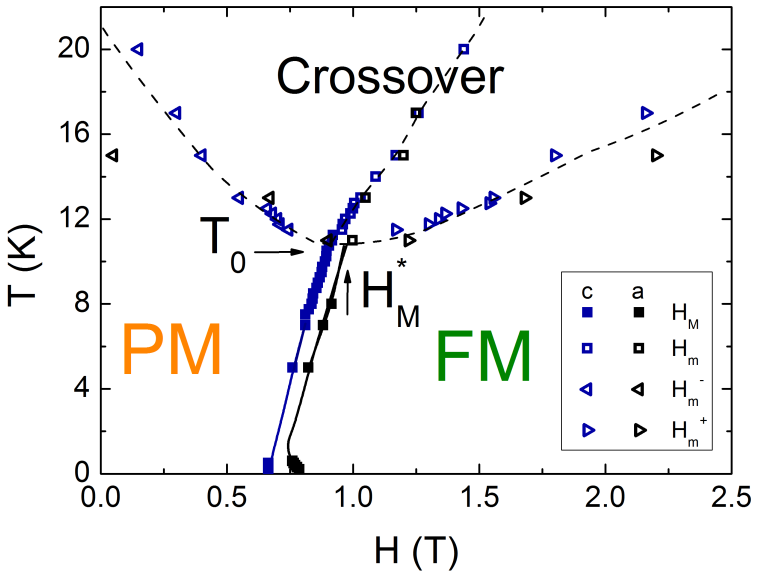

Figure 3.12: *(T, H) phase diagram obtained from magnetoresistance measurements. The (T, H) phase diagram obtained from transverse configuration is shown in blue symbols and the (T, H) for longitudinal configuration in black symbols. For both configurations, the filled symbols represent the first order transition and the open symbols represent the crossover.*

the possibility of a band splitting at the metamagnetic transition.

3.4.2 Charge Carriers at the Metamagnetic Transition

The great interest of thermopower measurements is to probe the evolution of the topology of the Fermi surface and the enhancement of the effective mass of the different types of carriers, electrons and holes. However, it is a rather difficult analysis in this multiband system. At first glance, it is usual to compare at very low temperature S/T and the electronic specific heat $\gamma = C/T$ experiments. In UCoAl, strong changes of the Fermi surface are expected at the metamagnetic transition (H_M) due to the strong discontinuity of the thermopower and the sign change in the longitudinal configuration. To estimate this discontinuity of $S(H)$ through the H_M, we represent in Fig.3.13 the field dependence of S/T at the lowest temperature measured (170mK) for transverse ($J \parallel a$ in black) and longitudinal ($J \parallel c$ in blue) configurations. For $J \parallel c$, S/T is almost field independent on both sides of H_M while for $J \parallel a$ in the PM phase S/T decreases with H below H_M and becomes constant above H_M. This different behavior of S/T is clearly associated with the quite unusual strong increase of S/T preserved at $H = 0$T for $J \parallel a$. For $J \parallel a$, the drop of S/T as a function of field at $T = 170$mK is at least 2.8μVK^{-2} at H_M while for $J \parallel c$, it is 2 μVK^{-2}. Thus, the relative thermopower drops are 68 % and 100 % for $J \parallel a$ and $J \parallel c$ configurations, respectively.

To compare the discontinuity of the $S/T(H)$ to the discontinuity of the γ at the metamagnetic transition (H_M), we evaluate the drop of the electronic specific heat γ from the results published in ref. [Aoki et al., 2011]. The variation of γ at H_M at 0.45K is only 15mJmol^{-1}K^{-2} decreasing from $\gamma(H < H_M) \sim 75$ mJmol^{-1}K^{-2} to $\gamma(H > H_M) \sim 60$ mJmol^{-1}K^{-2}. Thus, the relative γ drop is only 20 %, which is significantly smaller than the relative transverse

and longitudinal drops in S/T. The higher relative drop in S/T in relation to the relative drop of γ may be the consequence of the fact that S/T is a directional probe, very sensitive to the high entropy bands that are drastically affected at the metamagnetic transition whereas γ probe is sensitive to the complete thermodynamic of the system.

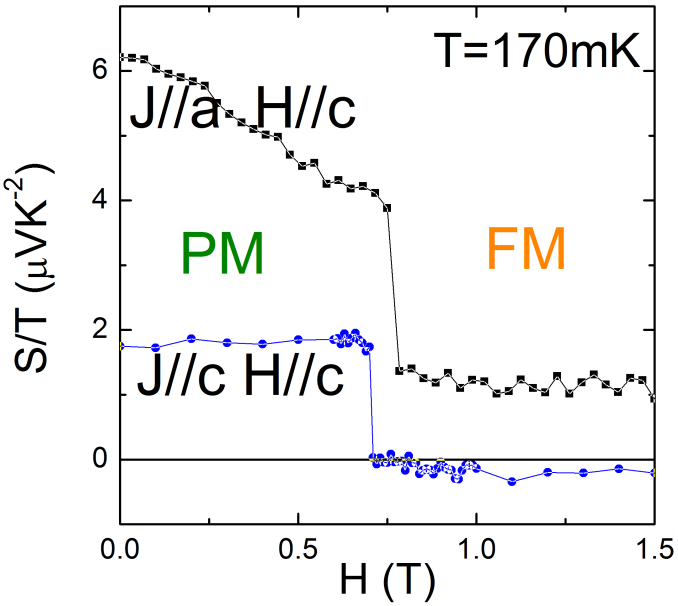

Figure 3.13: *Isothermal thermopower measurements as a function of increasing magnetic fields at* $170mK$ *for transverse (black points) and longitudinal (blue points) configurations.*

To evaluate the number of heat carriers in the PM and FM states, we determine the inverse of the q-factor. For that, γ value is taken below and above H_M. For $H < H_M$ the heat carriers (n) are $n_a = 0.12$ and $n_c = 0.36$ for $J \parallel a$ and $J \parallel c$, respectively. Above H_M n_a jumps to 0.57 and n_c seems to change its sign becoming -3.32. The strong change in the number of carriers per formula unit suggests an important Fermi surface change through the metamagnetic transition. Nevertheless, via a simple one band model, Hall resistance will lead to the conclusion that the number of carriers remains constant at the metamagnetic transition due to the fact that the hole coefficient is almost constant at this transition [Matsuda et al., 2000, Combier et al., 2013]. Moreover, Hall resistance suggests that hole bands are responsible for the electronic transport in the PM and FM states. The opposition of Hall resistance and thermopower results points out that the application of a one-band model description is unsuitable in this complex system.

In a two band model with spherical Fermi surfaces the contribution of each band will be weighted by their respective electrical conductivity (σ), i.e. $S = (\sigma_h S_h + \sigma_{e^-} S_{e^-})/(\sigma_h + \sigma_{e^-})$ [Miyake and Kohno, 2005]. In a first approximation, we assume the invariance of the Fermi surface through H_M, basing this assumption on Hall resistance results. The hole carrier with an average effective mass $m_h^\star \approx 2m_e^\star$ will dominate thermoelectric power response at low field in good agreement with the observed positive sign of the thermoelectric power. Entering in the FM domain through H_M will lead to a drastic decrease of $m_h^\star$, while the carrier concentration stays almost constant on crossing H_M. The opposite sign of the hole and electron response in S/T leads to magnify the reduction of the thermoelectric power on entering in the FM domain

and thus to a drop of S/T quite stronger than the drop of C/T. However, a quantitative description is a difficult task as electron and hole Fermi surfaces are far from spherical. In addition, electronic and hole band modifications are interconnected. Furthermore, in the FM polarized phase with a rather large magnetic moment ($0.3\mu_B$ per U atom), the spin up and spin down Fermi surfaces will differ, at least for the contribution coming from the electron band.

Finally, a direct confirmation of the strong change of the Fermi surface thought the metamagnetic transition has not been yet determined due to the fact that the quality of the samples of UCoAl are not good enough to perform direct measurements of the Fermi surface.

3.4.3 Exotic Magnetic Excitations

Paramagnetic Ground State

A Fermi liquid regime, below the coherence temperature, was expected in the PM phase. For that reason, constant value of the S/T coefficient at low temperatures defining the Fermi liquid regime was expected. However, S/T diverges at low temperature for $H < H_M$ pointing out the possible existence of an exotic PM ground state. We also performed resistivity measurements to verify this unexpected behaviour in the PM phase.

The inset of figures 3.7 a) and b) show the temperature dependence of S/T for $J \parallel c$ and $J \parallel a$ configurations in the low temperature regime, respectively. At $H = 0$, a continuous increase of S/T is observed down to the lowest temperature for both configurations. For the transverse configuration, the increase of S/T is more pronounced and seems to diverge at low temperatures. From the strong increase of S/T on cooling at constant field $H < H_M$, it is clear that at least down to 150mK, constant S/T equivalent to a Fermi-liquid regime is not observed [Zlatić et al., 2007], neither for the longitudinal nor for the transverse configurations. By contrast for $H > H_M$, as soon as the FM state is reached, a Fermi-liquid behavior is observed in the temperature dependence of S/T (constant value of $S/T(T)$). We conclude that the simple Fermi liquid response is observed only for $H > H_M$ below T_{coh}. In relation to the increase of S/T in the PM phase, we confirm that it is in agreement with the increase of the isothermal thermoelectric power in the low field regime in the PM state (see Fig.3.9).

The non-Fermi liquid behavior in the low field regime is also confirmed in resistivity measurements down to 50mK (see Fig.3.14). The resistivity in the PM phase at $H = 0$T (black curves) and the resistivity in the FM phase at $H = 0.8$T (blue curves) are plotted as a function of the square of the temperature for transverse and longitudinal configurations. In resistivity measurements, the Fermi liquid signature corresponds to a T^2 dependence which is only observed in the FM domain for UCoAl. Previous resistivity experiments above 2K reported in ref. [Kolomiets et al., 1999] showed a $T^{3/2}$ temperature dependence in the PM state while a Fermi liquid T^2 dependence occurs in the high field ordered state. They claim that this $T^{3/2}$ dependence of resistivity is related to the existence of spin fluctuations on the ground state [Karube et al., 2012]. Our resistivity measurements below 2K reveal that this $T^{3/2}$ dependence is observed down to 200mK. This $T^{3/2}$ dependence at low temperature of resistivity is characteristic of antiferromagnetic states as it is demonstrated by the self-consistent renormalization theory proposed by Moriya [Moriya, 1985]. We suggest that this behaviour might be related to the quasi-kagome lattice of UCoAl. Even for $T < 200$mK, resistivity

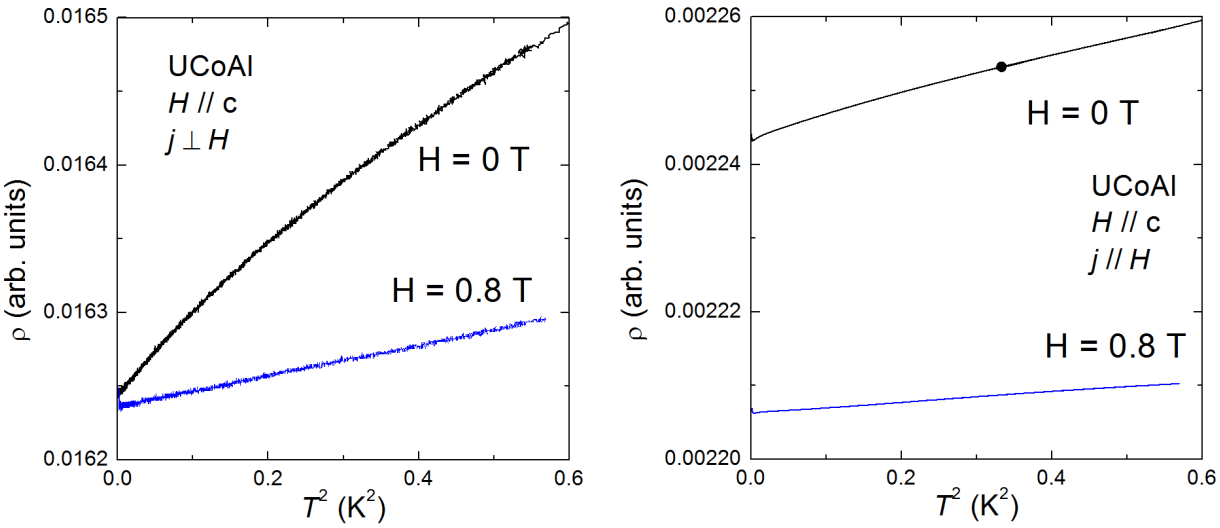

Figure 3.14: *Resistivity measurements of UCoAl for transverse (left) and longitudinal (right) configurations. The behaviour in the PM phase is shown by the black curves and in the FM phase by the blue curves.*

measurements show a temperarture dependence which is different from T^2. Consequently, no Fermi liquid signature is observed in UCoAl even at very low temperatures.

Specific heat measurements as a function of field, $C(H)$, were performed at different temperatures. Normalized specific heat curves, $C(H)/C(0)$, for each temperature regime are shown in Fig.3.15 (left). The color plot of Fig.3.15 (right) shows the (T, H) normalized specific heat phase diagram. The small black arrows shown in the right layer correspond to the temperatures for which $C(H)/C(0)$ measurements were performed. The coherence temperature is also shown in this graph by white filled circles. In the (T, H) normalized specific heat phase diagram, it is possible to distinguish two important areas; one around the CEP (that will be discussed in the following subsection) and another below the coherence temperature in the FM domain. This domain, shown in blue scale color, corresponds to the Fermi liquid regime that it is established in the FM low-temperature part of the (T, H) phase diagram. It is characterized by the lowest relative values of specific heat which is consistent with the cancellation of the spin fluctuations above H_M. To finish, we observe that it seems there is a coincidence between the Fermi liquid regime reported by magnetoresistance measurements to the entrance in the coherent regime in the FM phase.

The very low temperature transport properties of UCoAl in the PM phase point to the formation of an exotic PM phase. This may be related to the peculiar quasi-kagome lattice structure in this compound which can give rise to frustration as it has been stressed for example in YbAgGe [Sengupta et al., 2010]. Frustration often favors Dzyaloshinskii-Moriya exchange interaction. However, Dzyaloshinskii-Moriya exchange interaction has been excluded as explanation for the exotic PM state of UCoAl as it is not possible to induce a helimagnetism chiral order of a primary FM vector order in the space group P-62m of UCoAl [Kataoka and Nakanishi, 1981]. Other explanations of the exotic magnetic ground state might be the consideration of a weak antiferromagnetism (canting) present on the U-spin lattice, which is allowed in the P-62m structure and/or the possibility of the existence of relevant spin-

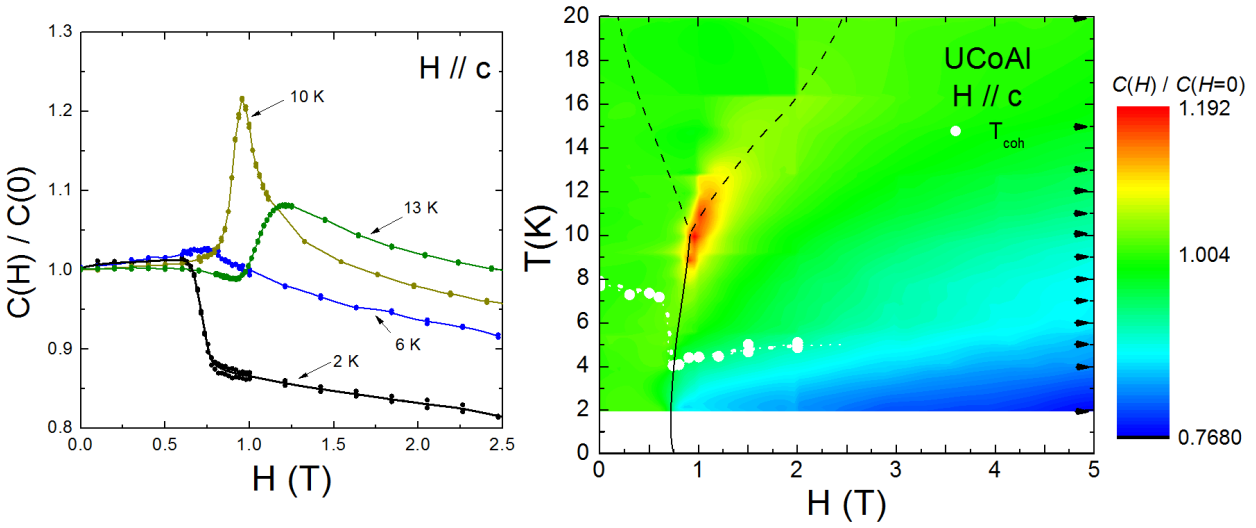

Figure 3.15: *Normalized specific heat as a function of magnetic field, $C(H)/C(0)$, at different temperature regimes (left figure). (T, H) color plot phase diagram of the normalized specific heat of UCoAl (right figure). The arrows in the right layer of the color plot indicate the temperatures at which $C(H)$ curves were performed. The color bar corresponds to the relative drop of $C(H)/C(0)$.*

polarization of the two Co-sites [Dzyaloshinskii, 1965]. More studies have to be performed to determine the nature of this exotic ground state.

Critical End Point

The existence of an exotic behaviour is not only restricted to the PM ground state. We have also observed an extra contribution to the anomalous Nernst effect around the CEP $(H_M^\star,\ T_0)$. To identify the physics related to this extra anomalous effect, specif heat and magnetoresistance measurements were also performed.

In Fig.3.16, the Nernst coefficient $\nu = N/H$ is plotted as a function of magnetic field for temperatures around T_0. The Nernst coefficient is almost constant at low magnetic fields which is consistent with the normal response of the Nernst effect in a PM state under magnetic field. At the metamagnetic transition for $T < T_0$, the Nernst effect shows a sharp transition with an increase of ν which is attributed to the presence of an anomalous Nernst effect (ANE) [Onose et al., 2007, Lee et al., 2007, Onoda et al., 2008]. For $T \backsim T_0$, the Nernst coefficient presents a sharp minimum at $T = T_0$. This minimum widens as temperature increases in the $T > T_0$ regime. The width of the minimum is consistent with the amplitude of the crossover shown in the phase diagrams determined by thermopower measurements (see Fig.3.10). The observation of an anomalous Hall effect (AHE) is well known in ferromagnets [Nagaosa et al., 2010]. It consists in a spontaneous Hall current flowing parallel to $\mathbf{E} \times \mathbf{M}$, where $\mathbf{E}$ is the electric field and $\mathbf{M}$ the magnetization. Karplus and Luttinger (KL) proposed that the AHE current originates from an anomalous velocity term which is non-vanishing in a ferromagnet [Luttinger and Karplus, 1954]. The topological nature of the KL theory has been of considerable interest recently [Onoda and Nagaosa, 2002]. Similarly, the Nernst signal is also sensitive to the anomalous velocity term generating a dissipationless thermoelectric

current, i.e. an anomalous Nernst effect. The abrupt change of the Nernst signal in UCoAl at H_M is similar to the anomaly observed in the Hall signal attributed to the AHE. Moreover, the negative sign of the AHE is in good agreement with previous measurements of ANE e.g. in the ferromagnet $CuCr_2Se_{4-x}Br_x$ [Lee et al., 2004].

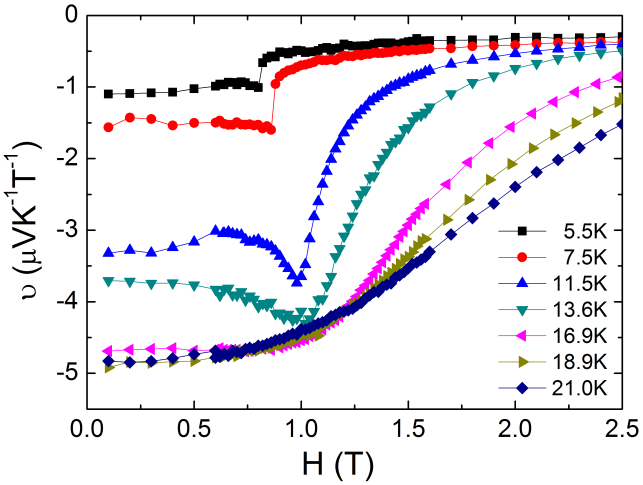

Figure 3.16: *Isothermal Nernst coefficient, ν, as a function of increasing field H.*

Close to the CEP, the Nernst effect shows a minimum. This minimum corresponds to an extra contribution in addition to the ANE which has also been observed in specific heat and magnetoresistance measurements. In specific heat measurements (see Fig.3.15), around the CEP, an increase of $C(H)/C(0)$ is observed. The maximum of $C(H)/C(0)$ is reached at $T_0 = 10$K. Magnetoresistance measurements shown in Fig.3.11 present the same behaviour as $C(H)$; e.g., an increase of the relative value of magnetoresistance at the CEP.

There are two approaches to explain this increase in transport and thermodynamic values around the CEP. One consists in considering the appearance of an extra anomalous current developed at the CEP associated to the field second order FM transition. The other one consists in interpreting the phenomena as an increase of the correlations between the carriers around the CEP thus, the increase of the scattering rate observed in magnetoresistance and the increase of the effective mass of the charges observed in γ measurements. This increase of correlations was identified by NMR measurements and correspond to the appearance of spin fluctuations of the longitudinal mode of U-atoms at the CEP [Nohara et al., 2011]. The enhancement of the Nernst effect can also be interpreted like an increase of correlations as the induced FM order may have the same origin.

3.5 UCoAl under Pressure

UCoAl is very sensitive to pressure variations (see Sec.3.2). Pressure changes the hybridization of the $5f - 3d$ bands inducing modifications on the magnetism of the compound. In order to study how the electronic properties follow the modifications in magnetism, we have extended previous thermopower measurements at ambient pressure into the $[0-2]$GPa pressure regime. A piston cylinder pressure cell setup was used to determine the evolution of the Seebeck

coefficient under pressure and magnetic field in the $[2-50]$K temperature range for the longitudinal configuration ($J \parallel H \parallel c$). Thermopower measurements reveal an increase of the critical field, H_M, with pressure and the continuous suppression of the wings toward the QCEP, see Fig.3.3. Up to the highest applied pressure (17.8kbar), no signature revealing the presence of the QCEP has been observed in $S(H)$ measurements; however, a rapid decrease of T_0 was observed.

3.5.1 Thermopower Measurements under Pressure

As indicated in subsec. 3.3, two different samples with similar quality factor were used in the pressure study of UCoAl. The critical field of sample1 was $H_{M_1} = 0.75$T and the one of the sample2 was $H_{M_2} = 0.65$T. The ratio between the volume of sample1 to the volume of the pressure chamber did not allow to go over 12kbar. Therefore, the results of sample1 were limited to study the low pressure regime of the wings. In the case of sampe2, the ratio ($V_{sample}/V_{P_{chamber}}$) was smaller allowing to perform thermopower measurements in the high pressure regime, around the QCEP. However, some measurements in the low pressure regime were also performed on sample2 to check the results (absolute value of thermopower and evolution of H_M and T_0) were not sample dependent. The analyzed pressures for sample1 and sample2 are shown in Tab. 3.1.

List of Pressures (kbar)	
sample1	sample2
0.7	1.3
2.1	7.2
6.0	11.2
8.7	14.5
10.1	16.1
12.0	17.2
	17.8

Table 3.1: *List of the analyzed pressures on sample*1 *and on sample*2*.*

3.5.2 Wing Structure under Pressure

In this section, the evolution of the wings as a function of magnetic field, temperature and pressure will be investigated. We will discuss first the modifications appeared at the critical field H_M; second, the temperature dependence of the CEP and finally, the evolution of the wings under pressure.

Evolution of H_M under Pressure

To determine the critical field, H_M, under pressure, isothermal thermopower measurements $S(H)$ at different temperatures have been performed. The parameters H_M, H_m, H_m^- and H_m^+ defining the $(T,H)|_{P_{fixed}}$ phase diagram are described in the same way as they were defined at

ambient pressure measurements. From $S(H)$ measurements, we will extract the $(T,H)|_{P_{fixed}}$ phase diagrams and consequently, the information related to the evolution of H_M and of CEP into the QCEP.

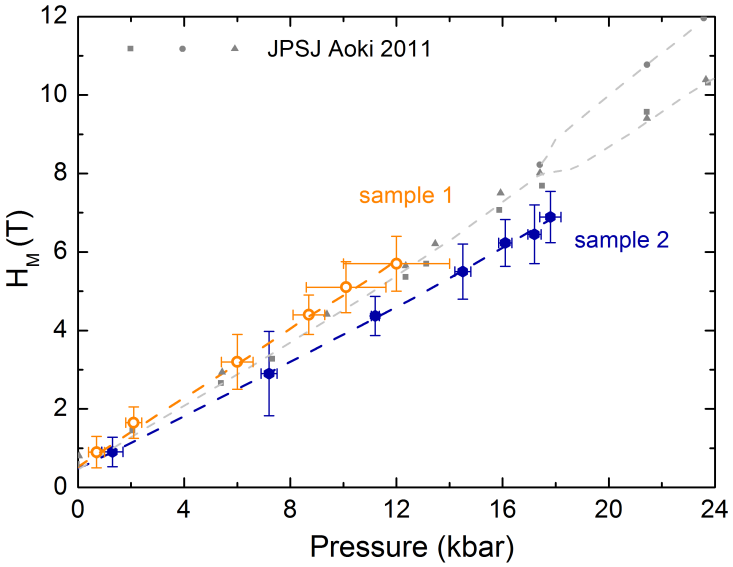

Figure 3.17: *Evolution of the critical field, H_M, under pressure for sample*1 *(orange symbols) and sample*2 *(blue symbols). In grey symbols, the evolution of H_M from magnetoresistance measurements [Aoki et al., 2011].*

In Fig.3.17, the critical field H_M of sample1, in orange open circles, and of sample2, in dark blue filled squares, are represented. H_M increases almost linearly with pressure in the two samples. For all the pressure range H_{M_1} is higher than H_{M_2} and we notice that H_{M_1} presents a higher slope. This is related to the lower value of H_{M_2} at ambient pressure. In this graph, the evolution of the critical field under pressure determined by magnetoresistance measurements ([Aoki et al., 2011]) is also shown by the grey symbols. As we predicted, the slope of H_M is sample depending as it depends on H_M value at ambient pressure.

Evolution of T_0 under Pressure

The second important characteristic of the wings is the determination of the the 2^{nd} order line of CEP towards the QCEP, then a (T,H) phase diagram for each pressure was plotted. In these diagrams, T_0 corresponds to the temperature at which the first order line H_M and H_m^-, H_m^+ crossover lines collapse (see Fig.3.18). This figure shows three superposed (T,H) phase diagrams corresponding to the following pressures: 6.0kbar (in black), 12.0kbar (in blue) and 17.8kbar (in orange). The squares correspond to the minimum of the 1^{st} order derivative (H_M if $T<T_0$ and H_m if $T>T_0$), the left triangles and the right triangles to the inflection points, H_m^- and H_m^+, of the 1^{st} derivative of the isothermal thermopower measurements $S(H)$, respectively.

An analogous technique to determine T_0 consists in taking the values of the two inflection points of the 1^{st} derivative of $S(H)$, H_m^- and H_m^+, and then to plot their gap as a function of temperature. Two regimes were observed: the first order transition regime which corresponds

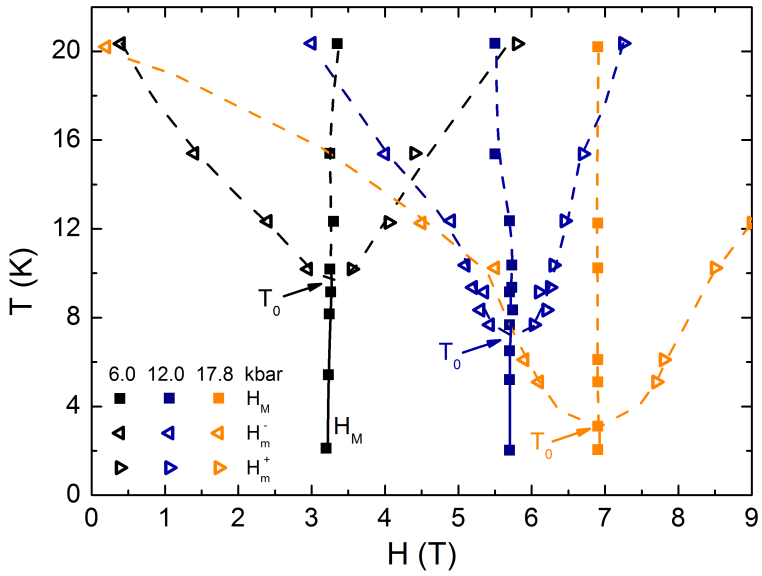

Figure 3.18: *(T, H) phase diagram of UCoAl at 6.0kbar (black symbols), at 12.0kbar (blue symbols) and at 17.8kbar (orange symbols).*

to a constant value width and crossover regime in which the distance between the two inflection points increases with temperature (the crossover width). The point of convergence of these two regimes indicates T_0.

As expected, the suppression of the wings was observed. T_0 decreases and tends to 0 at the QCEP ($p_{QCEP} \sim 1.5$GPa and $H_{MQCEP} \sim 7$T from previous resistivity [Aoki et al., 2011] and Hall resistance [Combier et al., 2013] measurements). To determine p_{QCEP} from thermopower measurements, we plot T_0 as a function of P and the location of p_{QCEP} is expected at $p \sim 1.9$GPa (see Fig.3.19- left-upper figure). The p_{QCEP} value obtained from thermopower is a little bit higher than the expected p_{QCEP} of literature. If the evolution of T_0 is represented as a function of the critical magnetic field, we verify that H_{QCEP} is located at ~ 7.2T (see Fig.3.19- middle-upper figure) which value is really close to the one of the literature. For field and pressure dependencies, T_0 decreases smoothly and drops, suddenly, when the systems is closed to the QCEP. Finally, each pressure can be identified with its critical magnetic field (see Fig.3.19- right-upper figure).

3D Image of the Wings

To obtain the 3D image of the wings of UCoAl, the evolution of H_M and T_0 with pressure and the evolution of T_0 with the critical field were analyzed. In Fig.3.19, those analysis are represented only for the pressures used for the reconstruction of the wings. We notice that the points obtained at low pressures correspond to the sample1 and those above 12kbar to the sample2. In the upper panel of Fig.3.19, the (T_0, P), (T_0, H_M), (H_M, P) phase diagrams are shown from right to left. In the lower panel, the representation of the 3D image of the wings in the $(T, P, H+)$ quadrant is shown. The CEP line is represented in pink color and the first order metamagnetic transition plane in purple color. We observe clearly the suppression of the wings towards the QCEP that is located at $H_M \sim 7.2$T and $p_{QCEP} \sim 1.9$GPa from

thermopower measurements performed on samples 1 and 2.

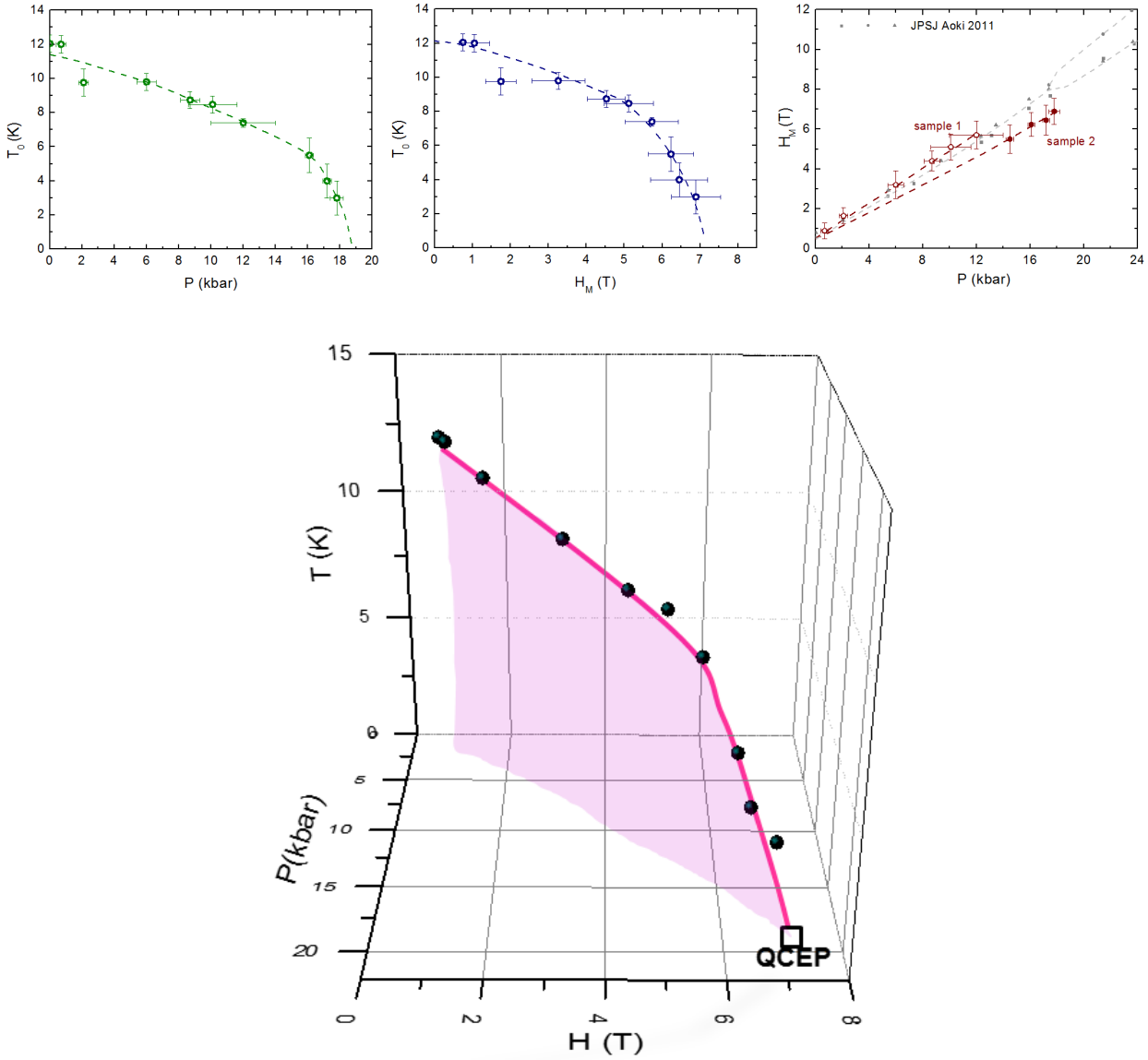

Figure 3.19: *In the upper panel, from the right to the left, (T_0, P), (T_0, H_M), (H_M, P) phase diagrams are shown. The lower pannel shows the $(T, P, H+)$ phase diagram of UCoAl. The $(T, P, H+)$ evolution of the wing is shown in black and the (T_0, P), (T_0, H_M), (H_M, P) proyections are shown in green, blue and dark red symbols, respectively.*

3.5.3 Carrier Behaviour inside the Wings

To analyze the carrier changes at the metamagnetic transition inside the wings, isothermal thermopower measurements as a function of increasing magnetic fields $S(H)$ were performed at different pressures. As the QCEP appears at $T \longrightarrow 0$, we chose the $S(H)$ curves at $T = 2$K to analyze the carrier modifications. We compare the behaviours of the $S(H)|_{2K}$ curves in

all the pressure regime. We notice that no signature in $S(H)$ measurements was observed approaching the QCEP.

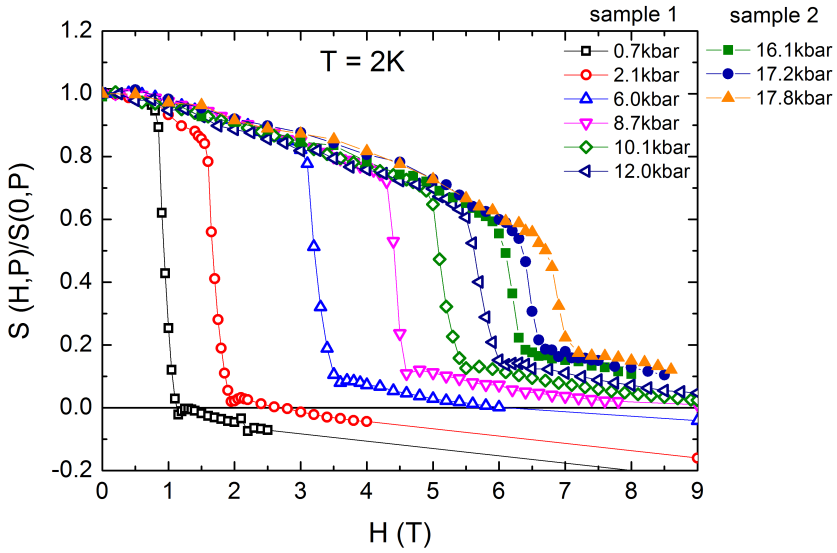

Figure 3.20: *Evolution of the normalized Seebeck coefficient $S(H,P)/S(0,P)$ as a function of magnetic field at $T = 2K$ at different pressures.*

To clear up the comparison of the evolution of $S(H)$ measurements in all the pressure range. We divide $S(H)$ by the absolute value of $S(H = 0)$ for each pressure. In Fig.3.20, normalized $S(H)/S(0)$ curves at $T = 2$K are represented. This renormalization causes that all the $S(H)$ curves are joined at $S(H,P)/S(0,P) = 1$ as shown in the graph. As it was note before, the low pressure regime measurements, which are represented by open symbols, come from sample1 and the high pressure regime measurements corresponding to the filled symbols of the figure were performed on sample2.

The information extracted from the simple analysis of the evolution of thermopower measurements under pressure shown in Fig.3.20 can be sum up as following. First, all the $S(H,P)/S(0,P)$ curves in the PM phase present the same slope as well as all the curves in the FM phase. Nevertheless, the slope in the PM phase is higher than the one in the FM phase. Second, the Seebeck coefficient in the FM phase changes from negative to positive as pressure increases; the pressure reinforces the transport properties carried by the hole bands. Third, a reduction of the jump of thermopower is observed as pressure increases. This last point is linked to the previous one because if the behaviour of the thermopower remains hole like, the jump should become smaller. To evaluate the evolution of this drop in thermopower, we represent $\Delta S(H)/\Delta S(0)$ at H_M as a function of the critical magnetic field (x-axis upper layer) and as a function of pressure (x-axis down layer) (see Fig.3.21). The scale of both x-layers, magnetic field and pressure, was chosen in such a way that H_{QCEP} and p_{QCEP} coincide in a line, the grey dashed line of the graph. The idea is to compare $\Delta S/S(0)$ field and pressure tendencies and to try to identify the signature of the QCEP in thermopower measurements.

In Fig.3.21, the normalized jump at the metamagnetic transition, $\Delta S(H,P)/\Delta S(0,P)|_{H_M}$, for sample2 at $T = 5$K is shown. In blue symbols, the normalized thermopower jump is represented as a function of the critical field, H_M, and, in orange symbols, it is plotted as a

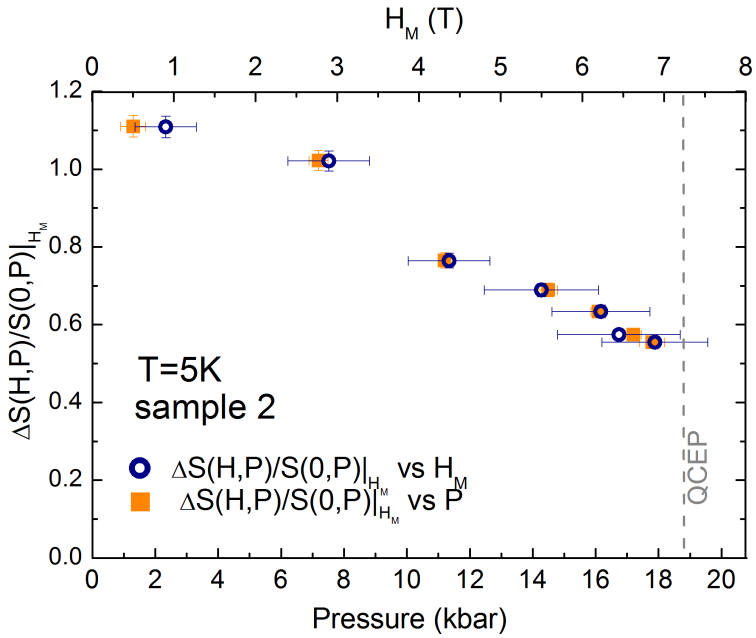

Figure 3.21: *Normalized thermopower jump $\Delta S(H)/\Delta S(0)|$ at H_M as a function of field (blue symbols) and as a function of pressure (orange symbols) for sample2 at $T = 5K$.*

function of pressure, P. The pressure error bars correspond to the width of the superconducting transition of the lead-manometer and the magnetic field error bars correspond to the width of the metamagnetic transition measured between the two inflection points of the 1^{st} derivative. For the normalized thermopower jump, the error bars were calculated as an error of 5% of its value. A decrease of thermopower to half of the initial value is observed from vacuum up to 17.8kbar. This decrease to the half of the initial value is also observed in T_0, but in this case, T_0 decreases to the half value for the pressure regime going from vacuum to 16kbar. In the pressure window from 16kbar to p_{QCEP}, T_0 drops abruptly to 0 whereas no signature in the isothermal thermopower measurements was observed. This might be related to the temperature regime in which the measurements were performed. The lowest temperature, $T = 2$K, was maybe not low enough to observe the singularities on thermopower approaching the QCEP. The other possibility is that the singularities of the QCEP are strongly localized in pressure and 17.8kbar is still too far away from it.

To determine the nature of the QCEP in UCoAl, we analyze the evolution of T_0 as a function of the control parameter, the pressure. In Fig.3.22, T_0 as a function of $|P - p_c|$ is represented considering $p_c = P_{QCEP} = 18.85$kbar. The evolution of T_0 around p_c is analyzed by renormalization group theory[Millis, 1993]. As UCoAl presents a ferromagnetic order ($z = 3$) and magnetic fluctuations in the three directions of the space ($d = 3$), then the renormalization group theory determines that T_0 must evolve as $T_0 = a|P - p_c|^{3/4}$. This law is represented in Fig. 3.22 by the green line. In addition, some fits of the real data are shown in the same graph. The orange and blue lines represent the fit of T_0 as a function of pressure for pressure windows of 2 and 3kbar, respectively. We observe that T_0 decreases faster than the theoretical prediction. Nevertheless, the fit of T_0 is done in a rather high temperature range although the pressures are quite close to the QCEP. We also notice that the exponent approaches the

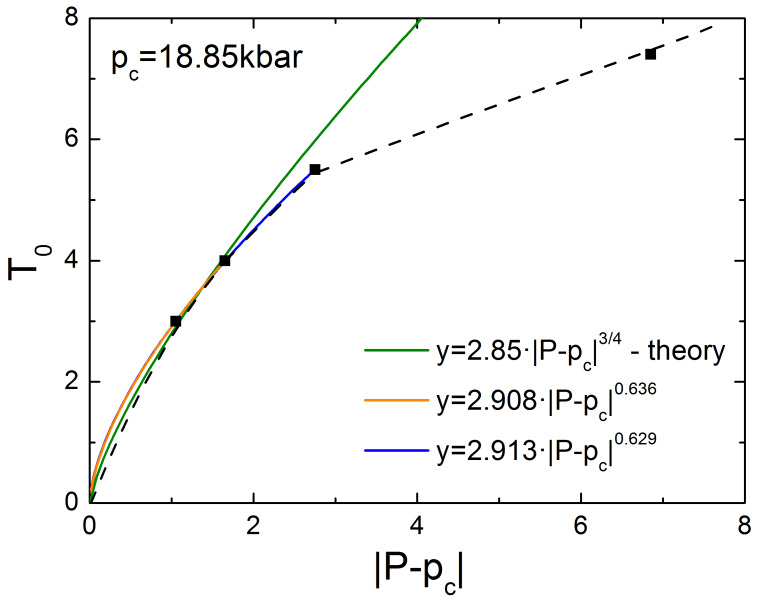

Figure 3.22: *(T_0, $|P - p_c|$) phase diagram obtained by thermopower measurements. The straight lines show the different fits of T_0 as a function of $|P - p_c|$ near the QCEP. The dashed line is a guide for the eyes.*

theoretical value as the pressure range of the fit decreases (i.e., as T_0 approaches $T \to 0$). This indicates the possibility of a good agreement with theoretical predictions. Nevertheless, we can not conclude about the physical meaning of the evolution of T_0 with $|P - p_c|$ in UCoAl as pressure and temperature are still quite far from the QCEP.

3.5.4 Other Probes versus Thermopower

In order to better understand the thermodynamic and transport modifications towards the QCEP, a comparison between magnetoresistance, Hall resistance and magnetization measurements has been done. First, the evolution of T_0 as a function of magnetic field and pressure for magnetoresistance, Hall resistance and thermopower measurements will be analyzed. Second, the evolution of the normalized jump of thermopower $\Delta S/S(0)|_{H_M}$ and the evolution of the amplitude of the observed peak in Hall resistance at the metamagnetic transition will be studied. Finally, we analyzed the jump in magnetization measurements against thermopower drop at H_M.

(T_0, P) and (T_0, H_M) Phase Diagrams

T_0 as a function of magnetic field and as a function of pressure, both are studied with the aim of determining the similarities and differences of the field and pressure location of the QCEP. In Fig.3.23, the evolution of T_0 as a function of magnetic field (upper figure) and as a function of pressure (lower figure) are represented for thermopower, Hall resistance [Combier et al., 2013] and magnetoresistance [Aoki et al., 2011] measurements. The blue symbols of T_0 vs H_M graph were determined by thermopower, the purple's one were determined by the Hall resistance and the ones in dark cyan were obtained from magnetoresistance measurements. We observed

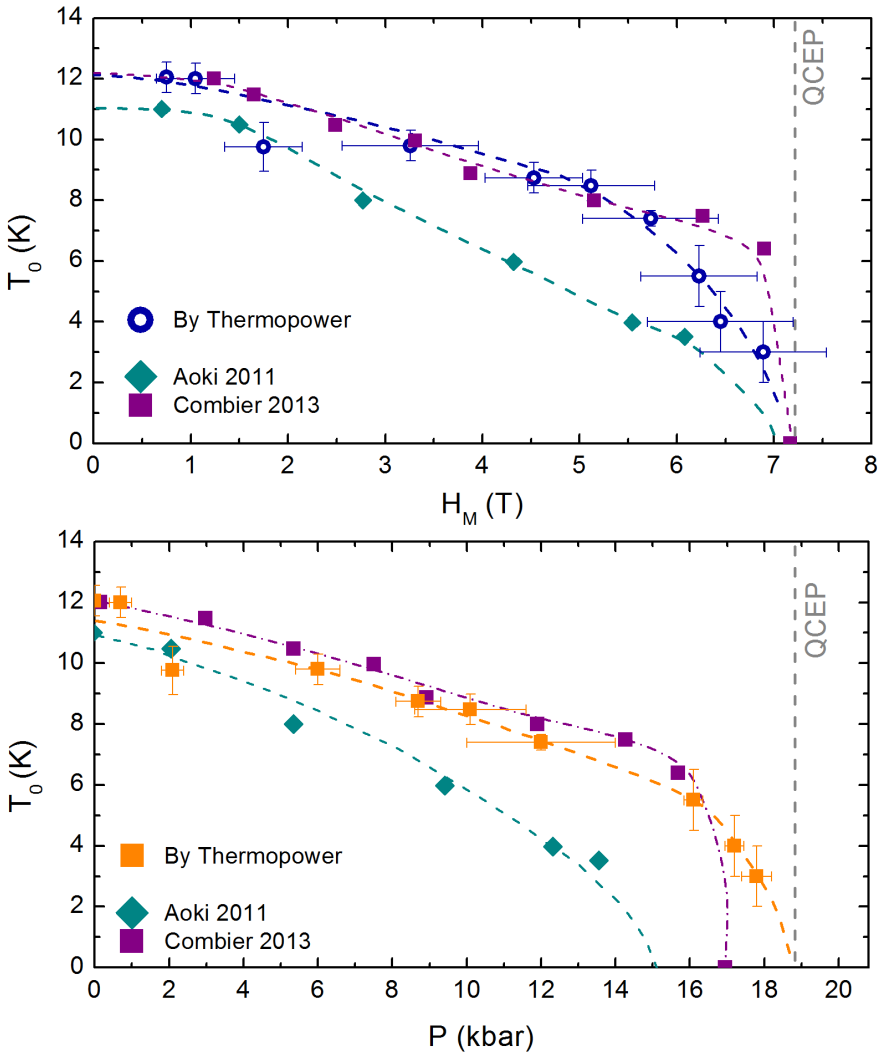

Figure 3.23: *(T_0, H_M) and (T_0, P) phase diagrams are shown in the up and down panels, respectively. The evolution of T_0 determined by thermopower (blue and orange symbols) by magnetoresistance measurements (dark cyan symbols) and by Hall resistance (purple symbols) are represented, simultaneously, in these phase diagrams.*

that all of them end up at the same value of H_{QCEP} although the decrease of T_0 towards the QCEP does not follow the same behaviour. For thermopower and Hall resistance, T_0 remains almost constant for low values of H_M and it suddenly drops to 0 at the QCEP. The rate T_0/H_M around the QCEP is higher in Hall resistance than in thermopower measurements. In the case of magnetoresistance, T_0 decreases constantly from the vacuum regime towards the QCEP. In (T_0, P) graph, the evolution of T_0 as a function of pressure is shown. In contrast to the magnetic field evolution, pressure evolution for thermopower (orange symbols), Hall resistance (purple symbols) and magnetoresistance (dark cyan symbols) measurements differ in the value of p_{QCEP}. The value of p_{QCEP} increases from 15kbar to $\sim$ 19kbar in the following order: magnetoresistance, Hall resistance and thermopower probes. The description of the evolution of T_0 by thermopower measurements consists in its almost linear decrease up to

16kbar where T_0 decreases to half of its value in vacuum. Above this pressure, T_0 vanishes suddenly to achieve the QCEP. The Hall resistance description corresponds to a T_0 linear decrease until 16kbar, with the same slope as thermopower, and its sudden disappearance at 17kbar. Hall resistance could not follow the vanishing of T_0. Magnetoresistance shows an almost linear decrease of T_0 to the QCEP with a higher slope than thermopower and Hall resistance measurements. Near the QCEP, as Hall resistance measurements, magnetoresistance measurements could not follow the rapid drop of $T_0 \to 0$. In both graphs of Fig.3.23, the error bars correspond to the width of the metamagnetic transition and to the width of the lead transition for magnetic field and pressure data, respectively.

The value of H_M at the QCEP is the same for these three probes as we observe from (T_0, H_M) phase diagram (see Fig.3.23 - upper figure). Nevertheless, the p_{QCEP} value obtained from thermopower measurements is slightly higher than the p_{QCEP} determined by Hall effect and magnetoresistance measurements (see Fig.3.23 - down figure). In conclusion, despite there is not sample dependence on the critical field at the QCEP, it exists a sample dependence on the critical pressure. This critical pressure dependence might be related to the value of $H_M|_{P=0}$ and as a consequence, to the evolution of H_M under pressure.

Modifications at H_M

To analyze the signature of the QCEP in thermopower measurements, we decided to represent the normalized jump of thermopower as a function of the critical field (see Fig.3.24) and compare it to other probes(see Fig.3.25). If we consider that the normalized jump of thermopower vanished linearly with field at the QCEP as shown in Fig.3.24, we obtain that the QCEP is located at $H_{QCEP} = 12.4$T. This value is far from the extrapolated value obtained from the (T_0, H) phase diagram which was $H_{QCEP} = 7.2$T (see Fig.3.23 (upper figure)). For that reason, we conclude that the linear decrease of the normalized jump of thermopower is not a good criterion to define the location of the QCEP. Moreover, we notice that the normalized thermopower at low critical magnetic field starts at 1.1 instead of 1. This is due to there is a small increase of the $S(H)$ around $H \lesssim H_M$ and $S(H)$ crosses the zero thermopower line at the metamagnetic transition.

In Fig.3.25, the normalized thermopower jump at H_M is represented as a function of the critical field (left layer). The magnetization jump [Mushnikov et al., 1999] and the variation of the Hall resistance [Combier et al., 2013] at the metamagnetic transition against the critical field are represented in the right layer of the same figure. The jump of the magnetization varies slightly with pressure. It decreases from $0.31\mu_B$/f.u. to $0.26\mu_B$/f.u. in the $[0-1.2]$Gpa pressure range. In the case of Hall resistance, authors argue that the main contribution comes from the jump of magnetization as we observe from the following simple approach. The variation of the Hall resistance can be written as $\Delta\rho_{xy} \propto \Delta(R_0 B) + \Delta(R_S M) \backsimeq R_S \Delta M$ where ρ_{xy} is the Hall resistance, B the applied magnetic field, M the magnetization, R_0 and R_S the normal and anomalous coefficients, respectively. They explain that the Hall resistance jump at the critical field corresponds to the anomalous contribution of the Hall effect at least up to $H = 6$T or $P = 1.2$GPa and above these conditions, the jump becomes negative and the signature of this first order metamagnetic transition (the jump in magnetization measurements) is not directly detected in Hall effect measurements. Hall effect observes a crossover above $H = 7.2$T or $P = 1.6$GPa. Hall resistance measurements conclude that the location of the QCEP is in

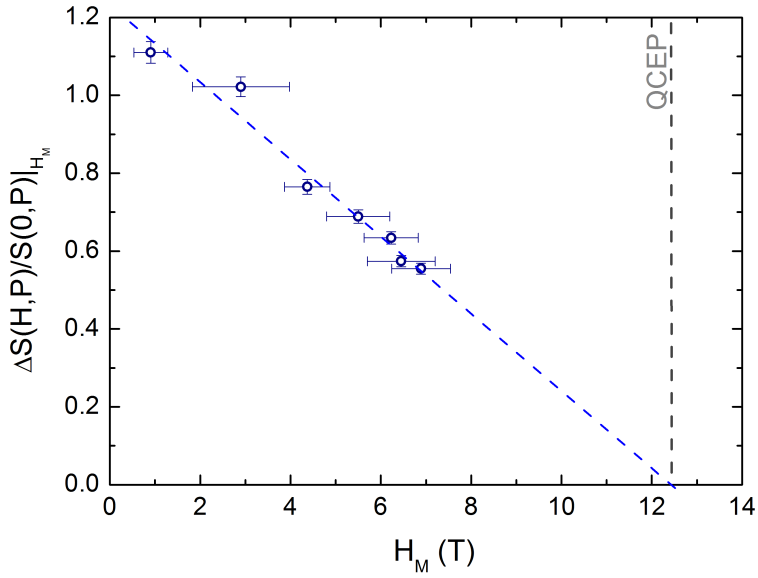

Figure 3.24: *Evolution of the normalized jump of thermopower as a fucntion of the critical magnetic field. The dashed line shows the linear extrapolation of the vanishing of the thermopower jump with field.*

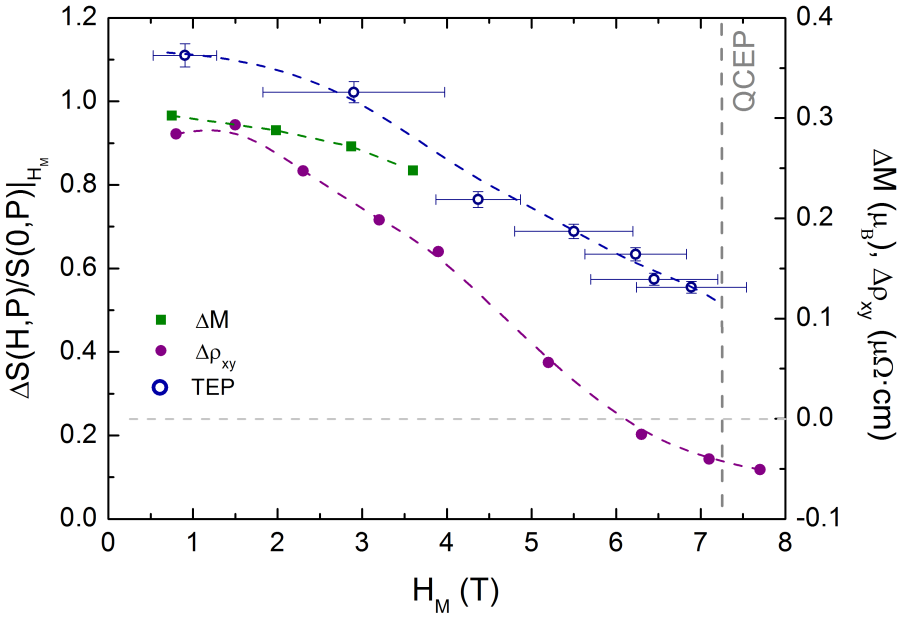

Figure 3.25: *Evolution of the normalized jump of thermopower (left layer) versus the jump of magnetization and Hall resistance (right layer) at H_M as a funtion of the critical magnetic field.*

the pressure range of $[1.2 - 1.6]$GPa. They could also measured the variation of the Hall resistance above the QCEP. However, we note that the number of data points obtained in the high pressure PM phase was not enough to determine the tendency of the transport carriers in this phase. Contrary to expected behaviour, we do not observe any singularity neither at $H = 6$T, as in Hall resistance measurements, nor close to the H_{QCEP} in thermopower

measurements. We suggest that the applied pressure to the system was smaller compared to the needed pressures to achieve the QCEP and that the temperature range of measurements $[2-50]$K was too high to observe the fluctuations of the QCEP. Thermopower measurements at higher pressure and lower temperature around the QCEP ought to be performed to observe the thermopower signature at the QCEP.

3.6 Conclusions for UCoAl

Zero Pressure

Thermoelectric power is a powerful probe to determine the (T, H) phase diagram of UCoAl. The metamagnetic transition is directly linked to the itinerant character of the quasi-particles. The comparison with Hall effect measurements indicates that UCoAl is a multiband compound with heavy and light bands. This is in good agreement with band structure calculations. The main drop in the effective mass at the metamagnetic transition seems to occur in the heavy hole channel. A singular point of UCoAl concerns the non Fermi-liquid properties in the low field PM phase even down to 200mK and the appearance of the Fermi-liquid regime only in the FM phase below the coherence temperature. We suggested that this behaviour is due to its quasi-kagome crystal structure with lack of inversion symmetry. Correlations at the CEP have also been observed in specific heat and Nernst effect. This correlations are also supported by NMR and magnetoresistance measurements.

Thermopower data performed in the compensated, moderate heavy fermion compound UCoAl, with a rather simple Fermi surface, may allow quantitative theoretical developments. It can serve as a reference for the recent thermopower measurements made in strongly correlated electron systems.

In the future, an issue will be to test the validity of the Fermi surface invariance through H_M via the direct observation of quantum oscillations or photoemission spectroscopy. That requires improvement of the crystal quality.

Under Pressure

Measurements towards the QCEP were performed in UCoAl. For the measured samples, the analyzed pressure regime, $[0-18]$kbar, was not high enough to reach the QCEP, therefore no singularities in the thermopower signal were observed. Unfortunately, the pressure restrictions coming from the piston cylinder pressure cell blocks the possibility to perform these measurements as above 18kbar, the teflon cap invades the pressure chamber cutting the wires of the setup. Moreover, the sample1 was too big to reach high pressures and the sample2 presented smaller value of H_M, hence large pressure chamber volume and higher pressures were needed to achieved the QCEP in sample1 and sample2, respectively.

We confirm the magnetic field invariance of H_{QCEP} which is located at $H_M \sim 7.2$T. The pressure dependence of the p_{QCEP} was observed and we suggest that it is related with the individual H_M of the sample in vacuum. We observed that lower was H_M in vacuum conditions, higher was the pressure we need to achieve the QCEP. For our samples, the p_{QCEP} was ~ 1.9GPa which is a little higher than the one published in literature. Thermopower

measurements could easily follow the rapid decrease of T_0 around the QCEP. We affirm that hole bands prevail over electron bands as pressure increases.

Thermopower measurements at high pressure and lower temperature are needed to conclude about the behaviour of the heat carriers around the QCEP because the singularities of the QCEP seems to appear in well-defined temperature and pressure regimes. A new setup will be designed to achieve higher pressures with the purpose of analyzing the thermopower singularities at the QCEP.

Chapter 4

Thermopower Analysis of UGe_2

In this chapter, we report the transport properties of the ferromagnet superconductor UGe_2 studied by thermopower and Shubnikov-de Haas effect. Thermopower temperature dependence measurements identified the paramagnetic to ferromagnetic first order transition and the crossover between the two ferromagnetic domains. In the low temperature regime, the q-factor was analyzed. Isothermal thermopower measurements as a function of increasing magnetic fields were performed. These measurements are the first example in which thermopower quantum oscillations were observed in heavy fermion compounds. An analysis of the FM2 Fermi surface (orbits, cyclotron masses and mean free path) of UGe_2 was performed using these measurements. Finally, we report the comparison of the Fermi surface parameters observed from thermopower quantum oscillations, Shubnikov-de Haas and de Haas-van Alphen techniques.

4.1 Context and Motivations

The study of quantum oscillations has been one of the most significant probes to map the Fermi surface of strongly correlated systems. The quantization of the energy levels of a system under magnetic field was observed by first time in susceptibility measurements. This technique was called de Haas van-Alphen effect (dHvA). The analysis of the oscillations in susceptibility, which is an equilibrium property of the Fermi sea, is summarized in the Lifshitz-Kosevich (LK) theory. This theory allows the reconstruction of the Fermi surface by first principles considering that the oscillatory part of the magnetization is the product of three terms: (i) the temperature evolution of the magnetization, (ii) the magnetic field evolution of the magnetization and (iii) the curvature factor [Shoenberg, 1984]. Latter, the quantum oscillations were also observed in the magnetoresistance transport measurements. This phenomenon is called Shubnikov-de-Haas effect (SdH) [Shubnikov and de Haas, 1930]. SdH also depends on the contribution of the electron scattering in magnetic fields; therefore, this contribution must be treated in the models. Nevertheless, SdH effect uses LK-theory to determine the parameters of the Fermi surface obtaining a good agreement with dHvA. This is possible if we assume that the scattering oscillates and we suppose that the probability of the scattering term is proportional to the density of states.

Thermopower quantum oscillations were observed in the 60's in classical metals and later in semi-metallic systems such as bismuth [Behnia et al., 2007]. A complete theory to analyze the properties of the Fermi surface from these measurements is still not established despite of the fact that transport properties cannot be treated from a thermodynamic approach like for dHvA effect. Nevertheless, there are some attempts to establish an ansazt for thermopower quantum oscillations technique. The ansatzs treat the oscillatory part of thermopower from first principles and made some assumptions in the thermopower signal such as the free-electron limit of the heat transport, the linear response of the thermopower or the oscillatory contribution depends on the density of states close to the extreme cross section of the Fermi surface [Trodahl and Blatt, 1969, Pantsulaya and Varlamov, 1989, Fletcher, 1981]. All these models verify that the amplitude of the thermopower quantum oscillations is usually larger than the monotonic background because the oscillatory part of the transport coefficient is the principal contribution to the thermopower. They demonstrate that the sign of thermopower depends on the type of heat carriers which allows to determine if the Fermi surface is hole or electron like and they also demonstrate that thermopower follows the Onsager relationship in the case where the oscillations are caused by Landau levels or interference effects. Quantum oscillations have recently been observed in the Nernst coefficient of semiconductor or high-temperature superconductor [Banerjee et al., 2008, Laliberte et al., 2011]. Despite of there are ansatzs developed for thermopower quantum oscillations, the most extended practice nowadays is to use LK-theory to determine the characteristics of the Fermi surface.

Thermopower has been used as a probe to analyze the properties of UGe_2. We first determined the transport properties in the low temperature regime. For that reason, we performed thermopower measurements as a function of temperature that identified the PM to FM1 and the FM1 to FM2 transitions, the heat carrier type and the carrier concentration *via* the q-factor. We also performed isothermal thermopower measurements in which the thermopower quantum oscillations were observed. As this was the first time that thermopower quantum oscillation were observed in heavy fermion systems, we performed the following studies. We

evaluated whether the study of thermopower quantum oscillations in metals can be extended and whether it is also valuable in the case of strongly correlated systems with heavy bands. Therefore, we analyzed the spectrum of the thermopower quantum oscillations as a function of temperature and as a function of the effective applied magnetic field. We determine the cyclotron mass and the mean-free-path of conduction carriers using the different ansatzs. Simultaneously, SdH measurements were also performed with the purpose to establish a relation between SdH results to thermopower quantum oscillation analysis. Finally, a comparison to dHvA effect shows the relevance of thermopower quantum oscillations compared to traditional probes and it supports the interest to develop this technique to look for the microscopic properties of the Fermi surface in heavy fermion systems.

4.2 Introduction to UGe_2

UGe2 crystallizes in an orthorhombic lattice with a $ZrGa_2$ type structure and *Cmmm* space group [Oikawa et al., 1996]. The interatomic distance between two first U neighbors, d_{U-U}, is 3.85Å situating this compound above the Hill limit; therefore, a localized magnetic moment was expected. Nevertheless, the magnetism of this compound was sometimes identified as itinerant magnetism due to the possible hybridization of the f electrons with other bands. Nowadays, the localized/itinerant nature of the magnetism in UGe_2 is still under discussion.

The lattice of UGe_2 is shown in Fig.4.1 -left, in which the U and the Ge atoms are represented in blue and in red, respectively. The arrows indicate the direction of the U magnetic moments which are aligned along the a-axis, the easy-axis [Ōnuki et al., 1992, Boulet et al., 1997]. UGe_2 has three well defined magnetization axis; an easy axis, the a-axis and two hard axis, the c- and the b-axis. Thus, UGe_2 presents a strong magnetic anisotropy. Neutron scattering confirms the Ising type magnetization of this compound by the observation of magnetic fluctuations isolated along the c-axis [Raymond and Huxley, 2004].

In Fig.4.1 -right, we show the magnetization measurements performed at $T = 4.2$K

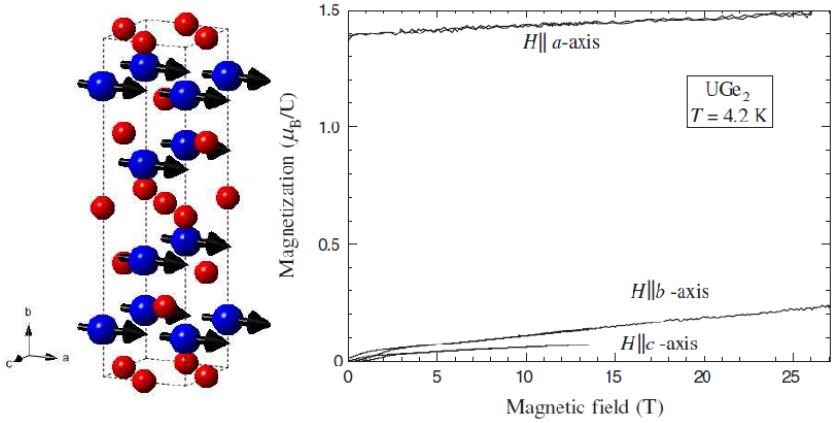

Figure 4.1: *The lattice structure of UGe_2 is shown on the left. The red atoms correspond to U atoms and the blue ones to Ge atoms. The arrows show the orientation of the magnetic moments of the system [Oikawa et al., 1996]. Magnetization measurements performed at $T = 4.2K$ along the 3 different axis of the lattice of UGe_2 are shown on the right [Sakon et al., 2007].*

along the 3 axis of this compound. The magnetic moment of UGe_2 at ambient pressure is $\mu_B = 1.4\mu_0/U$. Then, the magnetization measurements reveal that the measured value of the magnetic moment is smaller than the free U-atom magnetic moment. In addition, the magnetization does not show any saturation even at high fields which supports the idea of itinerant magnetism in this compound [Sakon et al., 2007].

At ambient pressure, UGe_2 is characterized by a 2^{nd} order transition from paramagnetism (PM) to ferromagnetism (FM1) at the Curie temperature, $T_C = 52$K and a crossover between two ferromagnetic phases (FM1→FM2) at $T_x = 27$K. In these conditions, the definition of the T_x transition is not so clear. Thermal expansion measurements performed for the three axis of the lattice observed that T_x presents a variation of few kelvins depending on the different axis. They conclude that this transition corresponds to a thermodynamic phase transition somehow broadened by sample defects or internal stress at ambient pressure [Hardy et al., 2009].

The pressure-temperature (T, P) phase diagram of UGe_2 is shown in Fig.4.2 -left. Pressure and magnetic field induce the suppression of the FM order decreasing the value of T_C. At $P > 10$kbar, the crossover T_x between the two ferromagnetic phases, FM1-FM2, becomes a 1^{st} order transition. The change of the T_x line into a first order transition is related to the enhancement of the ordered magnetic moment for temperatures below $T < T_x$ as T_x ends at the maximum of the superconducting phase [Tateiwa et al., 2001, Pfleiderer and Huxley, 2002]. At higher pressures, we notice that the suppression of the T_C line does not end in a quantum critical point as expected (see Fig.4.2 -right). Under pressure and magnetic field, the T_C second order line of the FM1-PM transition becomes first order at TCP. For $P > P_{TCP}$, the first order line is split into two first order FM planes that are suppressed under pressure into a quantum critical end point (QCEP). In UGe_2, the QCEP is located at high fields and high pressures ($H_{QCEP} \sim 18$T and $p_{QCEP} \sim 3.5$GPa) [Taufour et al., 2010].

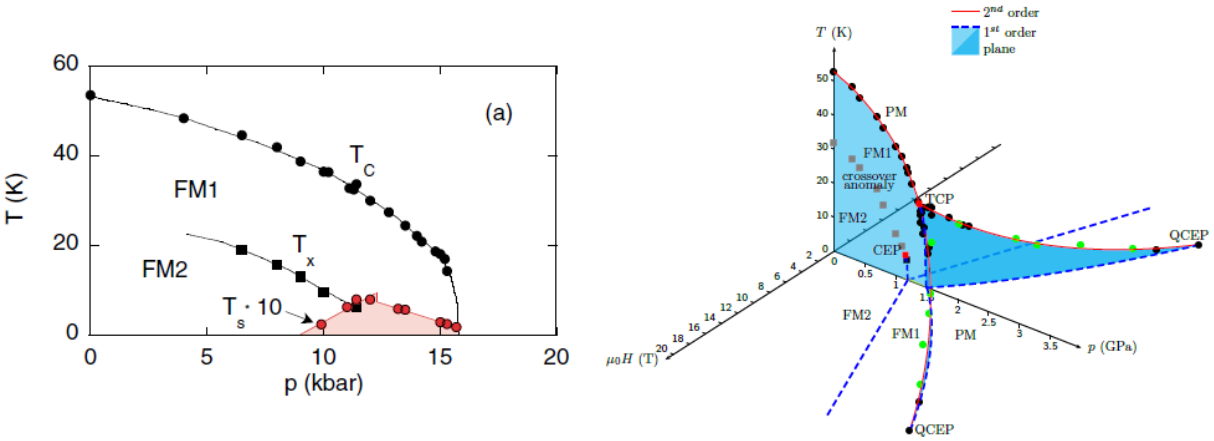

Figure 4.2: *(T, P) -on the left- and (T, P, H) -on the right- phase diagrams of UGe_2 obtained from refs. [Pfleiderer and Huxley, 2002] and [Taufour et al., 2010], respectively. The pink area of (T, P) phase diagram respresents the superconducting domain. In the (T, P, H) phase diagram, the suppression of the FM phase by pressure shows a magnetic wing structure.*

Under pressure, UGe_2 shows superconductivity inside the FM phase. The superconducting domain is characterized by spin triplet pairing. In addition, the maximum temperature of the superconducting domain coincides with the ferromagnetic transition FM1-FM2. Therefore,

the same electrons that are involved in the itinerant magnetism, are also responsible for the superconductivity in UGe_2 [Saxena et al., 2000].

UGe_2 is a compensated metal with a moderated heavy fermion behavior. The $5f$ electrons are localized at high temperatures and below T_C, the itinerant magnetism appears as the hybridization with the s, p, d emerges. The hybridization induces an increase of the specific heat and magnetic moments along the a-axis [Biasini and Troc, 2003]. The itinerant character of the ferromagnetism of UGe_2 comes from the U$5f$ electrons and also from the small contributions of U$6d$ and Ge$4p$ as observed from the density of states (DOS) calculations shown in Fig.4.3 -left [Samsel-Czekała et al., 2011]. This figure shows the DOS for each element (Fig.4.3 -left a)) and for each band (Fig.4.3 -left b) and c)) of UGe_2 as a function of the relative energy to the Fermi energy, $E - E_F$. A deeply analysis of the DOS reveals that the main contribution to the DOS of UGe_2 comes from the $5f_{5/2}$ electrons below the Fermi energy and from the $5f_{7/2}$ electrons above it.

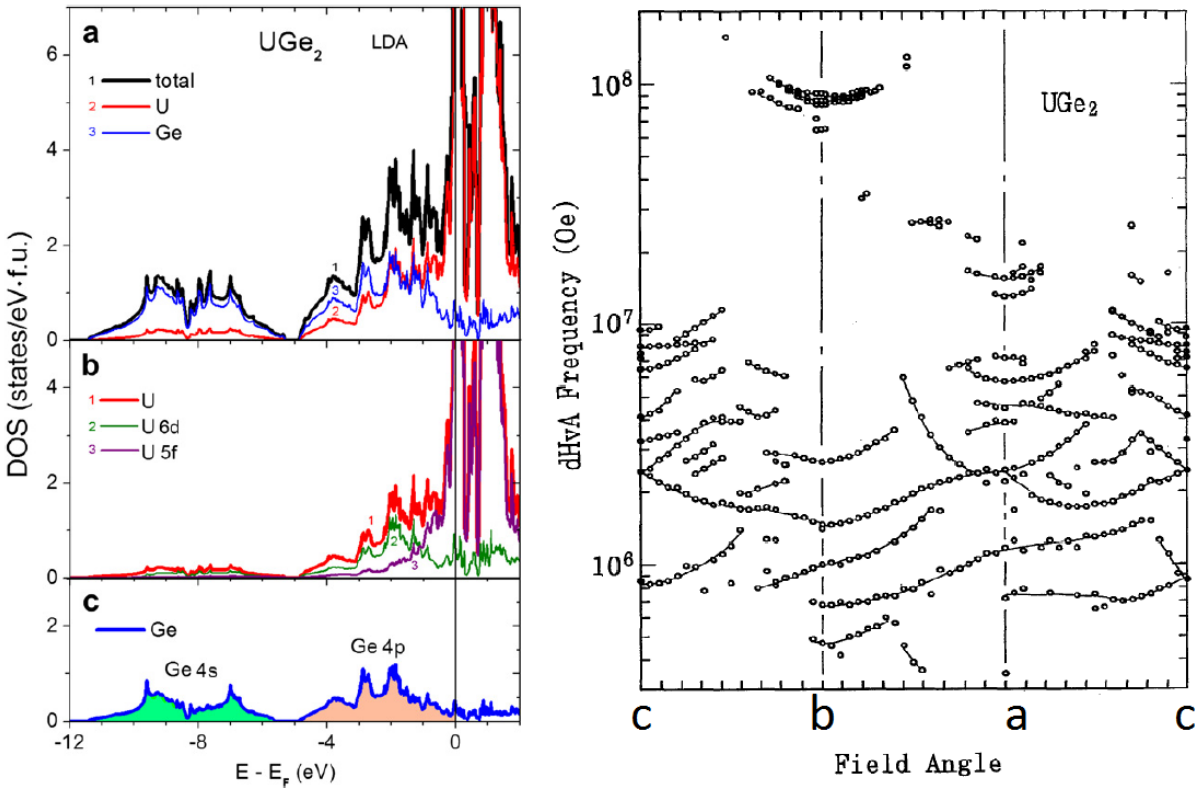

Figure 4.3: *Total and partial DOSs plots for UGe_2 obtained by FPLO in the LDA approach (left figure) [Samsel-Czekała et al., 2011]. Angular dependence of the dHvA frequencies of the Fermi surface of UGe_2 (right figure) [Satoh et al., 1992].*

The Fermi surface of UGe_2 was studied by the de Haas van Alphen effect (dHvA) technique. First dHvA measurements show that UGe_2 presents Fermi surfaces multiply-connected with open orbits along b- and a-axis and small closed ellipsoidal orbits [Ōnuki et al., 1991]. More precise measurements show that the effective masses of UGe_2 vary from 2 to $25m_0$ due to the itinerant character of the $5f$ electrons and its strongly correlated spin fluctuations [Satoh et al., 1992, Terashima et al., 2002, Haga et al., 2002]. The angular dependence of the

dHvA frequencies obtained by [Satoh et al., 1992] is shown in Fig.4.3 -right.

Fermi surfaces calculations performed by Linearized Augmented Planewave (LAPW) method are shown in Fig.4.4 (left) [Settai et al., 2002]. These calculations reveal that the Fermi surface volume of the hole like and electron like Fermi surfaces are the same (compensated metal). Moreover, in the ferromagnetic state, the bands are split into spin-up and spin-down Fermi surfaces; they are degenerated. The spin-up Fermi surface has a higher volume than the spin-down one indicating the existence of a non zero spin magnetic moment on the system. Improvements of the previous Fermi surfaces calculations were performed by [Samsel-Czekała et al., 2011] (see Fig.4.4 (right)). In this case, the calculations of the FM2 Fermi surface of UGe_2 were determined by Local Spin Density Approximation with Polarisation Correction approach(LSDA+OP) and they reveal that the ferromagnetic ordered state FM2 of UGe_2 presents three non-degenerated bands (136, 137 and 138). Previous calculations show that the band 136 of the FM2 phase presents a large hole Fermi surface having more pronounced quasi-two-dimensional character along the b-axis and it is accompanied by small hole pockets, cigars and discs. In addition, the bands 137 and 138 are characterized by a large electron-like Fermi surface containing an open structure along the a-axis and by small hole pockets, respectively.

Our study is focused on the low temperature properties of the FM2 Fermi surface of UGe_2 and in the analysis of the orbits of the Fermi surface with $H \parallel a$-axis by thermopower quantum oscillation technique. The comparison of the later technique to dHvA and SdH effects is also a main objective of this chapter.

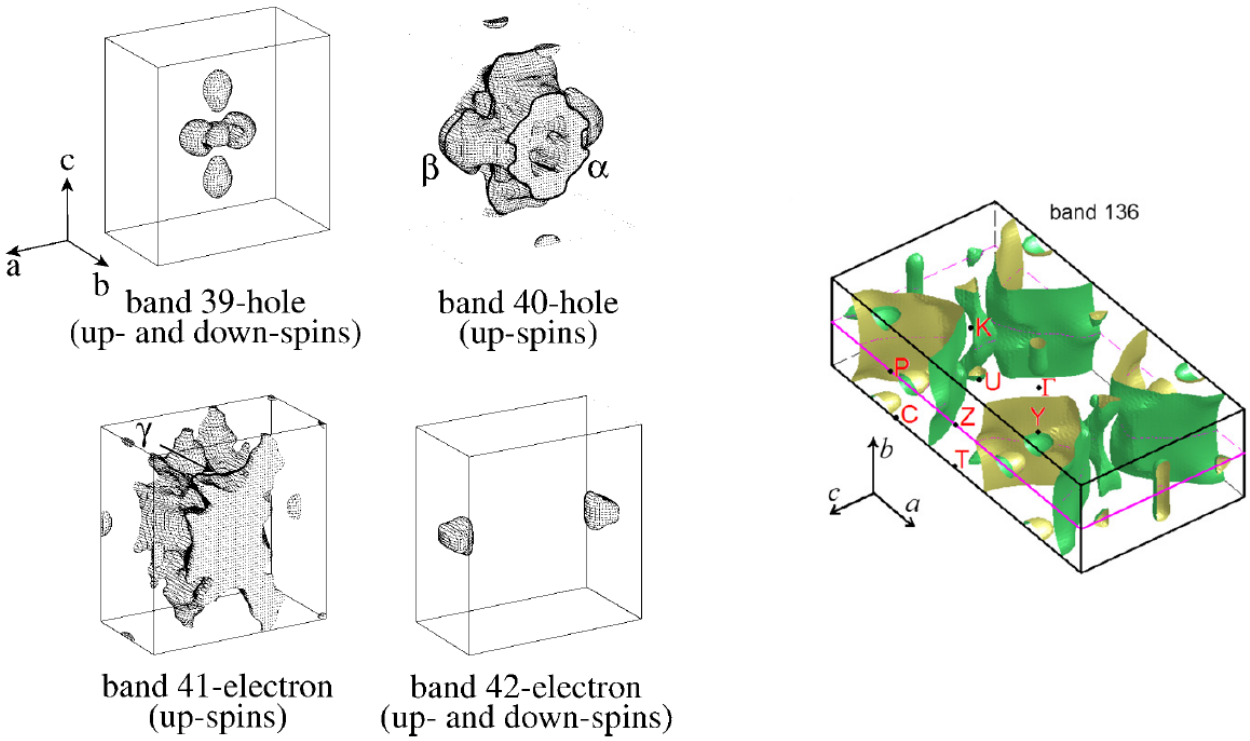

Figure 4.4: *Degenerated Fermi surfaces of the FM2 phase of UGe_2 obtain by LAPW method [Settai et al., 2002] (on the left). FM2 Fermi surface of UGe_2 calculated by LDSA approach [Samsel-Czekała et al., 2011] (on the right).*

4.3 Quantum Oscillation Theories

In this section, an overview of the quantum oscillations models is shown. I start with the well-known Lifshitz-Kosevich (LK) theory which is based on the oscillatory contribution of the magnetization of a system. In the variation of the magnetization of a system is based the analysis of the Fermi surface parameters obtained by the dHvA technique. I continue with a brief description of thermopower quantum oscillation ansazts as they were developed because the LK-theory cannot be used. LK-theory cannot treat non-equilibrium quantities such as magnetoresistance oscillations or thermopower oscillations. Nevertheless, it has been demonstrated that LK-theory works well for SdH technique under the assumption that the probability of the scattering is proportional to the density of states [Pippard, 1965]. Here, we perform an analysis of the ansazts developed for thermopower quantum oscillations and we check if the LK-theory is suitable to treat thermopower quantum oscillations in heavy fermion systems as it is the case for the SdH effect. Moreover, a comparison between former thermopower quantum oscillations ansazts and LK-theory will be done.

4.3.1 Lifshitz-Kosevich Theory

The de Haas-van Alphen effect corresponds to the oscillatory field dependence of the magnetic properties of the compound at low temperatures. The analysis of the oscillatory part of the magnetization is an important tool to study the electronic structure of metals because the periodicity of the oscillations is linked to the geometry of the Fermi surface. This link can be expressed through the Onsager relation, $F_i = (\hbar c/2\pi e)S_i$ with F_i the frequency of the Fermi surface and S_i the area of the Fermi surface.

Lifshitz-Kosevitch (LK) theory describes, from the free energy in an independent quasi-particle frame, the evolution of the oscillatory part of the magnetization with temperature and magnetic field.

Under strong magnetic fields, the orbital motion of the quasi-particles is quantized in k-space in Landau tubes with cross section $S(\varepsilon, k) = 2\pi eH/\hbar c(n + 1/2)$. These Landau tubes are structured in well defined energy levels equal to $E = \hbar\omega_c(n + 1/2)$ with $\omega_c = eH/m^*c$ that are called Landau levels. At $T = 0$K, if we apply a magnetic field, the energy and hence the magnetization should oscillate as the field is tuned. As a consequence, the states close to the Fermi level are modified inducing a change in the size of the Fermi surface. As the field is increased and a Landau tube with section s_i approaches the edge of the extremal cross section of the Fermi surface S_i, the density of states at the Fermi surface increases. However, once the tube leaves the Fermi surface, it cannot host occupied states and therefore, these states rapidly depopulate, leading to a sudden drop in the density of states at the Fermi surface. This vanishing of occupation occurs periodically as tubes of successively higher quantum number, n, pass through the Fermi surface. This quantization is reflected in the periodic variation with 1/H of the energy and hence of the magnetization with a frequency defined by the Onsager relation. From the field and temperature dependencies, we can obtain the extreme area S_i, the cyclotron mass m_i^* and the scattering lifetime τ_i for the cyclotron orbit.

The theoretical expression for the oscillatory component of magnetization M_{osc} due to the

conduction electrons was given by Lifshitz and Kosevich as follows:

$$M_{osc} = \sum_r \sum_i \frac{-1^r}{r^{3/2}} A_i sin\left(\frac{2\pi r F_i}{H} + \beta_i\right) \tag{4.1}$$

with A_i, R_T, R_D and R_S described as:

$$A_i \propto H^{1/2} \left|\frac{\partial^2 S_i}{\partial k_H^2}\right|^{-1/2} R_T R_D R_S \tag{4.2}$$

$$R_T = \frac{\lambda n m_i^* T/H_{eff}}{sinh(\lambda n m_i^* T/H)} \tag{4.3}$$

$$R_D = exp(-\lambda n m_i^* T_D/H) \tag{4.4}$$

$$R_S = cos(\pi g_i n m_i^*/2m_0) \tag{4.5}$$

$$\lambda = 2\pi^2 c k_B/e\hbar \tag{4.6}$$

The factors R_T, R_D and R_S are related to the thermal damping at finite temperature of the amplitude A_i, to the Landau level broadening $k_B T_D$ and to the spin factor, respectively. The spin factor given by R_S differentiates the phases between the Landau levels due to the Zeeman splitting. The Landau level broadening, governed by the Dingle temperature T_D, corresponds to lifetime broadening and inhomogeneous broadening caused by impurities, crystalline imperfections and strain. It can be calculated for each orbit by:

$$T_D = \frac{\hbar}{2\pi k_B}\frac{1}{\tau} \tag{4.7}$$

The variations of the magnetization are detectable if the following conditions are fulfilled:

- $\hbar\omega_c \gg k_B T$: the distance between Landau levels, $\hbar\omega_c$, is larger than the thermal broadening width, $k_B T$. For that, high fields and low temperatures are needed.
- $\omega_c\tau/2\pi > 1$ means that at least one cyclotron motion must be performed during the scattering time. High quality samples are needed to increase the mean free path of the conduction electrons and then, reduce the scattering rate.

The cyclotron effective mass of the orbits can be determined by the analysis of the temperature dependence of the amplitude of the oscillations from the R_T factor. It can be written as:

$$A(T) = A_i \frac{\lambda n m_i^* T/H_{eff}}{sinh(\lambda n m_i^* T/H_{eff})} \tag{4.8}$$

where A_i is the amplitude of the studied frequency at different temperatures. We note that H_{eff} is the effective field of the magnetic field range of the study [1]. Taking the natural

[1]The H_{eff} is determined from the FFT window in which the analysis of the frequencies and the amplitude variation are done. To determine it, we use the equation: $H_{eff} = 2(H_{min}^{-1} + H_{max}^{-1})^{-1}$ where H_{min} and H_{max} correspond to the magnetic field limits of the FFT window.

logarithmic of this equation, thus we obtain:

$$ln\left\{\frac{A_i}{T}\left[1-exp\left(\frac{-2\lambda m_i^* T}{H_{eff}}\right)\right]\right\} = -\frac{\lambda m_i^*}{H_{eff}}T + const \tag{4.9}$$

The cyclotron mass can be determined from the slope of the linear regression line of the plot $ln\{\frac{A_i}{T}[1-exp\left(\frac{-2\lambda m_i^* T}{H_{eff}}\right)]\}$ vs T by an iterative method. This plot is called mass-plot.

Analogous to the damping of the amplitude of the oscillations, we can determine the lifetime broadening of each orbit from R_D factor following the same mathematical procedure. Then, the equation of the amplitude variation, A_i, of a frequency with effective magnetic field, H_{eff}, follows:

$$ln\left[A_i H_{eff}^{1/2} sinh\left(\frac{\lambda m_i^* T}{H_{eff}}\right)\right] = -\lambda m_i^* T_{D_i}\frac{1}{H_{eff}} + const \tag{4.10}$$

To determine T_{D_i} of each orbit, the mass of the carriers of the orbit must be previously known. The Dingle-plot, $ln\left[A_i H_{eff}^{1/2} sinh\left(\frac{\lambda m_i^* T}{H_{eff}}\right)\right]$ vs $1/H_{eff}$, lets us obtain T_{D_i} from the slope of the regression line.

Finally, the mean free path, l_i, can be determined for each frequency from:

$$l_i = \frac{\hbar^2 k_{F_i}}{2\pi k_B m_i^* T_{D_i}} \tag{4.11}$$

and the relations $\hbar k_{F_i} = m_i^* v_{F_i}$ and $l_i = v_{F_i}\tau_i$.

4.3.2 Thermopower Quantum Oscillations Ansazts

As we have pointed out before, quantum oscillations of transport coefficients cannot be treated correctly from a thermodynamic approach because they are not equilibrium properties of the electron gas; therefore, they cannot be deduced from the free energy. Regardless the previous disadvantage, the study of thermopower quantum oscillations offers a large number of interests from an experimental point of view. These are: (i) the oscillations of the Seebeck effect are frequently substantially larger than the nearly field-independent non-oscillatory background, (ii) the observation of higher harmonics is strongly favoured, (iii) the sawtooth shape of the oscillations aids in the identification of electron and hole orbit contributions and (iv) the thermopower quantum oscillation effect is more sensitive to the magnetic breakdown.

There are two families of ansazts based on thermopower to analyze the quantum oscillations starting from the linear equations of the electrical and thermal current densities. Here, we explain Trodahl, Peschanskii and Young-Fletcher ansatzs [Trodahl and Blatt, 1969, Kirichenko et al., 2008, Fletcher, 1981]. Trodahl and Peschanskii belong to the first family of quantum oscillation ansazts and Young-Fletcher belong to the second one. The first family is characterized by expressing the oscillatory part of thermopower (i.e., the quantum oscillations) in terms of the L_{ij} tensor and of the thermodynamic properties whereas the second family considers that the oscillations are only linked to the derivative of the density of states, and then they use a modified LK-theory. In addition, all the proposed ansazts are based in the $j^e = 0$ framework (i.e., there is only a thermal gradient applied on the sample).

Derivative of the Density of States (YOUNG-FLETCHER)

The authors claim that thermopower quantum oscillations are based in the occurrence of oscillations in the conductivity with respect to the energy. They indicate that thermopower is sensitive to the derivative of the conductivity with respect to the energy; therefore, thermopower is particularly sensitive to these oscillations. They assumed that the oscillations in resistivity and in thermopower have identical physical origins and they also assumed that resistivity and thermopower have the same distribution, but with different averaging.

As we pointed out before, they assume $j^e = 0$ and they restrict the thermal gradient to the x direction $j^q_y = j^q_z = 0$ and the magnetic field along the z direction. As a consequence, they re-write the Seebeck coefficient $S = \nabla\varepsilon_x/\nabla T_x$, in terms of $S \propto \sigma^{-1}$. They claim that $\widetilde{S}/\overline{S} >> \widetilde{\rho}/\overline{\rho}$ and they finally find that the oscillatory part of the Seebeck coefficient can be expressed as:

$$\widetilde{S} = KR_D(x/sinh(x))' R_S sin\left(\frac{2\pi F_i}{H_{eff}} + \phi\right) \tag{4.12}$$

with $x = 2\pi^2 nk_B Tcm^*_i/\hbar eH_{eff} = n\lambda m^*_i T/H_{eff}$, K a constant and R_D and R_S the same terms as LK-theory. We observe that this equation is similar to eq.4.1 of the LK-theory and the unique diference resides in the R_T term. R_T term of this thermopower quantum oscillation ansazt is just the derivative of R_T term of the LK-theory only if we consider the relation $S \propto \partial\sigma/\partial\epsilon$ as valid. To determine m^*_i, we can fit directly the amplitude variation of the oscillations given by the R'_T equation or use the mass-plot technique. Then the mass-plot for Young-Fletcher can be written as:

$$ln\left\{\frac{A_i[1 - exp(-2x)]}{1 - xcoth(x)}\right\} = -x + const \tag{4.13}$$

Oscillatory Component of the Seebeck Coefficient (TRODAHL)

This ansazt is based on the linearity of j^e and j^q equations in the free-electron limit (spherical Fermi surface). Then the Seebeck coefficient can be re-written as:

$$S_{11} = \frac{1}{T}\sum_{j=1}^{3} \rho_{1j} L_{j4} \tag{4.14}$$

Authors claim that the longitudinal current ($J \| H$) and L_{24} are negligible. They indicate that the monotonic part of the magnetoresistance is substantially larger than the oscillatory one. Consequently, they express the oscillatory part of the Seebeck coefficient as $\widetilde{S} = \widetilde{S_{11}} = \rho_{11}\widetilde{L_{14}}/T$ with $\widetilde{L_{14}} \propto \alpha_1 A_3(x) + \alpha_2 A_4(x)$. In the $\omega_c\tau$ limit, the relation $A_3 >> A_4$ is fulfilled. The term $\widetilde{L_{14}}$ can be expressed as:

$$\widetilde{L_{14}} = \frac{5\sqrt{2}}{4}\frac{k_B Ten}{m^*\tau c^2}\left(\frac{\hbar\omega_c}{\varepsilon_F}\right)^{1/2} \sum_{\nu} \frac{-1^{\nu}}{\sqrt{\nu}} A_3(x) sin(2\pi F_i/H + \phi) \tag{4.15}$$

with $A_3(x) = -\pi cosh(x)[1 - xcosh(x)]$. This $A_3(x)$ term corresponds to the oscillatory part of the Seebeck coefficient and we can identify it to the damping factor R_T of the LK-theory.

As a consequence, we use this term, A_3, to determine the mass-plot for the Trodahl ansazt:

$$ln\left\{\frac{A_i[1-exp(-2x)]}{[1-xcoth(x)][1-exp(-4x)]}\right\} = -x + const \tag{4.16}$$

Usually, m_i^* can be determined by:

$$ln\left\{\frac{A_i[1-exp(-2x)]}{[1-xcoth(x)]}\right\} = -x + const \tag{4.17}$$

because $[1-exp(-4x)] << [1-exp(-2x)]$. We highlight that the latest Trodahl mass-plot is the same as the Young-Fletcher one. Hence, those previous techniques starting form different approaches collapses to obtain the same amplitude evolution with temperature.

Gradient of the Chemical Potential (PESCHANSKII)

Peschanskii ansazt is based in the linear behaviour of the thermoelectric coefficients with $\varepsilon = \varepsilon_j - \frac{1}{e}\frac{\partial \mu}{\partial x_j}$ with μ the chemical potential. They assume that the number of charge carriers per unit volume is constant which allows to determine the gradient of the chemical potential in the case of $j^e = 0$ as:

$$\nabla\mu \propto P_k(x)\left|\frac{\partial^2 S_i}{\partial k_H^2}\right|^{-1/2} sin(2\pi F_i/H + \phi) \tag{4.18}$$

with

$$P_k(x) = \frac{3}{x}\frac{sinh(x) - xcosh(x)}{sinh^2(x)} \tag{4.19}$$

$P_k(x)$ term shows the evolution of the amplitude of the quantum oscillations; consequently, this term is the equivalent to the damping factor R_T of the LK-theory. From this term, we can determine the Peschanskii mass-plot as:

$$ln\left\{\frac{A_i x[1-exp(-2x)]}{1-xcoth(x)}\right\} = -x + const \tag{4.20}$$

We notice that we cannot use the mass-plot to obtain m^* by this ansazt. The amplitude evolution must be fitted directly as the terms we neglect in the process of writing the mass-plot produces a misleading-enhancement of m^*. However, the direct fit gives the right values of this Fermi surface parameter, as we will see.

We conclude that the first family develops new equations for the parameters of the Fermi surface whereas the second family bases the thermopower quantum oscillations on the LK-theory. The latest family modifies the R_T term for its derivative as the Seebeck coefficient is linked to the derivative of the density of states instead of being directly related to the density of states as dHvA. A comparison between the ansazts is shown in Fig.4.5. In this figure we observe the evolution of the amplitude of the oscillations as a function of the x parameter. This parameter is directly related to the temperature following $x = (-\lambda n m^*/H_{eff})T$. We verify that LK and Peschanskii have similar amplitude evolution of the quantum oscillations with temperature. Trodahl ansazt starts at 1 as former ansazts but the amplitude suppression

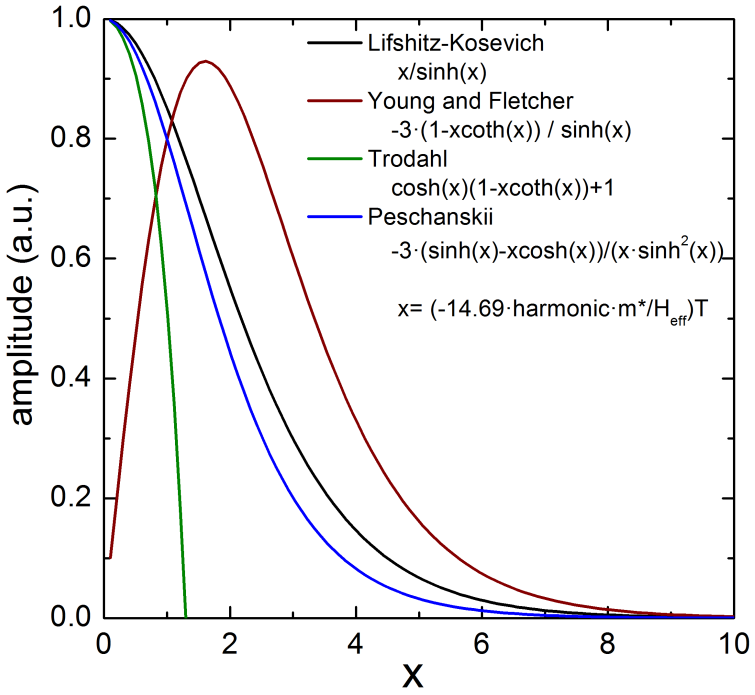

Figure 4.5: *Comparison between LK-theory (black curve) and the studied ansazts for thermopower quantum oscillations: Young-Fletcher (red curve), Trodahl (green curve) and Peschanskii (blue curve).*

of the oscillations is stronger and in a lower temperature range. In the case of Young-Fletcher ansazt, we observe that it starts at 0, has a maximum and then, decreases. In this model the suppression of the amplitude of the oscillations occurs at higher temperatures than for LK and Peschanskii models.

4.4 Quality Sample and Measuring Configuration

The single crystal of UGe_2 was grown by the Czochralski method in a tetra-arc furnace, oriented by X-ray Laue diffractometer and cut by a spark-cutter in a bar-shaped sample with dimensions $2460 \times 400 \times 305\mu$m. The residual resistivity ratio (RRR) of the studied crystal was $\sim$ 300. Thermopower and SdH measurements were performed applying the magnetic field along the a-axis and the thermal gradient and electrical current along the b-axis for thermopower and SdH effect, respectively. The b-axis corresponds to the long length of the bar-shape.

Thermoelectric measurements were performed at low temperatures down to 190mK and under magnetic fields up to 16T using a "One heater - Two thermometers" setup. The magnetic field was swept while a constant power was applied to the sample. The power was fixed at $H = 0$ for a value generating a relative thermal gradient of $\Delta T/T = 1 - 3\%$. For Seebeck measurements as a function of temperature, the $\Delta T/T$ was fixed at $\Delta T/T = 3\%$ and it was recalculated at each temperature point.

SdH measurements were performed at low temperature down to 30mK and magnetic field

up to 13.4T. The SdH setup was the standard four-probe AC lock-in technique with a current of $I = 10\mu V$. The AC signal was amplified by a low temperature transformer by a factor 1000 keeping the noise level very low.

All data shown were obtained by sweeping the magnetic field upwards. The correction to the applied magnetic field is given by $B = H + 4\pi(1 - D)M$, with H the external magnetic field, D the demagnetization factor and M the magnetization of the sample. The shape of the measured sample gives a demagnetization factor close to $\sim 0.9 - 1$, then $1 - D \sim 0$ for the measured field range (the saturated regime). Any modification has been observed in the frequencies of the spectrum of the Fermi surface of UGe_2 when the applied magnetic field H is corrected by the demagnetization factor; hence, the total applied magnetic field B to the sample can be considered equal to the external applied magnetic field, thus $B \sim H$.

4.5 Temperature Dependence of Thermoelectric Coefficients in UGe_2

In this section, we analyze the evolution of the thermopower coefficients as a function of temperature. First, we analyze the Seebeck coefficient and we compare it to others probes. In the second part of the section, we present the results in the Nernst coefficient, temperature $N(T)$ and field $N(H)$ dependencies. I decided to present the field evolution of the Nernst coefficient in this section because no quantum oscillations were observed in the Nernst coefficient[2].

4.5.1 Temperature Dependence of Thermopower

Thermopower as a function of temperature $S(T)$ for different magnetic fields with thermal gradient along the b-axis and magnetic field along the a-axis, the easy axis of UGe_2, are shown in Fig.4.6. In black, $S(T)$ at $H = 0T$ and in blue $S(T)$ under a magnetic field of $H = 9$T are shown. At zero magnetic field, we observe the FM2-FM1 crossover at $T_x = 27$K and the Curie temperature T_C corresponding to FM1-PM transition at $T_C = 52$K. The magnetic field favors the ferromagnetic domain. The FM2-FM1 crossover moves to higher temperatures, $T_x = 36$K. The FM1-PM transition also seems to appear at higher temperatures as we do not observe it in the $[0 - 60]$K temperature range. Nevertheless, we note that the detection of this transition under field seems to be quite difficult. It was shown that this transition is easily lost under field by other probes.

The evolution of $S(T)$ in the low temperature regime was deeply studied (see Fig.4.7). First, the Seebeck coefficient as a function of temperature $S(T)$ remains positive for all the temperature range. This means that the total band contribution to the thermopower signal is hole-like. However, the evolution of the Seebeck coefficient with temperature depends on the derivative of the electrical conductivity with respect to the free energy of the system ($\partial\sigma/\partial\epsilon$ - Boltzmann limit). As a consequence, the evolution of the $S(T)$ is a difficult task to understand in multiband compounds such as UGe_2. Second, $S(T)$ value is really small at low temperatures (like pure metallic behaviour). Moreover, we also notice the strong dependence

[2] The absence of quantum oscillations in the Nernst coefficient can be interpreted as a consequence of the non-dependence of the scattering time with the magnetic field as has been demonstrated by the semi-classical theory of the Nernst effect [Behnia, 2009].

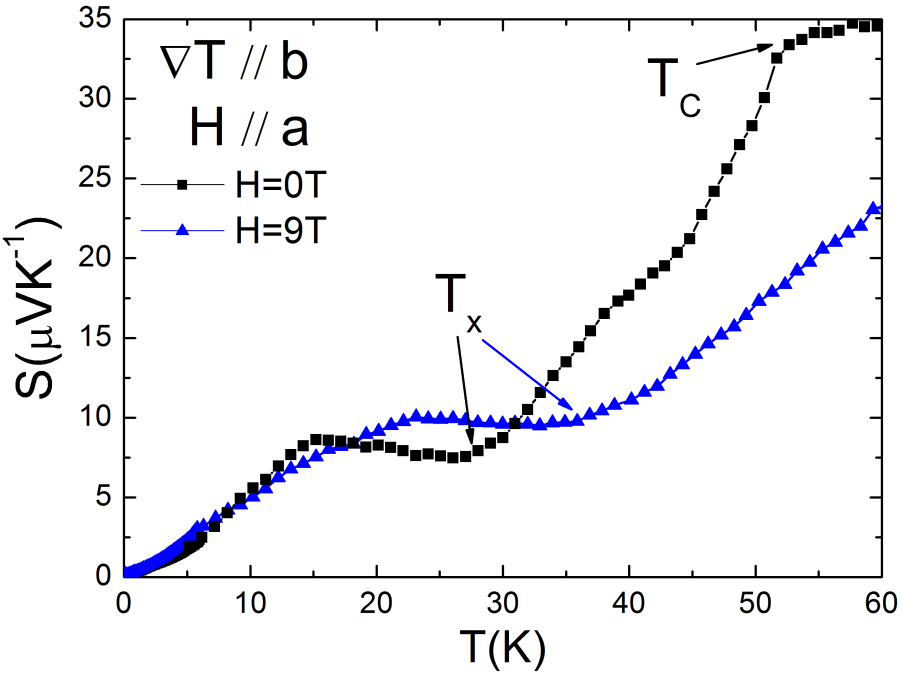

Figure 4.6: *Thermopower measurements as a function of temperature $S(T)$ at different magnetic fields: $S(T)$ at $H = 0T$ (black color) and $S(T)$ at $H = 9T$ (blue curve).*

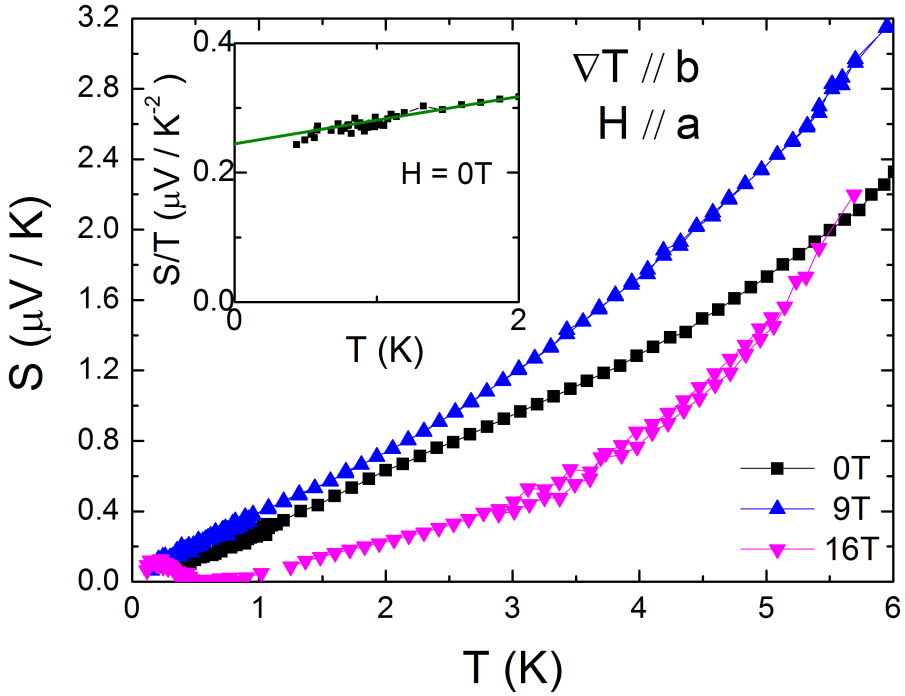

Figure 4.7: *Thermopower measurements as a function of temperature at different magnetic fields. The thermal gradient is applied along the b-axis and the applied magnetic field along the $a-$axis. The inset shows thermopower divided by temperature at zero magnetic field in the low temperature regime.*

of thermopower with the applied magnetic field. Small variations in this parameter induce strong changes in the thermopower signal as a consequence of the large amplitude of the quantum oscillations. This phenomenon is preferentially observed at low temperatures and under fields higher than 5T. These effects cause significant errors in the determination of average absolute values of the Seebeck coefficient below 0.5K under high magnetic fields. Finally, we observed that for a low fixed temperature, $S(T_{fixed})$ increases from low magnetic

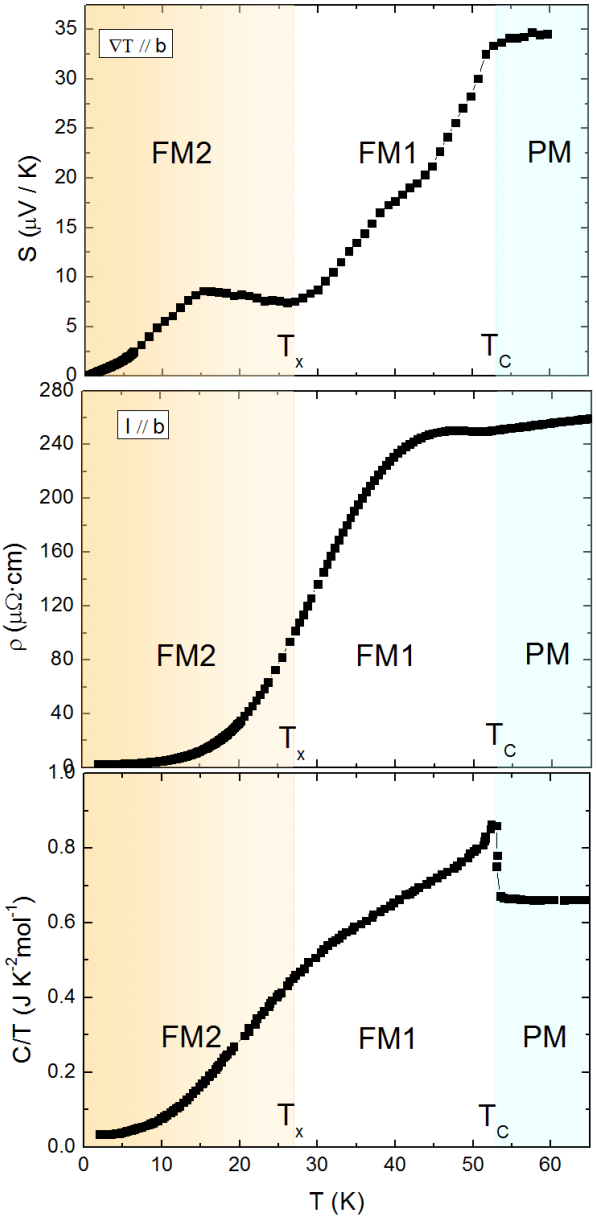

Figure 4.8: *Temperature dependece of thermopower S, resistivity ρ and specific heat C/T measurements at zero magnetic field. S and $\rho(T)$ measurements were performed with thermal gradient and current applied along the b-axis, respectively. The three magnetic regimes expected in UGe_2, FM2, FM1 and PM state, are observed in orange, white and blue colored areas, respectively. The degradation from orange to white colour indicates that the transition FM1-FM2 is a crossover.*

fields to 9T. At this field, $S(T_{fixed})$ achieves its maximum and then, it decreases for higher fields in accordance with isothermal thermopower $S(H)$ measurements shown in Fig.4.10. This increase with H is due to the strong magnetoresistance $\rho(H)$ (see Fig. 4.16). At low fields, $1 \gg \omega_c\tau$ and then, $\rho(H)$ dominates in the thermopower signal. At higher fields, the previous condition is inversed; i.e. $\omega_c\tau \gg 1$. In this regime, quantum oscillations control the thermopower signal and then the oscillatory component dominates in the signal. In addition, as the influence of ρ vanishes, S decreases.

Considering the one-band model of the free electron gas, we analyzed UGe_2 in the zero-temperature limit using the relation of the q-factor, $q = SN_Ae/(\gamma T)$ where S/T is the Seebeck coefficient over temperature, N_A Avogadro's number, $-e < 0$ the electronic charge and γ the electronic specific heat. The S/T values are taken from the inset of Fig.4.7 that shows the temperature evolution of S/T at $H = 0$T in the low temperature regime. The green line estimates the value of S/T in the $T \to 0$ limit at $S/T = 0.25\mu VK^{-2}$. The electronic specific heat γ was obtained from ref. [Lashley et al., 2006] and its value corresponds to $\gamma = 33.2mJmol^{-1}K^{-2}$. Then, the obtained q-factor is 0.73heat charge/f.u. which is positive and quite close to the universal value of 1. This means that UGe_2 can be considered a hole-like normal metal. A proof of that is the huge scattering that magnetoresistance measurements shown (see Fig.4.16). To finish, we notice that the one-band model is developed for spherical Fermi surfaces that are far from the complex topology of the Fermi surfaces of heavy fermion systems. Nevertheless, this model can be used as a first approximation in this family of compounds as S signal will be dominated by the heaviest bands.

Thermopower S, resistivity $\rho(T)$ and specific heat C/T measurements as a function of temperature at zero magnetic field are shown in Fig.4.8. The upper graph corresponds to $S(T)$ measurements with the thermal gradient along the b-axis, the graph in the middle presents $\rho(T)$ measurements performed for an electrical current applied along the b-axis and the bottom graph shows C/T. We observed the FM1-FM2 crossover at $T_x = 27$K and the FM1-PM second order transition at $T_C \simeq 53$K; both transitions occur at the same temperature for the three probes. In $S(T)$, there are a sharp anomaly at T_C, a small bump at $T \sim 40$K, a well defined anomaly at T_x (corresponding to a minimum) and a small bump at $T \sim 15$K. In $\rho(T)$ measurements, we notice there is an increase of ρ at T_C and at T_x no clear anomaly has been detected. In C/T, we identify a 2^{nd} order phase transition at T_C (discontinuity of C/T) and a broad anomaly at T_x. We conclude that this 2^{nd} order transition is observed clearly in the C/T and in $S(T)$. Nevertheless, the crossover and its width could be observed clearly only in thermopower measurements. The width of the crossover is estimated to be from 15K to 38K and it corresponds to the width between the slope changes near T_x observed in thermopower. We remark that thermal expansion demonstrates that T_x depends strongly on the crystallographic directions due to the strong magnetic anisotropy [Hardy et al., 2009]. Then, the determination of T_x could depend on the sensitivity of the probe.

4.5.2 Nernst Coefficient

The Nernst effect was measured as a function of temperature, $N(T)$, and as a function of magnetic field, $N(H)$ (see Fig.4.9 left and right graphs, respectively). We observe in $N(T)$ measurements that the Nernst coefficient is characterized by low positive absolute values, less than $0.40\mu VK^{-1}$, in the low temperature regime $[0-13]$K. At temperatures above ~ 13K the

Nernst coefficient changes sign. In $N(T)$ measurements, the crossover appears at $T_x = 27$K and the magnetic transition from FM1-PM states at $T_C \sim 50$K. This transition corresponds to the minimum of the Nernst signal. We remark that the temperature T_C in $N(T)$ measurements is slightly lower than in the other probes. In addition, $N(T)$ measurements demonstrate that under magnetic field, T_x and T_C are shifted to higher temperatures. This enhancement of the FM order with field was also observed at T_x by thermopower measurements.

The Nernst coefficient as a function of field, $N(H)$, shows a sharp decrease of its value in the low field range [0−0.5]T which is easily observable at high temperatures due to the higher value of the Nernst coefficient in this temperature range. This strong modification in the Nernst coefficient for low values of fields is in agreement with the magnetization measurements along the a-axis shown in Fig.4.1 -right- for which we observe a sharp increase of the magnetization at low fields. Then, we can attribute this signal to an anomalous Nernst effect similar to the anomalous Hall effect present in the ferromagnetic materials near T_C. We suggest that the slighty lower value of T_C reported by $N(T)$ measurements can be due to this anomalous effect.

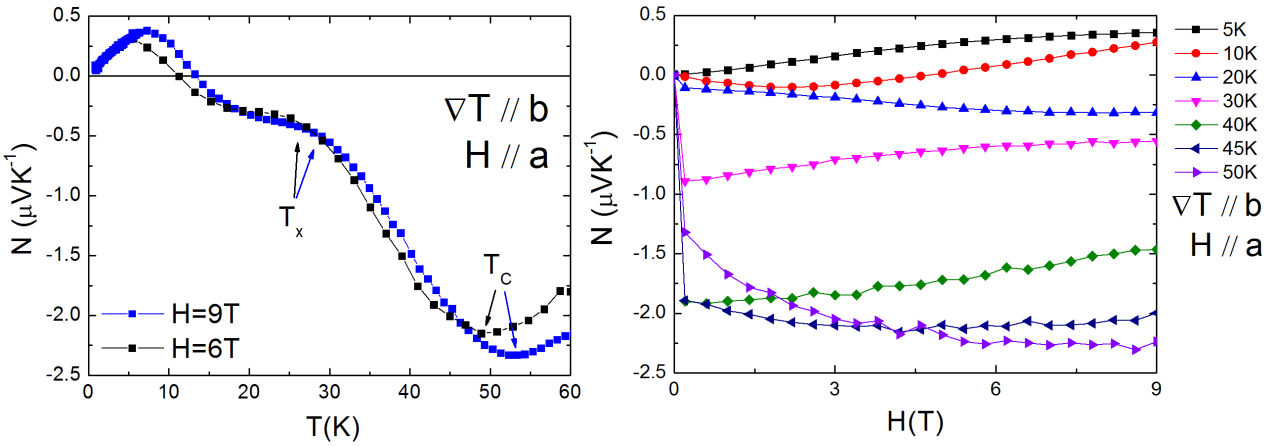

Figure 4.9: *Nernst coefficient as a function of temperature $N(T)$ at different magnetic fields (on the left) and field dependence of the Nernst coefficient $N(H)$ at different temperatures (on the right). The thermal gradient is applied along the b-axis and the applied magnetic field along the a-axis.*

To finish, we notice that the values of the Nernst coefficient are 10 times lower than the values of the Seebeck coefficient for all the temperature range. This is in agreement with the fact that the Nernst effect generated by normal quasi-particles in an ordinary metal should be negligible because the Nernst effect measures the ratio of the electron mobility to the Fermi energy [Behnia, 2009]. Therefore, the main part of the contribution we measured does not correspond to the normal quasi-particles contribution, but to the contribution related to the internal magnetization of UGe_2 (anomalous Nernst effect).

4.6 Analysis of the FM2 Fermi Surface of UGe_2

The Fermi surface properties of UGe_2 are directly linked to the itinerant carriers of the incomplete $5f$ and s, p and d bands. A detailed study of the Fermi surface of UGe_2 consisting on the analysis of the frequencies f_i, the effective mass m_i^* and the mean free path l_i of

each orbit by isothermal thermopower quantum oscillations has been done. The thermopower configuration was $\nabla T//b$ and $H//a$. To demonstrate the effectiveness of thermopower as a probe to determine the topology of the Fermi surface of a heavy fermion system, we also performed SdH measurements on the same sample in the same configuration, $j^e//b$ and $H//a$ follow by a comparison between S(H) and magnetoresistance techniques to analyze the Fermi surface. Finally, thermopower and SdH measurements were analyzed against dHvA effect [Haga et al., 2002, Satoh et al., 1992, Terashima et al., 2002].

4.6.1 Thermopower Quantum Oscillations

The observation of thermopower quantum oscillations in heavy fermion systems was not expected as a consequence of the heavy masses, the huge electronic scattering (q-factor$\sim$ 1) which complicate the detection of the oscillatory component of the thermopower signal. As we have pointed out before, there are some limitations to measure thermopower quantum oscillations. The temperature, the field and the quality of the sample must fulfill $\omega_c\tau \gg 1$ and $\hbar\omega_c \gg k_BT$ conditions. Specifically, we can follow the thermopower quantum oscillations of the FM2 phase of UGe_2 thanks to the good quality of the sample (RRR$\approx$ 300), the metallic behaviour at low temperatures (small absolute value of thermopower) and the existence of some Fermi surfaces with light effective mass. In Fig.4.10, we show isothermal thermopower measurements of UGe_2 as a function of increasing magnetic field in the low temperature regime. The conditions in which the measurements were performed were as follows: the fridge was regulated at a fixed temperature, the magnetic field was swept from 0 to 16T at a constant

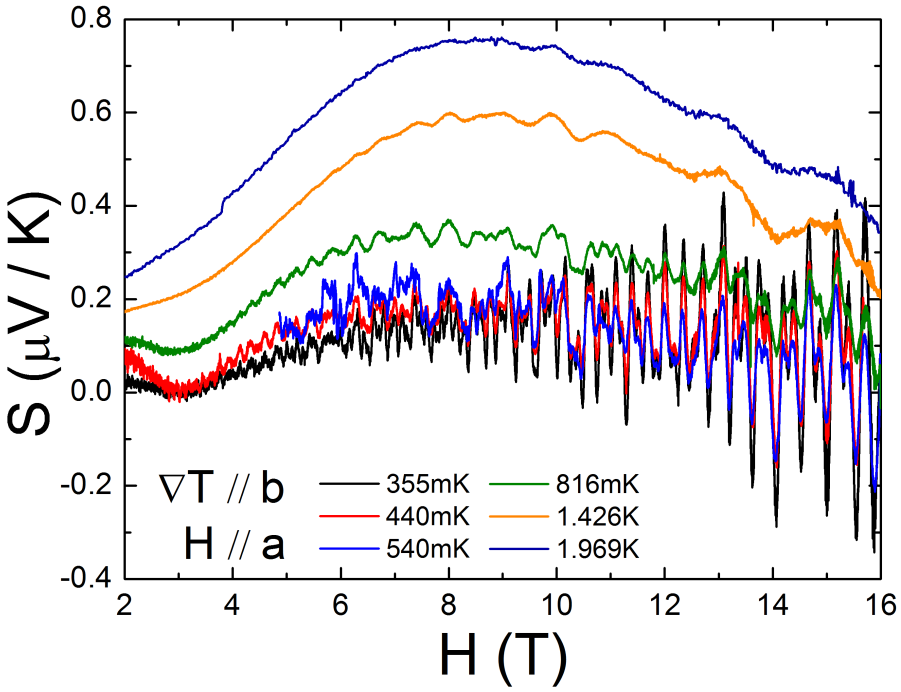

Figure 4.10: *UGe_2 isothermal thermopower measurements with applied thermal gradient along the b-axis and magnetic field along the a-axis performed at different temperatures. Thermopower quantum oscillations are observed in the low temperature regime* $[0-2]K$.

rate of 0.1T/min and a constant heat power was applied to the sample in all the field range to establish the thermal gradient. The thermal conductivity of UGe_2 varies with the magnetic field, decreasing as the magnetic field increases. As a consequence, an increase of the thermal gradient with field occurs and then, an increase of the average temperature of the sample was observed as the field was swept upwards. To determine the absolute value of thermopower, we took into account the thermal gradient at each value of the magnetic field. We observed that this decrease of thermal conductivity has more influence in the low temperature regime. The temperatures shown in the graph correspond to the average temperature of the sample in the complete field range of $S(H)$ measurements. We remark that the $\Delta T/T$ increments with field at the lowest temperature up to 3 times its initial value. In addition, the amplitude of the oscillations increases as temperature decreases and the oscillations are still observable for temperatures higher than 2K. As we pointed out before, the Seebeck coefficient increases from 0 to 9T at which value $S(H)$ achieves its maximum. For $H > 9$T, $S(H)$ decreases and crosses the zero. This maximum can be related to the huge magnetoresistance (see Fig.4.16) and the change from $\omega_c\tau < 1$ to $\omega_c\tau \gg 1$ regime entering in the quantum oscillations regime.

To determine the frequencies of the Fermi surface at which our probe is sensitive to, we performed a Fast Fourier Transformer (FFT) analysis of the $S(H)$ signal as it is done in dHvA or SdH effects. Other parameters related to the Fermi surface such as the cyclotron mass, m^*, the Dingle temperature, T_D, and the mean-free path, l, could be obtained from the temperature dependence of the amplitude and the field dependence of the amplitude of a frequency at fixed temperature. To analyze the temperature and field evolution and therefore, to obtain the previous characteristics of the Fermi surface, we employed different ansatzs as discussed before. We are going to study the differences of the previous analyzed ansazts and the relevance of each model to the experimental data.

In Fig.4.11, we show the spectrum of the $S(H)$ measurements obtained from an FFT analysis of $S(H)$ measurements. The FFT was performed for the $[10.5 - 16]$T FFT window and the temperatures shown in the figure correspond to the average temperature of the sample in the field range of the FFT window. The temperatures vary from 200mK, green color, to $\sim$ 2K, red color. The inset of the figure shows the spectrum for the lowest temperature for the $[5 - 10.2]$T FFT window. We decided to use two different FFT windows to maximize the amplitude of the low and high frequencies of the Fermi surface of the FM2 phase of UGe_2. In addition to this first reason, we chose two independent FFT windows to avoid the field range area in which it seems to appear the suppression of the quantum oscillations. This destructive superposition, beaten, can be associated to a slightly different Fermi surface below and above this anomaly.

The procedure followed to analyzed the spectrum consists in, first, to remove the tiny background of $S(H)$ measurements using a second order polynomial fit to perform the FFT even though, it is not necessary for determining precisely the frequencies. Second, we applied a Hamming window filter in both FFT ranges to enhance the frequencies corresponding to these two regimes (low frequencies in $[5 - 10.2]$T window and high frequencies in $[10.5 - 16]$T FFT window). The objective was to be as close as possible to the SdH procedure in order to compare our results with the results of the SdH effect. The frequencies obtained from the FFT analysis are shown in Table 4.1.

To investigate the cyclotron mass of each orbit, m_i^*, we have analyzed the temperature dependence of the amplitude for each orbit by the previous ansazts. An example for the orbit

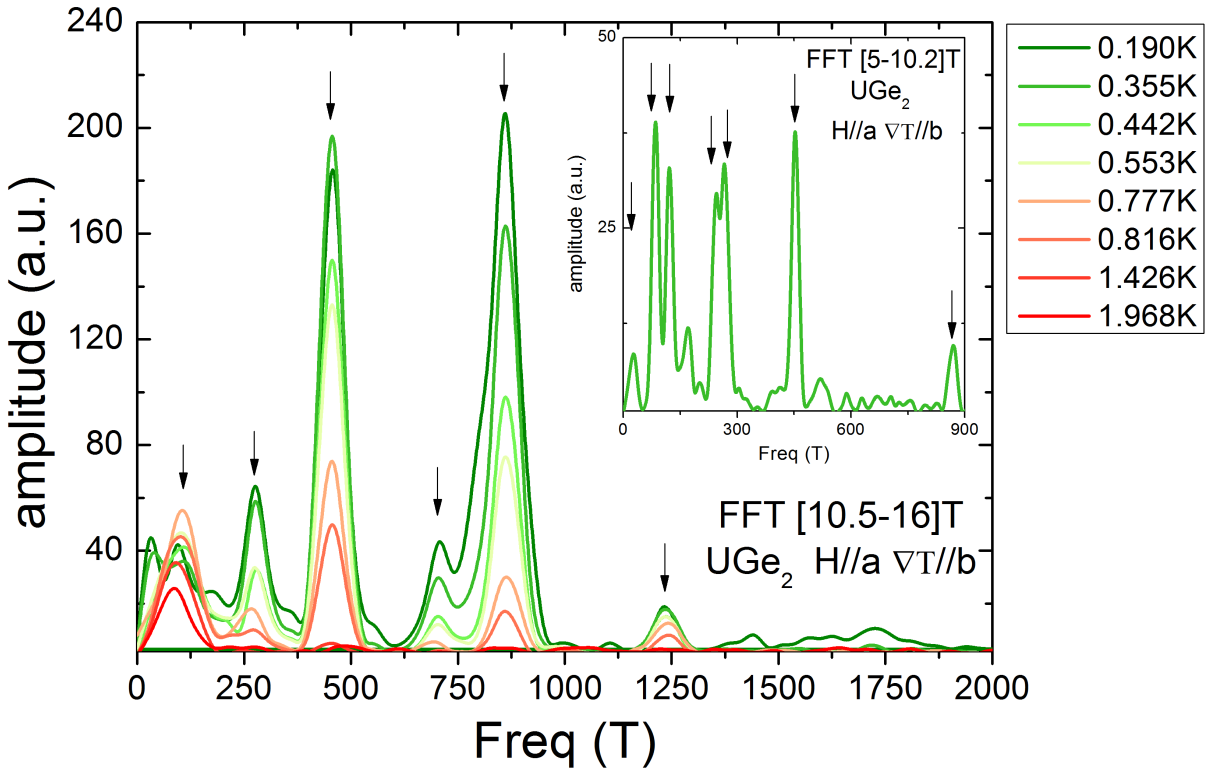

Figure 4.11: *Ensemble of FFTs of $S(H)$ measurements at different temperatures performed for a FFT window of $[10.5-16]\,T$. The inset shows the FFT for the lowest temperature of $S(H)$ measurements for the low frequency range (FFT window: $[5-10.2]\,T$).*

Orbits of the FM2 phase (T)	
$[5-10.2]$T	$[10.5-16]$T
20	
85	~ 100
119	
244	276
265	
454	456
	707
865	860
	1235

Table 4.1: *List of the orbits of the FM2 phase of UGe_2 in (T) obtained from isothermal thermopower measurements for $[5-10.2]\,T$ and $[10.5-16]\,T$ FFT windows.*

860T is shown in Fig.4.12. In this figure we represent the evolution of the amplitude of the 860T frequency as a function of the variable x that is defined as $x = (-\lambda n m^*/H_{eff})T$ with $\lambda = 14.69$, n the harmonic, m^* the cyclotron mass and H_{eff} the effective field of the FFT window. We notice that x is only temperature dependent, thus we represent the amplitude versus the temperature. The analysis was performed in the $[10.5-16]$T FFT window. m^*

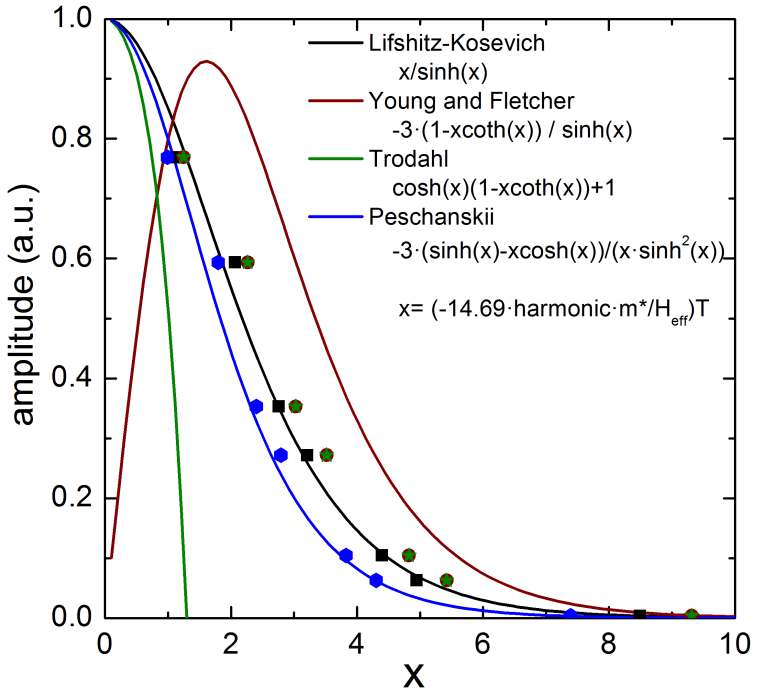

Figure 4.12: *We compare the conformity between the experimental data and LK (black), Young-Fletcher (red), Trodahl (green) and Peschanskii (blue) models. The symbols represent the experimental data obtained for each model taking into account their own calculated m^* and the lines represent the equations of the different models. A good agreement is observed for LK and Peschanskii ansazts.*

was determined from the slope of the mass-plot for LK, Young-Fletcher and Trodahl ansazts and from a direct fit of the amplitudes vs temperature for Peschanskii ansazt. We obtained $m^*(m_0)_{LK} = 5.0$, $m^*(m_0)_{Y-F\&Trodahl} = 5.9$ and $m^*(m_0)_{Pesch} = 4.5$. These m^* values were used to determine the individuals values of x of each ansazt. The (amplitude, x) experimental data points are shown in in Fig.4.12. A good agreement between the experimental data and theory are observed for LK-theory and Peschanskii ansazt. The other two ansazts, Throdahl and Young-Fletcher, can not fit correctly m^* nor by a mass-plot neither by a direct fit of the amplitude versus temperature as they do not describe in a correct way the amplitude variation with temperature. To well fit the experimental data to Trodahl ansazt, m^* must be of the order of $\sim 1-2m_0$ and in the case of Young-Fletcher ansazt, m^* should be of the order of $\sim 6-7m_0$. In addition, we highlight that these ansazts, Throdahl and Young-Fletcher, can not fit all the temperature regime with one value of m^*. The m^* of the orbit 870T orbit determined by dHvA is $m^*(m_0)_{dHvA} = 4.8$ [Haga et al., 2002] which is quite close to our m^* values obtained from thermopower measurements. Finally, we point out that Peschanskii ansazt obtains systematically lower m^* values than LK-theory applied to thermopower measurements.

Based on the previous analysis, we decided to use LK-theory to perform the analysis of the m^*, T_D and l. In principle, LK-theory is not the right theory to use to that purpose because thermopower is not an energy equilibrium property of the system. However, we verified that using it, we obtain m^* close values to the expected ones. Moreover, if we use this theory, the comparison between the 3 probes (dHvA, SdH and thermopower quantum oscillations) will be based on the same assumptions and hypothesis. In Fig.4.13, we show the mass-plot for

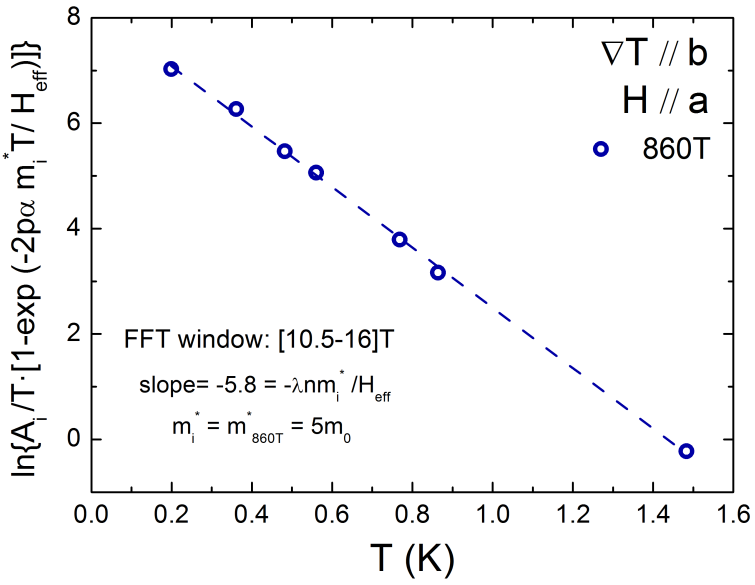

Figure 4.13: *LK-theory mass-plot obtained for the* $860T$ *orbit in the* $[10.5-16]T$ *FFT window. The corresponding cyclotron mass is* $m^* = 5m_0$.

the 860T orbit in the FFT window $[10.5-16]$T obtained by the LK-theory. The linear fit is represented by the dashed line. From the slope of this fit, we estimate m^* as indicated in the figure. The analysis was performed using the average temperature value of the sample in the FFT window. We also analyzed the cyclotron mass for fixed temperatures at the extreme of the FFT windows (5T, $\sim$ 10T and 16T). The cyclotron mass differences obtained for those different temperatures can be considered as negligible. As a result, it is important to remark that in the case of UGe_2, the temperature dependence of the cyclotron mass is small. The cyclotron masses for the average temperature of the FFT window are collected in the Table 4.2.

Cyclotron masses of the FM2 phase	
orbit	$m^*(m_0)$
20	1.0
85	1.1
119	1.8
244	3.4
265	3.6
456	4.0
707	5.5
860	5.0
1235	2.4

Table 4.2: *List of thermopower quantum oscillations cyclotron masses* m^* *of the detected orbits of the FM2 Fermi surface of* UGe_2 *determined by LK-theory.*

We highlight that LK-theory works well for UGe_2 due to low m^* values. However, in the

case of heavy orbits, a full analysis must be done and we will discover that none of the thermopower ansazts existing up to this moment is valid in this situation. At low temperatures, contrary to what we expect in LK-theory, the amplitude of the oscillations must decrease as a consequence of the entropy thermodynamic principle. The ansazts proposed to analyze the Fermi surface parameters by thermopower quantum oscillations do not follow this physical phenomenon.

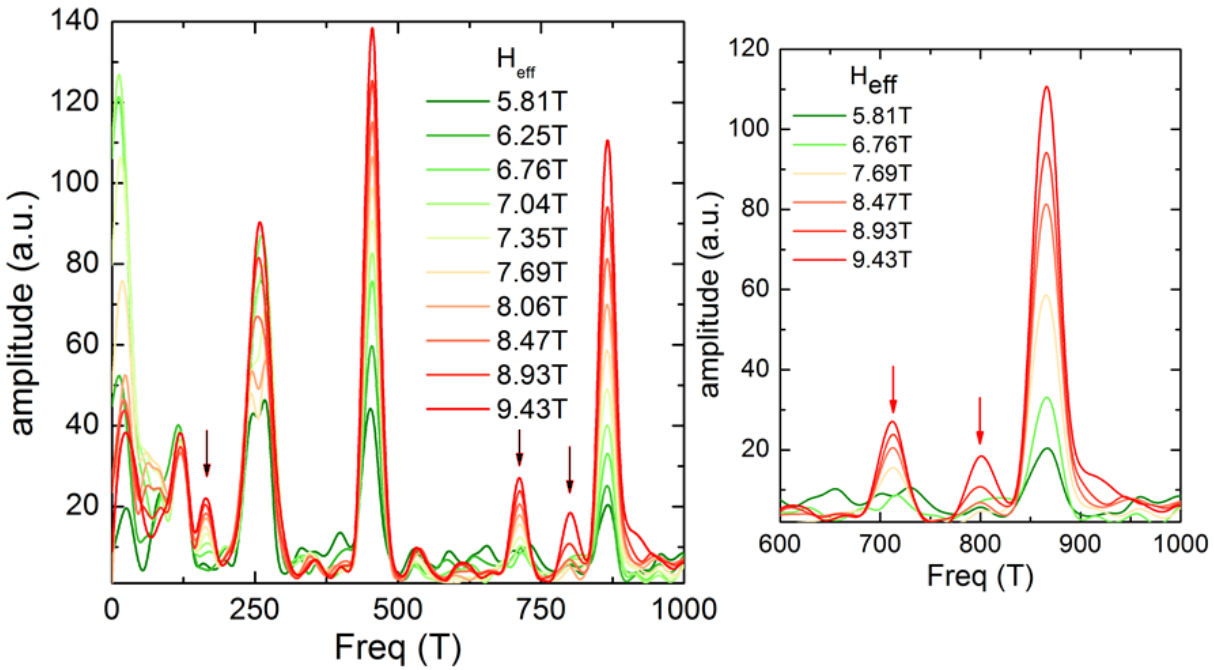

Figure 4.14: *Superposition of the ensemble of FFTs performed at the lowest temperature of the $S(H)$ measurement. The FFT window is 0.07 $1/T$ and it is swept in the $[4-16]\,T$ magnetic field range. The figure on the right is a zoom of the high frequencies. The arrows show the appearance of $165\,T$, $707\,T$ and $800\,T$ frequencies at high fields.*

The evolution of the frequencies with the effective magnetic field is analyzed from the evolution of the FFTs with a FFT window of 0.07 1/T in the [4−16]T range (see Fig.4.14). We observe that high H_{eff} favors the appearance of the 165T, 707T and 800T orbits. 800T orbit is characterized by high cyclotron mass; $m^* > 8.5m_0$ and the 160T orbit by a $m^* = 2.2m_0$. More frequencies for this FFT window were observed because 0.07 1/T FFT window size has a higher resolution than the $[10.5-16]$T one. We highlight that the beaten of oscillations at ~ 10.3T does not modify the spectrum of the Fermi surface of UGe_2, then the destructive superposition is not related to a Fermi surface modification.

The Dingle temperature T_D and the mean free path l were also determined for some bands at the lowest temperature 200mK. An example is shown in the Fig.4.15 in which we represent the Dingle-plot ($ln\left[AH^{1/2}sinh\left(\frac{\lambda m^* T}{H}\right)\right]$ vs $1/H$) for the orbit 860T. As we show, T_D is obtained from the slope of the regression line (dashed blue line) and l from eq. 4.11. All the frequencies observed have a l of the order of $1000-4000$ Å (see Table 4.3). The l obtained for the orbits of UGe_2 by thermopower quantum oscillations are of the same order of the l obtained from dHvA effect at 90mK, $l = 1000-2000$ Å [Haga et al., 2002]. As

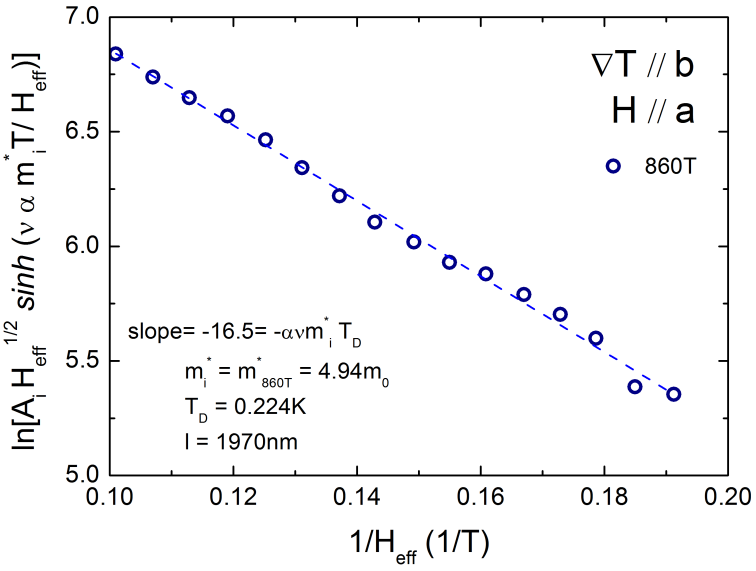

Figure 4.15: *Dingle temperature plot obtained from isothermal thermopower measurements at* $190mK$ *for the* $860\,T$ *branch of the Fermi surface of* UGe_2*. The corresponding Dingle temperature is* $224mK$ *with a mean free path of* 1970Å*.*

a consequence, we demonstrate that dHvA sample and thermopower quantum oscillations sample have similar quality. Therefore, the analysis performed about the comparison between dHvA and thermopower quantum oscillations is valid.

T_D and l of the FM2 phase		
orbit	T_D (K)	l (Å)
20		
85	1.1 ± 0.2	550 ± 80
119	0.90 ± 0.06	830 ± 50
160	0.30 ± 0.02	1500 ± 100
244		
265		
456	0.095 ± 0.002	4280 ± 70
707	0.14 ± 0.01	2600 ± 200
860	0.224 ± 0.004	1970 ± 40
1235	1.09 ± 0.09	1010 ± 80

Table 4.3: *List of Dingle temperatures and the mean free pahts of the detected orbits of the FM2 Fermi surface of* UGe_2 *obtained by thermopower quantum oscillations. No* T_D *and* l *were determined for* $244\,T$ *and* $265\,T$ *orbits as they collapses in one single orbit with increasing field (see Fig.4.14).*

4.6.2 Shubnikov-de Haas Effect

We compare Shubnikov-de Haas SdH effect to thermopower quantum oscillations. In Fig.4.16 -left, magnetoresistance measurements performed with $j^e//b$ and $H//a$ on the same sample as thermopower are shown. We notice the huge magnetoresistance behaviour of this sample. This goes with the high scattering rate because of the high sample quality. As a consequence, the background is quite strong and the SdH effect is not directly visible unlike for the thermopower quantum oscillations. The background of SdH measurements is fitted by a polynomial fit. In the right part of Fig.4.16, we show the amplitude of the oscillations, $\rho - \rho_0$, in the $[50-500]$mK temperature range. We note that the vanishing of the amplitude of the oscillations was estimated at $T \sim 700$mK.

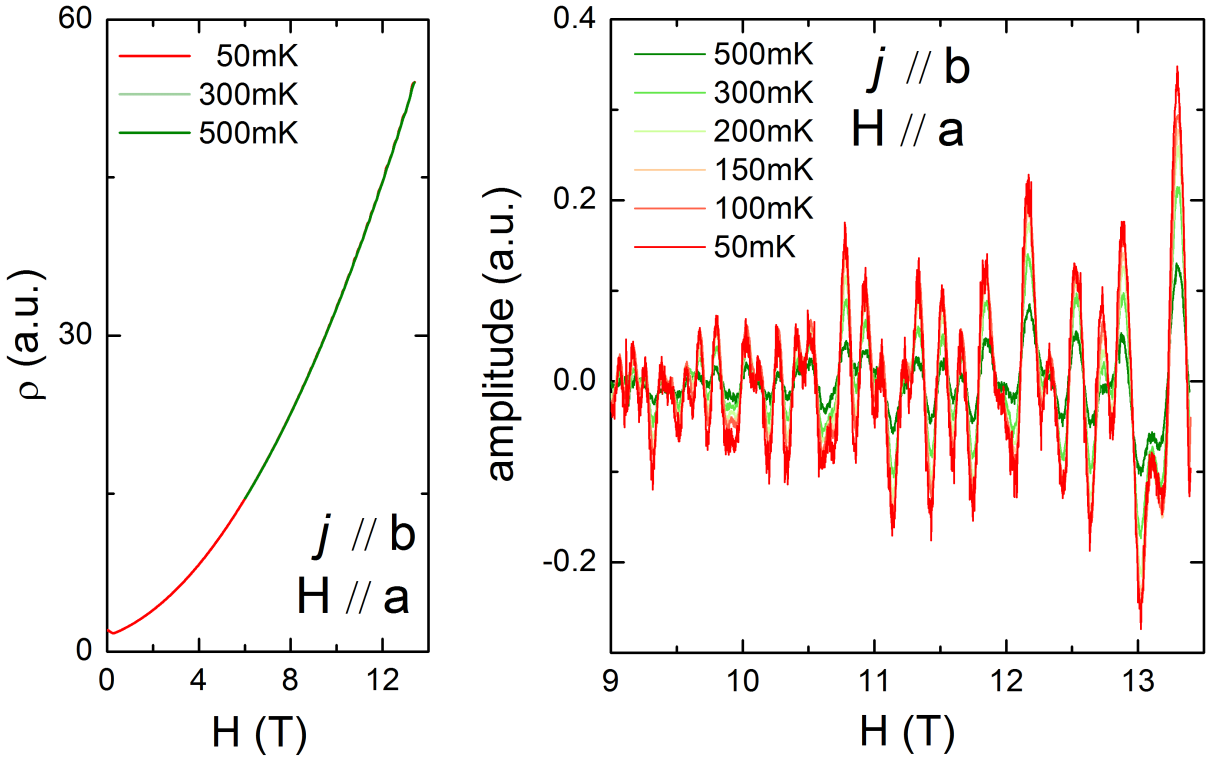

Figure 4.16: *Magnetoresistance measurements $\rho(H)$ at different temperatures with electrical current and magnetic field applied along the b- and a-axis, respectively (left graph). Isotermal $\rho(H) - \rho_0(H)$ dependency at different temperatures (right graph).*

The frequencies and the cyclotron masses obtained from SdH effect were calculated for $[6-10]$T and $[8-13.4]$T FFT windows following the equations of the LK-theory. The obtained values are listed in Table 4.4.

Thermopower and SdH comparison reveals that the measured frequencies by SdH effect are slightly different from those determined by thermopower quantum oscillations. This shift in the frequency values may come from a different tilt between the orientation of the a-axis of the crystal lattice and the external magnetic field. Both, thermopower and SdH measurements present a tilt and it is smaller than 10°.

The comparison between thermopower quantum oscillations and SdH also demonstrates the following features:

Cyclotron masses of the FM2 phase		
orbit (T)	$m^*(m_0)$ $[6-10]$T	$m^*(m_0)$ $[8-13.4]$T
185	3.5	3.1
236	3.3	3.3
284	4.0	4.0
453	3.7	3.9
671	5.0	5.9
855	4.8	5.4

Table 4.4: *List of cyclotron masses obtained for the FM2 phase of the Fermi surface of UGe_2 by SdH technique.*

- The oscillatory component of thermopower dominates the signal, thus thermopower quantum oscillations was directly observed. In the case of SdH, ρ dominates which causes that the amplitude of SdH oscillations were only observed after removing the background.

- Thermopower is able to observe more frequencies than SdH and to follow easily higher harmonics and frequencies as demonstrated in [Trodahl and Blatt, 1969].

- Thermopower follows quantum oscillations at higher temperatures than SdH effect did. In thermopower, there were still quantum oscillations at 2K while in the SdH they disappeared around 700mK as we observe from Figs.4.10 and 4.16, respectively.

- Thermopower presents limitations in the low temperature regime. The lowest temperature reached is $\sim$ 200mK which limits the study of the heaviest bands.

- Concerning the precision of the measurements, we evaluate two ratios: (i) the amplitude of the oscillations over the noise level and (ii) the amplitude of the oscillations over the signal at the lowest temperature and the highest field. Thermopower is characterized by a noise level of the order of nV, an amplitude of the oscillations of $0.35\mu VK^{-1}$, thus by a first ratio of 350. SdH presents a noise level of the order of $10^{-5}m\Omega cm$ and oscillations with amplitude $0.2\mu\Omega cm$ giving 20 for the first ratio. The signal in thermopower is $0.04\mu VK^{-1}$ and in SdH, it is $50\mu\Omega cm$, then the second ratio is 9 and 0.004 for thermopower and SdH effect, respectively. We conclude that the oscillatory part dominates the Seebeck measurements whereas the magnetoresistance dominates in SdH and a higher precision for thermopower quantum oscillations.

- LK-theory can be applied for thermopower quantum oscillations and SdH effect. We obtained similar values of m^* for most of the orbits in similar temperature and field conditions.

The comparison demonstrates the effectiveness of thermopower as a probe to determine the Fermi Surface of a heavy fermion system and the validity of the LK-theory to determine the parameters of the Fermi surface by thermopower quantum oscillations technique.

4.7 Discussion and Conclusions

Thermopower Quantum Oscillations against Traditional Probes

A full comparison between thermopower quantum oscillations, SdH and dHvA effects will be carried in this section. The idea is to prove that thermopower quantum oscillations can be use as a new probe of the Fermi surface in heavy fermion systems. We also highlight the advantages and disadvantages of this technique.

For this analysis, we compare the number of the detected orbits and their frequency values and their corresponding cyclotron mass. The orbits detected by these previous 3 techniques and their corresponding effective masses are shown in Table 4.5. The dHvA data were taken from refs. [Haga et al., 2002, Satoh et al., 1992, Terashima et al., 2002].

	Thermopower		SdH		dHvA	
	freq (T)	$m^*(m_0)$	freq (T)	$m^*(m_0)$	freq (T)	$m^*(m_0)$
	20	1.0			35	
ε	85	1.1			86	~ 1
f or ζ	119	1.8			117	1.4
2ε	165	2.2/2				
2ζ	244	3.4/2	185	3.1	220	
e or η	265	3.6	236	3.3	246	3.0
			284	4.0		
					388	3.1
d or θ	456	4.0	453	3.9	448	3.9
					573	9.7
b or ι	707	5.5	671	5.0	661	4.0
	800	> 8.5				
a or κ	860	5.0	855	4.8	852	4.8
c					980	5.3
	1235	2.4				
					1300	9.2
					1550	

Table 4.5: *Frequencies and cyclotron masses of the FM2 Fermi surface of UGe_2 obtained by thermopower quantum oscillations, SdH and dHvA effects. DHvA data taken from ([Haga et al., 2002, Satoh et al., 1992, Terashima et al., 2002]).*

First, we analyze the detected orbits. Thermopower observe the main bands and the second harmonic of ϵ and ζ orbits (see Table 4.5). Thermopower technique determines higher frequencies than SdH and dHvA with the exception of 244T and 1235T orbits. This is in agreement with the fact that the a-crystallographic direction of the sample was tilted with a higher angle respect to the external magnetic field.

The second aspect concerns the effective masses m^* of the orbits. All of them were obtained from LK-theory. The m^* values are exactly the same for the main branches (η, θ and κ). Nevertheless, for the secondary orbits, thermopower m^* values are slightly higher than m^* values obtained by SdH and dHvA effects (see Table 4.5).

The advantages of thermopower quantum oscillations over SdH and dHvA effects are: (i) the oscillations persist for temperatures up to one order of magnitude higher than for SdH and dHvA effects; (ii) no background need to be removed to observe the thermopower quantum oscillations as the amplitude of the oscillatory component of thermopower dominates the signal and (iii) thermopower quantum oscillations is more sensitive to higher frequencies and harmonics.

The disadvantages of thermopower quantum oscillation technique can be summed up as: (i) the lowest temperature in which the measurements can be performed will be all the time higher than the bath temperature and (ii) accordingly to the first disadvantage, we may not detect orbits with high m^*. The heaviest orbits could not be observed by thermopower quantum oscillation technique.

We point out the high sensitivity of thermopower to analyze the topology of the Fermi surface of a system by the direct measurement of quantum oscillations. The comparison between thermopower quantum oscillations, SdH and dHvA techniques demonstrate that LK-theory can be used by these three probes to analyze the cyclotron mass, the Dingle temperature and the mean free path of the Fermi surface even though the origin of these quantum oscillations is different. We can use LK-theory for all these three probes because the relative amplitude variation of the oscillations with temperature follows the same behaviour.

Finally, we may conclude that the suppression of the amplitude of the orbits with temperature might be considered as an universal characteristic. We have observed that the amplitude evolves with the same ratio independently of the physical origin of the oscillations in a first approximation. For that reason, we could apply LK-theory in the three different probes to study the characteristics of the topology of the Fermi surface of the system.

Topology of the Fermi Surface

The orbits determined by thermopower quantum oscillations are in good agreement with the bands detected by dHvA. Calculations of the topology of the Fermi surface of UGe_2 agree with the orbits detected by dHvA effect, therefore, we can also say that the orbits obtained by thermopower are also in good agreement with the band structure calculations [Settai et al., 2002, Samsel-Czekała et al., 2011]. In addition, we notice that isothemal thermopower measurements $S(H)$ has a positive value of thermopower, then we suggest that hole character of the bands predominates in thermopower. Finally, small and high frequencies were obtained. Then, our thermopower results are in agreement with the given Fermi surface descriptions of Fig.4.4.

The itinerant character of the magnetism of the system was also detected by thermopower quantum oscillations technique. We measured large bands and bands with relative large cyclotron masses. The highest cyclotron mass was observed for the orbit 800T with a value of $m^*_{800T} > 8.5m_0$. This suggests that UGe_2 presents itinerant magnetism with strongly correlations.

Thermopower Quantum Oscillations Ansazts

Overestimated cyclotron masses m^* were obtained for thermopower quantum oscillations than for SdH or dHvA effects although these three probes determined this parameter using the

same theory, LK-theory. We suggest that one possibility of this enhancement of the mass can be related with the different FFT window size. If now, we compare between the different thermopower quantum oscillations ansazts, we note that Peschanskii model determines, in the same conditions as LK-theory, slightly lower values of m^*.

Concerning thermopower quantum oscillations ansazts, we conclude that more effort has to be done to obtain a complete description of the Fermi surface from a point of view of thermopower quantum oscillations, notably in the case of heavy fermion systems. To my knowledge, no theory is able to completely analyze this behaviour at the present moment.

Chapter 5

Thermopower Measurements of $CeRh_2Si_2$

In this chapter, we present the field and pressure thermoelectric studies on $CeRh_2Si_2$. The first part of this chapter concerns the high field dependence of the thermoelectric power and the second part shows the thermoelectric response under high pressure. At ambient pressure, the temperature and field evolution of the Fermi surface modifications at the magnetic transitions will be analyzed. The (T, P) phase diagram was determined and a direct observation of the microscopic properties of the system was possible. To complete the at ambient pressure study, a comparison with other probes, such as magnetoresistance and magnetostriction, is presented. Under pressure, the suppression of the antiferromagnetic order to the paramagnetic state of $CeRh_2Si_2$ has been followed precisely, with special attention around the quantum critical point at P_c. We conclude the modifications on thermopower measurements match to the Fermi surface changes observed under pressure by the dHvA effect.

5.1 Context and Motivation

The study of the Ce family compounds revealed that for Ce systems with the same lattice structure the trivalent configuration is stable at large volumes of the lattice (or low pressures) since the valence mixing occurs between Ce^{3+} and Ce^{4+} at high pressure. Long range magnetic order is expected when the occupation number n_f of the trivalent configuration approaches. Heavy fermion behaviour appears in those systems where the valence of the Ce ion is slightly higher than 3, i.e. the occupation number of the trivalent configuration is slightly lower than one [Knebel et al., 2006, Boursier et al., 2008].

Ce systems with stoichiometry CeM_2Si_2, M=Cu, Ru, Rh, Pd or Au, are characterized by covering the entire range of Doniach's phase diagram from a dominant RKKY interaction to a dominant Kondo screening, e.g. from weak to strong hybridized $4f$ electrons. These systems present a $ThCr_2Si_2$ tetragonal structure and some of them show a magnetic order ground state that can be driven to a magnetic instability by applying pressure or magnetic field.

In the compensated system $CeRh_2Si_2$, the hybridization of the $4f$ bands with the s, p, d bands is close to the intersection of the temperature scales of the RKKY and Kondo interactions of the Doniach phase diagram [Abe et al., 1999]. For that reason, $CeRh_2Si_2$ can be easily driven to the quantum phase transition and magnetic instabilities by pressure and magnetic fields [Willers et al., 2012, Graf et al., 1997, Kawarazaki et al., 2000, Araki et al., 2002]. The easy access to tune the balance between dominant RRKY and dominant Kondo effects in $CeRh_2Si_2$ means that this compound is a good candidate to study quantum criticality. Field and pressure destroy the antiferromagnetic (AF) domain to non-ordered phases (see Fig.5.1). Transitions under field have been identified as a second order transitions for $T > 20$K and below this temperature as a first order metamagnetic transitions. Under pressure, the transition for $P < P_c$ is second order, and around P_c, the nature of the transition may change to first order. However, it is not clear due to the influence of the superconducting domain that appears at pressures close to P_c.

The Fermi surface (FS) of $CeRh_2Si_2$ show strong modifications at the field and pressure magnetic transitions as they are first order. In the case of the annihilation of the AF order state by pressure into a paramagnetic (PM) phase, a discontinuous modification in the FS is expected. The reasons are that the Brillouin zone changes and the localized to itinerant electron behaviour appears. Under field at $P = 0$, the modifications in the FS appear when the system is polarized. This is in agreement with the strong first order transition that shows $CeRh_2Si_2$ when moves from the AF phase into the polarized paramagnetic (PPM) phase. For $P > P_c$, then the transition between the PM and the PPM phase appears under high magnetic field. This transition, a crossover, is spread from $H_c^* = 42$T and follows the H_m line (with $H_c^* < H_m$). No strong modifications of the FS at H_m are expected, thus the FS of the PPM phase must be close to the FS of the PM phase.

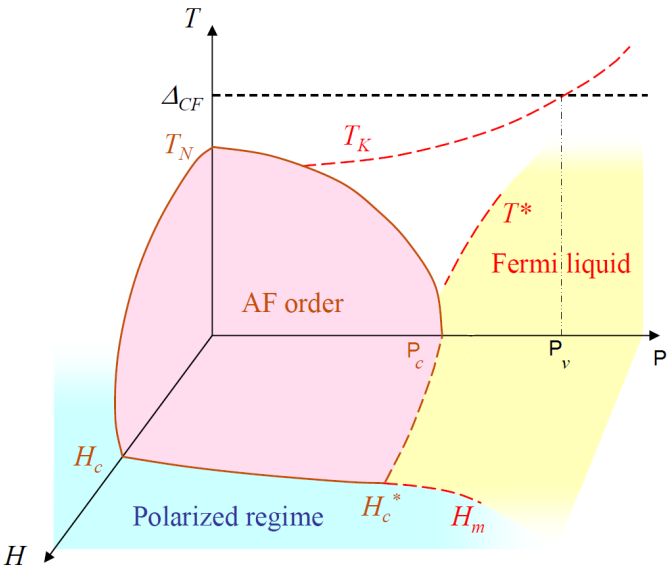

Figure 5.1: *Schematic (T, P, H) phase diagram of $CeRh_2Si_2$ taken from ref. [Knafo et al., 2010]. The suppression of the AF order by pressure and magnetic field yields to a Fermi liquid and a Polarized paramagnetic regimes, respectively. The nature of the transition between these two phases at H_m is still under debate.*

Our study is an attempt to analyze the transitions from the AF order to the non-ordered states induced by pressure and by magnetic field in $CeRh_2Si_2$. Measurements under magnetic field and under pressure were performed to study the signature of the suppression of the AF order by these tuning parameters in the thermopower signal. The purposes of these studies are, first, to understand the magnetic and pressure instabilities at the suppression of the AF phase and second, to analyze the conversion of the PM phase into PPM phase both from a thermopower point of view.

There are a few number of studies that can be comparable to the one presented in this thesis. An example is the study of transport properties of $CeRu_2Ge_2$ under high magnetic fields [Wilhelm and Jaccard, 2004, Wilhelm et al., 2005].

5.2 Introduction to $CeRh_2Si_2$

$CeRh_2Si_2$ orders antiferromagnetically at the Neel temperature, T_N, of 37K which is followed by a second magnetic transition at 25K. This transition corresponds to the transition between two AF phases. The AF phase seems to be a robust characteristic of this compound which points toward the presence of strong RKKY interactions in the AF phase. High magnetic fields modify drastically the electronic parameters whereas 10kbars of pressure are enough to suppress the ordered state [Araki et al., 2001].

The magnetization at the ground state of this compound is Ising like. The c-axis is the easy axis of the lattice. The ground state is characterized by the larger contribution of $J_z = |5/2>$ than $J_z = |3/2>$ states. This has been demonstrated by X-ray Absorption Spectroscopy (XAS) measurements [Willers et al., 2012]. Moreover, there are large differences between the magnetic moment measured by XAS ($\mu = 0.53\mu_B$), Nuclear Magnetic Resonance (NMR)

measurements ($\mu = 0.3\mu_B$) and neutron diffraction ($\mu \sim 1.7-2.4\mu_B$) pointing out the dynamic nature of the f electrons. These differences are due to the different time scale to determine the magnetic moments from these techniques [Willers et al., 2012, Kawarazaki et al., 2000]. In all the analysis a reduced moment was observed. This is consistent with partial Kondo-like spin compensation of the Ce^{+3} moment [Severing et al., 1989].

In Fig.5.2, the schematic (T, H) and (T, P) phase diagrams of $CeRh_2Si_2$ are presented on the left and right figures, respectively. The solid lines represent first order transitions while the dashed lines represent second order transitions. The dotted line in the (T, P) phase diagram represents the superconducting domain that appears under pressure at $P \sim P_c$.

The (T, H) phase diagram is characterized by the AF ground state which is suppressed by high magnetic fields applied along the c-axis (see Fig.5.2 (left)). The AF phase develops at $T_N = 36$K at $H = 0$T through a second order transition from the PM to the AF_1 phase. At lower temperature, a second transition is observed between the AF_1 and the AF_2 states at $T_{AF_1-AF_2} = 25$K which is a first order transition between two AF phases. These AF phases are characterized by the following AF vectors detected by neutrons. AF_1 presents the AF vector $q_1 = (1/2, 1/2, 0)$ and the AF_2 is characterized by two AF vectors; q_1 of the AF_1 phase and $q_2 = (1/2, 1/2, 1/2)$. The appearance of this second AF vector in the AF_2 phase is related to the appearance of two different values of the atomic magnetic moments in the lattice [Kawarazaki et al., 2000]. T_N and $T_{AF_1-AF_2}$ decrease slowly with the magnetic field. Above $H_{TCP} = 24.5$T, T_N is divided into two first order lines, T_{2-3} and T_{3-PM} which define a new AF domain, AF_3. T_{3-PM} line can be considered as a prolongation of the second order T_N line that becomes a first order line at TCP. For magnetic fields above H_{TCP}, the H_{2-3} and the $H_{3-PM} = H_c$ lines show a strong decrease reaching zero ($T \to 0$) at $H_{2-3} = 25.5$T and $H_c = 26.2$T [Knafo et al., 2010].

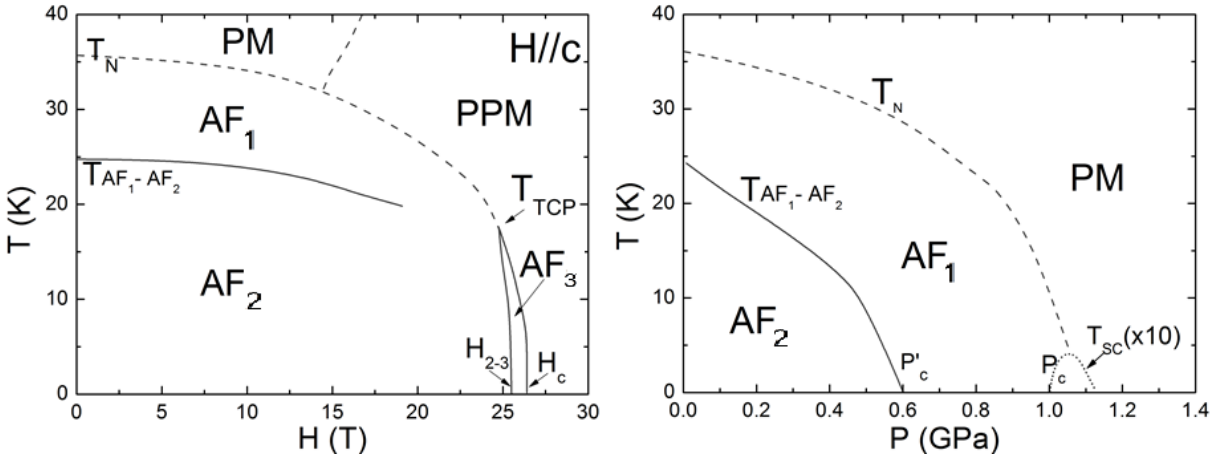

Figure 5.2: *(T, H) and (T, P) phase diagrams of $CeRh_2Si_2$ on the letf and on the right, respectively.*

As shown in the (T, H) phase diagram, at low temperature, the suppression of the AF phase is produced in a two step transition. Magnetization measurements in static field show that this two step transition is characterized by the reduction of the magnetic moment to the half of its initial value for the AF_2-AF_3 transition and the second-half of the magnetic moment vanishes at the AF_3 to the PPM transition, H_c [Abe et al., 1997]. Thermal expansion and magnetostriction measurements show an elongation of the lattice of $CeRh_2Si_2$ along the

c-axis at the same magnetic field values (the dilation along the a-axis is much smaller than the one along the c-axis) [Araki et al., 1998]. This elongation of the lattice along the c-axis supports the reduction of the magnetic moments in $CeRh_2Si_2$ because it is associated to a decrease of the hybridization between the Ce atoms. Resistivity measurements observed the suppression of the AF order into a PPM phase which is characterized by a strong drop of magnetoresistance. This drop and the analysis of the A coefficient demonstrate that this transition seems to be characterized by a Fermi surface change driven by the collapse of the antiferromagnetic fluctuations and the enhancement of the low-energy ferromagnetic ones. These ferromagnetic fluctuations are responsible for the increase of the effective mass of the quasi-particles at the transition [Knafo et al., 2010].

The (T, P) phase diagram shown in Fig.5.2 (right), corresponds to the pressure evolution of the AF ground state of $CeRh_2Si_2$. T_N and $T_{AF_1-AF_2}$ transitions, defined at $P = 0$ and $H = 0$ conditions, are also suppressed by pressure. The $T_{AF_1-AF_2}$ line ends up at $P_c^{'} \sim 0.5$GPa and the T_N line ends at $P_c \sim 1.03$GPa. The quantum phase transition at P_c is hidden by the superconducting domain that appears in this pressure range. The superconducting domain reaches its maximum temperature ($T_{SC} = 400$mK) at P_c. Therefore, the nature of this AF_1-PM second order transition inside the bulk superconductivity, in the vicinity of P_c, is not clear [Araki et al., 2002, Araki et al., 2003]. The coincidence of the maximum of T_{SC} and P_c suggests that magnetic fluctuations may play an important role in the superconducting pairing [Movshovich et al., 1996].

Neutron diffraction measurements indicated that the AF phase of $CeRh_2Si_2$ is characterized by an itinerant behaviour supported by the evidence that the magnitude of the saturated ordered moment is proportional to the transition temperature up to pressures close to P_c; i.e., $T_N \sim M$ with M the magnetic moment. This is rather unexpected in this compound because its high T_N should involve well localized magnetic moments [Kawarazaki et al., 2000]. At pressures close to P_c, a strong deviation from this linear behaviour is observed. Then, the system undergoes two different electronic states: the low-pressure state (proportionality of the magnetic moment and T_N) and the critical-pressure state. This analysis seems to be in contradiction to other probes such as dHvA effect. dHvA relates the modifications of the system from a localized behaviour at low pressures to an itinerant one at higher pressures. We will discuss it in more detail after the Fermi surface description of $CeRh_2Si_2$.

The electronic specific heat increases linearly with pressure from $\gamma|_{P=0} = 23\text{mJK}^{-2}\text{mol}^{-1}$ to $\gamma|_{P_c} = 80\text{mJK}^{-2}\text{mol}^{-1}$ (see Fig.5.3-left). Above P_c, γ decreases slowly with pressure. The slope $\partial\gamma/\partial P$ changes at P_c and it is associated to the balance from RKKY dominance to Kondo dominance above the transition. At low pressures, the redistribution of the magnetic entropy from localized degrees of freedom to Kondo-like spin fluctuations in combination with the suppression of the internal magnetic field through the Kondo effect produces an increase of the γ. As pressure increases and reaches values close to P_c, the interactions shift in favor of increasing dominance of Kondo-spin compensation of the localized $4f$ moments and induce the redistribution of the magnetic entropy, both to higher temperatures and from localized degrees of freedom to Kondo-like spin fluctuations. Above P_c, γ decreases as in non-ordering heavy fermion compounds [Graf et al., 1997, Araki et al., 2002]. This behaviour has also been observed in the A coefficient of the resistivity measurements ($\rho = \rho_0 + AT^2$) see Fig. 5.3 [Graf et al., 1998, Araki et al., 2002].

Thermal expansion under pressure demonstrated that the suppression of the AF order is

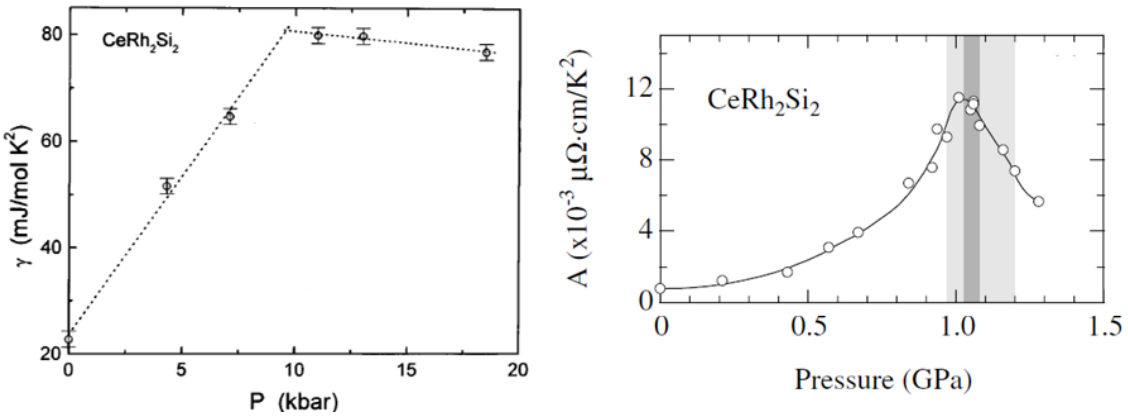

Figure 5.3: *Specific heat [Graf et al., 1997] and A coeffiecient [Araki et al., 2002] of $CeRh_2Si_2$ as a function of pressure.*

related to the increase of the α_a/α_c ratio from 0.2 at ambient pressure to 1 at P_c, with α the thermal expansion coefficient along the a- and c-axis. Pressure increases the hybridization of the $4f$ electrons with the other light electrons (s, p, d) driving the system from a localized $4f$ behaviour to an itinerant one. At pressures close to P_c, a clear volume discontinuity was detected. The suppression of the ordered state with pressure does not follow the laws for antiferromagnetic fluctuation theories [Villaume et al., 2008].

The Fermi surface of $CeRh_2Si_2$ has been determined by dHvA effect at ambient pressure [Abe et al., 1998, Araki et al., 2001] and under high pressure [Settai et al., 2003] conditions. The angle- and the pressure- dependencies of the dHvA frequencies are shown in Fig.5.4. In the low field AF state, quantum oscillations of $CeRh_2Si_2$ correspond to the frequencies calculated for $LaRh_2Si_2$ based on the $4f$ localized model. This suggests that $CeRh_2Si_2$ present a localized behavior in the AF phase and has a multiple connected Fermi surfaces. At high fields, the Fermi surface with H||c was measured in the AF_2 phase. The analysis of the AF_3 phase, due to the narrow magnetic field window, was impossible. Finally, the PPM phase shows an unique frequency at 16kT with high cyclotron mass (frequency only visible at $T < 50$mK) [Sheikin, 2013]. Under pressure, dHvA effect shows modifications of the Fermi surface at $P_c^{'}$ and P_c. The changes related to $P_c^{'}$ corresponds to the change of the AF structure between the AF_1 and AF_2 phases. At P_c the topology of the Fermi surface changes discontinuously from localized to itinerant behaviour [Araki et al., 2001, Settai et al., 2003]. The strong change of the Fermi surface is coherent with the increases of hybridization. The system presents a balance from dominant RKKY interactions to dominant Kondo screening as a consequence of the delocalization of the extra electron of $CeRh_2Si_2$ compared to $LaRh_2Si_2$ into the conduction Fermi surface. The delocalization presents strong correlations as the cyclotron mass of the PM phase are of the order of $m^* \sim 20 - 30m_0$. Finally, none of the frequencies of the PM phase correspond to the unique measured frequency in the PPM phase; therefore, the Fermi surfaces of the PPM and PM phases should be similar but, not exactly the same.

In [Miyake and Ikeda, 2006], the "localized" to "itinerant" duality observed by dHvA effect is explained from a point of view of the Fermi liquid behaviour. Authors clarify that the f-electrons of heavy fermion systems are never localized and remains in a metallic state. The localized point of view corresponds to the localized regime when the f electrons do not

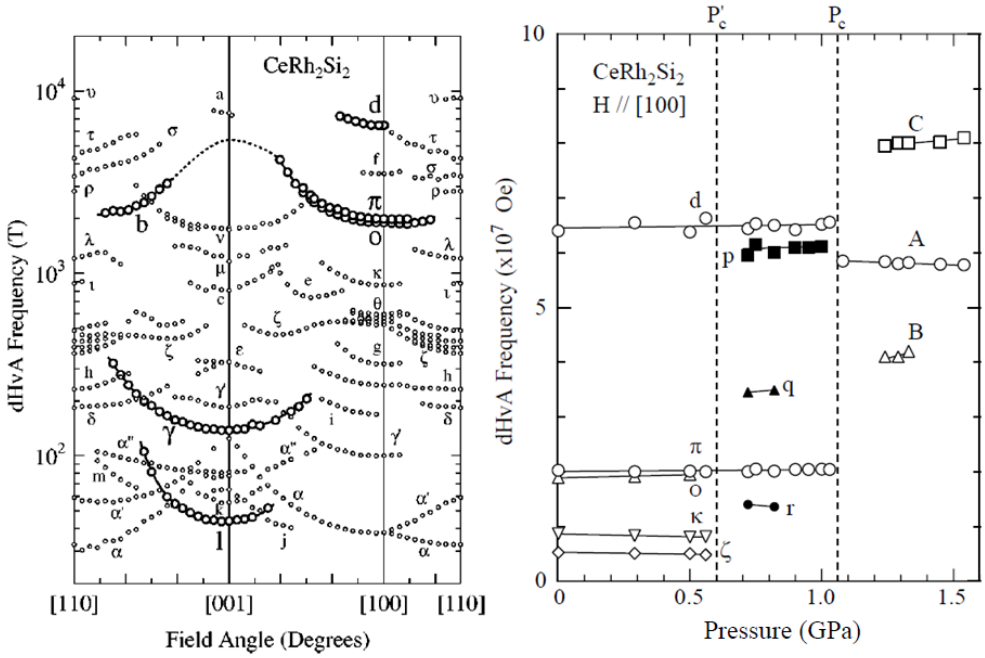

Figure 5.4: *Angular- (left) and pressure- (right) dependence of the dHvA frequencies of $CeRh_2Si_2$ [Araki et al., 2001, Settai et al., 2003].*

contribute to the Fermi surface and it corresponds exactly to the loss of one f electron per Ce ion. In this case, the Fermi surface measured by dHvA corresponds ideally to the Fermi surface of the PM ground state of the $LaRh_2Si_2$ compound, which has a small Fermi surface. As field or pressure increases, the f electrons start to participate in transport characteristics of the system. Thus, a large Fermi surface associated with the itinerant character is detected. The system shows a transition between the uncompensated metallic character of $LaRh_2Si_2$ to the compensated one of $CeRh_2Si_2$ system. The duality "localized" to "itinerant" is related to a drastic change of the Fermi surface. This theory also treats the character of the transition at P_c and it indicates that a gradual vanishing to the AF order should not entail strong modifications on the Fermi surface, then the Fermi surface of AF and PM phases are expected to be essentially the same. Nevertheless, dHvA measurements [Araki et al., 2002] in $CeRh_2Si_2$ demonstrated a strong Fermi surface reconstruction at P_c. This phenomenon is discussed by the previous theory as an unconventional quantum critical point due to a local valence scenario. They claim that if a *pseudo*-valance transition appears at P_c, it must be characterized by an abrupt increase of the Kondo temperature (energy scale) from the value of the Kondo limit to the intermediate valence state. Then, the observed signature of this behaviour will be the drastic decrease of the Kadowaki-Woods ratio. This behaviour is observed for $CeRh_2Si_2$ (see Fig.5.5), then a *pseudo*-valance transition appears at P_c for this compound.

The "localized" to "itinerant" duality analyzed by [Hoshino and Kuramoto, 2013] is controlled by the sign and magnitude of the exchange between the magnetic moments. They also demonstrate that the transition from "localized" to "itinerant" behaviours at the QCP can also occur inside the AF order. This transition requires a strong symmetry at both sides of the transition and nearly flat bands below and above it. Indeed, it occurs only if the Kondo temperature exceeds the Heisenberg interaction.

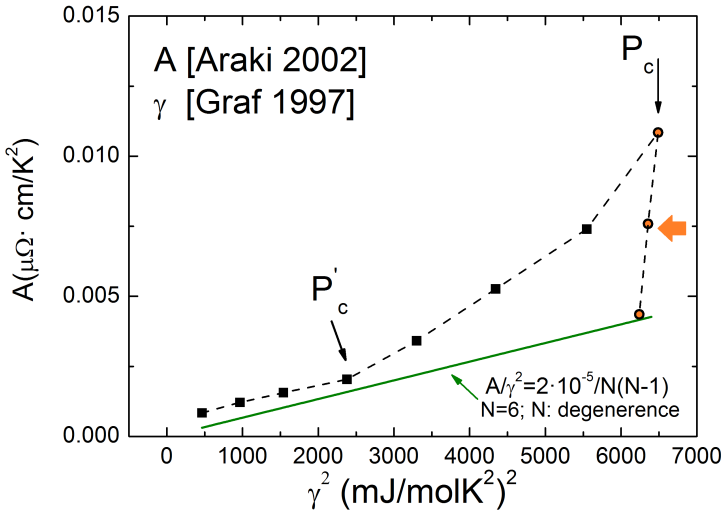

Figure 5.5: *Kadowaki-Woods ratio obtained from the γ and the A coefficient shown in Fig.5.3. A strong decrease is observed above the critical pressure P_c (orange circles).*

Finally, we notice that $\gamma(H_c, P = 0)$ and $\gamma(H = 0, P_c)$ are comparable. This indicates that the mechanisms which control the magnetic field and the pressure enhancements of the γ value may be linked as proposed the comparison of A/A_{max} as a function of $P - P_c/P_c$ and $H - H_c/H_c$ (see Figs.9 and 11 of ref. [Knafo et al., 2010]).

5.3 Quality Samples and Measuring Configurations

Single crystals of $CeRh_2Si_2$ were grown by the Czochralski method in a tetra-arc furnace. The samples were cut by spark cutter and oriented by X-ray Laue diffractometer displaying very sharp spots.

For the ambient pressure study, two bar-shaped samples from the same single crystal, with sizes around $2.8 \times 0.8 \times 0.4$mm, were cut. The magnetic field was applied along the c-axis and the thermal gradients along the a-axis and the c-axis defining transverse and longitudinal configurations respectively (see Fig.5.6). Transverse configuration is characterized by measuring the transport properties on the Ce-basal planes while longitudinal configuration measures the transport properties across the Ce-layers. The quality of the samples was evaluated through the RRR coefficient. For transverse configuration, the RRR of the sample was 300 and for longitudinal configuration, it was 30.

Under pressure, for the piston cylinder pressure cell, we performed thermopower measurements on a long-bar shape sample with the long axis along the a-crystallographic axis of $CeRh_2Si_2$. The dimensions of this sample were $2.25 \times 0.70 \times 0.33$mm and the RRR factor was ~ 10. No magnetic field was applied in this configuration. In the case of the Bridgman pressure cell, the sample had a $RRR \sim 10$ and dimensions $1018 \times 160 \times 80\mu$m; the thermal gradient was applied along the a-axis and the magnetic field along the c-axis (transverse configuration). The cross section of the sample for the Bridgman pressure cell was ~ 18

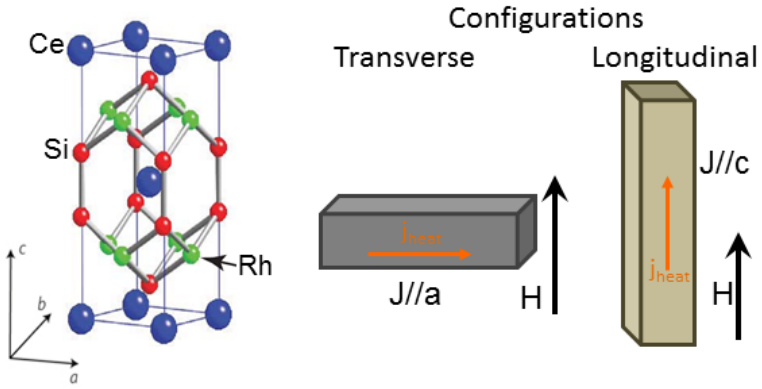

Figure 5.6: *$CeRh_2Si_2$ crystallographic structure is represented on the left figure. Transverse and longitudinal measuring configurations are shown on the middle and on the right figures, respectively.*

times smaller than the cross section of the sample for the piston cylinder cell and ~ 25 times smaller than the cross section of the measured samples at ambient pressure. The length of the Bridgman sample was 2 and 3 times shorter than the length of the piston cylinder and at ambient pressure samples, respectively.

5.4 Temperature Evolution of the Thermoelectric Coefficients at Ambient Pressure

In this section, we discuss the evolution of the Seebeck coefficient of $CeRh_2Si_2$ as a function of temperature at ambient pressure $S(T)$. First, the signature of the Seebeck coefficient is studied following by the analysis of the suppression of the AF domain by magnetic field. After that, a comparison between transverse and longitudinal configurations is carried out which stresses the importance that the orientation of the thermal gradient and the magnetic field has in transport characteristics. To finish the thermopower analysis, a study of the heat carriers at $T \to 0$ at zero magnetic field is done.

The Nernst coefficient is briefly analyzed in this section. First, we discuss the evolution with temperature, and then the evolution under magnetic field at fixed temperature.

5.4.1 The Seebeck Coefficient and the Suppression of the Antiferromagnetic Domain

In Fig.5.7, the temperature evolution of the Seebeck coefficient $S(T)$ for transverse configuration is shown. In black symbols, $S(T)$ at zero magnetic field and in green, $S(T)$ under a magnetic field of $H = 9$T. We analyze $S(T)$ from high to low temperatures and we observed that as temperature decreases, the system orders antiferromagnetically along the c-axis below $T_N = 36$K which corresponds to the PM-AF_1 transition. At lower temperatures, a new configuration of the magnetic moments from the antiferromagnetic state AF_1 to the antiferromagnetic phase AF_2 is observed at $T_{AF_1-AF_2} = 24$K. The transition PM-AF_1 is a second order while the AF_1-AF_2 is a first order transition. AF_1-AF_2 magnetic transition entails strong thermopower modifications; e.g., a strong drop of the Seebeck coefficient and a change of the

sign of the heat carriers. Around $T \sim 10$K, the Seebeck coefficient shows a minimum. This minimum might be related to a coherence temperature of the compound supported by the almost linear behaviour of the Seebeck coefficient when it approaches $S(T)|_{T\to 0} \longrightarrow 0$. Under field, the suppression of the AF order is observed by the shift of T_N and $T_{AF_1-AF_2}$ to lower temperatures. We observe that $T_{AF_1-AF_2}$ and T_N under a magnetic field of 9T are reduced by 1K and $1.5-2$K, respectively. Moreover, the thermopower values increase with magnetic field; i.e., the magnetic field favours the transport by hole like thermopower bands in the temperature and field ranges of the study. $T_{AF_1-AF_2}$ and T_N obtained from $S(T)$ measurements agree with those of the literature as shown in the phase diagram of Fig.5.26 (purple and orange symbols, respectively).

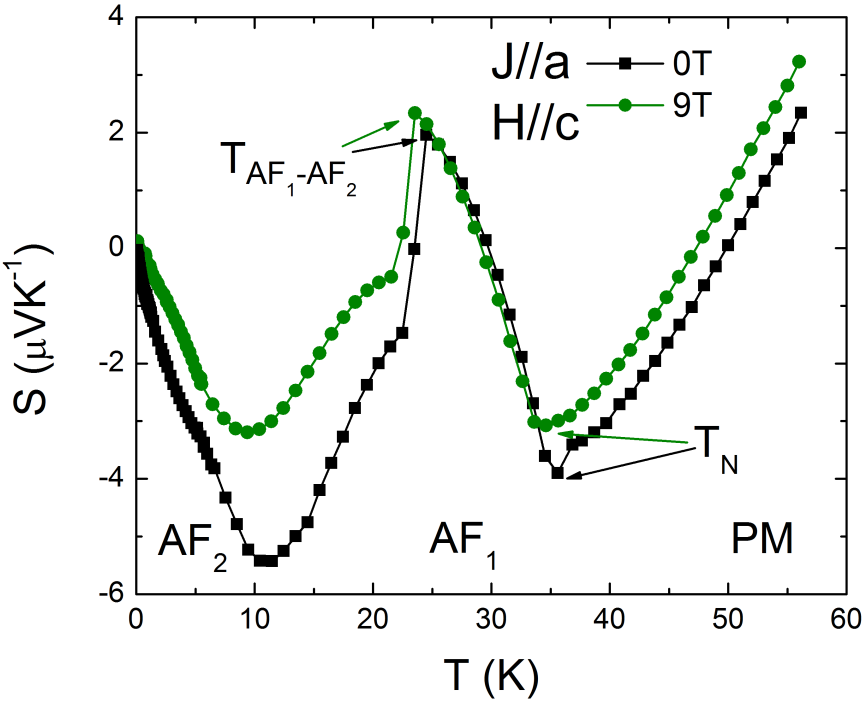

Figure 5.7: *Evolution as a function of temperature of the Seebeck coefficient $S(T)$ at ambient pressure for transverse configuration. The black curve corresponds to $S(T)$ at $H = 0$ and the green one to the evolution of $S(T)$ under a magnetic field of $9T$.*

5.4.2 Heat Carriers in the Low Temperature Regime

The study of the very low temperature regime of the Seebeck coefficient is a key point of the analysis of a system. It reveals information about the nature of the ground state of the system and combining it with other measurements, such as specific heat, we can obtain information about the heat carrier concentration. To achieve these two purposes, we analyze the extrapolation to $T \to 0$ of the Seebeck coefficient as a function of temperature over temperature, $S(T)/T$.

In Fig.5.8, we show $S/T(T)$ in the low temperature regime for transverse (left figure) and longitudinal (right figure) configurations, respectively. The extrapolation of the $S/T(T)$

coefficient to $T = 0$K is represented by the fit (dark red line) as we can observe in the graphs of the figure.

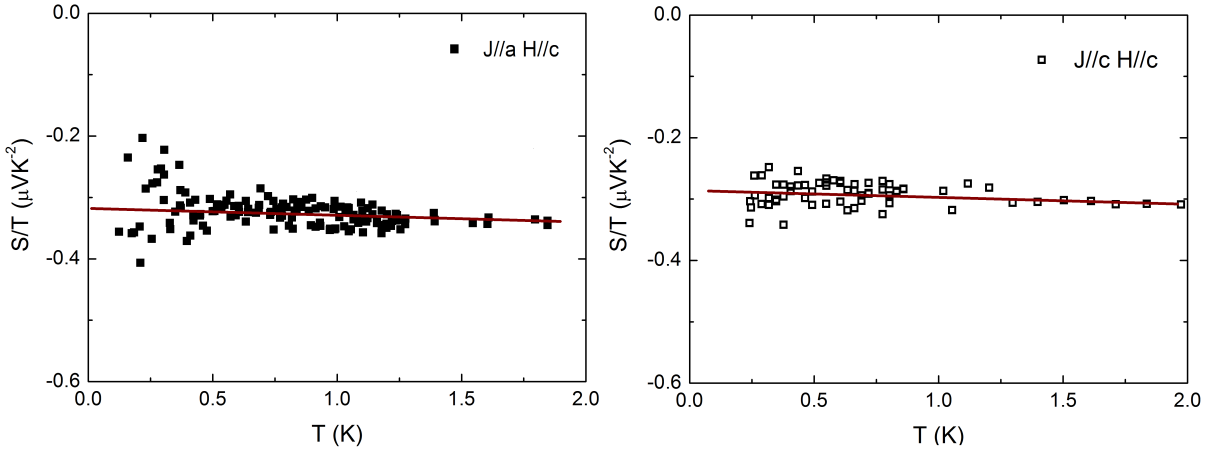

Figure 5.8: *$S/T(T)$ at $H = 0\,T$ and at low temperature for transverse (left panel) and longitudinal (right panel) configurations. The dark red lines indicate the extrapolation of the $S(T)/T|_{T\to 0}$ for each configuration.*

The Seebeck coefficient divided by temperature as a function of temperature shows a nearly constant value of this parameter in the low temperature regime, $S(T)/T \sim cte$. This $S(T)/T$ evolution corresponds to the signature of a Fermi liquid behaviour in the AF domain of $CeRh_2Si_2$. The result is in agreement with resistivity measurements [Araki et al., 2002]. The small slope of the extrapolated line of $S(T)/T$ when $T \to 0$ can be due to a higher error in the measurement of the thermal gradient as we can notice from the increase of the noise of the data points. The reasons are: (i) below 1K, the Seebeck coefficient is lower than -1μVK^{-1} which corresponds to low values of thermopower and (ii) the high quality of the sample which complicates the generation of a significant thermal gradient. These reasons affect the precision of the measurements because low values of $S(T)$ need high thermal gradient to be precisely determined.

The values of the $S/T(T = 0)|_{H=0}$ for transverse and longitudinal configurations are -0.31μVK^{-2} and -0.29μVK^{-2}, respectively. These values of $S/T|_{T=0} \sim 0.3\mu$VK^{-2} are quite similar which means that the heat transport in $CeRh_2Si_2$ is roughly isotropic at $H = 0$T and at low temperature. Moreover, the sign in the ordered phase of $S/T|_{T=0}$ is negative. Then $CeRh_2Si_2$ shows an opposite sign to the normal sing of Ce-based heavy fermion systems at low temperatures.

To calculate the number of heat carriers per formula unit, the inverse of the q-factor is determined. To evaluate the q-factor[1], the electronic specific heat, γ, in the low temperature regime of $CeRh_2Si_2$ was taken from ref. [Graf et al., 1997]. The extrapolated γ at $T = 0$ value is $\gamma = 23$mJmol^{-1}K^{-2}. The q-factor for transverse and longitudinal configurations are $q_{trans} = -1.3$ and $q_{long} = -1.2$. Therefore, the number of heat carriers per formula unit, n, are $n_{trans} = -0.77$ and $n_{long} = -0.82$. These values of $n \sim -0.8$ are close to -1 which means

[1]More information related to the q-factor parameter is shown in sub-subsec. 1.4.4

that $CeRh_2Si_2$ presents an almost classical electronic metallic behaviour from a point of view of a one band model [Behnia et al., 2004].

We point out that we will not carry out the analysis of the evolution of the q-factor under field because the dominance of quantum oscillations on the thermopower signal for $H > 4$T prevents the determination of the average value of thermopower signal at fixed magnetic fields.

5.4.3 Thermopower: Transverse versus Longitudinal Configurations

Thermopower is a directional probe which allows the analysis of the heat transport in a specific configuration. In this subsection, we study the thermopower similarities and differences of longitudinal and transverse configurations.

In Fig.5.9, the Seebeck coefficient as a function of temperature for the transverse (full symbols) and the longitudinal (open symbols) configurations are shown on the left figure. For both configurations, $S(T)|_H$ are represented at $H = 0$T, $H = 3$T and $H = 9$T in black, red and blue symbols, respectively. $CeRh_2Si_2$ is an anisotropic multiband compound at high temperatures. We measured different behaviour of the Seebeck coefficient for transverse and longitudinal configurations due to the fact that the thermopower signal is directional dependent; i.e., the contribution of the bands to the thermopower signal depends on the orientation of the thermal gradient on the lattice cell (the magnetic field was applied along the c-axis for all the measurements).

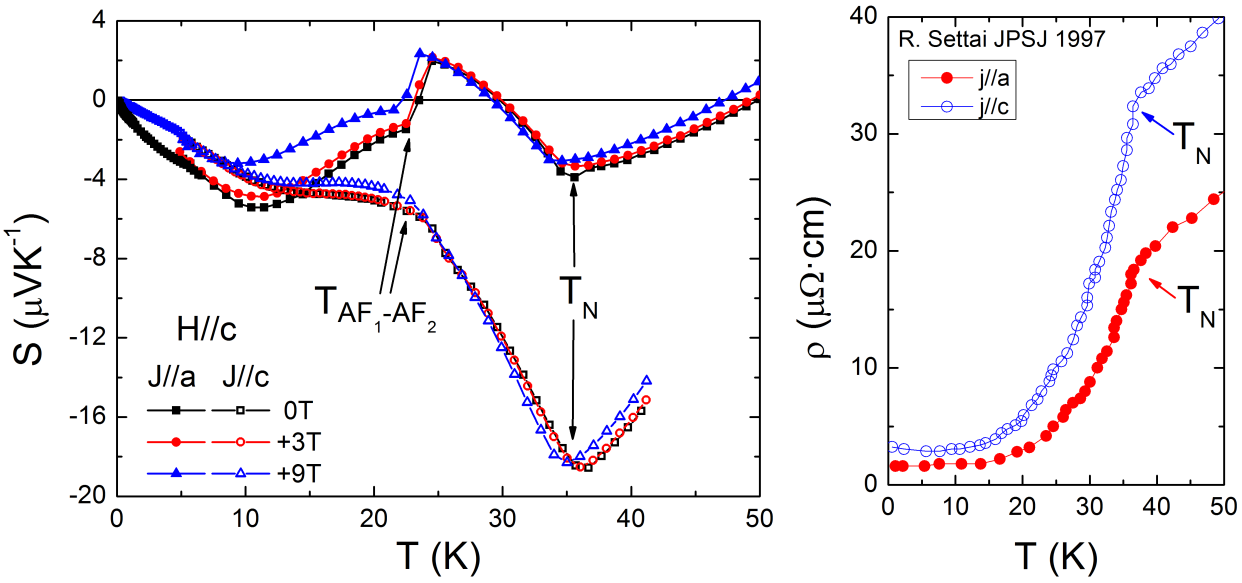

Figure 5.9: *Thermopower as a function of temperature, at different magnetic fields, for transverse and longitudinal configurations shown by full and open symbols, respectively (left figure). Resistivity at zero magnetic field for transverse (red curve) and longitudinal (blue curve) configuration (right figure).*

The major difference of these two studied configurations is the change of the sign of thermopower. The longitudinal configuration never crosses the zero thermopower line in the measured temperature range which means that the average of the bands contributing

to the thermopower in this lattice direction appear electron like. Against this uniform sign behaviour, the thermopower of the transverse configuration crosses the zero thermopower line three times in the $[2-50]$K temperature range. Special attention must be given to AF_1-AF_2 transition in which the sign change of thermopower and the narrow temperature range of the transition verify that this is a first order transition [Graf et al., 1998]. We also observe that the thermopower behaviour at the AF_1-AF_2 transition, for both configurations, is opposite; e.g., thermopower increases at the transition for the transverse configuration whereas it decreases for the longitudinal one.

On the other hand, a large number of similarities exist between the transverse and the longitudinal configurations which most of them are related to the bulk properties of the system: (i) the temperature of the transitions are the same in both configurations and the values of the thermopower are of the same order of magnitude; (ii) we confirm not only the suppression of the ordered state with magnetic field, but also that both configurations have a similar temperature decrease of $T_{AF_1-AF_2}$ and T_N under field; (iii) S/T for $T \to 0$ presents a similar value at low temperatures; (iv) both thermopower configurations show a similar $S(T)$ minimum behaviour around T_N; (v) we notice that the fundamental entropy law, $S(T)|_{T\to 0} \longrightarrow 0$, is certified for both configurations at zero field and under field and we point out that no divergence has been observed for the Seebeck coefficient normalized by temperature, $S(T)/T$, in the low temperature regime. We expect at high temperatures $T \gtrsim 100$K that both configurations join together in a common $S(T)$ behaviour.

In Fig.5.9 (right), resistivity measurements of $CeRh_2Si_2$ are shown for transverse (red curve) and longitudinal (blue curve) configurations. The transition T_N is indicated by arrows; nevertheless, $T_{AF_1-AF_2}$ is not easy to observe in this kind of measurements. We notice the similar temperature evolution with a higher increase of the value of the resistivity for the longitudinal configuration measurements. This is in agreement with the higher thermopower change for the longitudinal configuration than for the transverse one at T_N.

5.4.4 Nernst Coefficient

The Nernst coefficient measures the transverse transport in relation to the thermal gradient and to the magnetic field orientation. The heat carriers measured by the Nernst coefficient are those deviated from the longitudinal path generated by the thermal gradient. As a consequence, only the light mass carriers can be measured. In heavy fermion systems, the Nernst coefficient is a probe to analyze the heat light carriers involved in transpor and it is equivalent to the Hall effect.

In Fig.5.10, the Nernst coefficient as a function of temperature and as a function of magnetic field is shown on the left and on the right graphs respectively. The temperature range of the measurement was $[5-50]$K and the field range was $[0-9]$T. For these conditions, we notice that the Nernst coefficients present low values, lower than $0.1\mu VK^{-1}$ in all the temperature range and fields up to $H = 9$T. For that reason, we could not perform measurements of the Nernst coefficient for $T < 5$K.

From the temperature dependence of the Nernst coefficient $N(T)$ for $H = 3$T and $H = 9T$, blue and red curves of Fig.5.10 -left-, we observe that the minimum of the Nernst coefficient coincides with the temperature of the AF_1-PM transition, $T_N = 36$K. At low temperatures, the Nernst coefficient increases linearly with temperature up to $T = 13$K; we notice that

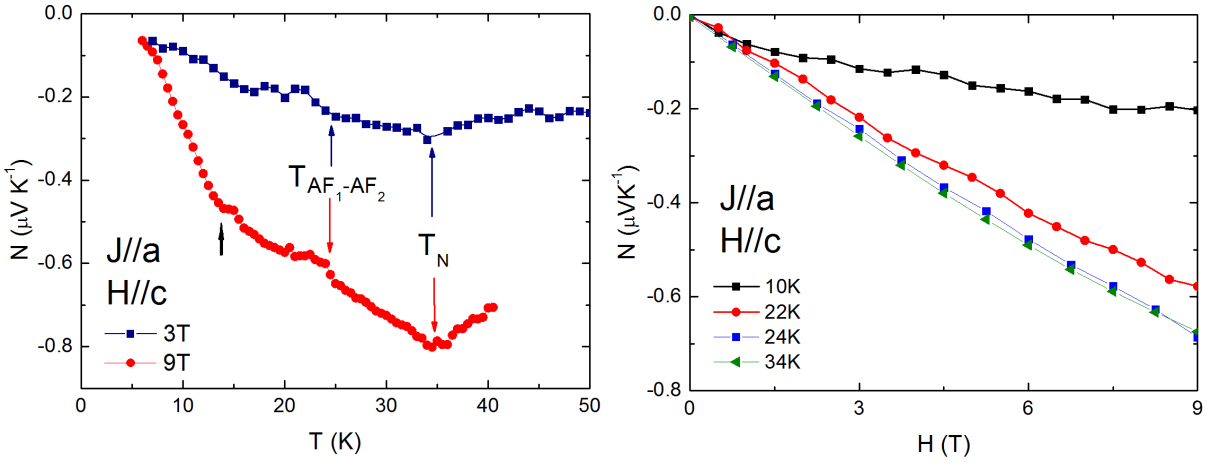

Figure 5.10: *Nernst coefficient of $CeRh_2Si_2$ as a function of temperature (left figure) and as a function of the magnetic field (right figure).*

this temperature is slightly higher than the coherence temperature defined by themopower measurements. Above $T = 13$K, the slope of $N(T)$ decreases and the Nernst coefficient tends to saturate. At $T = 24$K, a sudden jump appears in $N(T)$ which corresponds to the AF_1-AF_2 transition. In the PM phase $N(T)$ increases to 0.

From the Nernst coefficient as a function of magnetic field, we observed an almost linear increase of $N(H)$ for all the temperatures measured. Due to the low applied magnetic fields, we do not see the suppression of the AF order in $N(H)$ measurements at low temperatures. In addition, AF_1-PM phase transition is not observable by $N(H)$ measurements because the modification of the Nernst coefficient associated to this second order transition seems to be smaller than the resolution. We verify that the dependence of the $N(H)$ coincides with the temperature dependence of the Nernst coefficient.

5.5 Thermopower at High Magnetic Fields

The evolution of the thermopower as a function of magnetic field is studied to probe the modifications of the Fermi surface of $CeRh_2Si_2$ through the different phase transitions. For that reason, we performed thermopower measurements under very high magnetic fields at the Laboratoire National de Champs Magnétiques Intenses at Grenoble (LNCMI-Grenoble). The purposes were to determine the variation of the heat carrier concentration through the metamagnetic transitions AF_2-AF_3 and AF_3-PM and to study the topology and the evolution of the Fermi surface in the AF_2, AF_3 and PPM phases. A comparison with previous dHvA measurements completes this study.

5.5.1 Fermi Surface Reconstruction

In the first part of this section, we analyze the isothermal thermopower measurements, $S(H)$, performed at high magnetic fields for transverse and longitudinal configurations. Second, we analyze thermopower quantum oscillations for $CeRh_2Si_2$ and prove the validity of this tech-

nique for this compound. Third, we compare the previous technique to dHvA measurements.

In the second part, we determine the Fermi surface of $CeRh_2Si_2$ *via* the analysis of the spectrum of $S(H)$ measurements. We obtain the orbits of the Fermi surface and afterwards, their evolution with temperature to determine the cyclotron masses of the detected branches of the Fermi surface. Finally, the evolution of the spectrum with the applied effective magnetic field at the lower temperature was analyzed to determine the Dingle temperature and the mean free path of the conduction electrons in the orbits.

Isothermal Thermopower Measurements

Isothermal thermopower measurements in the temperature range of $[0.5-22.5]$K and magnetic field range of $[0-29]$T were studied. In Fig.5.11 and in Fig.5.12, we show $S(H)$ measurements for transverse and longitudinal configurations, respectively.

In the field range corresponding to the AF phase, in the low temperature range, quantum oscillations in the Seebeck coefficient were observed. This oscillatory component of the Seebeck coefficient exists for a very large temperature window $[0-7]$K. The oscillations are visible directly in the signal, no background was removed, and their amplitude increases as temperature decreases. At low temperatures, the amplitude of the oscillations is larger than the absolute value of the Seebeck coefficient. This seems to be in contradiction to the usually entropy law of thermopower that says that $S \to 0$ when the temperature approaches 0. Nevertheless, the temperature range of our measurements does not allow the verification of this assumption because the lowest reached temperature was ~ 480mK.

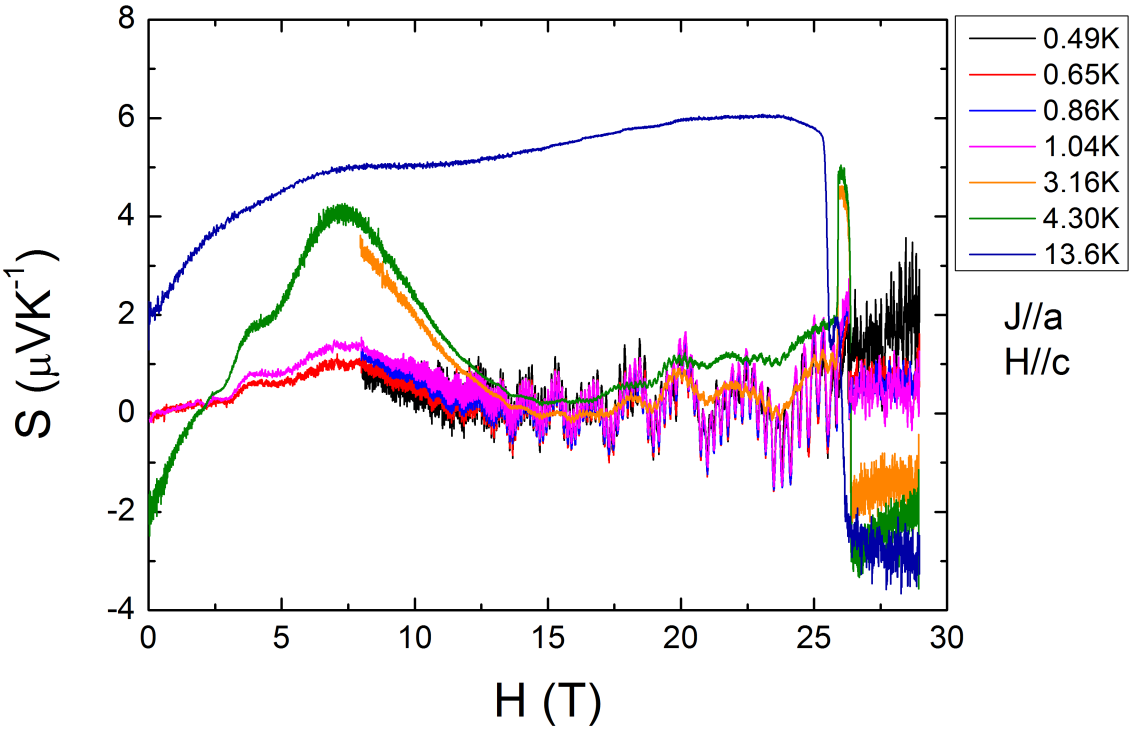

Figure 5.11: *Isothermal thermopower measurements, $S(H)|_{T=ctn}$, at high magnetic fields for the transverse configuration.*

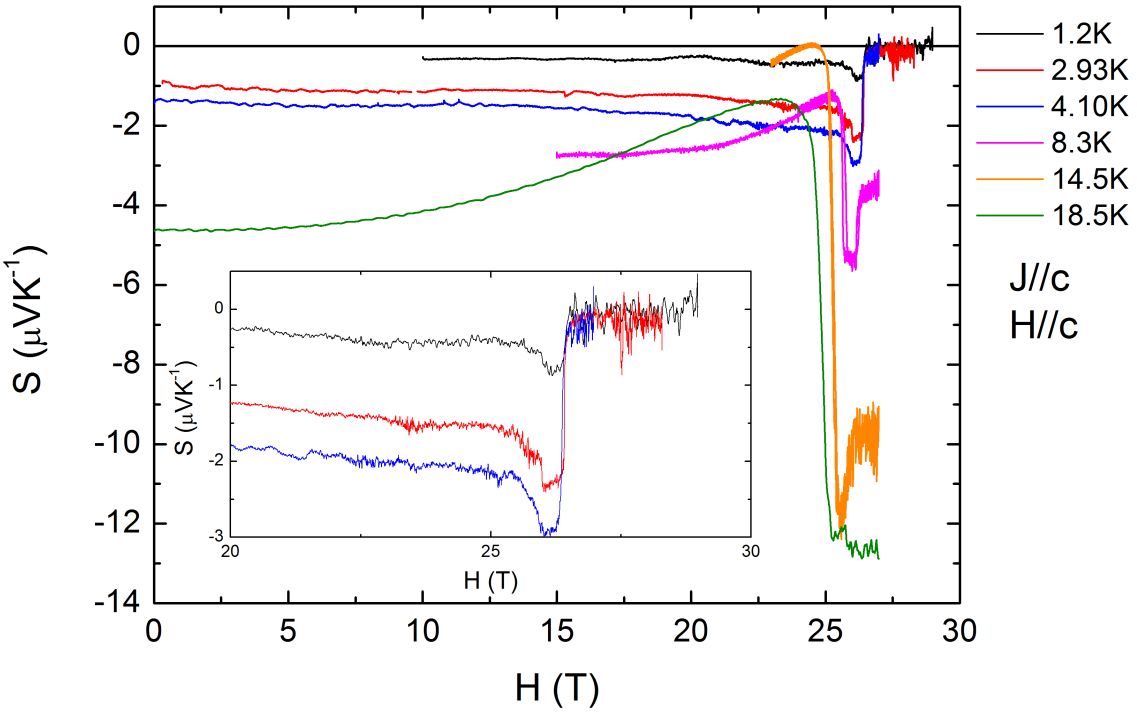

Figure 5.12: *Isothermal thermopower measurements, $S(H)|_{T=ctn}$, at high magnetic fields for the longitudinal configuration. The inset shows a zoom of the $S(H)|_{T=ctn}$ for the low temperature curves close to the magnetic trasitions.*

Above H_c, in the PPM phase, no oscillations have been observed. We note that the noise level of the measurements increases from $1-5$nV at low fields to 40nV above 20T (see Fig.5.13 black curve). We suggest that this increase in the noise level could mask the oscillations of the PPM phase. Besides, the background is almost field independent; it changes in +20nV for the complete magnetic field range $[0-29]$T and the variation seems to be linear with field. For that reason, the $V_{background}$ was measured most of the times at 0 and at 29T and it was removed to the Seebeck signal following the equation 2.10 of "Thermopower Quantum Oscillations" technique. We note that this increase of the noise level was also observed for previous thermopower experiments at the LNCMI laboratory.

The oscillations are the main part of the thermopower signal. Fig.5.13 shows Seebeck voltage signal for $\Delta T/T|_{blue} = 1\%$ and $\Delta T/T|_{green} = 5\%$ relative thermal gradients. We notice that even for small values of $\Delta T/T$, the amplitude of the oscillations dominates the thermopower signal (see the blue curve of Fig. 5.13). For relative high thermal gradients (green curve of Fig. 5.13), the oscillations prevail over the signature of the metamagnetic transitions.

In Fig.5.14, we compare $S(H)$ for transverse and longitudinal configurations, in black and in blue curves respectively, at $T \simeq 1$K. First, we note that the absolute value of the Seebeck coefficient for both configurations is in average close to 0.5μVK^{-1} in the AF phase and that the quantum oscillations of the thermopower signal are observed for both configurations although the quality of the sample for longitudinal configuration is 10 times lower than the quality of the transverse configuration. As a consequence of this different quality sample, we note that the amplitude of the oscillations for the longitudinal configuration are reduced and surprisingly,

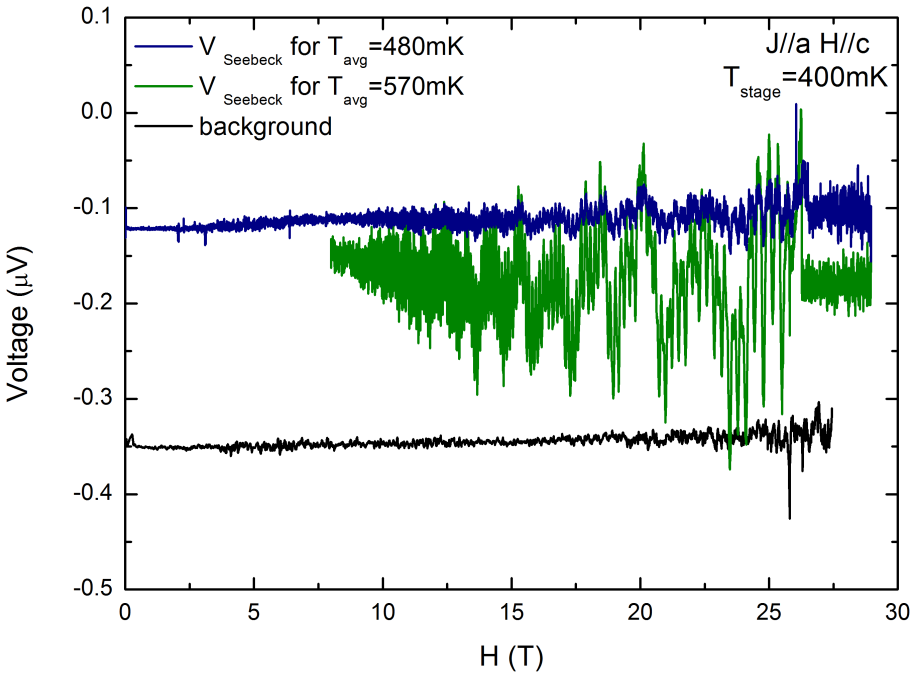

Figure 5.13: *Electrical response to a small and a high thermal gradients in blue and green curve colors, respectively. The black curve shows the background of $S(H)$ at the lowest temperature, $T = 400mK$.*

the amplitude is reduced in the same factor as the quality sample, by 10 times.

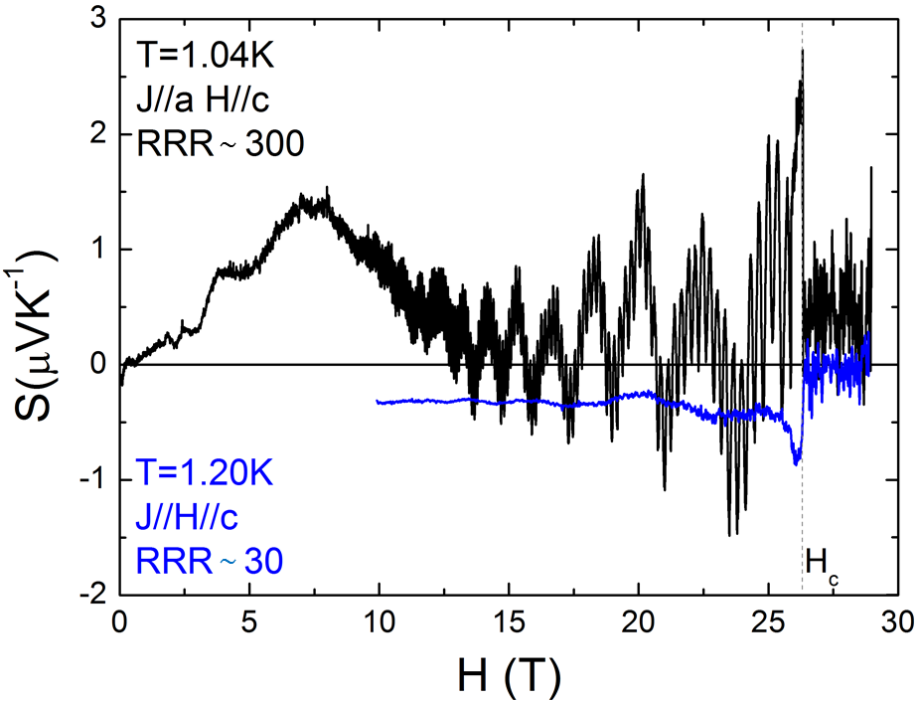

Figure 5.14: *Isothermal thermopower measurements, $S(H)|_{T=ctn}$, at high magnetic fields for transverse (black) and longitudinal (blue) configurations at temperatures around $T \sim 1K$.*

Transverse and longitudinal configurations, both present a strong change of its value at the metamagnetic transitions in the low temperature range. Thermopower temperature dependence $S(T)$ has shown that $CeRh_2Si_2$ is an isotropic compound at $H = 0$. However at high temperatures, transverse and longitudinal configurations present different behaviours due to the directional sensitivity of the thermopower measurement. Under field at H_c, the isotropic thermopower signal is also destroyed. Thermopower shows opposite behaviour at H_c for longitudinal (jump of $S(T)$) and transverse (drop of $S(T)$) configurations. The sharp modifications of the thermopower signal at the metamagnetic transitions H_{2-3} and H_c will be studied in detail in subsec. 5.5.2.

Another consequence of the anisotropy may be related to the change of the sing of the average of thermopower signal at high fields only for the transverse configuration. This sign change was also observed previously in $S(T)$ measurements for the transverse configuration where $S(T)_{trans}$ crosses the zero line of thermopower whereas $S(H)_{long}$ remains negative for all the field range.

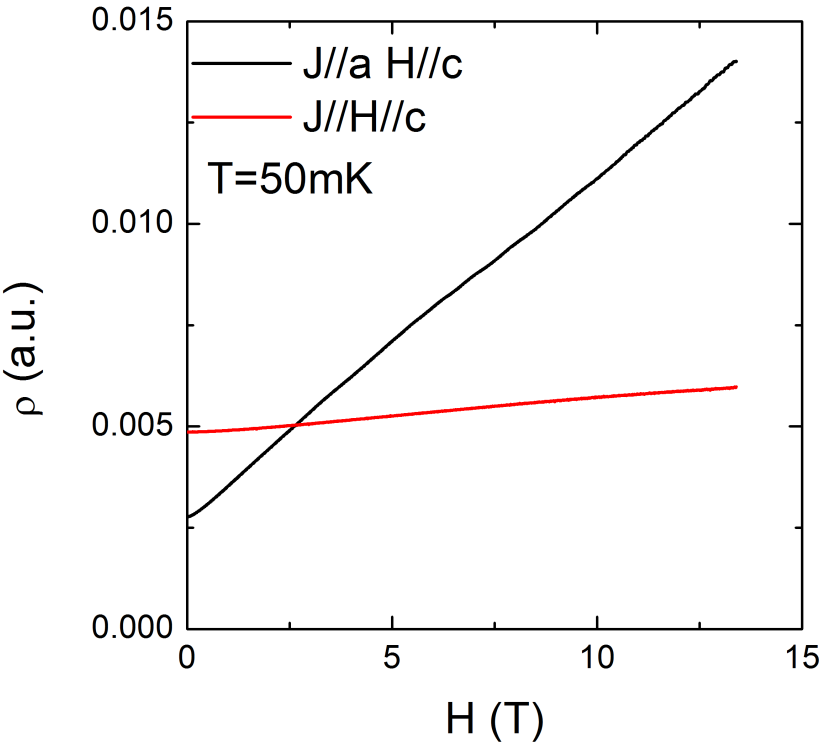

Figure 5.15: *Magnetoresistance measurements for transvserse (black) and longitudinal (red) configurations performed at $T = 50mK$ in the $[0 - 13]\,T$ magnetic field range.*

Another phenomena only observed for the transverse configuration consists in an increase of the thermopower signal reaching its maximum at 7T from the low temperature regime up to $T = 8$K. Magnetoresistance measurements for transverse (black) and longitudinal (red) configurations performed at $T = 50$mK shown in Fig. 5.15 are used to better understand this anomaly. A small increase of magnetoresistance value with maximum a 5T appears in the transverse configuration while longitudinal configuration does not present any anomaly. This is in agreement with $S(H)$ measurements. However, these two maximums are decoupled.

We cannot conclude about this, but we consider this can be due to the fact that the system is in the quantum oscillations regime ($\omega_c\tau >> 1$). In this regime, the weight of each orbit plays a significant role in the total conductance contribution. In addition, thermopower depends on the weighting of the conductance of each orbit with a non linear relation; therefore, thermopower can present this increase with delay. We also note the strong different behaviour of the evolution of magnetoresistance for transverse and longitudinal configurations.

Fermi Surface of $CeRh_2Si_2$

To get the information of the Fermi surface properties of $CeRh_2Si_2$, we performed a Fast Fourier Transform (FFT) of the Seebeck signal. The analysis of the FFT, which corresponds to the spectrum of the Fermi surface, gives the extremal orbits f_i of the Fermi surface and its size through the Onsager relation $S_i = (2\pi e/\hbar c)f_i$. The spectrum also shows the relative relevance of the different orbits through the relative amplitudes of each branch in the FFT. The relative weight of the orbits also depends on the effective magnetic field, H_{eff}, of the FFT window.

As expected from the analysis of Fig.5.14, the spectrum for the longitudinal configuration shows less branches and lower amplitudes than the spectrum of the transverse configuration at similar temperatures. This is due to the lower quality of the longitudinal sample. Accordingly to that, we perform the analysis of the topology of the Fermi surface (cyclotron mass, Dingle temperature and mean free path) only in the transverse configuration experiments.

In Fig.5.16, the spectrum for the AF_2 phase of $CeRh_2Si_2$ for the highest quality sample (transverse configuration) is shown. No oscillations have been observed in the spectrum for the AF_3 and PPM phases. In the AF_3 phase, we could not follow the frequencies due to the small size of the window of the FFT (the FFT window of the AF_3 phase is $[25.8 - 26.3]$T, which is smaller than 1T). In the case of the PPM phase, we could not observe the branches of this Fermi surface due to three effects: first, the thermal gradient in this phase collapses thus, the amplitude of $V_{Seebeck}$ is strongly suppressed; second, the noise increases for $H > 20$T and may mask the low amplitude of the $V_{Seebeck}$; third, thermopower measurements are performed at $T > 450$mK. Only one branch with $F = 16$kT at $T < 50$mK associated to a high effective mass has been reported [Sheikin, 2013]. Therefore, so high temperature for thermopower analysis of the PPM phase can destroy $\omega_c\tau \gg 1$ condition. Thus, our analysis of the Fermi surface is focused on the AF_2 phase of $CeRh_2Si_2$ for the transverse configuration.

The spectrum of the AF_2 phase for a FFT window of $[12 - 25]$T obtained from the lowest temperature isothermal thermopower measurements, $S(H)_{T=468mK}$ is shown in Fig.5.16. The upper panel corresponds to the complete spectrum of the AF_2 phase in which we indicate the main frequency and its harmonics and the lower panel is a zoom concerning only the first harmonics of the previous spectrum. Thermopower was sensitive up to the fourth harmonic of the main branch, ν. Concerning the first harmonics, thermopower detected the frequencies of the Fermi surface listed in Table 5.1. We verified that thermopower branches are in good agreement with the branches measured by dHvA technique ([Araki et al., 2001]) although thermopower measurements cannot detect the low frequencies of the Fermi surface of the AF_2 state. The frequencies which correspond to dHvA frequencies shown in literature are called with the dHvA name. However, thermopower is more sensitive to the high frequencies of the Fermi surface. The frequencies corresponds to new orbits of the AF_2 Fermi surface except

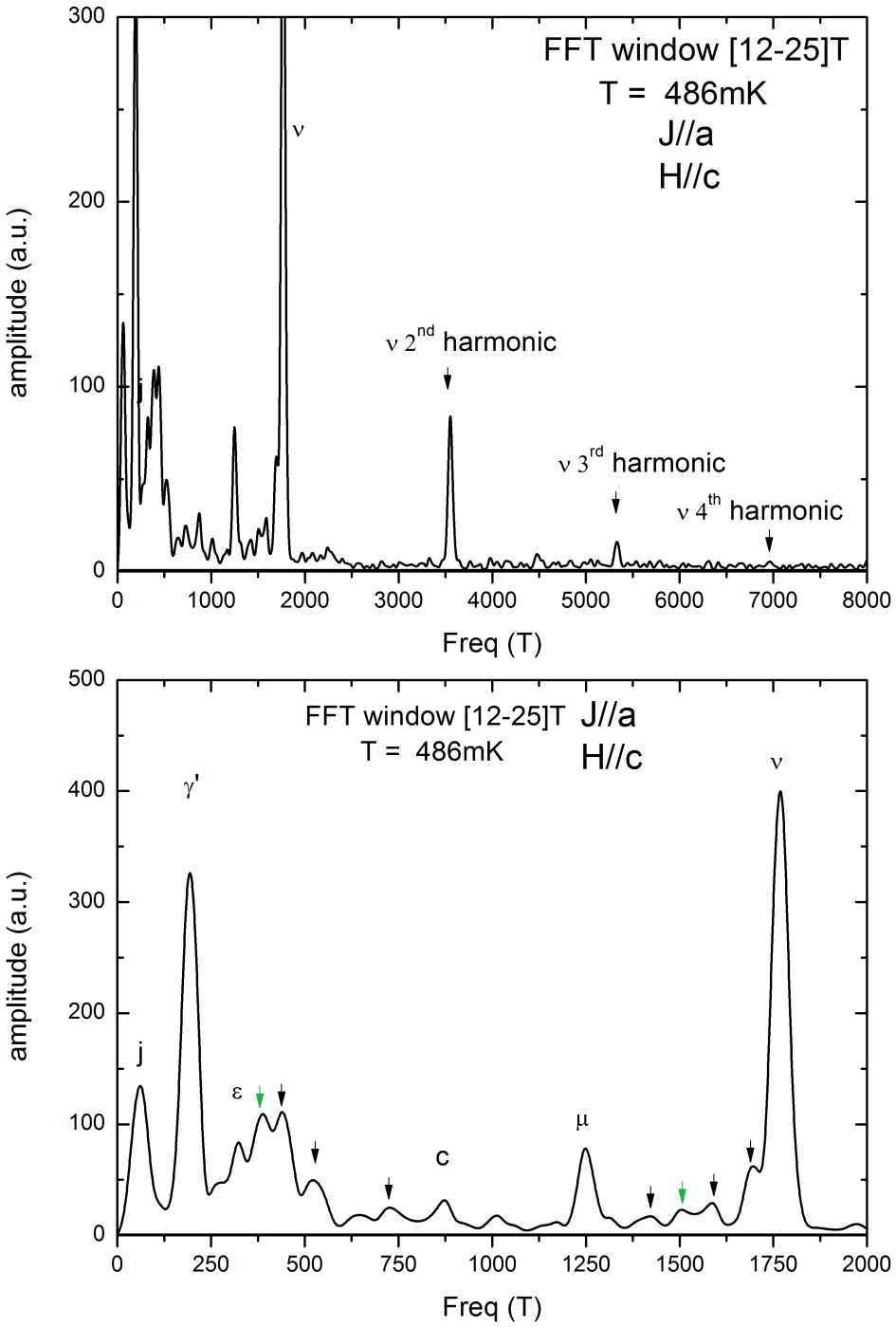

Figure 5.16: *Spectrum of the AF_2 phase of $CeRh_2Si_2$ for a FFT window of $[12-25]\,T$ obtained from isothermal thermopower measurements performed at $T = 468mK$. In the upper panel we show the main frequency ν and its harmonics and in the down pannel a zoom of the first harmonics of the AF_2 phase. The orbits of $CeRh_2Si_2$ are indicated by dHvA names and by arrows (new frequencies).*

for the frequencies 387T and 1505T. A proof of that is that these frequencies are not second harmonics of the other orbits. We will discuss the origin of the frequencies 387T and 1505T later in this subsection.

Frequencies of the AF_2 phase (T)		
orbit	by dHvA $[13-16.9]$T	by $S(H)$ $[12-25]$T
l	44	
k	56	
j	66	61
	77	
α''	81	
γ	137	
γ'	184	194
ε	327	324
		387
		440
		520
		727
c	804	870
μ	1160	1249
		1422
		1505
		1587
		1693
ν	1770	1768
a	7560	

Table 5.1: *List of the orbits of the AF_2 phase obtained from dHvA measurements (ref. [Araki et al., 2001]) and from $S(H)$\| measurements at $T = 468mK$ for the transverse configuration.*

Higher frequency values for γ', c and μ branches were detected by thermopower than by dHvA measurements. For j and ε branches, lower thermopower frequencies in comparison to dHvA frequencies were obtained. These frequency disparity between thermopower and dHvA are the consequence of a tilt on the thermopower sample between the *c*-axis, the easy axis of the compound along which the intrinsic magnetic moments of the system are orientated, and the external magnetic field. From the dHvA frequency angle dependence shown in Fig.5.17 -left- with dHvA frequencies in black symbols and thermopower orbits in red symbols, we estimate that the shift in frequencies corresponds to an angle between $4-8^o$ from the [001] direction to the [100]. No evidence of the tilt has been observed for the main orbit ν because the frequency of this branch remains the same for small angles. To finish, we point out that as a consequence of the tilt, we cannot observe the *a* branch with frequency 7560T because this branch vanishes rapidly when the magnetic field turns from [001] direction to [100]. In Fig.5.17, we also show the branches observed by SdH effect in $[8-13.4]$T and $[10-13.4]$T FFT windows by blue and dark cyan symbols, respectively. We remark that SdH also observed more frequencies than dHvA but less than thermopower quantum oscillations and that these new frequencies are similar to the thermopower orbits.

To determine the evolution of the orbits with the effective field, H_{eff}, we analyze the

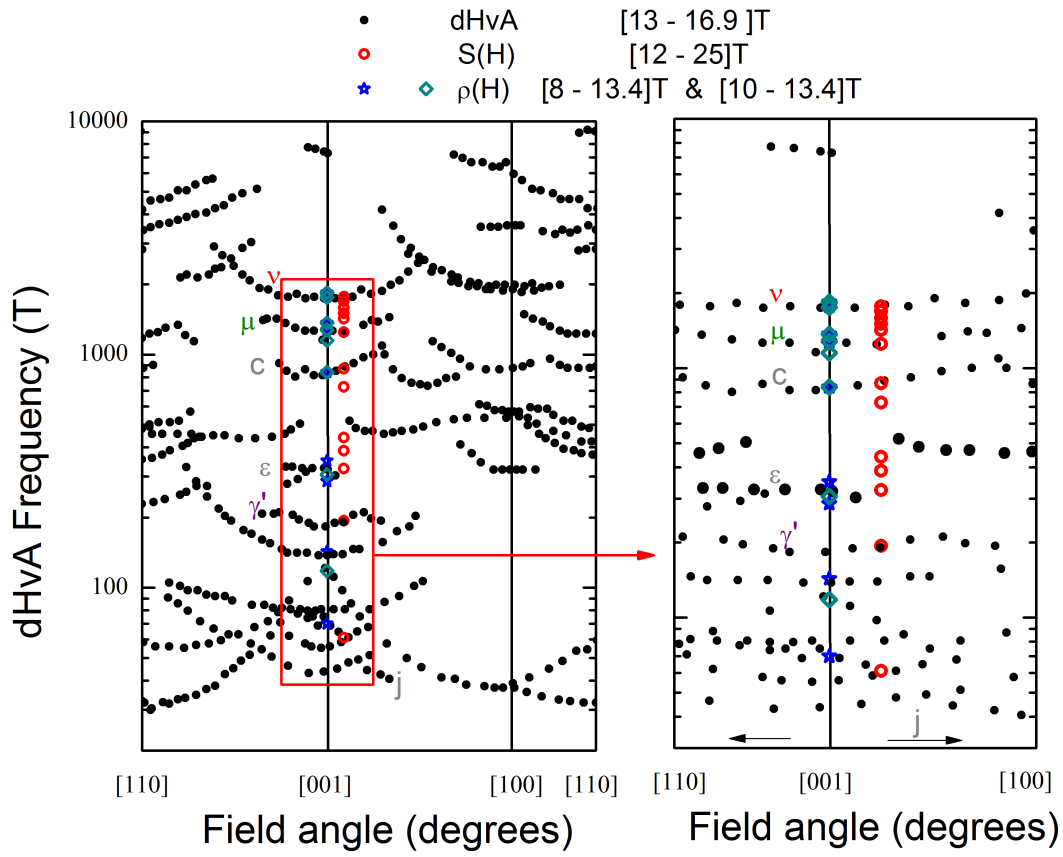

Figure 5.17: *Comparison between the orbits of the AF_2 phase of $CeRh_2Si_2$ detected by dHvA (in black), SdH (in blue) and thermopower quantum oscillations (in red).*

evolution of the spectrum of the AF_2 phase as a function of H_{eff}. For that, we performed several FFTs with a 0.039 1/T FFT window in 1/H; the constant FFT window size has as objective to keep the same resolution for each spectrum. This window is shifted along the $[8 - 25.5]$T magnetic field range with a step of 0.002 1/T. The ensemble of the obtained spectrum reflects how the increase of H_{eff} from $[7.9 - 15.9]$T affects the amplitude of the orbits of the Fermi surface (see Fig.5.18).

Complementary to Fig.5.18, we plotted the frequencies as a function H_{eff} (see Fig.5.19). We observe that the main frequency of the AF_2 phase, the frequency ν, does not depend on H_{eff}. The frequencies μ and γ' show at low values of H_{eff} a small shift to lower frequencies and above $H_{eff} > 12$T, the frequencies remain invariant. To finish, we observed the appearance of new frequencies at high magnetic fields, $H_{eff} \gtrsim 11$T, such as 387T, 440T, 520T, 727T, 1422T, 1505T, 1587T or 1693T. The last one, 1693T, seems to be a split of the main frequency, ν as we will explain at the end of this subsection.

Surprisingly, for $H_{eff} > 13$T, the increase of the amplitude of the main orbit ν, 1768T, is not any more increasing in a orderly way with H_{eff}. Unexpectedly, a decrease of the amplitude of the ν orbit at high fields is observed. We suggest that this is related to the strong increment of the scattering at high fields close to H_c that induces an increase of T_D. This is in agreement with the high magnetoresistance presented in resistivity measurements shown in ref. [Knafo et al., 2010].

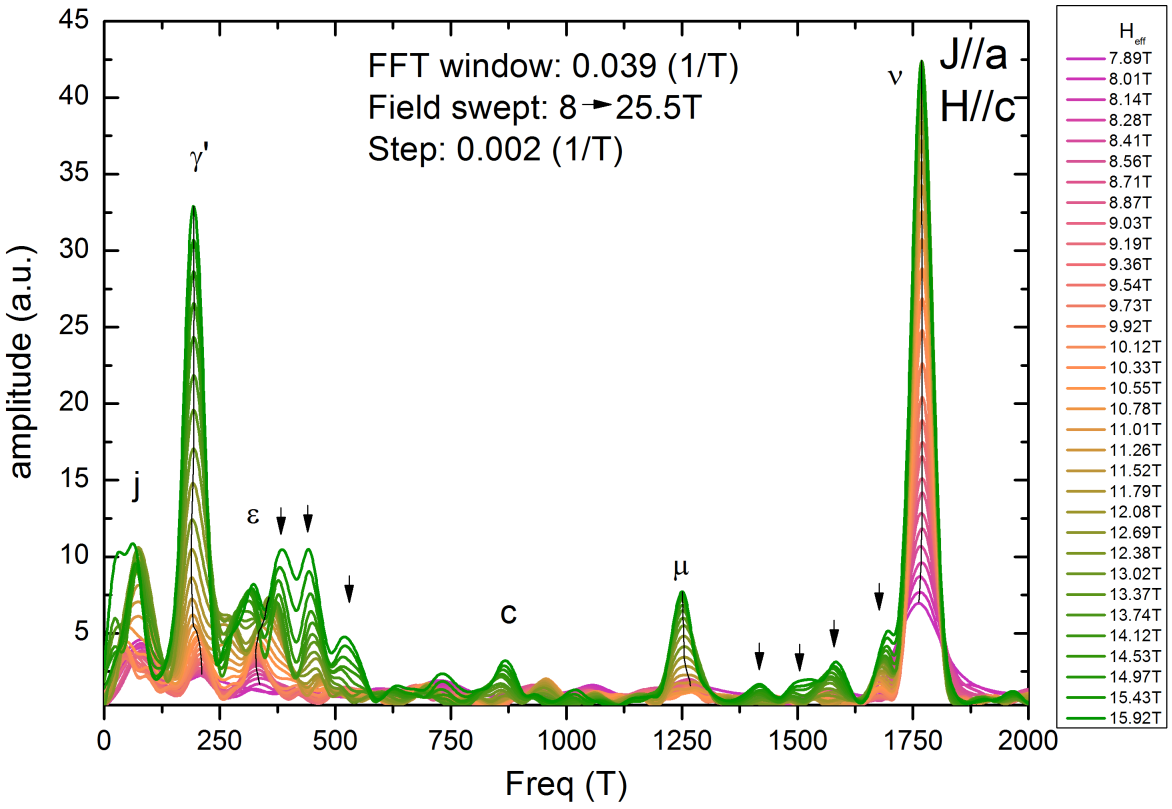

Figure 5.18: *Spectrums of the AF_2 phase by increasing effective fields, H_{eff}. H_{eff} increases from pink to green color. The spectrums are determined for a FFT window of* 0.039 $1/T$ *which was swept from* $8T$ *to* $25.4T$ *with a step of* 0.002 $1/T$.

To obtain the effective mass, m^*, of the carriers of each orbit, the variation of the amplitude for each individual branch with temperature is analyzed. First, we analyze m^* for the same FFT window as dHvA effect (FFT window $[13-16.9]$T). We notice that the spectrum of thermopower quantum oscillations do not observed all the frequencies of the Fermi surface as it was embodied in the analysis of Fig.5.18. The m^* determined for $[13-16.9]$T FFT window are shown in Table 5.2 in which m^* is expressed in units of m_0, the free electron mass. We observe that m^* for dHvA and thermopower quantum oscillations are of the same order of magnitude, except for $\gamma^{'}$ orbit. We suggest that the small differences for most of the frequencies are due to the different temperature range as thermopower temperature range is one order of magnitude higher than the one of dHvA effect. In the case of $\gamma^{'}$ orbit we cannot understand the physical origin of this strong difference unless our frequency of $\gamma^{'}$ corresponds to the γ dHvA orbit.

FFTs at higher magnetic fields were performed to determine the completely Fermi surface of $CeRh_2Si_2$. In Fig.5.20, the amplitude evolution of the frequencies with temperature is shown for the $[12-25]$T FFT window. We note that the temperatures shown in this figure correspond to the average of the temperature of the sample in the FFT range. The amplitude of the orbits decreases with temperature and is rapidly suppressed between 1K and 3K. The FFT spectrum for $T > 3$K are close to the noise level and it is for that reason we will use the first five temperatures to determine m^*. The effective masses obtained are listed in Table

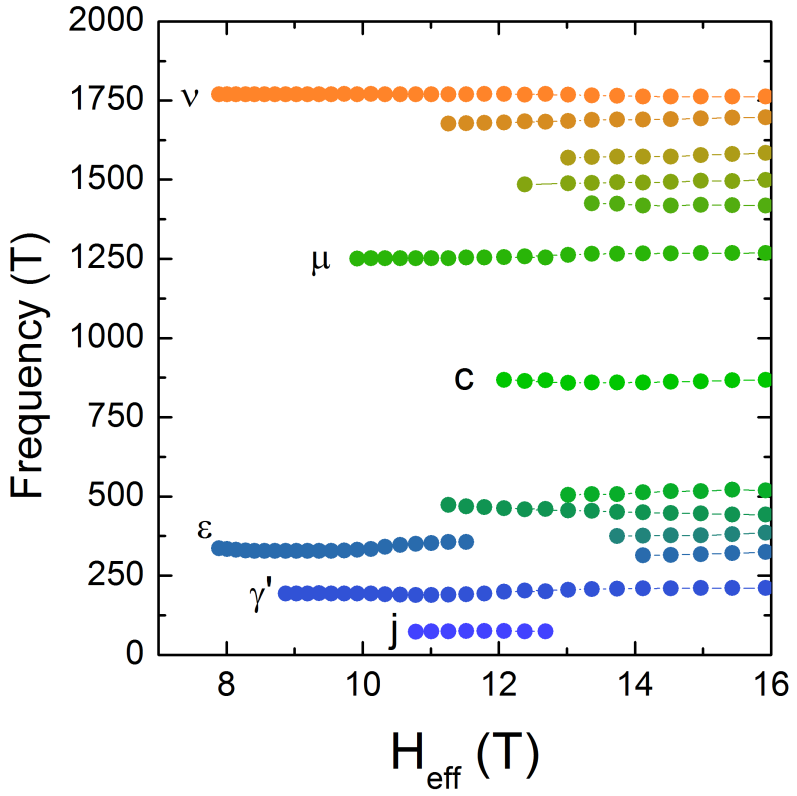

Figure 5.19: *Evolution of TEP orbits as a function of H_{eff} obtained for a FFT window size of* 0.039 $1/T$ *wept from* $[8-25.5]\,T$.

5.2. We observe that the m^* of the orbits determined by thermopower measurements are similar to the m^* obtained by the dHvA effect with the exception of γ' orbit. Here, the small differences can come from the different size of the FFT window and then, the different H_{eff} of the FFT. The second possibility of these differences is related to the appearance of new bands in the high field range, as we have observed in Figs.5.18 and 5.19, that may modify the values of the m^* of the different branches. Comparing the m^* obtained by thermopower quantum oscillations for $[13-16.9]$T and $[12-25]$T FFT windows, we notice an increase of the values for ε, c and ν; μ orbit remains unchanged and the 440T and 1587T orbits show a decrease of their values at high fields where more than one new orbit appears with frequencies close to these branches. We conclude that the increase of the m^* of the main bands is in agreement with the increase of the A coefficient [Knafo et al., 2010].

The Dingle temperature T_D of $CeRh_2Si_2$ is also obtained from the field dependence of the amplitude. The size of the FFT window was fixed at 0.039 1/T which corresponds to the size of the FFT window used for the analysis of the m^* (see Fig.5.18). Taking into account the field dependence of the orbits as shown in Fig.5.19, we adapted for each orbit the magnetic field range to determine T_D. The temperature of the sample was calculated for each FFT because the temperature depends on the field range. Thus, these modifications were taken into account to determine T_D and the mean free path, l. Both were determined in the same conditions. The obtained values for transverse configuration are listed in Table 5.3. There are large differences between T_D and l of the dHvA sample and our sample. The quality comparison is focused

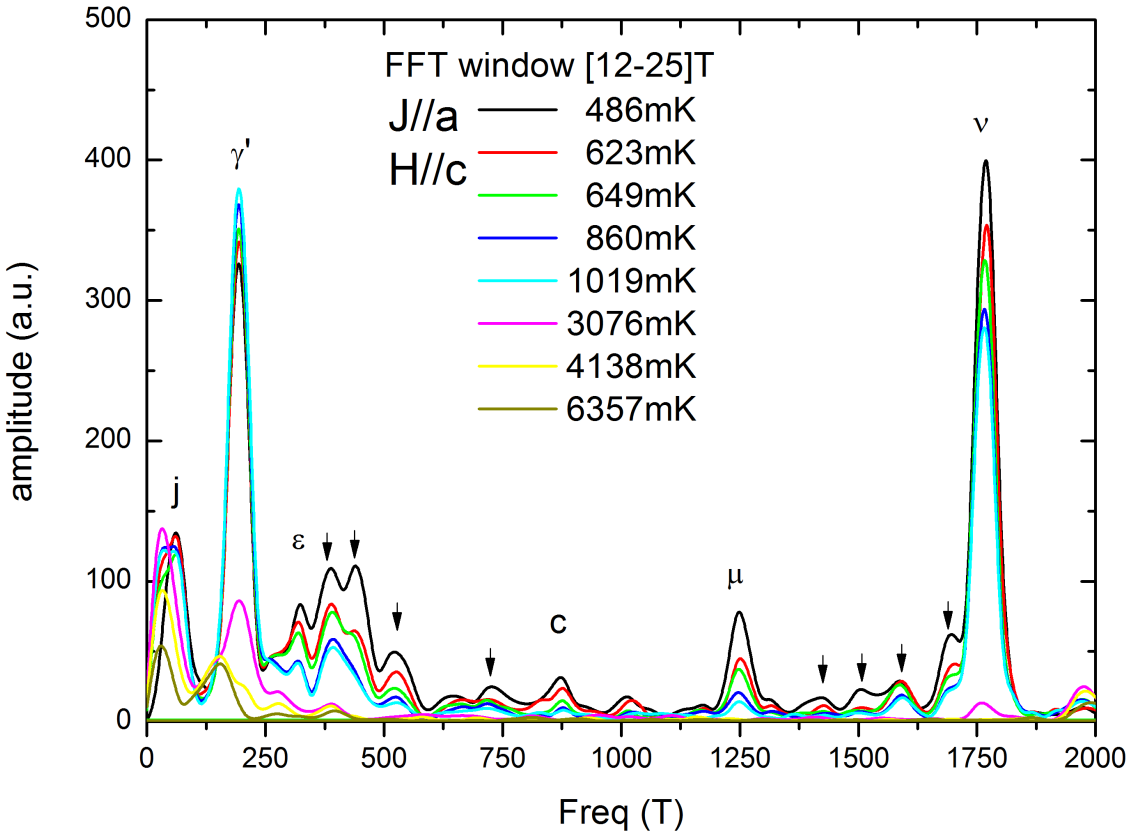

Figure 5.20: *FFT spectrum of the AF_2 phase for different temperatures. The spectrums are determined for the $[12-25]\,T$ FFT window for the transverse configuration.*

on the analysis of the l parameter. For example, we note that the main frequency ν presents almost double l for the dHvA effect than for the sample we studied. From this comparison, we could suggest that the quality of the dHvA sample was higher. Nevertheless, thermopower quantum oscillations technique is able to observe more frequencies than the dHvA effect which contradicts the fact that $l_{dHvA} > l_{S(H)}$. Therefore, these differences on the determined values of l are the consequence of the temperatures at which we perform the analysis. In dHvA effect, this analysis is performed at $T(dHvA) = 28.5$mK while for thermopower it is done at $T_{avg}(S) = 486$mK. The strong difference in temperature does not allow us to perform a precisely comparison about the differences of quality between these samples.

We also calculated T_D and l of ν orbit for the longitudinal configuration. The values are $T_D(\nu)_{long} = 1.78 \pm 0.08$K and $l(\nu)_{long} = 850 \pm 50$Å. This $l(\nu)_{long}$ value is smaller than $l(\nu)_{trans}$.Thus, the c-long configuration sample presents lower quality than the a-long configuration sample. This difference of quality was enough to not be able to follow all the frequencies of the Fermi surface and to have lower amplitudes as indicated at the beginning of the section.

The high applied magnetic field modified the Fermi surface of the system in such a way that some orbits of the Fermi surface could be coupled. As a consequence, new frequencies concerning this coupling can be determined. This mix of orbits can be understood in terms of the schema shown in Fig.5.21 (left). In this schema, two independent Fermi surfaces are represented (orbit1 in red and orbit2 in black). At high fields, these two Fermi surfaces are

$m^*(m_0)$ of the AF_2 phase			
orbit	by dHvA $[13-16.9]$T	by $S(H)$ $[13-16.9]$T	by $S(H)$ $[12-25]$T
l	0.43		
k	0.41		
j	0.39		
77	0.26		
α''	1.4		
γ	0.45		
γ'	1.4	0.64	0.45
ε	1.9	1.8	2.7
387			2.76
440		5.0	3.5
520			4.0
727			3.0
c	4.9	4.1	4.8
μ	3.7	5.0	4.9
1422			3.9
1505			3.5
1587		4.0	2.5
1693			3.4
ν	2.4	1.9	2.2
a	6.4		

Table 5.2: *List of cyclotron masses of the orbits of the AF_2 phase obtained from dHvA measurements of ref. [Araki et al., 2001] and from isothermal thermopower measurements for the transverse configuration.*

coupled and the intersection of the areas of the Fermi surfaces defines a new frequency "a". In this new situation, thermopower quantum oscillations technique can measure the frequencies: orbit1, orbit1 + a and orbit1 + $2a$ =orbit2. This phenomenon is called magnetic breakdown [Shoenberg, 1984]. We note that the amplitude of this new frequency orbit1 + a do not be larger than the amplitude of the orbit1 and orbit2 and the m^* must be between m_1^* and m_2^*. In our sample, this magnetic breakdown has been observed for the frequencies 387T and 1505T as shown in Fig.5.21 (right). The orbit 387T is due to the intersection of ϵ and 440T orbits with $a \sim 60$T. The intersection of 1422T and 1587T orbits causes the 1505T frequency that can be expressed as $(1422 + a)$T with $a = 82$T, the Fermi surface of the interception. In addition, the magnetic breakdown of these orbits is also supported by the fact that the m^* of these orbits have an intermediate value of the m^* of the extreme orbits; i.e., m_1^* and m_2^*.

As we have pointed out before, the main frequency ν seems to present a spin dependence of the effective mass at high magnetic fields, $H_{eff} > 11$T. At high fields, the ratio $m_\uparrow^*/m_\downarrow^*$ will diverge from 1 when $\hbar^2 k_F^2/2m^* \simeq \mu_B m g B$, with m the total angular momentum, g the Lande g-factor and B the total applied magnetic field. The orbits with low m^* will not be affected against the orbit with high m^* which will appear at high fields with a lower frequency (shrink

T_D and l of the orbits of AF_2 phase				
orbit	dHvA		Thermopower	
(T)	T_D(K)	l (Å)	T_D(K)	l (Å)
l				
k				
j				
77			-	-
α''				
γ	2.87	700		
γ'	0.42	1770	8.4 ± 0.4	250 ± 10
ε	0.42	1760		
387			0.96 ± 0.06	560 ± 30
440			1.18 ± 0.03	380 ± 10
520			0.74 ± 0.06	580 ± 50
727			2.5 ± 0.1	270 ± 10
c			0.55 ± 0.03	1000 ± 50
μ	0.39	1870	0.94 ± 0.03	580 ± 20
1422			0.9 ± 0.1	800 ± 100
1505			-	-
1587			1.76 ± 0.06	690 ± 20
1693			0.45 ± 0.05	1800 ± 100
ν	0.66	2050	1.05 ± 0.06	1150 ± 80
a	0.78	1540		

Table 5.3: *List of Dingle temperatures and mean free paths of the orbits of the AF_2 phase obtained from the dHvA measurements of ref. [Araki et al., 2001] and from the isothermal thermopower measurements for transverse configuration.*

of the Fermi surface). We observe that ν orbit splits into two orbits 1693T and 1768T (see Figs.5.18 and 5.19). The splitting is supported by (i) the huge relative amplitude difference of these two orbits, 1768T orbit presents a larger amplitude than 1693T orbit; (ii) the appearance of 1693T orbit at high fields; (iii) the effective masses of these two orbits, $m^*_{1693T} = 3.4m_0$ and $m^*_\nu = 2.1m_0$, being m^*_{1693T} higher than the m^*_ν by a factor 1.7 and (iv) the existence of a dephasing at high fields of the ν frequency. In Fig.5.22, we show $S(H)$ for $T = 1.04$K and $T = 3.16$K in the field range of $[18.8 - 20.5]$T. In this field window, we notice there is a shift of π on the signal of $S(H)|_{T=3.16K}$ respect to the $S(H)|_{T=1.04K}$. This shift corresponds to a shift of the ν orbit of the AF_2 phase of $CeRh_2Si_2$. Therefore, it may be attributed to a change of the weight of the spin-up and spin-down Fermi surfaces at high fields. The same phenomenon was observed in the compound $CeRu_2Si_2$ in which the dephasing was understood as a zero spin-splitting condition [Takashita et al., 1996]. We conclude that ν orbit splits into a spin-up and spin-down branches at high fields and the spin-down Fermi surface is the one with higher m^* and lower frequency.

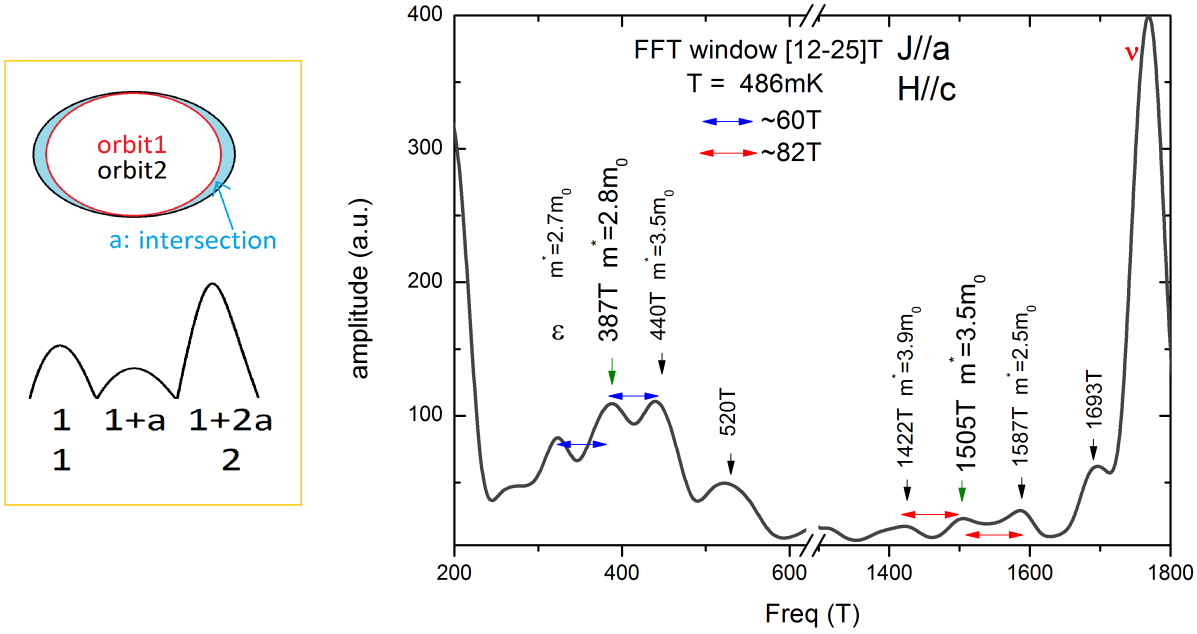

Figure 5.21: *The schema of magnetic breakdown is represented on the left figure. This schema shows two independent orbits and their interception. The different orbits that can be detected in this situation are represented below. A zoom of the parts of the spectrum of the AF_2 phase of $CeRh_2Si_2$ corresponding to the magnetic breakdown situations are shown on the right figure. In this spectrum the magnetic breakdown of the orbits $387\,T$ and $1505\,T$ are represented. The arrows are used as a guide for the eye to show the size of the "a" orbit for each magnetic breakdown, blue for $387\,T$ and red for $1505\,T$.*

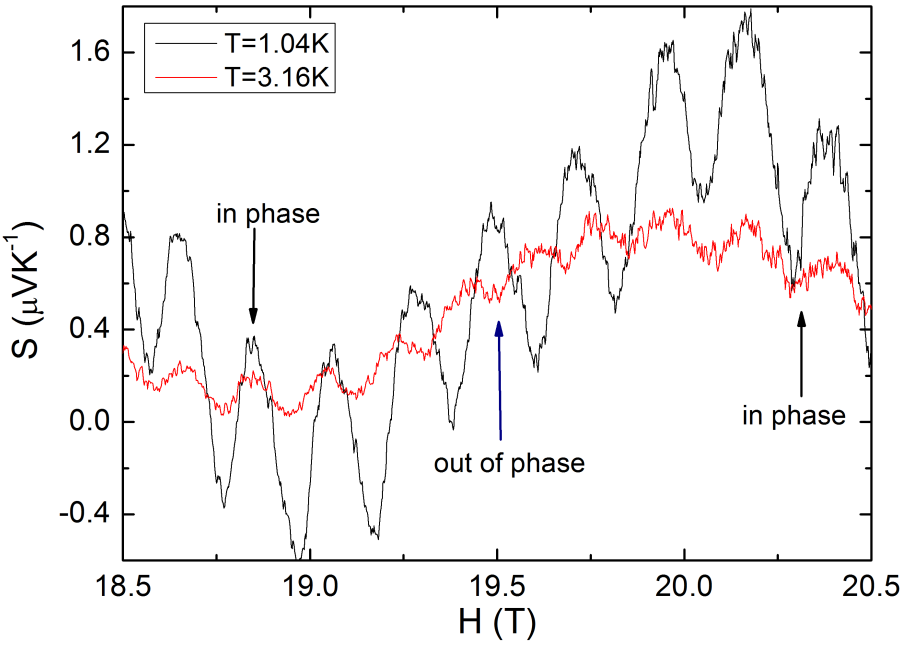

Figure 5.22: *Isothermal thermopower measurements, $S(H)|_T$, at high magnetic fields for transverse configurations at $T = 1.04K$ (black curve) and $T = 3.16K$ (red curve).*

Thermopower Quantum Oscillations against traditional probes

We highlight that thermopower is a good probe to analyze the Fermi surface of a system through the quantum oscillations thanks to its high sensibility to any change of the Fermi surface. In this subsection, we have compared the branches obtained by thermopower quantum oscillations and the branches obtained by dHvA measurements for samples, ideally, with comparable sample quality. We conclude that the results of both techniques are similar. However, if we compare the signal of thermopower quantum oscillations and dHvA, we notice that thermopower oscillations are directly observable without removing any background as the amplitude of the oscillations is larger than the absolute value of the signal of thermopower. We can notice that thermopower oscillations appear even at temperatures one order of magnitude higher than dHvA oscillations and more frequencies have been observed by thermopower quantum oscillations as well as orbits due to magnetic breakdown.

The disadvantages of thermopower quantum oscillations in relation to the dHvA measurements are: (i) the higher value of the lowest temperature of the measurements (500mK instead of 30mK), (ii) the variation of the average temperature of the sample as a consequence of the variation of the thermal conductivity of the sample.

5.5.2 Metamagnetic Transitions

We analyze isothermal thermopower measurements $S(H)$ of $CeRh_2Si_2$ for transverse and longitudinal configurations to determine the suppression o the AF state.

In Figs.5.23 and 5.24, $S(H)$ measurements in the high field range, $H \gtrsim 22$T, are shown. For temperatures lower than T_{TCP}, we observe the suppression of the AF state in a two-step transition. The transitions are AF_2-AF_3 and AF_3-PPM and both are first order. Above T_{TCP}, the domain AF_1 is suppressed into a PPM phase in one step transition. This transition is a second order type. We analyze the specifications of this transition for transverse and longitudinal configurations separately.

For the transverse configuration (see Fig.5.23), AF_2-AF_3 and AF_3-PPM transitions are step-like. They are characterized by a rapid change in the absolute value of the Seebeck coefficient and by an hysteric behaviour because of the first order nature of the transitions. Moreover, these transitions show an opposite thermopower behaviour in the low temperature regime. AF_2-AF_3 transition presents an increase in the thermopower signal whereas AF_3-PPM transition shows a drop in thermopower. In addition, the variation of thermopower is higher at the AF_3-PPM transition than at the AF_2-AF_3 one. In the $[3-6]$K range, the thermopower jump at AF_3-PPM transition increases with temperature while the one of AF_2-AF_3 transition decreases. For $6K < T < T_{TCP}$ temperature range, thermopower changes its evolution into an increase of thermopower in the AF_2-AF_3 transition. For $T > 15$K, we observe only one step transition in $S(H)|_{T=cts}$ and above 17K$= T_{TCP}$, the transition, AF_1-PPM, becomes broad and the broadening marks the suppression of the AF order by a second order transition. The field dependence of the transition is characterized by a shift to lower values at $T > 8$K. The thermopower evolution of the AF_3 phase shows an increase of thermopower signal $S(H)$ with field at low temperatures. In the $[3-6]$K range, thermopower becomes constant for the first half of the field window of the AF_3 phase and decreases in the second half of the field window of this phase. At $T > 8$K, the magnetic field window of the AF_3 transition shrinks and ends

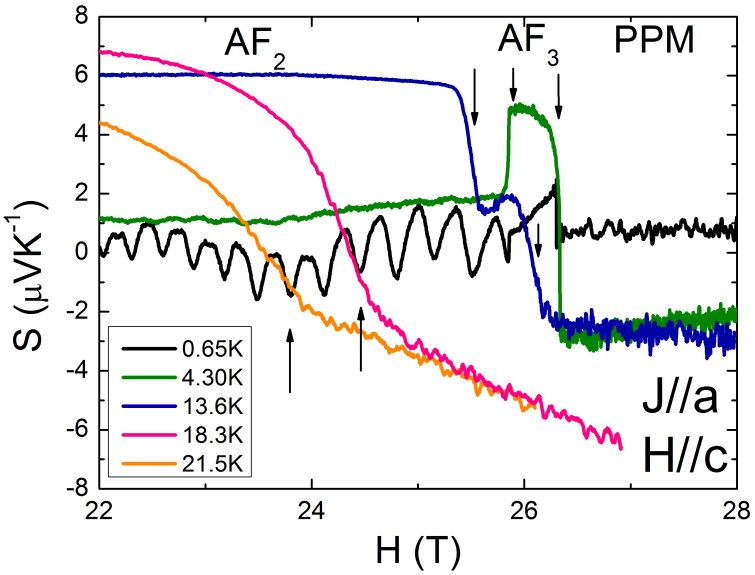

Figure 5.23: *Evolution of the metamagnetic transitions, AF_2-AF_3 and AF_3-PM, at high magnetic fields for the transverse configuration obtained from $S(H)$ measurements.*

up at T_{TCP}.

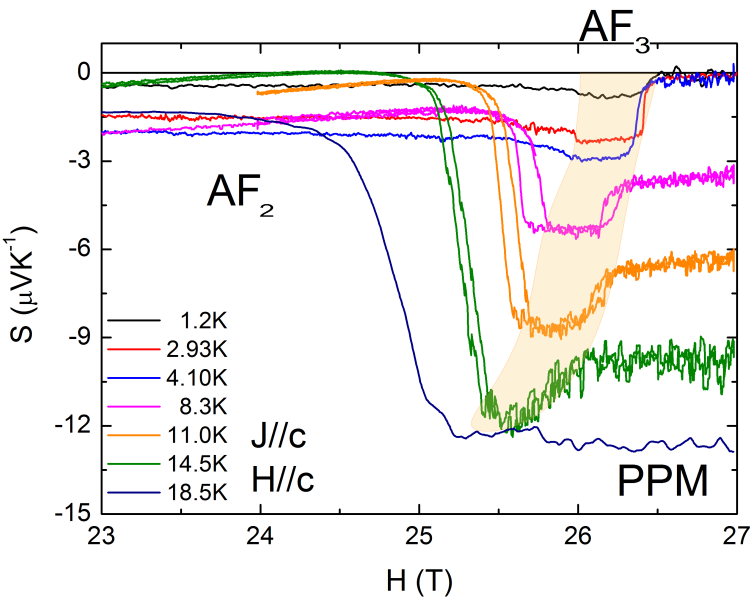

Figure 5.24: *$S(H)$ measuremtns at high fields for longitudinal configuration. The metamagnetic transitions, AF_2-AF_3 and AF_3-PPM, at high field are shown. The orange area shows the evolution of the AF_3 phase.*

For the longitudinal configuration (see Fig.5.24), we observe that AF_2-AF_3 and AF_3-PPM transitions are characterized by a rapid modification of the thermopower signal. These rapid modifications consist in a drop of thermopower for the AF_2-AF_3 and an increase for the AF_3-PM metamagnetic transitions. The hysteresis in thermopower signal marks the first order

character of the transitions. We notice that the jump of thermopower the AF_2-AF_3 transition increases with temperature whereas the jump of the AF_3-PPM transition decreases. The orange area of the figure shows the temperature and field evolution of the AF_3 phase. For $T > 8$K, AF_3 phase is shifted to lower fields as temperature increases and for $T > 12$K, the field range of the AF_3 phase starts to decrease vanishing at $T_{TCP} \sim 18$K. Above T_{TCP}, only one transition was observed. Moreover, this transition does not present hysteresis, then it corresponds to the AF_1-PPM second order transition.

Transverse and longitudinal behaviours at the metamagnetic transitions depend strongly in the orientation of the thermal gradient with the crystallographic orientations contrary to the isotropic behaviour at low temperatures without field. At $H = H_c$, transverse and longitudinal configuration showed just opposite thermopower behaviour at the lowest temperature measurements. Transverse configuration presents a drop of thermopower signal while longitudinal configuration presents an increase of the signal. Nevertheless, the magnetic field of the transitions, H_{2-3} and H_c, are independent of the configurations as well as the vanishing of the AF_3 phase at T_{TCP}. Both configurations show a similar themopower behaviour with temperature at the PM phase which is characterized by the decrease of the absolute value with temperature and both configurations present the collapse of the lines in the T_{TCP} as shown in the (T, H) phase diagrams of Fig.5.26.

Other probes

In this subsection, we compare thermopower to other probes that were performed at high fields to determine the nature of the suppression of the AF state. These other probes are magnetoresistance measurements shown in Fig.5.25 a), the relative length expansion shown in Fig.5.25 b) and magnetostriction shown in Fig.5.25 c) with the relative length expansion as $\Delta L_c/L_c$ and the magnetostriction as $\lambda_c = 1/L_c \times \partial L_c/\partial(\mu_0 H)$ [Knafo et al., 2010]. These measurements were performed in a sample with quality $RRR \sim 60$.

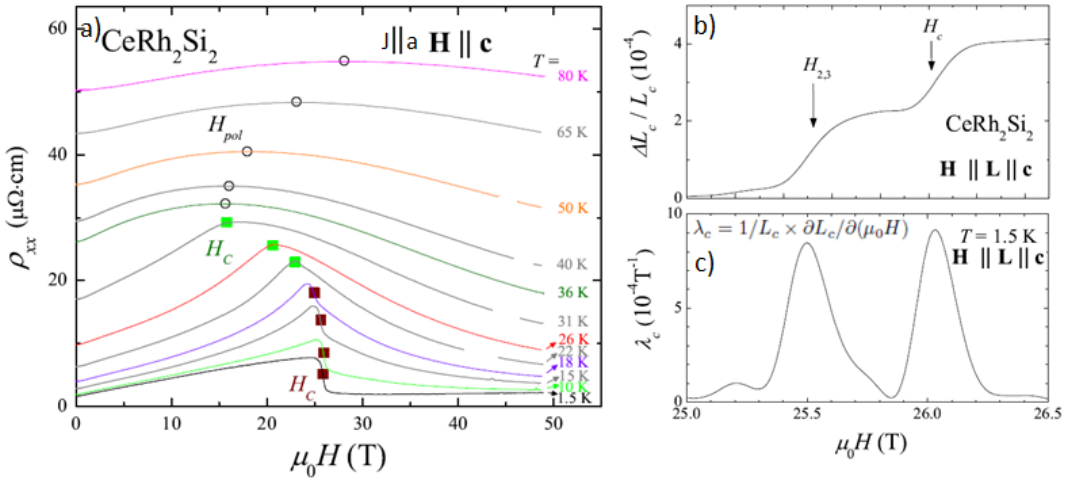

Figure 5.25: *Magnetoresistance measurements a), the relative length expansion along the c-axis b) and magnetostricition measurements c). All the shown measurements are taken from ref. [Knafo et al., 2010].*

The strong variation of the thermopower signal at H_{2-3} is related to an expansion of the

c-axis of the lattice, thus a decrease in the correlations between the Ce-basal planes. As a result, an increase of the localization of the magnetic moment appears in the AF_3 phase that are screened by Kondo effect. This transition was not visible for magnetoresistance pulse field measurements. We suggest that this is due to the extremely high speed in which the pulse magnetic field is applied and the low magnetic field range in which the AF_3 phase exists.

At the metamagnetic transition H_c, a second increase in the length of the lattice along the c-axis is observed which matches to the sharp drop of the magnetoresistance value, $\rho(H)$. Just below H_c, $\rho(H)$ reaches its maximum value pointing out that the system becomes polarized above H_c. Comparing $\rho(H)$ to $S(H)$, we note that $S(H)$ also shows a strong modification in the absolute values of the Seebeck coefficient at the transition. This abrupt change of the thermopower signal at H_c indicates that this transition is discontinuous, hence first order. Moreover, this strong modification in the value of $\rho(H)$ is associated with a reconstruction of the Fermi surface as has been detected by torque measurements [Sheikin, 2013]. Thermopower quantum oscillations also support the hypothesis of the reconstruction of the Fermi surface at H_c because the orbits of the AF phase at the metamagnetic transition are completely suppressed in the PPM phase.

5.5.3 Phase Diagram

In this section, the (T, H) phase diagrams of $CeRh_2Si_2$ determined by temperature dependence of the thermopower, $S(T)$, and the isothermal thermopower measurements $S(H)|_T$ are shown for transverse (Fig.5.26 - left graph) and longitudinal (Fig.5.26 - right graph) configurations. We determine $T_{AF_1-AF_2}$ and T_N from $S(T)|_H$ measurements as we showed in the subsect. 5.4.1. The H_{2-3}, H_c and H_{1-PPM} are obtained from $S(H)|_T$ measurements shown in subsec. 5.5.2. In the case of the transverse configuration, we could also follow the $H_{AF_1-AF_2}$ metamagnetic transition in $S(H)|_T$ measurements.

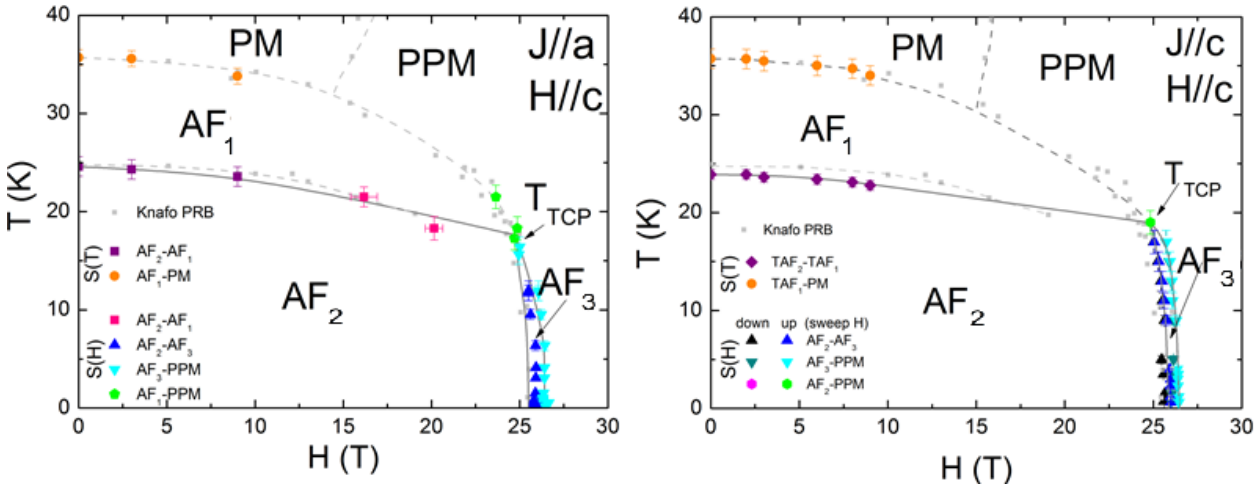

Figure 5.26: *(T, H) phase diagram obtained from $S(H)|_T$ and $S(T)|_H$ measurements for transverse (left graph) and longitudinal (right graph) configurations.*

Both phase diagrams, transverse and longitudinal, are almost the same. $T_{AF_1-AF_2}$ (violet symbols) and T_N (orange symbols) follow the same temperature variation against field and the

variation is in agreement with published results [Knafo et al., 2010]. The H_{2-3} (blue symbols), H_c (cyan symbols) describe first order lines and the H_{AF_1-PPM} (green symbols) describes a second order line. All of them evolve in a similar way. A small difference of the temperature of the tricritical point (TCP) exists between these configurations. T_{TCP} is slightly smaller in the transverse configuration than in the longitudinal one. The difference may be due to the different quality of the sample. Nevertheless, the collapse at the tricritical point of the former H-lines is a common characteristic for transverse and longitudinal configurations, and then quality independent.

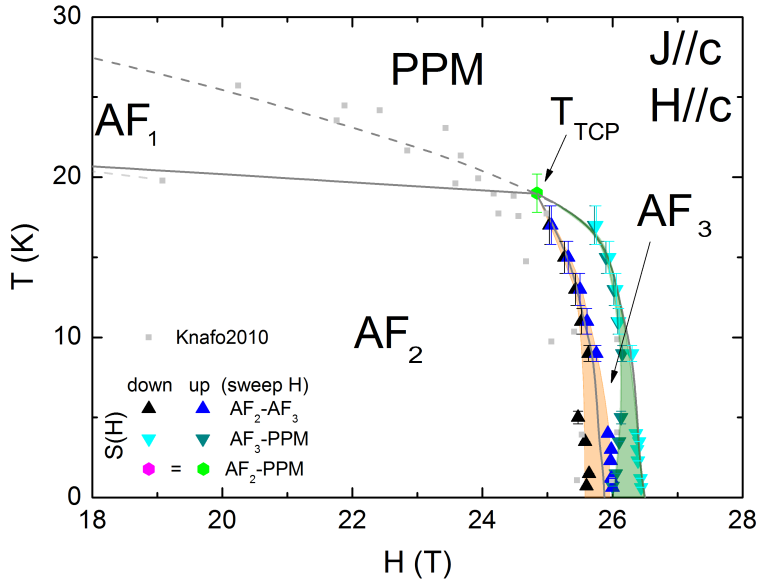

Figure 5.27: (T, H) *phase diagram for the longitudinal configuration of* $CeRh_2Si_2$ *in the high field range obtained from isothermal thermopower measurements,* $S(H)|_T$.

We could follow the $H_{AF_1-AF_2}$ transition for the transverse configuration contrary to the longitudinal configuration. Two $H_{AF_1-AF_2}$ points were obtained in the transverse phase diagram (pink symbols) as TCP has a lower temperature for this configuration than for the longitudinal one. The fact that we could observe the $H_{AF_1-AF_2}$ transition for transverse configuration suggests that the signature of this anomaly in field, $H_{AF_1-AF_2}$, might be linked to the tricritical point. Indeed, from a theoretical point of view, the line defined by $T_{AF_1-AF_2}$ (at low fields) and $H_{AF_1-AF_2}$ (at high fields) must intercept at least with one of the other lines (T_N, H_{2-3}) because it is not possible to transform continuously the magnetic structure of the AF_1 phase into the magnetic structure of the AF_2 phase and *viceversa*. From an experimental point of view, the most probable is that the line ends up the TCP generating a multi-critical point. Nevertheless, the other possibility is the interception with the T_N line. The nature of $T_{AF_1-AF_2}$ is first order under fields up to 9T. However, for $H > 9$T, we could say nothing. $H_{AF_1-AF_2}$ points are determined from $S(H)$ measurements and the tangential way of measuring this phase transition gives broad signatures even if the transition is a first order type.

The hysteresis of the first order transitions measured by $S(H)$ are shown in Fig.5.27 in which we represent only the high magnetic field range phase diagram. The orange and green

areas for H_{2-3} and H_c transitions, respectively, indicate the evolution of the hysteresis with temperature. The hysteresis increases as temperature reaches 0.

5.6 Thermopower under Pressure

In this section, we study the evolution of the Seebeck coefficient of $CeRh_2Si_2$ as a function of pressure when the thermal gradient is applied along the a-axis.

We follow precisely the suppression of the AF domain with the piston cylinder pressure cell setup. The analysis of the band contributions to the thermopower at low temperatures was shown. A comparison between the different thermopower anomalies and the modifications observed by dHvA under pressure was performed. We also performed thermopower measurements in the paramagnetic phase of $CeRh_2Si_2$ for the transverse configuration ($J \parallel a$ and $H \parallel c$) using the Bridgman pressure cell.

5.6.1 Piston Cylinder Pressure Cell

Thermopower under Pressure

The suppression of the AF domain of $CeRh_2Si_2$ with pressure is analyzed by thermopower as a function of temperature, $S(T)$. This analysis is shown in Fig.5.28. The black curve represents $S(T)$ measured at ambient pressure by the "One heater-Two thermometers" technique. As shown in Subsec. 5.4.1, $S(T)$ curve shows a first order transition from AF_2 to AF_1 state at $T_{AF_1-AF_2} = 24$K and a second order transition from AF_1 to PM state at $T_N = 36$K. The

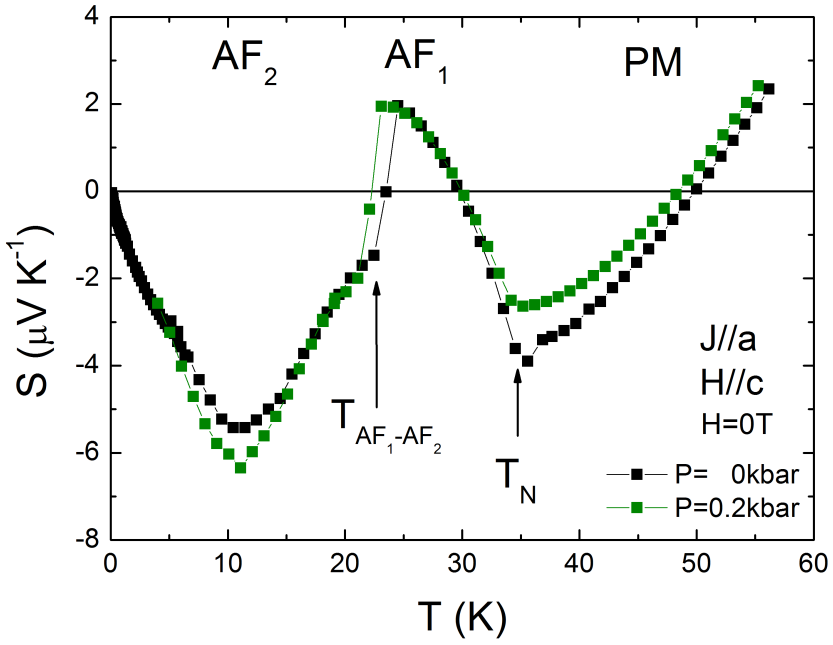

Figure 5.28: *Thermopower as a function of temperature for transverse configuration at $P = 0$ (black curve) and $P = 0.2$kbar (green curve) obtained by "One heater-Two thermometers" and "RTG" techniques, respectively.*

green curve shows $S(T)$ at low pressure, $P = 0.2$kbar, obtained by "RTG Technique". The comparison between these $S(T)$ curves performed at $P = 0$ and under pressure allow us to conclude about the good agreement between the absolute thermopower values of those techniques. Therefore, this validates the pressure setup to obtain absolute values of $S(T)$ under pressure. Moreover, we also observe that pressure tunes the transitions, $T_{AF_1-AF_2}$ and T_N, towards lower temperatures.

$CeRh_2Si_2$ Phase Diagram under Pressure

To determine the (T, P) phase diagram of $CeRh_2Si_2$, we performed thermopower measurement as a function of temperature, $S(T)$, in the different pressure regimes (AF_2, AF_1 and PM phases) with thermal gradient along the a-axis in the temperature range of $[2 - 55]$K (see Fig.5.29).

- For $P < P_c^{'}$, the suppression of the AF_2 and AF_1 phases is observed. As pressure increases, the drop of $S(T)$ corresponding to the AF_1-AF_2 transition becomes smaller and $T_{AF_1-AF_2}$ decreases. At $P >$ 4kbar, the signature of the AF_1-AF_2 transition cannot be identified by thermopower measurements in the temperature range of our measurements. In relation to the AF_1-PM transition, we observe that this transition corresponds to a minimum at low pressure. For $P >$ 3kbar, the AF_1-PM transition becomes a step like transition and two temperatures, just below the step and the maximum above the step, define the width of the transition. We also verify the suppression of the T_N with pressure.

- In the regime $P_c^{'} < P < P_c$, the evolution of the AF_1-PM transition was followed. At low temperature, $S(T)$ becomes positive when the system was far from the magnetic transitions, $P_c^{'}$ and P_c. For pressures around the $P_c^{'}$ and P_c; i.e., the suppression of the AF_1 and the AF_2 phases respectively, $S(T)$ signal is dominated by the magnetic fluctuations related to the instabilities of the AF state and becomes negative.

- For $P > P_c$, if the applied pressure to the compound is high enough to be far from the instabilities related to the suppression of the ordered state, $S(T)$ becomes positive for all the temperature range. Else, $S(T)$ is led by the spin/valence fluctuations and $S(T)$ is negative in the low temperature regime. At high enough pressure, we recover the usual $S(T)$ behaviour for the Kondo Ce-family in the PM phase; a positive Seebeck coefficient in the low temperature range [Amato and Sierro, 1985].

We performed some $S(T)$ measurements, at least one for each phase and close to the AF transitions, in the dilution temperature regime. We verify that, for pressures close to the AF transitions, thermopower does not show divergence and goes to 0 when $T \to 0$. A deeper analysis of the influence of the instabilities in thermopower will be done in the following sub-subsection.

The temperature transitions determined from $S(T)$ curves as a function of pressure, T_N and $T_{AF_1-AF_2}$, are shown in the (T, P) phase diagram of Fig.5.30. The blue symbols of the (T, P) phase diagram of $CeRh_2Si_2$ represent the AF_1-PM transition and the blue error bars show the width of the AF_1-PM transition. The green symbols represent the AF_1-AF_2 transition and their error bars represent the temperature error of the $T_{AF_1-AF_2}$ line. In grey

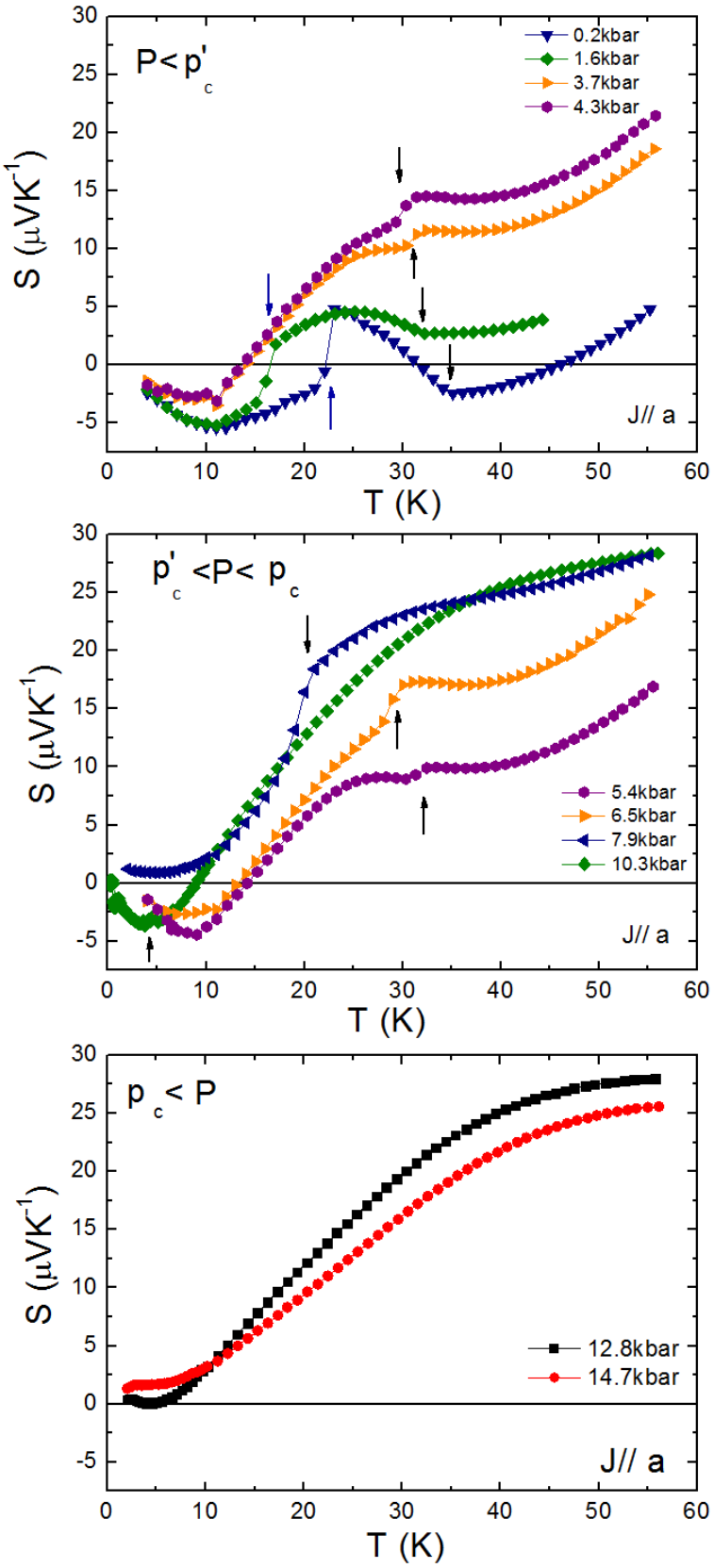

Figure 5.29: *$S(T)$ curves of $CeRh_2Si_2$ with thermal gradient along the a-axis in the $P < P_c^{'}$ (top), $P_c^{'} < P < P_c$(middle) and $P < P_c$ (bottom) pressure ranges. The arrows indicate the transitions.*

symbols, we show the phase diagram obtained from magnetoresistance and neutron measurements. The T_N line and the superconducting domain were determined by resistivity measurements [Araki et al., 2002] and $T_{AF_1-AF_2}$ was determined by neutron measurements [Kawarazaki et al., 2000]. $T_{AF_1-AF_2}$ and T_N determined by thermopower follow the same behaviour than the ones determined by magnetoresistance and neutron measurements. From the thermopower T_N line, we estimate that P_c is located at $P \sim 1.08$kbar. Thermopower could not follow $T_{AF_1-AF_2}$ above 4kbar. The value of $P_c^{'}$ from the $T_{AF_1-AF_2}$ was estimated by the comparison of the shape of this curve to the one obtained by neutrons measurements. To finish, I remark that the quality of the sample we measured, $RRR \sim 10$, was too low to present the superconducting domain.

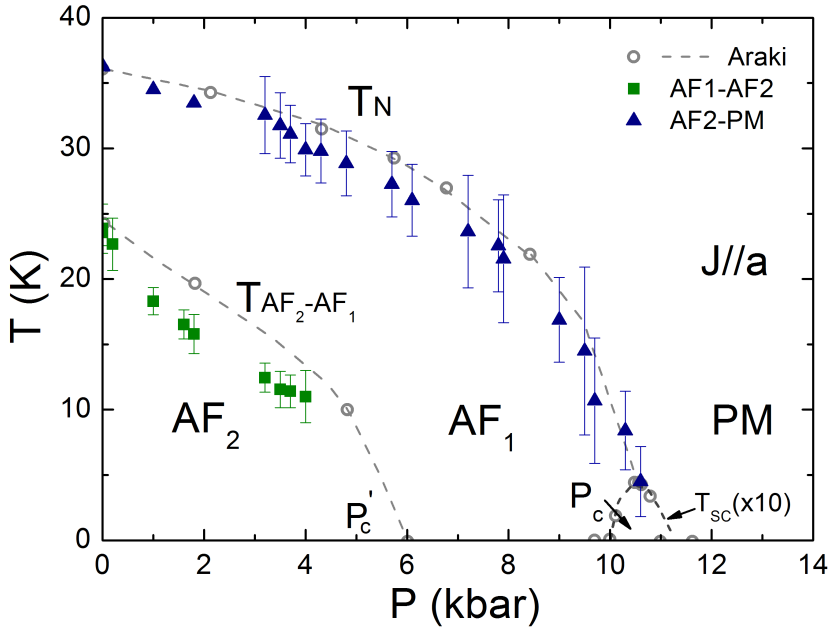

Figure 5.30: *(T, P) phase diagram of $CeRh_2Si_2$. In blue, the AF_1-PM transition is shown and the AF_2-AF_1 transition is indicated by green symbols. The grey symbols show the (T, P) phase diagram determined in [Araki et al., 2002].*

$CeRh_2Si_2$: Main Bands' Contribution under Pressure

We analyze the evolution of the contribution of the main bands to the thermopower signal under pressure at $T = 3$K. We note that $T = 3$K is a rather high temperature. Nevertheless, the Fermi liquid behaviour appears in a large temperature range $T_{FL}^{max} = [7 - 10]$K. Under pressure, T_{FL} reaches its temperature upper limit at P_c [Araki et al., 2002]. Thus, the analysis of the main band contribution under pressure is performed in the Fermi liquid regime of the system although the high temperature of the analysis. For that, we compare S/T as a function of pressure (see Fig.5.31 -left) and we link the modifications in the thermopower signal to the observed changes in the pressure dependence of the dHvA frequencies (see Fig.5.31 -right).

In Fig.5.31 -left, $S/T(P)$ behaviour with thermal gradient along the a-axis at $T = 3$K is shown. In the AF_2 phase, thermopower is negative and increases slowly with pressure. At the magnetic transition between AF_2-AF_1 phases, $P_c^{'}$, a change in the sign of the thermopower

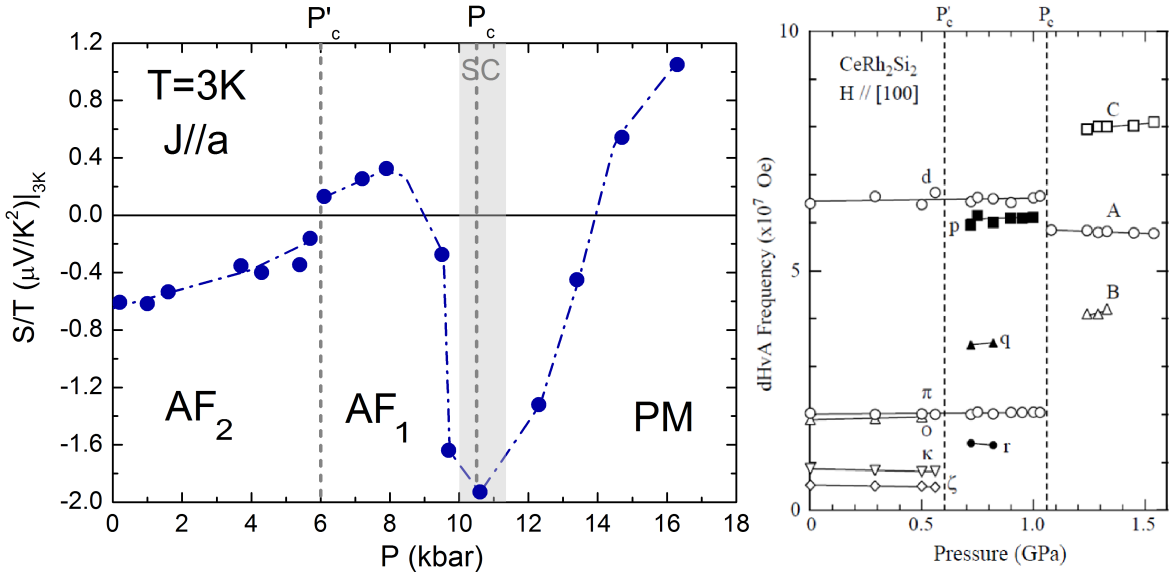

Figure 5.31: *Evolution of S/T at $T = 3K$ as a function of pressure (left figure). Pressure dependence of the dHvA frequencies obtained from ref. [Settai et al., 2003] (right figure).*

occurs. This indicates that the AF_2-AF_1 transition is discontinuous. The Brillouin zone (BZ) changes due to the modifications in the AF phase. This is supported by the dHvA measurements that observe the suppression of the low frequencies (κ, ζ and O bands) at P_c' (see Fig.5.31 -right). The change of the sign might be related to the vanishing of κ, ζ and O bands, electronic-like bands, and the appearance of new hole-like bands, q, p and r, in the AF_1 domain. However, we cannot conclude if d and π bands are hole-like or electron-like because the sign change at P_c' is certainly influenced by the new branches that appear in the AF_1 phase. We can conclude that the addition of the contributions of each band to the thermopower signal is positive in the AF_1 phase. For pressures in the vicinity of P_c; e.g., pressures close to the suppression of the AF order, we observe that thermopower is strongly influenced by the spin and valence fluctuations of the quantum critical point that induce a negative strong contribution to the thermopower signal. As a result, thermopower decreases strongly and reaches its minimum value at P_c. Above P_c and far from the QCP, thermopower becomes positive in the PM domain and shows the normal behaviour for Kondo Ce-based compounds. DHvA measurements show that this transition also causes a strong change of the Fermi surface [Settai et al., 2003]. All the frequencies of the AF phase disappear at P_c and three new higher frequencies appear in the paramagnetic state. The total thermopower contribution in the PM phase is positive, then the total electronic contribution is hole-like. S/T increases in the PM phase with pressure. The nature of this Fermi surface reconstruction was not observed in thermopower measurements as it is coupled to the quantum fluctuations of the QCP which dominates the signal.

We have also analyzed S/T as a function of pressure at $T = 10$K for the same thermal gradient configuration, $J \parallel a$ (see Fig.5.32). We observed that S/T increases with pressure from negative values to positive in the AF_2 state and at the AF_1-AF_2 transition, a sudden change of the sign of the thermopower appears. In the AF_1 state, thermopower remains constant. At the AF_1-PM transition, contrary to what we expect, thermopower does not

reflect the strong Fermi surface reconstruction at P_c and the transition was referenced as second order. The magnetic fluctuations related to the QCP were also not observed in the vicinity of P_c. This is in agreement with the relative high temperature of the analysis as the magnetic fluctuations are expected to be observed in the $T_N/10$ temperature range. In the paramagnetic state, S/T increases with pressure.

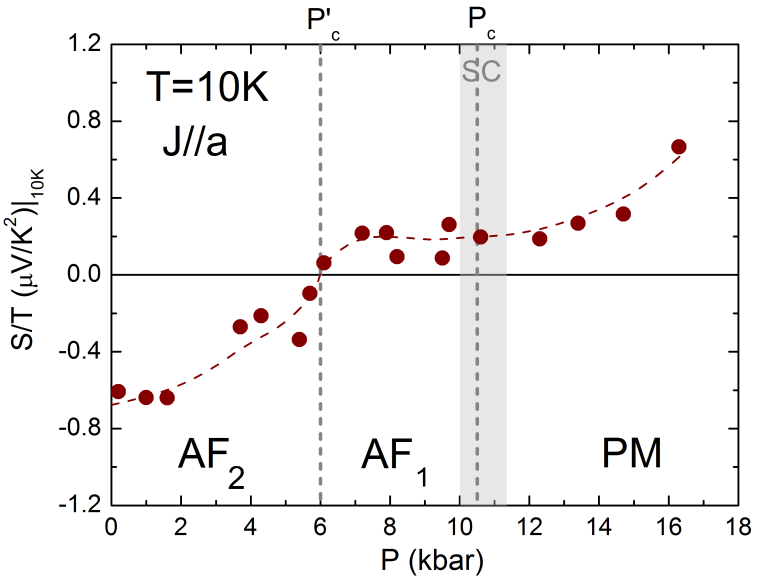

Figure 5.32: *Evolution of S/T at $T = 10K$ as a function of pressure.*

5.6.2 Bridgman Pressure Cell

In this section, we study the thermopower behaviour under pressure and under magnetic field of $CeRh_2Si_2$. The configuration inside the Bridgman cell is: thermal gradient applied along the a-axis and magnetic field along the c-axis. This configuration allows to cover the space between (T, H) and (T, P) phase diagrams obtaining a complete (T, P, H) phase diagram. Analyzing $S(H)$ and $S(T)$ under pressure, we may understand the relation between the suppression of the AF phase by pressure and by magnetic field and in turn the relation between the paramagnetic and the polarized paramagnetic phases. The key point is to understand how pressure and magnetic field external parameters convert the ordered state into non-ordered states.

Previous magnetoresistance measurements under pressure, performed by Knafo at LNCMI-Toulouse, demonstrated that the transition from the PM to the PPM is really large and it is located at fields around 50T for the pressure we studied.

In the first loading of the Bridgman pressure cell, the system reached $P = 14$kbar and the AF order of the compound was suppressed for this pressure value. As a consequence, we performed only thermopower studies in the PM phase through the PPM phase (see the green line of the (T, P, H) phase diagram shown in Fig.5.33). $S(T)$ measurements carried out in the PM phase of $CeRh_2Si_2$ are shown in Fig.5.34. We observed that for this pressure the system is almost out of the influence of the magnetic fluctuations appearing at the P_c which do not depend on increasing the magnetic field. For the applied magnetic fields, up to 9T, the PM

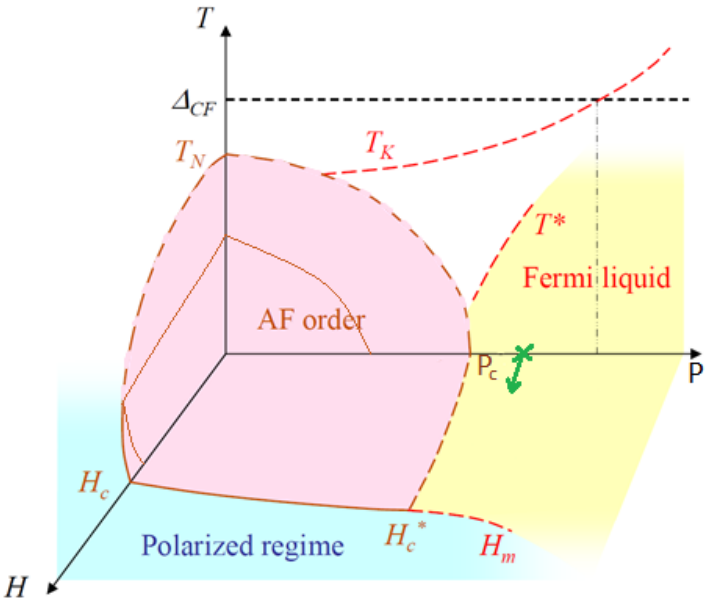

Figure 5.33: *Schematic (T, P, H) phase diagram of $CeRh_2Si_2$. The green arrow shows the thermopower measurements performed using the Bridgman pressure cell.*

phase does not show any change. Then, the Fermi surface change from PM to PPM phases does not occur progressively from the low field regime. We notice that even if this transition is very large, at 9T we are far from it. Therefore, we did not observe any signature in the thermopower signal.

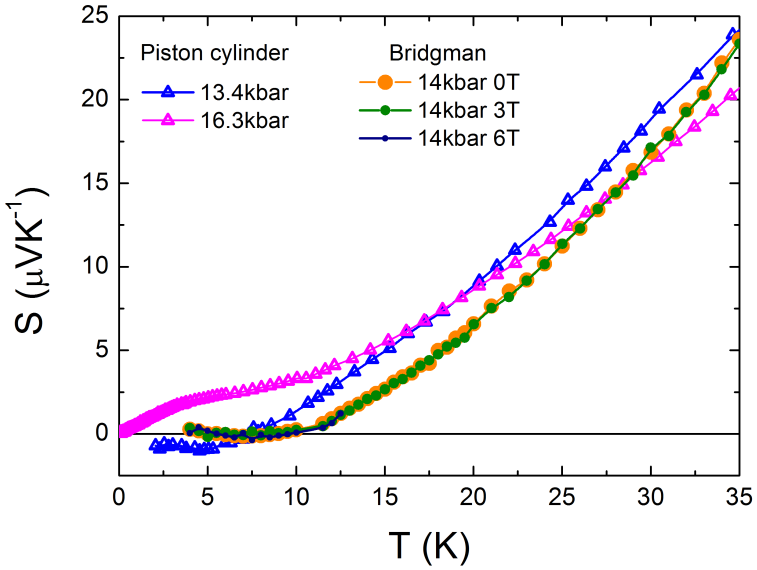

Figure 5.34: *$S(T)$ measurements performed in a Bridgman pressure cell (filled symbols) under pressure and under magnetic field. $S(T)$ measurements obtained in the piston cylinder pressure cell (open symbols) are shown to compare both pressure setups.*

To finish, we observe the agreement of thermopower measurements under pressure performed in the piston cylinder and in the Bridgman pressure cells. They present similar

thermopower absolute values and similar evolution of the thermopower behaviour with temperature.

Lower pressures could not be applied to the system to study the suppression of the AF order by the combination of field and pressure because the Bridgman pressure cell is not adapted to low pressure regimes.

5.7 Discussion

In this section, we compare the suppression of the AF order by magnetic field and pressure. Isothermal thermopower measurements $S(H)$ as a function of magnetic field revealed the suppression of the AF domain by a two step transition. The $S/T(P)$ dependence at fixed temperature shows a change of the thermopower sign between the two AF phases, which matches with the suppression of the electron-like bands of the AF_2 phase. At P_c, the spin/valence fluctuations dominates the thermopower signal and mask the signature of the Fermi surface instability appearing close to P_c. Nevertheless, dHvA measurements under pressure demonstrate the complete reconstruction of the Fermi surface at P_c.

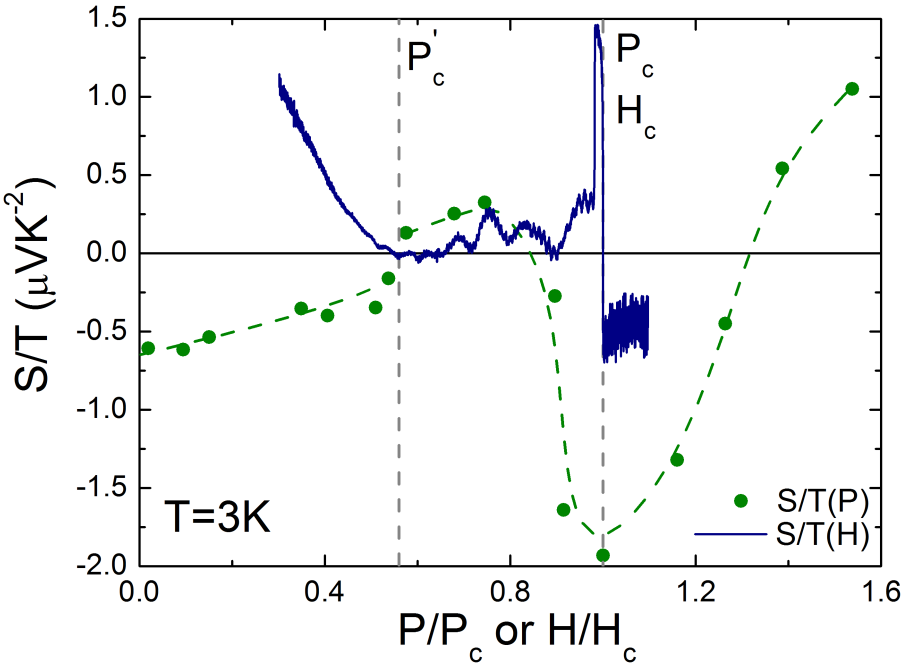

Figure 5.35: *Evolution of S/T as a function of P/P_c (in green) and as a fucntion of H/H_c (in blue) of $CeRh_2Si_2$ at $T = 3K$.*

In Fig.5.35, the evolution of thermopower signal as a function of magnetic field and as a function of pressure is compared. $S/T(H)$ as a function of H/H_c is shown by the blue curve and the $S/T(P)$ as a function of P/P_c by the green curve. Both thermopower behaviours are represented at $T = 3$K. We observe from $S/T(H/H_c)|_{T=3K}$ measurement that the magnetic transition is very sharp at H_c indicating that this is clearly a first order transition. In addition, the short width of the transition points out that the magnetic fluctuations, which drive the

transition, are located in a narrow area of the phase diagram and they affect the complete Fermi surface. Concerning $S/T(P/P_c)$ measurements, we demonstrate that the signature of the suppression of the AF order in the thermopower signal was dominated by valence/spin fluctuations associated to this Fermi surface instability. These fluctuations are spread in a large pressure range and avoid to determine the signature of the first order magnetic transition at low temperature close to P_c, as expected from the Fermi surface reconstruction indicated by dHvA measurements. In despite of no signature of this transition was observed in $S/T(P/P_c)$ study, a strong decrease of T_0 value at pressures close to P_c was observed. This strong decrease of T_0 is in agreement with the first order transition in the vicinity of the QCP. The existence of a QCP and a Fermi surface reconstruction at the same pressure complicates the analysis of the nature of the transition. We suggest that the transition may be considered as a weak first order transition as a Fermi surface reconstruction is associated. Then an unconventional QCP scenario [Miyake and Ikeda, 2006], associated to the discontinuity at P_c, is proposed to describe the behaviour around this critical pressure. We note that the spin/valence fluctuations were observed in a large pressure range as they are localized in space.

The "localized" to "itinerant" duality analyzed in ref. [Hoshino and Kuramoto, 2013] suggest that this duality may also occur at $P_c^{'}$ in $CeRh_2Si_2$ as this compound presents a strong symmetry at both sides of the transition. The main frequencies remain above the transition and nearly flat bands are below and above it. In this case, the transition between AF_1 and PM is from an itinerant behaviour to an another itinerant one with a first order nature due to the strong Fermi surface reconstruction. Moreover, the low pressure and low magnetic field regime presents a sign change of the $S/T(P/P_c)$ at AF_1-AF_2 transition that matches with the sudden increase of $S/T(H/H_c)$ for $H/H_c \leqslant P_c^{'}/P_c$. This signature appears for $T < 8$K and supports the [Hoshino and Kuramoto, 2013] description of the Fermi surface transitions under pressure.

The non-ordered states, PM and PPM for pressure and field dependencies respectively, present an opposite thermopower behaviour. $S/T(H/H_c)$ measurements present a negative sign in the PPM whereas $S/T(P/P_c)$ measurements present a positive sign in the PM phase. In addition, this antagonist phenomenon is reinforced with temperature evolution; i.e., as the temperature increases, then $S/T(H/H_c)$ becomes more negative while $S/T(P/P_c)$ increases its thermopower value. Therefore, the Fermi surfaces of the non-ordered states are different.

Field and pressure suppressor mechanisms of the AF state seem to be different from a thermopower point of view (sharp and negative vs broad and positive). Surprisingly, analysis of the field dependence of the T^2 term of the resistivity, $A(H)$ coefficient [Knafo et al., 2010], show that the relative field variation $A(A)/A_{max}$ as a function of $(H - H_c)/H_c$ mimics the relative pressure variation $A(P)/A_{max}$ as a function of $(P - P_c)/P_c$. Clearly, the thermopower response in field is dominated by the drastic Fermi surface change which occurs at the well defined first order transition H_c. By contrast, the good scaling of A/A_{max} in $(H - H_c)/H_c$ or $(P - P_c)/P_c$ may reflect the key role of local fluctuations and rather short range of the intersite magnetic interactions.

Under pressure, the pressure range of fluctuations at the QCP was also analyzed by thermopower. To carry this analysis out, we performed a comparison between normalized thermopower over temperature at 3K, $-S/T(3K)|_{norm}$, and the $\sqrt{A_{norm}}$ coefficient, ${A/A_{max}}^{1/2}$, as a function of P/P_c (see Fig.5.36). Thermopower is represented in dark cyan symbols and

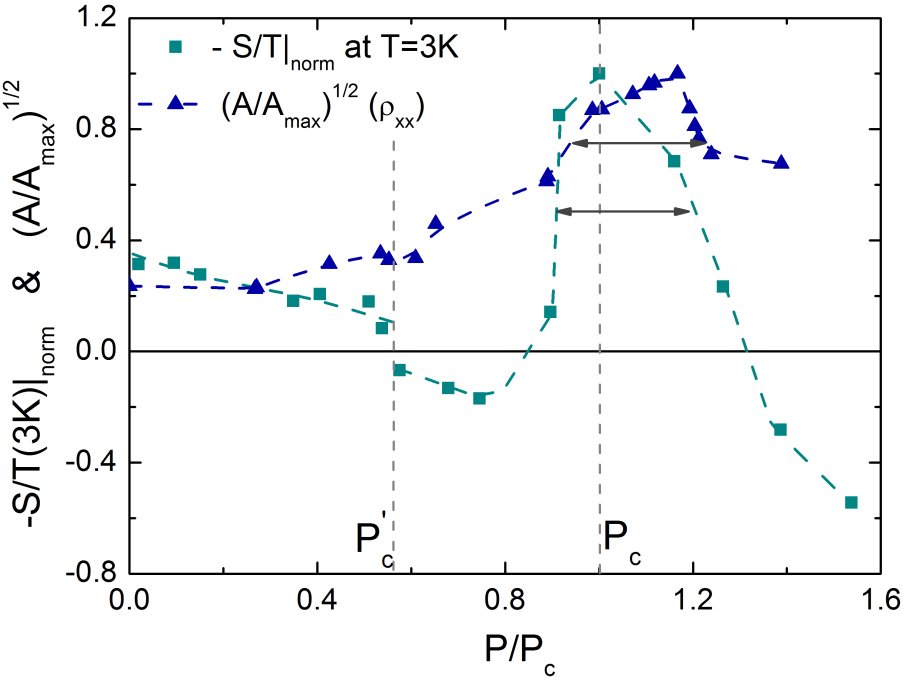

Figure 5.36: *Comparison of the S/T_{norm} (dark cyan symbols) and of $\sqrt{A_{norm}}$ coefficient (blue symbols) obtained from ref. [Boursier, 2005]) as a function of pressure.*

the $\sqrt{A_{norm}}$ coefficient is traced in dark blue. In one single band scheme, S/T and $\sqrt{A}$, both depend linearly with m^*. The pressure range, in which the influence of the fluctuations at the QCP or the Fermi surface instability is observed in thermopower measurements, has a similar width that the one of the $\sqrt{A_{norm}}$ coefficient close to P_c of ref. [Boursier, 2005]. We note that $S/T|_{norm}$ is different than $\sqrt{A_{norm}}$ as S/T is more sensitive to the Fermi surface changes. The clear signature of the Fermi surface change will only appear by modifications on the thermopower quantum oscillation frequencies as detected by dHvA experiments [Araki et al., 2002].

Fig.5.37 shows the comparison as a function of pressure between the residual resistivity ρ_0 and $S/T(3K)|_{norm}$. We observe that both parameters seems to be in good agreement as (i) the sharp modification at $P_c^{'}$ is observed in both quantities and (ii) development of a localized maximum/minimum value around the critical pressure P_c is correlated. We notice that this behaviour is as expected due to thermopower is weighted by the value of ρ_0^{-1} of each orbit ($S = \frac{\Sigma\sigma_i S_i}{\sigma}$). At $P < P_c^{'}$, the increase of the ρ_0 value is detected by an increase of thermopower, then the decrease of $\Delta\Sigma\sigma_i S_i$ must be smaller than decrease of $\Delta\sigma$; σ_i should only modify light thermopower bands. At $P_c^{'}$, we note that ρ decreases and as it is expected in a simple one band system, S/T increases. In addition, the relative decrease in S/T is higher than the relative increase of ρ. We suggest the spin/valence fluctuations around the QCP modify stronger the thermopower signal as it depends not only on σ, but also on its derivative (Mott formula). Finally, at P_c, ρ and S/T shows a moderate increase of their values. A simple analysis is quite difficult in $CeRh_2Si_2$ as it is a complex multiband system. Calculations are needed to well understand the modifications that appear at the transitions on the system.

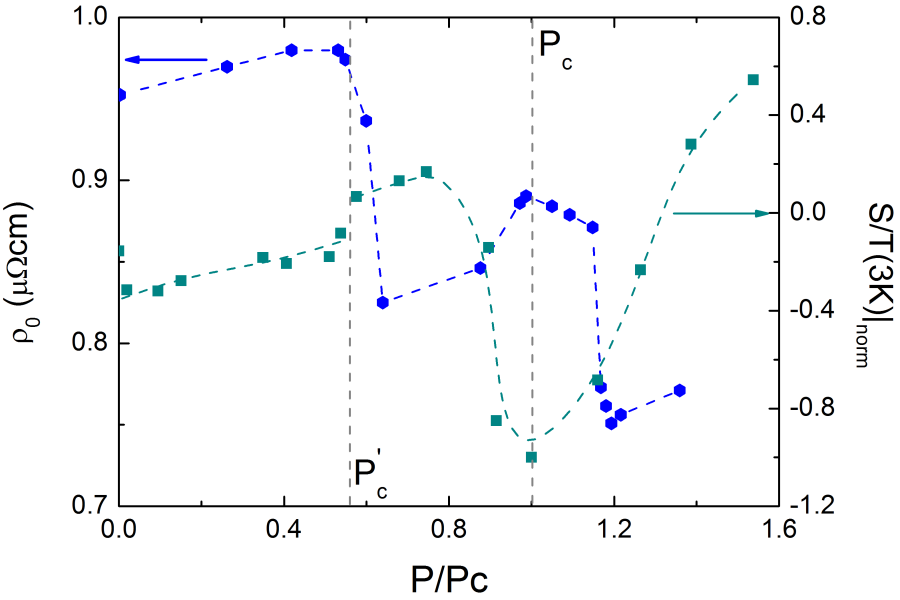

Figure 5.37: *Comparison between $S/T|_{norm}$ (dark cyan symbols) and ρ_0 extrapolated at $T = 0$ (blue symbols obtained from ref. [Boursier, 2005]) as a function of pressure.*

Fermi surface reconstructions are sharp and localized transitions, thus the effects are only visible in their vicinity. Sometimes, they may be coupled to other type of phenomenon such as spin or valence fluctuations. Therefore, the strong change related to the Fermi surface reconstruction in the thermopower signal can be masked as the contribution belonging to the other effect can dominate. This is due to the fact that thermopower is very sensitive to the band reorganization, the weight of each band and to the energy derivative of the density of states. $CeRh_2Si_2$ is a clear example of a system in which the spin/valance fluctuations are associated to a Fermi surface change.

5.8 Conclusions for $CeRh_2Si_2$

These measurements confirm the interest to perform thermopower measurements to analyze the modifications of the Fermi surface. As we showed, thermoelectricity is a sensitive probe to macroscopic thermodynamic properties (sign of carriers, effective mass renormalization) and to scattering. Observation of quantum oscillations is a direct opportunity to demonstrate without ambiguity if there is a Fermi surface change at the transitions.

Ambient pressure: Temperature Evolution

The temperature dependence of the Seebeck coefficient $S(T)$ at ambient pressure indicates the AF_1-PM magnetic transition at 36K and AF_1-AF_2 metamagnetic transition at 24K. These transitions are second order and first order, respectively and they were identified with changes in the magnetic configuration along the c-axis by neutron measurements.

Thermopower measurements probe the isotropy of $CeRh_2Si_2$ in the low temperature regime. The extrapolated value of $S/T(T \to 0)$ is similar for transverse and longitudinal configurations

at $H = 0$.

Ambient pressure: Magnetic Field Evolution

We measured the Seebeck coefficient sweeping the magnetic field upwards at a constant rate from 0 to 30T. The obtained results are:

- A direct measurement of quantum oscillations in the AF_2 phase. The Fermi surface of the AF_3 phase was not possible to be measured because of the short magnetic field range of this phase (smaller than 1T) and in the PPM phase no frequency was observed.
- The orbits of the AF_2 and their evolution increasing the magnetic field were analyzed. The cyclotron mass, the Dingle temperature and the mean free path for each orbit were determined. A good agreement with dHvA measurements was observed.
- At high fields, new orbits were detected. The magnetic breakdown and the mass spin splitting of the ν orbit phenomenon were observed.
- We demonstrated the advantages of thermopower quantum oscillations over other Fermi surface mapping probes: no background has to be removed to observe the quantum oscillations, the oscillations appears for temperatures of one order magnitude higher compare to traditional probes and high harmonics of the main frequency, ν, were easily detected.
- The suppression of the AF order by magnetic field was studied. At low pressure, it is first order and the AF phase is suppressed by a two-step transition. The transition becomes second order above the TCP point.
- Reconstruction of the (T, H) phase diagram. Existence of a multi-critical point.

Under Pressure

We demonstrate that our pressure setups, piston cylinder and Bridgman pressure cells, determine absolute values of thermopower and thermopower is very sensitive to all the modifications of the system. We verify the suppression of the AF domain into a paramagnetic domain by pressure as shown in the (T, P) phase diagram. Pressure moves the system from dominant RKKY interaction to dominant Kondo interaction balancing the system from a localized to an itinerant behaviour of the f electrons.

S/T measurements as a function of pressure for a fixed temperature reveal a sudden change of the sign of the thermopower signal at the AF_1-AF_2 transition indicating that it is a first order transition. At the AF_1-PM transition for pressures close to P_c, the spin/valence fluctuations appearing close to the QCP and the Fermi surface instability due to the Fermi surface reconstruction are strongly coupled.

Finally, the comparison between the absolute values of $S(H)$ and $S(P)$ in the PPM and PM phases suggests the Fermi surfaces of PM and PPM are not equivalent. In addiction, the suppression of the AF order by field is clearly first order whereas under pressure it seems to be weakly first order.

Conclusion

The aim of this thesis involves two different but related projects: the development of new thermoelectric instrumentation and its application to study the different phases of heavy fermion compounds.

Concerning the first project, I have designed two novel setups to measure thermoelectricity under pressure at low temperature, $[0.3 - 50]$K, and under magnetic field. These new setups fit inside a piston cylinder and a Bridgman pressure cells.

The second part of my PhD work is related to the physics of heavy fermion systems. Specially, I have studied the (T, P, H) phase diagram and the magnetic competing order. Various measurements techniques, such as thermopower and magnetoresistance, were used to explore the physics of these compounds. Moreover, thermopower quantum oscillations were used to analyze the topology of the Fermi surface as an alternative method to standard de Haas-van Alphen or Shubnikov-de Haas effects for the first time in heavy fermion systems.

The investigated compounds were UCoAl, UGe_2 and $CeRh_2Si_2$. These are strongly correlated electron systems with a value of the electronic specific heat of the order of $\gamma \lesssim 100\text{mJmol}^{-1}\text{K}^{-1}$ which corresponds to a moderate heavy fermion behaviour. They are characterized by having different ground states (UCoAl is a paramagnet, UGe_2 is a ferromagnet and $CeRh_2Si_2$ presents an antiferromagnet ground state) and for being close to quantum phase transitions.

The analysis at an ambient pressure of the first compound, UCoAl, by thermopower measurements reveals that it is characterized by a strong and sharp discontinuity at the metamagnetic transition below T_0 indicating the first order character of the transition. This first order line of transitions ends up the critical end point CEP(T_0, H_M^*) where an increase of the correlations was observed. Above it, a crossover regime appears. Exotic magnetic excitations were also observed in the paramagnetic ground state of UCoAl at low temperatures in the Seebeck coefficient over temperature. They were associated to the magnetic frustration of the quasi-Kagome lattice of the compound. Under pressure, we observe the suppression of the ferromagnetic order towards the quantum critical end point (wing structure). Inside this magnetic structure, we notice the decrease of the jump of thermopower signal at the metamagnetic transition and the enhancement of the hole thermopower contributions with pressure. When magnetic field and pressure tune the system to the QCEP, a rapid decrease of T_0 was measured. However, no signature on the Seebeck coefficient was observed. We expected to have a divergence on the thermopower signal due to the entropy accumulation at the QCEP. This suggests that the singularities under pressure are restricted to very low temperature and well determined field and pressure conditions.

We deeply analyzed thermopower quantum oscillations to determine the Fermi surface of

heavy fermion systems as UGe_2. We also studied the Fermi surface of UGe_2 by Shubnikov-de Haas (SdH) effect and we compared these studies to on literature the de Haas-van Alphen (dHvA) measurements. Thermopower quantum oscillation measurements were analyzed by different thermopower models (Young-Fletcher, Trodahl and Peschanskii) and by the Lifshitz-Kosevich (LK) theory of the dHvA effect. We demonstrate that the LK theory is valid for the analysis of thermopower quantum oscillations in heavy fermion systems. We verified that the main contribution to the thermopower signal is the oscillatory one, that the oscillations persist in a higher temperature range compared to SdH or dHvA effects and that no background has to be removed to observe the thermopower quantum oscillations. We confirmed the good agreement in the results obtained by these three probes that in turn, are in good agreement with the calculations of the topology of the Fermi surface.

Finally, thermopower measurements also show the suppression of the antiferromagnetic (AF) order of $CeRh_2Si_2$ by magnetic field and by pressure. Magnetic field destroys the AF order by a first order transition at low temperatures. Pressure moves the system from an uncompensated to a compensated state as a result of the modification of the hybridization of the system (dominant RKKY interaction to dominant Kondo interaction from low to high pressures). The transition at P_c has been identified as a weak first order transition due to it is masked by the spin/valance fluctuations of the QCP. A clear proof of this first order nature is the strong change of the Fermi surface measured by dHvA measurements. The evolution of the thermopower over temperature signal was analyzed as a function of P/P_c and as a function of H/H_c. Thermopower signal shows different signs in the PPM and in the PM phases. We conclude that $CeRh_2Si_2$ has two different Fermi surfaces for the PPM and the PM phases. This is also supported by the different Fermi surface frequencies associated to the PPM and PM phases obtained by torque and dHvA effects, respectively. Moreover, a direct detection of the AF_2 phase by thermopower quantum oscillations was performed. New frequencies of the Fermi surface were detected. In addition, the spin dependence of the effective mass of the main frequency ν was observed at high fields.

We conclude that thermopower indicates first order transitions by a strong change of the thermopower signal. It usually presents a discontinuity on its value and sometimes, it shows a change in the sing depending on the Fermi surface modifications along the direction of the thermal gradient. Second order transitions are indicated by a well defined change in the slope and the crossover by large anomaly in the thermopower signal. Nevertheless, the limit between second order and crossover transitions is not so clear in thermopower measurements. Concerning thermopower quantum oscillations, we conclude that the oscillatory contribution dominates the thermopower signal in the case of high quality samples and we indicate that LK theory is valid to determine the parameters of the Fermi surface of heavy fermion systems by thermopower quantum oscillations.

Résumé de la thèse en français

.1 Résumé

Cette thèse porte sur l'étude sous conditions extrêmes (basse température, fort champ magnétique et haute pression) des composés fortement corrélés du type fermions lourds. Trois composés ont été analysés UCoAl, UGe_2 et $CeRh_2Si_2$, en utilisant principalement de mesures thermoélectriques; une technique récente et très sensible dans le domaine des fermions lourds. À cette fin, de nouvelles dispositives de mesures de pouvoir thermoélectricité sous pression ont été développés au cours de cette thèse.

Concernant le composé d'UCoAl, notre étude a permis d'analyser précisément la transition metamagnétique, induite par le champ magnétique, entre la phase paramagnétique (PM) et la phase ferromagnétique (FM) ainsi que, son évolution sous pression. Ainsi, nos mesures du pouvoir thermoélectriques ont permis de compléter le diagramme de phase (T, P, H) et notamment, de mettre en évidence la structure magnétique originale qui apparaît sous pression en forme de "'wings".

Une fine analyse de la surface de Fermi de la phase FM2 d'UGe_2 a été réalisée grace à l'observation des oscillations quantiques du pouvoir thermoélectrique. Les résultats obtenues ont été comparés aux études conventionnelles des oscillations quantiques comme de "de Haas-van Alphen" (dHvA) et de "Suhbnikov-de Hass" (SdH) effets. Un très bon accord entre les trois techniques a été constatée.

Finalement, dans le système $CeRh_2Si_2$, la suppression du domaine antiferromagnétique (AF) sous champ magnétique $H_c \sim 26$T et sous pression $p_c \sim 1$GPa a été étudiée. Un très fort changement de la surface de Fermi à H_c correspondant à la transition de l'ordre AF vers une phase paramagnétique polarisée (PPM), a été observé. Sous pression, des fluctuations magnétiques et une reconstruction de la surface de Fermi apparaissent autour de p_c. Ces fluctuations cachent la nature de la suppression de l'ordre AF vers un ordre paramagnétique (PM). L'étude du diagramme de phase (T, H, P) révèle que les phases PM et PPM sont différentes, cependant des points en commun demeurent.

Mots clés:
Composés fortement corrélés-Fermion lourds
Criticalité quantique
Coefficients thermoélectriques
Mesure de la surface de Fermi
Conditions extrêmes: basses températures, forts champ magnétiques et hautes pressions

.2 Introduction française

Les fermions lourds sont une famille de composés fortement corrélés du type liquide de Fermi caractérisés par une très forte re-normalisation de la masse effective. La re-normalisation est due à la présence des orbitales 4 ou 5 f incomplètes des lanthanides ou actinides. Les orbitales f de ces atomes sont plus ou moins localisées près du noyau. En plus, elles ont une énergie proche à l'énergie de Fermi ce qui leurs permet de s'hybrider avec les électrons de conduction (orbitales s, p et d). Cette hybridation est également à l'origine de la nature complexe de diagrammes de phase de ses composés, car ces orbitaux f incomplètes introduisent des moments magnétiques dans le system. Les fermions lourds présentent un grand nombre d'ordre électroniques en compétition. La température de Fermi est aussi renormalisée à une valeur basse ce qui est une caractéristique propre des fermions lourds contrairement aux autres familles des composés fortement corrélées comme les systèmes à haute température critique (cuprates, pnictides). Leur faible température de Fermi et donc, la facilité de modifier l'état fondamental de ces composés par champ magnétique, dopage et pression ont permis l'étude des ordres en compétition.

Récemment, la thermoélectricité a eu un regain d'intérêt dans l'étude des transitions de phases et des propriétés à très basse températures des systèmes fortement corrélés. Ainsi, cette thèse se basse principalement sur l'étude des fermions lourds sous conditions extrêmes par le pouvoir thermoélectrique.

D'un point de vue expérimental, les fermions lourds impliquent de fortes conditions extrêmes pour leur étude comme les basses températures, les hautes pressions, les dopages et/ou les forts champs magnétiques. Ces parametres ont permit de modifier l'hybridation des bands du système qui gouverne le caractère itinérant/localisé du magnétisme. Dans ces systèmes, cette compétition peut être comprise en général à travers du diagramme de phase de Doniach. Un spécial intérêt a les points critiques quantiques par des mesures de thermoélectricité. Pour procéder à ces études, nous avons notamment utilisé la pression au lieu du dopage comme paramètre de contrôle, car la pression modifie le système sans introduire de désordre. De plus, la pression peut être appliquée de façon contrôlé et quasi-réversiblement.

Une des motivations principales de cette thèse a été de concevoir et d'optimiser des montages de pouvoir thermoélectrique sous pression, à basse température et fort champ magnétique pour l'étude de la compétition d'ordres magnétiques. En effet, les différents phénomènes physiques qui arrivent autour des points critiques quantiques comme la suppression/apparition de l'ordre magnétique, la phase non-liquide de Fermi et/ou la supraconductivité, présentent une très forte dépendance de la pression. Dans cette thèse nous avons aussi étudié les transitions magnétiques induites sous champ magnétique et nous avons aussi analysé la surface de Fermi à travers les oscillations quantiques du pouvoir thermoélectrique.

.3 Le plan de la thèse

La thèse est divisée en 5 chapitres. Le premier correspond à la description théorique de la physique des fermions lourds ainsi qu'une description précise des différents principes de thermoélectricité. Le deuxième chapitre décrit les techniques de mesures utilisées et les conditions extrêmes de basse température, fort champ et hautes pressions sous lesquelles les mesures ont

été faites. Les chapitres suivants exposent les résultats obtenus pendant la thèse. Le chapitre 3 présente l'analyse d'UCoAl. La première partie de ce chapitre concerne la transition metamagnétique induite par le champ magnétique et la deuxième partie, l'étude des wings sous pression jusqu'au point critique quantique. Le chapitre 4 montre les résultats de l'étude de la surface de Fermi ferromagnétique FM2 d'UGe_2 obtenus à travers les oscillations quantiques du pouvoir thermoélectrique. Ainsi, la comparaison entre les différents modèles du pouvoir thermoélectrique afin de déterminer les paramètres de la surface de Fermi. Le dernier chapitre est dédié à la suppression du domaine antiferromagnétique (AF) du composé $CeRh_2Si_2$ par le champ magnétique et la pression. Enfin, une conclusion générale finalisera cette thèse.

.4 Résumé des chapitres

Chapitre 1 - Contexte scientifique

Dans ce chapitre, le contexte scientifique général est présenté rapidement. On commence par la physique des fermions lourds et la théorie du liquide de Fermi, on continue avec la présentation de l'ordre magnétique en compétition dans ce type de composés et on finit par les théories des non liquides de Fermi. Une description mathématique des coefficients thermoélectriques est aussi proposée. Un point aussi important est la description de l'effet Seebeck par la formule de Mott qui considère que la dynamique du système est divisé en bandes lourdes et bandes légères sans imbrication dans la limite $T \to 0$.

Chapitre 2 - Techniques expérimentales

Les techniques expérimentales ainsi que les conditions extrêmes de basse température, fort champ magnétique et haute pression sont montrées dans ce chapitre. Un des enjeux de la thèse a été de développer des montages de pouvoir thermoélectrique sous pression; ces montages (cellule piston cylindre et cellule Bridgman) sont détaillés dans le chapitre. Dans la suite, on montre les techniques de mesure: mesures sous conditions stables et mesures en continue ainsi que les équations utilisées pour chaque technique. Une comparaison entre les montages et techniques des mesures sous vide et sous pression est faite au long du chapitre.

Chapitre 3 - UCoAl

L'analyse du diagramme de phase (T, H) d'UCoAl est faite dans la première partie de ce chapitre. La transition metamagnétique du paramagnétisme (PM) au ferromagnétisme (FM) induite sous champ magnétique est étudiée. Une possible explication des modifications de la surface de Fermi à travers la transition metamagnétique en fonction des modifications du pouvoir thermoélectrique et du calcule de bandes est proposée. Les coefficients thermoélectriques ont servi à l'observation des excitations magnétiques exotiques à basse température dans la phase paramagnétique, excitations qui seraient liées aux frustrations de la structure de quasi-kagomé d'UCoAl et autour du point final critique (CEP) qui sont liés à la modification de la transition metamagnétique du premier ordre vers un crossover. Cette analyse est soutenue par des mesures complémentaires de résistivité et chaleur spécifique. En deuxième partie, l'analyse des "wings" sous pression montre l'évolution du CEP (diminution de

T_0 et augmentation du H_M^*) vers le point critique quantique final (QCEP). On a constaté la décroissance rapide de T_0 aux alentours du QCEP. Néanmoins, les gammes de température et de pression de nos mesures ne nous permettent pas d'identifier la signature du QCEP dans le coefficient Seebeck.

Chapitre 4 - UGe_2

L'analyse de la surface de Fermi FM2 d'UGe_2 grâce à l'observation d'oscillations quantiques du pouvoir thermoélectrique est montrée dans ce chapitre. Une comparaison sur les différents modèles théoriques indique que la théorie de Lifshitz-Kosevich peut être utilisée pour déterminer la masse effective, la température de Dingle et le libre parcours moyenne à partir des oscillations quantiques thermoélectriques. Le bon accord des résultats avec d'autres sondes plus communes telles que l'effet de "Shubnikov-de Haas" (SdH) et l'effet de "de Haas-van Alphen" (dHvA) suggère que même si l'origine des oscillations est partialement différente dans ces techniques, la variation de l'amplitude des oscillations avec la température et le champ semble être la même; c.à.d, l'evolution est indépendent de la technique de mesure.

Chapitre 5 - $CeRh_2Si_2$

Le composé $CeRh_2Si_2$ à basse température montre un état antiferromagnétique isotrope. En fonction de la température, il suit une transition du premier ordre entre deux états antiferromagnétiques à 24K et la suppression de l'état antiferromagnétique est caractérisée par une transition du deuxième ordre à 36K. Les transitions peuvent être amenées à $T = 0$ par le champ magnétique et la pression. On a analysé la suppression de l'ordre magnétique en déterminant les diagrammes de phases (T, H) et (T, P). Les mesures de $S/T(H)$ et $S/T(P)$ indiquent des fortes modifications de la surface de Fermi à H_c et p_c, champ magnétique et pression correspondant à la suppression de la phase antiferromagnétique. La comparaison de ces mesures indique que les surfaces de Fermi de phases PM et PPM ne sont pas équivalentes entre elles. Cette analyse est en accord avec les mesures de dHvA.

Enfin, une analyse précise de la surface de Fermi a pu être obtenue grâce à l'observation d'oscillation quantique thermoélectrique dans ce composée. De forts changements du régime du pouvoir thermoélectrique ont été observés aux transitions de phases, notamment près de H_c.

.5 Conclusion générale en français

Le but de cette thèse a été de développer de nouveaux montages pour les mesures du pouvoir thermoélectrique sous pression et ensuite d'appliquer cette technique pour l'analyse des diagrammes de phase des fermions lourds.

Pendant la première phase du projet, deux nouveaux dispositives expérimentaux permettant de mesurer le pouvoir thermoélectriques sous pression ont été développés. Ces montages ont été conçus pour s'ajuster au volume restreint des cellules de pression de type piston cylindre et Bridgmann. Ils sont calibrés pour des mesures dans la gamme de températures comprise entre 0.3 et 50K et sous un champ magnétiques pouvant aller jusqu'à 16T.

Pour la deuxième phase du projet, l'analyse de la physique des fermions lourds, j'ai spécialement étudié les diagrammes de phases (T, P, H) à basse temperature. L'état fondamental, la compétition de l'ordre magnétique et l'analyse des paramètres microscopiques ont été explorés par des mesures de pouvoir thermoélectrique ainsi que de résistivité. Les composés explorés sont UCoAl, UGe_2 et $CeRh_2Si_2$. Ce sont des fermions lourds moderés avec des états fondamentaux très différents: l'état fondamental d'UCoAl est une phase paramagnétique (PM), pour UGe_2 c'est une phase ferromagnétique (FM) et dans $CeRh_2Si_2$ l'état fondamental est antiferromagnétique (AF).

Les résultats majeurs sur le composé UCoAl à pression ambiante portent sur l'analyse de la transition metamagnétique induite sous champ magnétique de l'état fondamental à l'état FM, ainsi que sur la divergence du pouvoir thermoélectrique dans la phase PM à basse températures produite par la frustration magnétique de la maille du type quasi-kagomé des atomes d'Uranium. Les contributions anormales dans l'effet Nernst liées á la modification de la transition metamagnétique ont été aussi observées. La transition est une transition du premier ordre à basse température qui devient un "crossover" au-dessus du CEP(T_0, H_M^*). Sous pression, l'évolution des "wings" (la structure ferrommagnétique) vers le point critique quantique final (QCEP) a été observée. Le saut du pouvoir thermoélectrique à la transition metamagnétique devient de plus en plus petit lorsqu'on s'approche du QCEP. Il est associé à une contribution des charges positives au pouvoir thermoélectrique qui augmente sous pression. La température T_0 diminue avec la pression et aux alentours du QCEP, elle montre une rapide diminution vers $T = 0$K. La divergence du pouvoir thermoélectrique autour du QCEP était attendue comme conséquence de l'accumulation d'entropie liée aux fluctuations. Néanmoins, aucune réelle divergence n'a été observée. On suggère que les singularités liées au QCEP n'apparaissent qu'à très basse température et donc, elles ne sont pas visibles par nos mesures s'arretant au dessus de 2K.

Une analyse détaillée de la composante oscillatoire du pouvoir thermoélectrique a été réalisée dans le composé UGe_2. Cette contribution oscillatoire donne l'information liée à la surface de Fermi des composées. Elle est analogue à la contribution oscillatoire de la magnétorésistance, SdH, ou de la susceptibilité magnétique, dHvA et c'est pour cela qu'une comparaison entre ces trois techniques a été réalisée dans ce système. Les oscillations quantiques du pouvoir thermoélectrique ont été analysées par différents modèles (Young-Fletcher, Trodahl and Pescahnskii) ainsi que par la théorie de Lifshitz-Kosevich (LK) de l'effet dHvA. On a démontré que la théorie de LK est valable dans le cas des oscillations quantiques du pouvoir thermoélectrique dans les composés des fermions lourds. Les paramètres fondamentaux obtenus de la surface de Fermi sont en bon accord avec les calculs de la surface de Fermi. On a aussi vérifié que la contribution oscillatoire domine le signal thermoélectrique et persiste pour des températures jusqu'à un ordre de magnitude supérieure aux sondes traditionnelles (SdH et dHvA).

Dans le dernier fermion lourd de cette étude, $CeRh_2Si_2$, une comparaison entre la suppression du domaine AF par le champ magnétique et par la pression est donnée. Ce composé se caractérisé par des échelles d'énergie liées à l'effet RRKY et à l'effet Kondo similaires ce qui permet de faire basculer le système d'un magnétisme localisé (où RKKY domine) vers un magnétisme itinérant (où Kondo domine) assez facilement par l'application d'un champ magnétique et/ou d'une pression. La transition de la phase AF sous champ magnétique vers une phase paramagnétique polarisée (PPM) correspond à une transition du premier ordre.

L'évolution du pouvoir thermoélectrique sous pression montre que les fluctuations de spin et/ou de valence et les instabilités magnétiques liées à la suppression du domaine AF sont étendues dans une large gamme de pression autour de p_c. Si on tient compte des mesures de dHvA qui montrent le fort changement de la surface de Fermi à p_c, on peut conclure que la transition sous pression est une transition faiblement du premier ordre. La comparaison de S/T en fonction de H/H_c et en fonction de P/p_c montre que le pouvoir thermoélectrique de la phase PM est positive pendant que celle de la phase PPM est négative. Cela indique que les phases non ordonnées, PM et PPM, sont différentes. Une analyse de la surface de Fermi de la phase AF_2 a été réalisée dans ce composé. De nouvelles fréquences ont été détectées ainsi que le "splitting" de la fréquence ν dû à la dépendance de la masse effective selon le spin.

Ces études des ordres en compétition ont montré que le pouvoir thermoélectrique est une sonde très sensible pour l'étude des transitions de phases. Les transitions de premier ordre sont caractérisées pour présenter une discontinuité du pouvoir thermoélectrique et parfois, un changement de signe. Cela dépend des modifications de la surface de Fermi à la transition de phase et de la direction vers laquelle on mesure. Les transitions de phases de deuxième ordre présentent un changement de la pente et les "crossover" une anomalie dans le signal du coefficient thermoélectrique. Néanmoins, la différence dans le signal du pouvoir thermoélectrique entre transitions de phase de deuxième ordre et "crossover" n'est pas très claire.

Les études microscopiques utilisant le pouvoir thermoélectrique comme sonde macroscopique ont permis de démontrer que la partie oscillatoire révèle les paramètres fondamentaux de la surface de Fermi. Notre étude valide l'utilisation des oscillations quantiques thermoélectriques pour caractériser la surface de Fermi (masse effective, température de Dingle et libre parcours moyen des orbites) à partir de l'analyse de l'évolution des fréquences selon la théorie de Lifshitz-Kosevich. De plus, la contribution oscillatoire domine et apparait dans une gamme de températures plus haute que les autres sondes traditionnelles (dHvA et SdH); ce qui facilite son observation.

Bibliography

[Abe et al., 1998] Abe, H., Kitazawa, H., and Aoki, H. (1998). De Haas-van Alphen Effect Study of $CeRh_2Si_2$. J. Phys. Soc. Jpn., **67**:1852.

[Abe et al., 1999] Abe, H., Suzuki, H., and Kitazawa, H. (1999). High-Field Magnetization of $CeRh_2(Si_{1-x}Ge_x)_2$. *PhysicaB : Cond.Matt.*, **259&261** : 56.

[Abe et al., 1997] Abe, H., Suzuki, H., Kitazawa, H., Matsumo, T., and Kido, G. (1997). Successive Field Induced Magnetic Phase Transitions of Heavy Fermion Compound $CeRh_2Si_2$. J. Phys. Soc. Jpn., **66**:2525.

[Abrikosov and Khalatnikov, 1959] Abrikosov, A. A. and Khalatnikov, I. M. (1959). The Theory of a Fermi Liquid (the Properties of Liquid ^{3}He at Low Temperatures). Rep. Prog. Phys, **22**:329.

[Amato and Sierro, 1985] Amato, A. and Sierro, J. (1985). Thermopower of CeM_2Si_2 (M = Au, Pd, Rh, Ru) Compounds. J. Magn. Magn. Mater., **47&48**:526.

[Aoki et al., 2011] Aoki, D., Combier, T., Taufour, V., Matsuda, T. D., Knebel, G., Kotegawa, H., and Flouquet, J. (2011). Ferromagnetic Quantum Critical Endpoint in UCoAl. J. Phys. Soc. Jpn., **80**:094711.

[Araki et al., 1998] Araki, S., Misawa, A., Settai, R., Takeuchi, T., and Ōnuki, Y. (1998). Thermal Expansion and de Haas-van Alphen Effect of $CeRh_2Si_2$. J. Phys. Soc. Jpn., **67**:2915.

[Araki et al., 2003] Araki, S., Nakashima, M., and Settai, R. (2003). Superconductivity in $CeRh_2Si_2$ under Pressure. Acta Phys. Pol. B, **34**:439.

[Araki et al., 2002] Araki, S., Nakashima, M., Settai, R., Kobayashi, T. C., and Ōnuki, Y. (2002). Pressure-Induced Superconductivity in an Antiferromagnet $CeRh_2Si_2$. J. Phys.: Condens. Matter, **14**:L377.

[Araki et al., 2001] Araki, S., Settai, R., Kobayashi, T. C., Harima, H., and Ōnukii, Y. (2001). Fermi Surface Instability in $CeRh_2Si_2$ under Pressure. Phys. Rev. B, **64**:224417.

[Banerjee et al., 2008] Banerjee, A., Fauqué, B., Izawa, K., Miyake, A., Sheikin, I., Flouquet, J., Lenoir, B., and Behnia, K. (2008). Transport Anomalies across the Quantum Limit in Semimetallic $Bi_{0.96}Sb_{0.04}$. Phys. Rev. B, **78**:161103.

[Behnia, 2009] Behnia, K. (2009). The Nernst Effect and the Boundaries of the Fermi Liquid Picture. J. Phys.: Condens. Matter, **21**:113101.

[Behnia et al., 2004] Behnia, K., Jaccard, D., and Flouquet, J. (2004). On the Thermoelectricity of Correlated Electrons in the Zero-Temperature Limit. J. Phys.: Condens. Matter, **16**:5187.

[Behnia et al., 2007] Behnia, K., Méasson, M.-A., and Kopelevich, Y. (2007). Oscillating Nernst-Ettingshausen Effect in Bismuth across the Quantum Limit. Phys. Rev. Lett., **98**:166602.

[Belitz et al., 2005] Belitz, D., Kirkpatrick, T. R., and Rollbühler, J. (2005). Tricritical Behavior in Itinerant Quantum Ferromagnets. Phys. Rev. Lett., **94**:247205.

[Belitz et al., 1999] Belitz, D., Kirkpatrick, T. R., and Vojta, T. (1999). First Order Transitions and Multicritical Points in Weak Itinerant Ferromagnets. Phys. Rev. Lett., **82**:4707.

[Betsuyaku and Harima, 2000] Betsuyaku, K. and Harima, H. (2000). Electronic Structure and Electric Field Gradient of UCoAl. Physica B, **281&282**:778.

[Biasini and Troc, 2003] Biasini, M. and Troc, R. (2003). Fermi Surface of UGe_2 in the Paramagnetic Phase. Phys. Rev. B, **68**:245118.

[Boulet et al., 1997] Boulet, P., Daoudi, A., Potel, M., Noël, H., Gross, G., André, G., and Bourée, F. (1997). Crystal and Magnetic Structure of the Uranium Digermanide UGe_2. J. Alloys Compounds, **247**:104.

[Boursier, 2005] Boursier, R. (2005). Le Reseau Kondo $CeRh_2Si_2$: Magnetisme, Localisation des Electrons et Transport. PhD thesis, Universite Joseph Fourier.

[Boursier et al., 2008] Boursier, R., Villaume, A., Lapertot, G., Aoki, D., Knebel, G., and Flouquet, J. (2008). Comparison between Ce and Yb Heavy Fermion Compounds: $CeRh_2Si_2$ versus $YbRh_2Si_2$. Physica B: Cond. Matt., **403**:726. Proceedings of the International Conference on Strongly Correlated Electron Systems.

[Chaussy et al., 1981] Chaussy, J., Guessous, A., and Mazuer, J. (1981). Simultaneous Measurements of Thermopower, Thermal Conductivity and Electrical Resistivity between 1.2 and 350 K. Rev. Sci. Instr., **52**:1721.

[Coleman, 2007] Coleman, P. (2007). Heavy Fermions: Electrons at the Edge of Magnetism, volume 1 of Handbook of Magnetism and Advanced Magnetic Materials, pages 95–148. John Wiley & Sons, Ltd.

[Colombier and Braithwaite, 2007] Colombier, E. and Braithwaite, D. (2007). Simple Adaptation of the Bridgman High Pressure Technique for use with Liquid Media. Rev. Sci. Instr., **78**:093903.

[Combier et al., 2013] Combier, T., Aokio, D., Knebelm, G., and Flouquet, J. (2013). Ferromagnetic Quantum Criticality Studied by Hall Effect Measurements in UCoAl. J. Phys. Soc. Jpn., **82**:104705.

[Doniach, 1977] Doniach, S. (1977). The Kondo Lattice and Weak Antiferromagnetism. Physica B+C, **91**:231.

[Dzyaloshinskii, 1965] Dzyaloshinskii, I. (1965). The Theory of Helicoidal Structures in Antiferromagnets. II. Metals. J. Exp. Theor. Phys., **20**:223.

[Enss and Hunklinger, 2005] Enss, C. and Hunklinger, S. (2005). Low-Temperature Physics. Springer Science & Business Media.

[Eriksson et al., 1989] Eriksson, O., Johansson, B., and Brooks, M. S. S. (1989). Meta-Magnetism in UCoAl. J. Phys.: Condens. Matter, **1**:4005.

[Fletcher, 1981] Fletcher, R. (1981). On the Amplitude of the Quantum Oscillations in the Thermopower of Metals. J. Low Temp. Phys., **43**:363.

[Flouquet, 2005] Flouquet, J. (2005). Progress in Low Temperature Physics, Vol. 15, chapter 2, page 139. Elsevier, Amsterdam.

[Gegenwart and Steglich, 2008] Gegenwart, P., S. Q. and Steglich, F. (2008). Quantum Criticality in Heavy-Fermion Metals. Nat. Phys., **4**:186.

[Graf et al., 1998] Graf, T., Hundley, M. F., Modler, R., Movshovich, R., Thompson, J. D., Mandrus, D., Fisher, R. A., and Phillips, N. E. (1998). Magnetic Phase Transitions in $CeRh_2Si_2$: Specific Heat, Susceptibility and Resistance Studies. Phys. Rev. B, **57**:7442.

[Graf et al., 1997] Graf, T., Thompson, J. D., Hundley, M. F., Movshovich, R., Fisk, Z., Mandrus, D., Fisher, R. A., and Phillips, N. E. (1997). Comparison of $CeRh_2Si_2$ and $CeRh_{2-x}Ru_xSi_2$ Near their Magnetic-Nonmagnetic Boundaries. Phys. Rev. Lett., **78**:3769.

[Haga et al., 2002] Haga, Y., Nakashima, M., Settai, R., Ikeda, S., Okubo, T., Araki, S., Kobayashi, T. C., Tateiwa, N., and Ōnuki, Y. (2002). A Change of the Fermi Surface across the Metamagnetic Transition under Pressure in UGe_2. J. Phys.: Condens. Matter, **14**:L125.

[Hardy et al., 2009] Hardy, F., Meingast, C., Taufour, V., Flouquet, J., v. Löhneysen, H., Fisher, R. A., Phillips, N. E., Huxley, A., and Lashley, J. C. (2009). Two Magnetic Grüneisen Parameters in the Ferromagnetic Superconductor UGe_2. Phys. Rev. B, **80**:174521.

[Hill, 1970] Hill, H. H. (1970). Nucl. Metall., **17**:2.

[Hoshino and Kuramoto, 2013] Hoshino, S. and Kuramoto, Y. (2013). Itinerant Versus Localized Heavy-Electron Magnetism. Phys. Rev. Lett., **111**:026401.

[Ishii et al., 2003] Ishii, Y., Kosaka, M., Uwatoko, Y., Andreev, A., and Sechovský, V. (2003). Ferromagnetism Induced in UCoAl under Uniaxial Pressure. Physica B: Cond. Matt., **334**:160.

[Jaccard and Sengupta, 2010] Jaccard, D. and Sengupta, K. (2010). Multiprobe Experiments under High Pressure: Resistivity, Magnetic Susceptibility, Heat Capacity and Thermopower Measurements around 5 GPa. Rev. Sci. Instr., **81**:043908.

[Javorský et al., 2001] Javorský, P., Sechovský, V., Schweizer, J., Bourdarot, F., Lelièvre-Berna, E., Andreev, A. V., and Shiokawa, Y. (2001). Magnetization Densities in UCoAl Studied by Polarized Neutron Diffraction. Phys. Rev. B, **63**:064423.

[Karube et al., 2012] Karube, K., Hattori, T., Kitagawa, S., Ishida, K., Kimura, N., and Komatsubara, T. (2012). Universality and Critical Behavior at the Critical Endpoint in the Itinerant-Electron Metamagnet UCoAl. Phys. Rev. B, **86**:024428.

[Karube et al., 2014] Karube, K., Kitagawa, S., Hattori, T., Ishida, K., Kimura, N., and Komatsubara, T. (2014). Anisotropic Uniaxial Pressure Response in UCoAl Studied by Nuclear Magnetic Resonance Measurement. J. Phys. Soc. Jpn., **83**:084706.

[Kataoka and Nakanishi, 1981] Kataoka, M. and Nakanishi, O. (1981). Helical Spin Density Wave Due to Antisymmetric Exchange Interaction. J. Phys. Soc. Jpn., **50**:3888.

[Kawarazaki et al., 2000] Kawarazaki, S., Sato, M., Miyako, Y., Chigusa, N., Watanabe, K., Metoki, N., Koike, Y., and Nishi, M. (2000). Ground-State Magnetic Structure of $CeRh_2Si_2$ and the Response to Hydrostatic Pressure as Studied by Neutron Diffraction. Phys. Rev. B, **61**:4167.

[Kirichenko et al., 2008] Kirichenko, O. V., Kozlov, I. V., Krstovska, D., and Peschanski, V. G. (2008). Quantum Oscillations of the Thermomagnetic Coefficients of Layered Conductors in a Strong Magnetic Field. Low Temp. Phys., **34**:538.

[Knafo et al., 2010] Knafo, W., Aoki, D., Vignolles, D., Vignolle, B., Klein, Y., Jaudet, C., Villaume, A., Proust, C., and Flouquet, J. (2010). High-Field Metamagnetism in the Antiferromagnet $CeRh_2Si_2$. Phys. Rev. B, **81**:094403.

[Knebel et al., 2006] Knebel, G., Boursier, R., Hassinger, E., Lapertot, G., Niklowitz, P. G., Pourret, A., Salce, B., Sanchez, J. P., Sheikin, I., Bonville, P., Harima, H., and Flouquet, J. (2006). Localization of $4f$ State in $YbRh_2Si_2$ under Magnetic Field and High Pressure: Comparison with $CeRh_2Si_2$. J. Phys. Soc. Jpn., **75**:114709.

[Kolomiets et al., 1999] Kolomiets, A. V., Havela, L., Sechovsky, V., Delong, L. E., Watkins, D. B., and Andreev, A. V. (1999). Non-Fermi-liquid behaviour of UCoAl. Physica B, **261**:415.

[Kondo, 1964] Kondo, J. (1964). Resistance Minimum in Dilute Magnetic Alloys. Progr. Theor. Exp. Phys., **32**:37.

[Kotegawa et al., 2011] Kotegawa, H., Taufour, V., Aoki, D., Knebel, G., and Flouquet, J. (2011). Evolution toward Quantum Critical End Point in UGe_2. J. Phys. Soc. Jpn., **80**:083703.

[Kucera et al., 2002] Kucera, M., Kunes, J., Kolomiets, A., Divis, M., Andreev, A. V., Sechovský, V., Kappler, J.-P., and Rogalev, A. (2002). X-Ray Magnetic Circular Dichroism Studies of $5f$ Magnetism in UCoAl and UPtAl. Phys. Rev. B, **66**:144405.

[Laliberte et al., 2011] Laliberte, F., Chang, J., Doiron-Leyraud, N., Hassinger, E., Daou, R., Rondeau, M., Ramshaw, B., Liang, R., Bonn, D., Hardy, W., Pyon, S., Takayama, T., Takagi, H., Sheikin, I., Malone, L., Proust, C., Behnia, K., and Taillefer, L. (2011). Fermi-Surface Reconstruction by Stripe Order in Cuprate Superconductors. Nat. Commun., **2**:432.

[Lashley et al., 2006] Lashley, J., Fisher, R., Flouquet, J., Hardy, F., Huxley, A., and Phillips, N. (2006). Ambient-Pressure Specific Heat of Single-Crystal. Physica B: Cond. Matt., **378&380**:961.

[Lee et al., 2007] Lee, M., Onose, Y., Tokura, Y., and Ong, N. P. (2007). Hidden Constant in the Anomalous Hall Effect of High-Purity Magnet MnSi. Phys. Rev. B, **75**:172403.

[Lee et al., 2004] Lee, W.-L., Watauchi, S., Miller, V. L., Cava, R. J., and Ong, N. P. (2004). Anomalous Hall Heat Current and Nernst Effect in the $CuCr_2Se_{4-x}Br_x$ Ferromagnet. Phys. Rev. Lett., **93**:226601.

[Löhneysen et al., 2007] Löhneysen, H. V., Rosch, A., Votja, M., and Wölfle, P. (2007). Fermi-Liquid Instabilities at Magnetic Quantum Phase Transitions. Rev. Mod. Phys., **79**:1015.

[Lounasmaa, 1979] Lounasmaa, O. V. (1979). Dilution Refrigeration. J. Phys. E: Sci. Instr., **12**:668.

[Luttinger and Karplus, 1954] Luttinger, J. M. and Karplus, R. (1954). Hall Effect in Ferromagnetics. Phys. Rev., **94**:782.

[MacDonald, 2006] MacDonald, D. K. C. (2006). Thermoelectricity: An Introduction to the Principles. Dover Books on Physics.

[Matsuda et al., 2000] Matsuda, T. D., Sugawara, H., Aoki, Y., Sato, H., Andreev, A. V., Shiokawa, Y., Sechovsky, V., and Havela, L. (2000). Transport Properties of the Anisotropic Itinerant-Electron Metamagnet UCoAl. Phys. Rev. B, **62**:13852.

[Matsuda et al., 2013] Matsuda, T. D., Tateiwa, N., Yamamoto, E., Haga, Y., Ōnuki, Y., Aoki, D., Flouquet, J., and Fisk, Z. (2013). Magnetic Phase Diagram of UCoAl. J. Korean Phys. Soc, **63**:575.

[Millis, 1993] Millis, A. J. (1993). Effect of a Nonzero Temperature on Quantum Critical Points in Itinerant Fermion Systems. Phys. Rev. B, **48**:7183.

[Miyake and Ikeda, 2006] Miyake, K. and Ikeda, H. (2006). True Meaning of "Localizeded" f-Electrons Measured by dHvA Experiments in Ce-Based Heavy Fermion Metals. J. Phys. Soc. Jpn., **75**:033704.

[Miyake and Kohno, 2005] Miyake, K. and Kohno, H. (2005). Theory of Quasi-Universal Ratio of Seebeck Coefficient to Specific Heat in Zero-Temperature Limit in Correlated Metals. J. Phys. Soc. Jpn., **75**:254.

[Moriya, 1985] Moriya, T. (1985). Spin Fluctuations in Itinerant Electron Magnetism. Springer-Verlag.

[Moriya and Kawabata, 1973] Moriya, T. and Kawabata, A. (1973). Effect of Spin Fluctuations on Itinerant Electron Ferromagnetism. J. Phys. Soc. Jpn., **34**:639.

[Movshovich et al., 1996] Movshovich, R., Graf, T., Mandrus, D., Thompson, J. D., Smith, J. L., and Fisk, Z. (1996). Superconductivity in Heavy-Fermion $CeRh_2Si_2$. Phys. Rev. B, **53**:8241.

[Mushnikov et al., 2002] Mushnikov, N. V., Goto, T., Andreev, A. V., Sechovský, V., and Yamada, H. (2002). Effect of External Pressure on the Magnetism of $UCo_{0.98}Fe_{0.02}Al$. Phys. Rev. B, **66**:064433.

[Mushnikov et al., 1999] Mushnikov, N. V., Goto, T., Kamishima, K., Yamada, H., Andreev, A. V., Shiokawa, Y., Iwao, A., and Sechovsky, V. (1999). Magnetic Properties of the 5f Itinerant Electron Metamagnet UCoAl under High Pressure. Phys. Rev. B, **59**:6877.

[Nagaosa et al., 2010] Nagaosa, N., Sinova, J., Onoda, S., MacDonald, A. H., and Ong, N. P. (2010). Anomalous Hall Effect. Rev. Mod. Phys., **82**:1539.

[Nohara et al., 2011] Nohara, H., Kotegawa, H., Tou, H., Matsuda, T. D., Yamamoto, E., Haga, Y., Fisk, Z., Ōnuki, Y., Aoki, D., and Flouquet, J. (2011). Strong Longitudinal Magnetic Fluctuations Near Critical End Point in UCoAl: A ^{59}Co-NMR Study. J. Phys. Soc. Jpn., **80**:093707.

[N.W. Ashcroft, 1976] N.W. Ashcroft, N. M. (1976). Solid State Physics. Brooks/cole Cengage Learning.

[Oikawa et al., 1996] Oikawa, K., Kamiyama, T., Asano, H., Ōnuki, Y., and Kohgi, M. (1996). Crystal Structure of UGe_2. J. Phys. Soc. Jpn., **65**:3229.

[Onoda and Nagaosa, 2002] Onoda, M. and Nagaosa, N. (2002). Topological Nature of Anomalous Hall Effect in Ferromagnets. J. Phys. Soc. Jpn., **71**:19.

[Onoda et al., 2008] Onoda, S., Sugimoto, N., and Nagaosa, N. (2008). Quantum Transport Theory of Anomalous Electric, Thermoelectric and Thermal Hall Effects in Ferromagnets. Phys. Rev. B, **77**:165103.

[Onose et al., 2007] Onose, Y., Li, L., Petrovic, C., and Ong, N. (2007). Anomalous Thermopower and Nernst Effect in $CeCoIn_5$: Loss of Entropy Current in Precursor State. EPL, **79**:17006.

[Ōnuki et al., 1992] Ōnuki, Y., Ukon, I., Won Yun, S., Umehara, I., Satoh, K., Fukuhara, T., Sato, H., Takayanagi, S., Shikama, M., and Ochiai, A. (1992). Magnetic and Electrical Properties of U-Ge Intermetallic Compounds. J. Phys. Soc. Jpn., **61**:293.

[Ōnuki et al., 1991] Ōnuki, Y., Won Yun, S., Ukon, I., Umehara, I., Satoh, K., Sakamoto, I., Hunt, M., Meeson, P., Probst, P., and Springford, M. (1991). High Field Magnetoresistance and de Haas-van Alphen Effect in UGe_2. J. Phys. Soc. Jpn., **60**:2127.

[Pantsulaya and Varlamov, 1989] Pantsulaya, A. and Varlamov, A. (1989). Possibility of Observation of Giant Oscillations of Thermoelectric Power in Normal Metal. Phys. Lett. A, **136**:317.

[Pfleiderer and Huxley, 2002] Pfleiderer, C. and Huxley, A. D. (2002). Pressure Dependence of the Magnetization in the Ferromagnetic Superconductor UGe_2. Phys. Rev. Lett., **89**:147005.

[Pippard, 1965] Pippard, A. B. (1965). Magnetic Breakdown in a Dislocated Lattice. Proc. R. Soc. Lond. A., **287**:165.

[Raymond and Huxley, 2004] Raymond, S. and Huxley, A. (2004). Spin Dynamics of the Ferromagnetic Superconductor UGe_2. Physica B: Cond. Matt., **350**:33. Proceedings of the Third European Conference on Neutron Scattering.

[Ruderman and Kittel, 1954] Ruderman, M. A. and Kittel, C. (1954). Indirect Exchange Coupling of Nuclear Magnetic Moments by Conduction Electrons. Phys. Rev., **96**:99.

[Sakon et al., 2007] Sakon, T., Saito, S., Koyama, K., Awaji, S., Sato, I., Nojima, T., Watanabe, K., and Sato, N. K. (2007). Experimental Investigation of Giant Magnetocrystalline Anisotropy of UGe_2. Physica Scripta, **75**:546.

[Samsel-Czekała et al., 2011] Samsel-Czekała, M., Werwiński, M., Szajek, A., Chełkowska, G., and Troć, R. (2011). Electronic Structure of UGe_2 at Ambient Pressure: Comparison with X-Ray Photoemission Spectra. Intermetallics, **19**:1411.

[Satoh et al., 1992] Satoh, K., Yun, S. W., Umehara, I., Ōnuki, Y., Uji, S., Shimizu, T., and Aoki, H. (1992). De Haas-van Alphen Effect in UGe_2. J. Phys. Soc. Jpn., **61**:1827.

[Saxena et al., 2000] Saxena, S. S., P. Agarwal, K. A., Grosche, F. M., Haselwimmer, R. K. W., Steiner, M. J., Pugh, E., Walker, I. R., Julian, S. R., Monthoux, P., Lonzarich, G. G., Huxley, A., Sheikin, I., Braithwaite, D., and Flouquet, J. (2000). Superconductivity on the Border of Itinerant-Electron Ferromagnetism in UGe_2. Nature, **406**:587.

[Schofield, 2010] Schofield, A. J. (2010). Quantum Criticality and Novel Phases: Summary and Outlook. Phys. Status Solidi (b), **247**:563.

[Schulz, 1995] Schulz, H. (1995). Fermi Liquids and Non-Fermi Liquids, volume 61 of Les Houches Summer School Session. Elsevier Science Public B. V.

[Sechovsky et al., 1986] Sechovsky, V., Havela, L., de Boer, F., Franse, J., Veenhuizen, P., Sebek, J., Stehno, J., and Andreev, A. (1986). Systematics across the UTX Series (T = Ru, Co, Ni; X = Al, Ga, Sn) of High-Field and Low-Temperature Properties of Non-Ferromagnetic Compounds. Physica B+C, **142**:283.

[Sengupta et al., 2010] Sengupta, K., Forthaus, M. K., Kubo, H., Katoh, K., Umeo, K., Takabatake, T., and Abd-Elmeguid, M. M. (2010). Geometrical Frustration versus Magnetic Order in the Heavy-Fermion Antiferromagnet YbAgGe under High Pressure. Phys. Rev. B, **81**:125129.

[Settai et al., 2003] Settai, R., Araki, S., Shishido, H., Inada, Y., Haga, Y., Yamamoto, E., Kobayashi, T., Tateiwa, N., and Ōnuki, Y. (2003). De Haas Van Alphen Experiments under Extreme Conditions of Low Temperature, High Field and High Pressure, for High-Quality Cerium and Uranium Compounds. J. Magn. Magn. Mater., **262**:399. Special Issue on the Occasion of the Hanoi International Symposium on Magnetism:Cryolab 25.

[Settai et al., 2002] Settai, R., Nakashima, M., Araki, S., Haga, Y., Kobayashi, T. C., Tateiwa, N., Yamagami, H., and Ōnuki, Y. (2002). A Change of the Fermi Surface in UGe_2 across the Critical Pressure. J. Phys.: Condens. Matter, **14**:L29.

[Severing et al., 1989] Severing, A., Holland-Moritz, E., and Frick, B. (1989). Spin dynamics of ceX_2si$_2$ (x=au, pd, rh, ru). Phys. Rev. B, **39**:4164.

[Sheikin, 2013] Sheikin, I. (2013). HDR: Heavy Fermions in High Magnetic Fields.

[Shoenberg, 1984] Shoenberg, D. (1984). Magnetic Oscillations in Metals. Cambridge Monographs on Physics.

[Shubnikov and de Haas, 1930] Shubnikov and de Haas (1930). A New Phenomenon in the Change of Resistance in a Magnetic Field of Single Crystals of Bismuth. Nature, **126**:500.

[Si and Steglich, 2010] Si, Q. and Steglich, F. (2010). Heavy Fermions and Quantum Phase Transitions. Science (New York, N.Y.), **329**:1161.

[Sidorov and Sadykov, 2005] Sidorov, V. A. and Sadykov, R. A. (2005). Hydrostatic Limits of Fluorinert Liquids Used for Neutron and Transport Studies at High Pressure. J. Phys.: Condens. Matter, **17**:S3005.

[Stewart, 1984] Stewart, G. R. (1984). Heavy-Fermion Systems. Rev. Mod. Phys., **56**:755.

[Stewart, 2006] Stewart, G. R. (2006). Addendum: Non-Fermi-Liquid Behavior in d- and f-Electron Metals. Rev. Mod. Phys., **78**:743.

[Sumiyama et al., 1986] Sumiyama, A., Oda, Y., Nagano, H., Ōnuki, Y., Shibutani, K., and Komatsubara, T. (1986). Coherent Kondo State in a Dense Kondo Substance: $Ce_xLa1 - xCu_6$. J. Phys. Soc. Jpn., **55**:1294.

[Takashita et al., 1996] Takashita, M., Aoki, H., Terashima, T., Uji, S., Maezawa, K., Settai, R., and Ōnuki, Y. (1996). dHvA Effect Study of Metamagnetic Transition in $CeRu_2Si_2$ II - The State above the Metamagnetic Transition. J. Phys. Soc. Jpn., **65**:515.

[Tateiwa et al., 2001] Tateiwa, N., Hanazono, K., Kobayashi, T. C., Amaya, K., Inoue, T., Kindo, K., Koike, Y., Metoki, N., Haga, Y., Settai, R., and Ōnuki, Y. (2001). Magnetic Properties of a Pressure-Induced Superconductor UGe_2. J. Phys. Soc. Jpn., **70**:2876.

[Taufour et al., 2010] Taufour, V., Aoki, D., Knebel, G., and Flouquet, J. (2010). Tricritical Point and Wing Structure in the Itinerant Ferromagnet UGe_2. Phys. Rev. Lett., **105**:217201.

[Terashima et al., 2002] Terashima, T., Matsumoto, T., Terakura, C., Uji, S., Kimura, N., Endo, M., Komatsubara, T., Aoki, H., and Maezawa, K. (2002). Magnetic Phase Diagram and the Pressure and Field Dependence of the Fermi Surface in UGe_2. Phys. Rev. B, **65**:174501.

[Trodahl and Blatt, 1969] Trodahl, H. and Blatt, F. (1969). Quantum Oscillations in Peltier Effect of Zinc. Phys. Rev., **180**:706.

[Uchida et al., 2008] Uchida, K., Takahashi, S., Harii, K., Ieda, J., Koshibae, W., Ando, K., Maekawa, S., and Saitoh, E. (2008). Observation of the Spin Seebeck Effect. Nature, **455**:778.

[Villaume et al., 2008] Villaume, A., Aoki, D., Haga, Y., Knebel, G., Boursier, R., and Flouquet, J. (2008). Collapse of Antiferromagnetism in $CeRh_2Si_2$: Volume Versus Entropy. J. Phys.: Condens. Matter, **20**:015203.

[Wilhelm and Jaccard, 2004] Wilhelm, H. and Jaccard, D. (2004). Probing the Phase Diagram of $CeRu_2Ge_2$ by Thermopower at High Pressure. Phys. Rev. B, **69**:214408.

[Wilhelm et al., 2005] Wilhelm, H., Jaccard, D., Zlatic, V., Monnier, R., Delley, B., and Coqblin, B. (2005). High-Pressure Transport Properties of $CeRu_2Ge_2$. J. Phys.: Condens. Matter, **17**:S823.

[Willers et al., 2012] Willers, T., Adroja, D., Rainford, B., Hu, Z., Hollmann, N., Körner, P., Chin, Y., Schmitz, D., Hsieh, H., Lin, H., Chen, C., Bauer, E., Sarrao, J., McClellan, K., Byler, D., Geibel, C., Steglich, F., Aoki, H., Lejay, P., Tanaka, A., Tjeng, L., and Severing, A. (2012). Spectroscopic Determination of Crystal-Field Levels in $CeRh_2Si_2$ and $CeRu_2Si_2$ and of the $4f^0$ Contributions in CeM_2Si_2 (M=Cu, Ru, Rh, Pd, and Au). Phys. Rev. B, **85**:035117.

[Yokogawa et al., 2007] Yokogawa, K., Murata, K., Yoshino, H., and Aoyama, S. (2007). Solidification of High-Pressure Medium Daphne 7373. Jpn. J. Appl. Phys., **46**:3636.

[Zlatić et al., 2007] Zlatić, V., Monnier, R., Freericks, J. K., and Becker, K. W. (2007). Relationship Between the Thermopower and Entropy of Strongly Correlated Electron Systems. Phys. Rev. B, **76**:085122.

List of Figures

List of Tables